SYNTHESIS AND EVALUATION OF BIOCERAMICS FOR ORTHOPEDICS AND TISSUE

CULTURE APPLICATIONS

by

HANDE DEMİRKIRAN

Presented to the Faculty of the Graduate School of

The University of Texas at Arlington in Partial Fulfillment

of the Requirements

for the Degree of

DOCTOR OF PHILOSOPHY

THE UNIVERSITY OF TEXAS AT ARLINGTON

May 2009

Dedication

To my parents Nilgün and Selçuk Demirkıran for their belief in my education…

ACKNOWLEDGEMENTS

ABSTRACT

SYNTHESIS AND EVALUATION OF BIOCERAMICS FOR ORTHOPEDICS AND TISSUE

CULTURE APPLICATIONS

Hande Demirkiran, PhD.

The University of Texas at Arlington, 2009

Supervising Professor: Pranesh B. Aswath

Hydroxyapatite is the most well known phosphate in the biologically active phosphate ceramic family by virtue of its similarity to natural bone mineral. Among all bioglass compositions Bioglass®45S5 is one of the most bioactive glasses. This study initially started by adding different amounts (1, 2.5, 5, 10, and 25 wt. %) of Bioglass®45S5 to synthetic hydroxyapatite in order to improve the bioactivity of these bioceramics.

The chemistries formed by sintering and their effect on different material properties including bioactivity were identified by using various techniques, such as powder and thin film x-ray diffraction, scanning electron microscopy coupled with energy dispersive X-ray spectroscopy, X-ray absorption near edge spectroscopy, compression test, and nano indentation. All the results demonstrated that 10 and 25 wt. % Bioglass®45S5 addition to hydroxyapatite and sintering at 1200ºC for 4 hours yield new compositions with main $Ca_5(PO_4)_2SiO_4$ and $Na_3Ca_6(PO_4)_5$ crystalline phases dispersed in silicate glassy matrices, respectively. In addition, *in vitro* bioactivity tests such as bone like apatite formation in simulated body fluid and bone marrow stromal cell culture have shown that the crystalline and amorphous phases have an important role on improving bioactivity of these bioceramic compositions. Besides, compression test and nano indentation has given important information on compression strength and nano structure

properties of these newly composed bioceramic materials and the bone like apatite layers formed on them, respectively. Finally, the effect of silicate addition on both formation and bioactivity of $Na_3Ca_6(PO_4)_5$ bioceramics were shown. These findings and different techniques used assisted to develop a phenomenological approach to demonstrate how the novel bioceramic compositions were composed and aid improving bioactivity of known bioceramic materials.

TABLE OF CONTENTS

viii

LIST OF ILLUSTRATIONS

xv

xvi

LIST OF TABLES

xxi

CHAPTER 1

INTRODUCTION

Biomaterials are designed and fabricated for implantation within or incorporation with a living system to replace or repair the living tissues or organs which form an interface between the living and non-living parts [1, 2]. Biomaterials are based on polymers, metals, ceramics, or composites of these [3]. There is no foreign material placed within a living body that is completely compatible. The only substances that have complete compatibility are those produced by the body itself (autogenous), and any other material that is recognized as foreign initiates some type of reaction. Therefore, it has been well accepted that all biomaterials elicit a specific biological response at the interface of the material and the tissue, and this response defines their role in the body [4]. According to the tissue response, biomaterials are categorized into four groups as shown in Table 1.1. The first category is toxic, in which case the tissue surrounding the implanted material will die or be damaged. The second category of interaction is non-toxic and biologically inactive, living tissue will form a capsule around the material. Metals and most polymers exhibit this kind of interaction. Metals are used as joint replacements, bone plates, or dental root implants and strong, tough, and ductile materials. However, they are dense and can cause defective body reactions. The polymers are used as replacement of soft tissues and are resilient, but they are not strong and easily deformed by time. Resorbable materials, the third category, are non-toxic and dissolve to be replaced by surrounding tissue. The dissolved products of the material should be non-toxic and easily disposed of without any damage to the cells. Some polymers and ceramics fit into this group. The last category is non-toxic and biologically active materials. In this interaction, an interfacial bond will form between the implanted material and the surrounding tissue. They are called bioactive materials, and most ceramics display this kind of interaction. Ceramics are used widely in dental applications, are very biologically compatible, do

1

not ionize in the body, and have high compression strength. However, they are brittle and not resilient. Therefore they are chosen to be used either in non-load bearing places or as composites [1, 3].

Table 1.1: Consequences of implant – tissue interaction [1].

Implant – Tissue Interaction	Consequence
Toxic	Tissue dies
Biologically nearly inert	Tissue forms a non-adherent fibrous capsule around the implant
Dissolution of implant	Tissue replaces implant
Bioactive	Tissue forms an interfacial bond with the implant

Ceramics started to be systematically investigated in biomedical engineering field in the early 1970s, and have been designed, synthesized, and extensively used over the last 40 years. Ceramics specific to biomedical applications are called bioceramics [5]. Bioceramics are more biocompatible with an organism than other implanted materials, and they have less effect on the immune system. They can be adapted to a wider range of functional possibilities because of their broader range of chemical, mechanical, and biological properties which ensures the lifetime requirements in the organisms. A characteristic feature of the reaction of a material with a bio-system is the defining role of its structure. Therefore, ceramics by their nature are optimally suited for use in bio-systems. The use of bioceramics in the biomedical field is substantially more effective than that of any other implanted materials [6].

1.1 Drive for The Research

Hydroxyapatite ($Ca_{10}(PO_4)_6(OH)_2$) is the most well known phosphate in the biologically active phosphate ceramic family by virtue of its similarity to natural bone mineral. Synthetic and biologically harvested hydroxyapatite finds a variety of biological applications and elicits the formation of an apatite layer at the interface with bone tissue [7-11]. The most common

applications of hydroxyapatite include bone repair in prosthetics [12], and dental applications [13]. Due to its osteoconductive nature hydroxyapatite is known to form a direct contact with tissues without the formation of a fibrous intermediate layer. However, the use of its synthetic form has often led to a limited regeneration rate of bone defects, which is attributable to its slow degradation rate and low bioactivity as compared with the biological form of apatite [14-17]. In addition, even it supports osteogenic differentiation of bone marrow stromal cells [18]. Hydroxyapatite requires longer time and large number of bone marrow stromal cells to differentiate them into osteoblasts [18]. Even though hydroxyapatite forms a new bone along the interface, medical applications is restricted due to the fact that hydroxyapatite is too stable *in vivo* to be absorbed and substitute the bone [19].

Among all bioglass compositions Bioglass®45S5 developed by Larry L. Hench and co-workers [20] consisting of 45 wt.% SiO_2, 24.5 wt.% Na_2O, 24.5 wt.% CaO, and 6 wt.% P_2O_5 has been found to be one of the most bioactive glasses [16]. Bioglasses have also been extensively studied and are known to achieve direct apposition to bone through the newly formed apatite layer at the interface [17]. Moreover, it has the potential to be used in many more bioactive applications than hydroxyapatite [21], because they are more dissolvable and have higher bone-forming ability than synthetic hydroxyapatite, which is due to their initial rapid surface reaction with the body fluid [17]. Therefore, it is mainly used to augment the repair of boney defects [1].

The Bioglass®45S5 by itself is not structurally viable and as a structural material sintered hydroxyapatite is a very brittle ceramic which is more or less strong in compression and week in tension [22]. Therefore, Bioglass®45S5 is used in conjunction with hydroxyapatite either as a sintering aid (<5wt %) or second phase (>5wt %) [8, 23, 24] which may also result in improved mechanical properties specifically compressive strength.

Another important concern in bioceramic materials is the porosity. Porous bioceramics have an advantage over dense bioceramics in tissue engineering. Proper sized pores and having enough interconnection to pass through the bioceramics are desirable due to the penetration of

cells, blood vessels, and extracellular matrices deep into the bulk which means that the new tissue can regenerate not only around the surface but also inside [25]. It is shown that new compositions formed by sintering hydroxyapatite with different amounts of Bioglass®45S5 at relatively elevated temperatures causes a liquid phase sintering which resumes with a significant improved densification [16]. However, successful tissue in-growth which will furthermore enhance the tissue attachment can only be maintained with an optimum level of porosity [26]. In contrast, substantial porosity will negatively affect the structural viability of the implant. Therefore, it is very crucial to achieve enough porosity while maintaining a viable structure to support the damaged bone.

1.2 Objectives of The Research

All the shortcomings and challenges mentioned in the previous section may be tackled by designing a unique, simple, and cost effective production process in order to synthesize a novel bioceramic composition with improved material properties including bioactivity.

The bioactive glasses and calcium phosphate ceramics such as Bioglass®45S5, hydroxyapatite, and different mixtures of them have been developed and used as bone substitutes in many biomedical applications. There have been many attempts to combine hydroxyapatite with bioactive glasses of different compositions in order to produce composites with improved mechanical and biological properties [16, 17, 23, 27]. Significant gains in mechanical properties with improved bioactivity have been reported; however, the least important property for bioceramic materials is the mechanical requirements, because the implant will be buried in the body and it will only be subjected to a small compressive load [1]. On the other hand, the reaction between bioactive glasses and hydroxyapatite and the alterations of the initial phase compositions may occur even in the case of small variations in the bioactive glass composition and amount or sintering temperature which results in compositions with different physical, chemical, and structural properties that diversely affect their bioactivity. The objective of this research is to investigate the bioactive behavior of different mixtures of Bioglass®45S5 and

4

synthetic hydroxyapatite sintered at different temperatures and to discuss composition and bioactivity deviations from the original materials related to alterations in phase composition due to thermal processes as well as to demonstrate the variation of the compressive strength.

In this research, hydroxyapatite and Bioglass®45S5 are chosen to be investigated for developing new bioceramic compositions which aimed to enhance the material and biological properties of both bioceramics. In this regard, the effects of different compositions on the physical, microstructural, and biological properties of the hydroxyapatite – Bioglass®45S5 blends formed by sintering are investigated. Furthermore, assessment of chemical and molecular structure by identifying the reaction stages in the sintering process will give a deeper understanding of how the new compositions form. These findings can be utilized to develop a cost effective production method for a novel bone substitute which has never been used as a main phase that has similar or improved properties of synthetic hydroxyapatite and Bioglass®45S5. On top of this, the experimental design can be concluded by characterizing their structure and physical characteristics and examining for biocompatibility and feasibility as substrates for mineralization and differentiation and proliferation of bone marrow stromal cells. Therefore, this research will guide to an improved understanding of the relationship between the chemical composition and the material properties of a unique bioceramic composition as a promising implant for orthopedic and tissue culture applications which may excite other researchers to delve deeper into this line of research.

<u>1.3 Structure of The Research</u>

This dissertation is composed of ten chapters. This episode is aimed to outline each chapter with a brief description. Chapter 1 introduces the reader to bioceramics and sets for the objectives for this research. Chapter 2 gives a basic background about biomaterials, the significance, classification, and applications of bioceramics mainly focusing on calcium phosphate ceramics and bioactive glasses in orthopedic applications. The bone structure and bone mineralization, bioactivity, and mechanism of bioactivity are also explained in detail in Chapter 2.

Chapter 3 gives an overview of experimental procedures and the material analysis and characterization techniques followed in this research. Different experimental procedures and characterization techniques included in this chapter are *in vitro* bone marrow stromal cell culture and immersion in simulated body fluid, powder and thin film X-ray diffraction analyses, scanning electron microscopy coupled with energy dispersive X-ray spectroscopy, X-ray absorption near edge spectroscopy, and nano indentation. Chapter 4 concerns processing, physical, chemical, microstructural, and mechanical characterization, and *in vitro* bone marrow stromal cell culture of hydroxyapatite – Bioglass®45S5 co-sintered bioceramic materials and their relative bioactivities. The basic concept behind formation of novel bioceramic compositions with various crystalline and amorphous phases and their roles in bioactivity are defined in Chapter 5 by employing X-ray absorption near edge structure spectroscopy. Chapter 6 presents preliminary *in vitro* bone like apatite formation behavior in simulated body fluid and its relation to bioactivity of the newly composed bioceramic compositions. In addition XANES is employed to evaluate and compare the silicon, phosphorus, and calcium structure environments in apatite layers formed by immersion in simulated body fluid. Chapter 7 exhibits nano scale properties of hydroxyapatite – Bioglass®45S5 co-sintered bioceramic compositions and the *in vitro* bone like apatite layers formed on their surfaces in simulated body fluid using single and cyclic nano indentation. Chapter 8 discusses the effect of silicate addition on formation of a novel bioceramic composition mainly composed of sodium calcium phosphate and its bioactivity. Chapter 9 gives a phenomenological approach on how new compositions are formed by addition of different amounts of Bioglass®45S5 to synthetic hydroxyapatite and details how Bioglass®45S5 improves bioactivity of these bioceramic materials.

CHAPTER 2

BACKGORUND

The surgical repair or replacement is often necessary because of trauma, degeneration, or disease of bone. The main concern for a person with a joint pain is the relief of pain and return to healthy and functional life style. This usually requires replacement or repair of skeletal parts such as knees, hips, finger joints, elbows, vertebrae, teeth, and mandible. The ageing population, increasing preference by younger to middle aged candidates to undertake surgery, improvements in the technology and life style, a better understanding of body functionality, improved aesthetics, and need for better function are expected to cause an expand in worldwide biomaterials market (valued $24,000M in 2000) especially in orthopedic and dental applications which represents approximately 55% of the total biomaterial market. In addition, it has been reported that the cost of orthopedic products exceeded $13billion in 2000 with an increase of 12% over previous year revenues [4].

Biomaterial by definition is "a non-drug substance suitable for inclusion in systems which augment or replace the function of bodily tissues or organs" [4]. Some of the earliest biomaterial applications date back to antiquity with limited use on the body surface such as loose teeth was bound together with gold wires for tying artificial ones to neighboring teeth. However, the biomaterials and devices have successfully started to be developed to replace various components of the human body as a century ago. In the early 1900's bone plates were successfully implemented to stabilize bone fractures and to accelerate their healing. While by the time of the 1950's to 1960's, blood vessel replacement were in clinical trials and artificial heart valves and hip joints were in development. These materials are capable of being in contact with bodily fluids and tissues for prolonged periods of time, while eliciting little if any adverse reactions

7

[2-4]. Even in the preliminary stages of this field, surgeons and engineers identified materials and designed problems that resulted in premature loss of implant function through mechanical failure, corrosion, or inadequate biocompability of component. Key factors in a biomaterial usage are its biocompability, bio-functionality, and availability to a lesser extent. Therefore, ceramics are ideal candidates with respect to all the above functions, except for their brittle behavior [4].

During the past four decades there has been a major advance in the development of medical materials which has been an innovative step for ceramic materials used in skeletal repair and reconstruction [28, 29]. Ceramics particularly used to replace or repair the damaged skeletal system are named bioceramics. They are frequently used to augment both soft and hard tissues, to repair cardiovascular system, or for some treatments of tumors. Bioceramics have been inherently attracted wide attention due to their cheapness, easy production, and most important good biocompability. Therefore, much research has focused on development of new types of bioceramics. Bioceramics can be used in many forms such as fillers, coatings, a second phase in a composite, or a bulk material in a specific shape. In many applications bioceramics are chosen to be used as bulk materials which are named implants, prosthesis, or prosthetic devices [1, 30]. Also, the significant increase in the number of patents and publications in this field and constant increasing number of major international conferences and themed meetings shows that the range of biomedical applications has been expanding. The developments for the past 40 years makes it possible to choose by compositional control whether these materials are biologically stable once incorporated within the skeletal structure or whether they are resorbed over time [29].

Bioceramics are now used in a number of different applications throughout the body. According to the type of bioceramics used and their interaction within the host tissue, they can be categorized as either bio-inert or bioactive, and bioactive ceramics may be resorbable or non-resorbable. They can be polycrystalline materials such as glasses, glass ceramics and ceramic filled bioactive composites, and all these may be manufactured either in porous or in dense form in bulk, as granules or in the form of coatings [29].

8

Human body fluid is supersaturated with respect to apatite even under normal conditions. The reason that apatite formation only occurs in bone tissue in the human body is the high activation energy for the homogeneous nucleation of apatite in human body fluid. Therefore, if an artificial material has a functional group such as Ti-OH, Si-OH, Zr-OH, Ta-OH, COOH, and PO_4H_2, that could be an effective apatite nucleation site on its surface, later it will easily form apatite nuclei on its surface. Once the apatite nuclei are formed they spontaneously grow by consuming calcium and phosphate ions from the surrounding body fluid. Therefore, prerequisite for apatite formation on an artificial material in a living body is the presence of a type of functional group that could be an effective site for apatite nucleation on its surface. The formed apatite is very similar to bone mineral in its composition and structure. Therefore, osteoblasts preferentially proliferate and differentiate to produce apatite and collagen on this apatite layer. Consequently, the surrounding bone can come into direct contact with the surface apatite layer. When this occurs, a strong chemical bond is formed between the bone minerals and the surface apatite layer to reduce the interface energy between them [5, 31].

The nature of the bioceramics and its surface characteristics play important roles in determining bone adaption to the implant material. Surface reactivity is the common characteristics of bone bioactive ceramics. It contributes to their bone bonding ability and their enhancing effect on bone tissue formation. During implantation, reactions occur at the material-tissue interface that leads to changes in the surface characteristics of the implant material and the tissues at the interface which eventually maintains an interfacial bonding between the implant and the host tissue as describe in the previous paragraph. However, the bonding time, strength, mechanism, or thickness varies depending on the chemical activity those bioceramics exhibit [1, 32].

A comparison of the relative chemical activity of these different types of bioceramics is listed and shown in Table 2.1 and Figure 2.1 which is closely correlated with the rate of an interfacial bond formation with the bone. Type 1 is called nearly inert bioceramics, and they do

9

not form any bond with the bone. Alumina and zirconia are the most common examples of this type of bioceramics. When a bioceramic is nearly inert the interface is not chemically or biologically bond which results in the movement and progressive development of a non-adherent fibrous capsule in both soft and hard tissues. This movement at the interface eventually causes deterioration in function of the bioceramic implant, tissue, or both. The only way to have successful bonding between the nearly inert bioceramic and the tissue is a very tight mechanical implantation and loaded only in compression. Otherwise, the implant moves and the fibrous capsule grows thick and results in implant loosening leading to a clinical failure by fracture of the implant or the bone adjacent to the implant. Type 2 is called porous inert bioceramics, and they form a mechanical bond via in-growth of bone into the pores. Porous hydroxyapatite and porous hydroxyapatite coated metals are typical examples of Type 2 bioceramics. The increased surface area by the pores maintains a stronger bond between the implant and the tissue which does not let the movement of the implant in the tissue. This type of attachment is usually called biological fixation. Even though the tissue remains viable and healthy, it is necessary to have the pore size 100-150μm in diameter due to the need to provide a blood supply to the ingrown connective tissue. Yet again if micro-movement happens at the interface, the tissue will be damaged, the blood supply may be cut off, tissues will die, inflammation follows, and eventually the interfacial can be destroyed. However, large porosity requirement decreases the strength of the bioceramic that is used. Therefore, this type of bioceramics is only good when used as porous coating on metals or as unloaded space fillers in tissues. Type 4 is called resorbable bioceramics that degrade over a period of time and are replaced by the natural host bone tissue. Porous and particulate tricalcium phosphate and bioactive glasses are good examples of this type. The natural tissues can repair themselves and are gradually replaced throughout life by a continual turnover cell population. The resorbable bioceramics based on the same principle. However, matching the resorption rate of these implants to repair rates of body tissue and maintaining the strength and the stability are very complicated, because the dissolving rate of these bioceramic

10

materials varies extremely according to the compositions. This property limits the compositional design of resorbable bioceramics. Another approach to solve problems of interfacial attachment is using bioactive ceramics. Type 3 is called bioactive bioceramics which forms a bond with the adjacent bone tissue via chemical reactions at the interface. Bioactive glasses, glass ceramics, and hydroxyapatite can be listed in this type of bioceramics [1, 28].

Table 2.1: Types of tissue attachment of bioceramic materials [1].

Type of implant	Type of attachment	Example
(1) Nearly inert	Mechanical interlock (Morphological fixation)	Al_2O_3, Zirconia
(2) Porous	Ingrowth of tissues into pores (biological fixation)	Hydroxyapatite (HA) HA coated porous metals
(3) Bioactive	Interfacial bonding with tissues (Bioactive fixation)	Bioactive glasses Bioactive glass-ceramics HA
(4) Resorbable	Replacement with tissues	Tricalcium phosphate Bioactive glasses
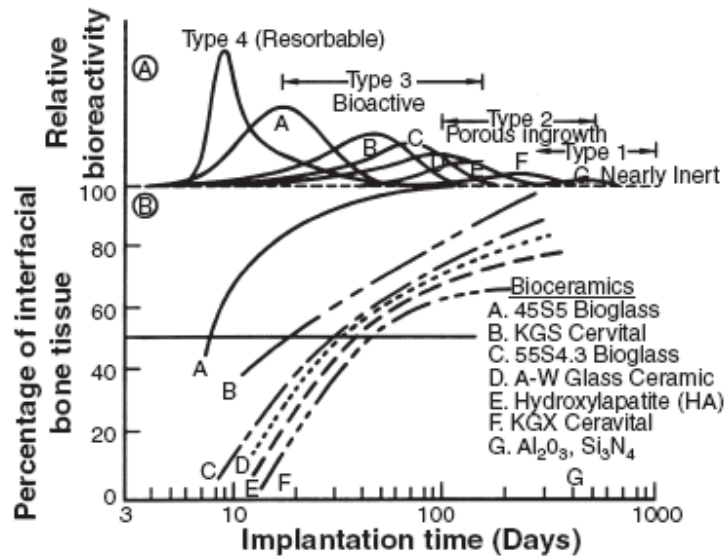
Figure 2.1: Bioactivity spectra for various bioceramic implants. **(A)** Relative rate of bioactivity **(B)** Time dependence of formation of bone bonding at an implant interface [1].

11

By changing the composition of the bioceramic material the reaction kinetics can be controlled which alters the rate of the tissue formation at the bioactive ceramic implant interface. Thus, the relative bioreactivity of the bioceramic material is thoroughly composition dependent. The initial concentration of the cells present at the interface such as stem cells or osteoblasts varies as a function of the fit of the implant and the condition of the bony defect. Consequently, all bioactive ceramic implants require an incubation period before bone proliferates and bonds. The length of the incubation period at which this process occurs varies over a wide range depending on bioceramic implant composition which controls the kinetics of the surface reactions explained in detail in "mechanism of bioactive bonding" in section 2.4. For the ceramic material to be bioactive and form an interfacial bond, the time of stages 4 and 5 must match the time of bio-mineralization that normally occurs *in vivo*. If the surface reactions are too rapid the implant is resorbable (Type4). If the surface reactions are too slow, the implant is not bioactive meaning the implant has a Type1 response [28].

2.1 Nearly Inert Ceramics

Nearly inert ceramics elicit minimal response from the host body by maintaining their physical and mechanical properties when they are implanted within the body. All these bioceramics exhibit high compressive strength, have excellent resistance to corrosion and wear, are nontoxic and biocompatible [3]. Aluminum oxide, commonly known as alumina, and partially stabilized zirconia are the most widely used nearly inert ceramics. Additionally, high density and purity (>99.5%) alumina was the first widely clinically used inert oxide bioceramics. It could be used in load-bearing areas like hip prostheses, dental implants, knee prostheses, bone screws, etc. due to the properties mentioned above. Alumina has a load-bearing life time of 30 years at 12000N loads similar to those expected from hip joints [28]. However, its modest tensile strength and toughness, tendency to fracture, and excessive elastic modulus (10 to 50 times higher) as well as relative movement on the interface resulting in forming a fibrous capsule that causes

12

failure in the interface due to not having a chemical or biological bond with the host tissue which makes it less desirable for many orthopedic applications [28, 33].

2.2 Nearly Inert Porous Ceramics

The biggest advantage of porous inert bioceramics is their inertness combines with the mechanical stability of the highly convoluted interface developed by bone tissue in-growth into the pores of the bioceramic implant. However, porous bioceramics used in biomedical applications are limited to non-load bearing areas due to its low mechanical strength. Porous materials are weaker than their equivalent dense forms. As the porosity of a material increases, its strength decreases as proven by Ryshkewitch's equation. Studies show that when the pore size exceeds 100µm and load bearing is not a primary requirement, inert porous bioceramics can be a functional implant by maintaining both its vascularity and long term viability. Also having porosity creates more surface of the implant exposed to the environment that causes *in vitro* or *in vivo* aging leading to decrease in strength. Aging of inert porous bioceramic implants with their subsequent mechanical strength decrease raises the questions as to the successful long-term application of porous bioceramics. Therefore, they should be more designed to be resorbable [28].

2.3 Bioactive Glasses and Glass Ceramics

Certain compositions of glasses and glass-ceramics have been proven to directly bond to both soft and hard tissues. These materials have become to be known as bioactive materials. Bioactive glasses are amorphous silicate based materials which are compatible with the human body, bond to bone and can stimulate new bone growth while dissolving over time. Therefore, they have the potential to restore diseased or damaged bone to its original state and function which is called bone regeneration [5].

Forming a carbonated hydroxyl apatite layer upon implantation in the body causing the implant to bond to the tissue is a common characteristic of all bioactive materials. This carbonated hydroxyapatite layer formed between the implant and tissue is chemically the same

as the mineral phase of bone. This apatite layer develops an adherent interface with tissues that could resist substantial mechanical forces that is equivalent or greater strength of cohesive strength of the implant material or the tissue bonded to the implant material. This interface is so strong that mechanical failure almost never happens there [28]. This kind of bonding was fist demonstrated by Larry Hench and coworkers in 1969, and was the first material seen to form an interfacial bond with the host tissue after implantation [20]. The glass composition of the first bioactive glass was 45 wt% SiO_2, 6 wt% P_2O_5, 24.5 wt% CaO, 24.5 wt% Na_2O and called Bioglass®45S5. This bioglass composition has three key distinguishing properties from traditional glasses. It has less than 60 mol% SiO_2, high Na_2O and CaO content with some P_2O_5 in a Na_2O-SiO_2 matrix. It also has a high CaO/P_2O_5 ratio. These compositional features make the surface of the glass highly reactive when exposed to human body fluids. However, the bioactivity of these glasses is highly dependent on their composition and the bone bonding behavior of bioactive glasses. After Hench's discovery it was shown that other compositions and glass types are also bioactive and even some of them can bond to soft tissue. The interest in bioactive glasses now focuses their ability to stimulate new bone growth and its potential to be used in the development of constructs that can stimulate the body's own regenerative mechanisms to bone regeneration [5].

The compositional range for bonding of bone to bioactive glasses is shown in Figure 2.2 [5]. The glasses with the highest level of bioactivity lie in the middle section (Region A) also called bioactive bone bonding boundary. These bioglass compositions develop a rapid bond with bone, and also form an adherent, interdigitating collagen bond with soft tissues [28, 34]. When SiO_2 amount reaches between 52-60 wt%, the bonding rate slows down. And greater than 60 wt% SiO_2 the glass is not bioactive anymore. These glasses behave as Type1, nearly inert materials and elicit a fibrous capsule at the implant-tissue interface and no bone-bonding occurs [5, 28]. The glasses in region C are resorbable and they disappear within the body no more than 30 days. Region D glasses are not technically practical therefore never tested as implants.

14
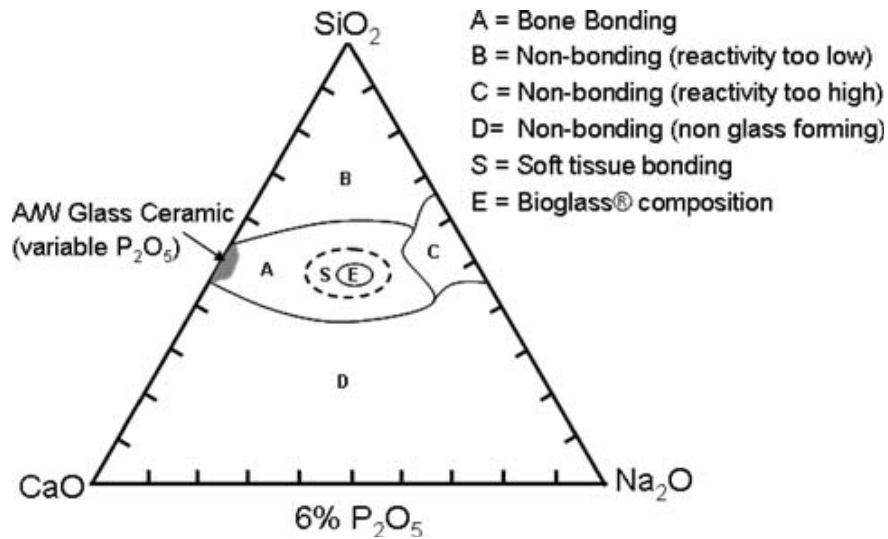
Figure 2.2: Compositional diagram for bone bonding [20].

There have been many attempts on modifying the glass composition by adding multivalent cations such as Al^{3+}, Ti^+, or Ta^+ to improve the rate of surface reactions which leads to a higher bioactivity [35-37]. However, Gross and co-workers found that even small amounts of Al_2O_3, Ta_2O_5, TiO_2, Sb_2O_3, or ZrO_2 addition to bioactive glasses slows down the bone bonding [28, 36, 38]. Also, a Kyoto university team developed a glass-ceramic called A/W which is a two-phase silica-phosphate composed of apatite and wollastonite crystals and a residual glassy SiO_2 matrix. They found that where a second phosphate phase does not inhibits bond bonding, addition of Al_2O_3 or TiO_2 to A/W glass ceramic does [28, 39-41]. Another bioactive glass-ceramic was developed with two main crystal phases that are mica and apatite which was also bioactive and in additional machinable. Afterwards, additional bioactive glasses and glass ceramics have been developed [28]. However, it has found that compositions within boundaries similar to those in Figure 2.2 bonded to bone, and glasses outside the bioactive boundary did not bond. Therefore, it is now certainly known that the bioactivity of glasses highly depends on their composition [5].

15

2.4 Calcium Phosphate Ceramics

The word *apatite* means "deceive" in Greek language which is given to a group of mineral crystals appearing in different colors that were mistaken for more precious stones. Mineral apatites such as hydroxyapatite, fluorapatite, chlorapatite, carbonate hydroxyapatite, fluor carbonate apatite present in nature with different colors. Based on the similarity in the X-ray diffraction (XRD) patterns of sintered bone to those of mineral apatites and on chemical analyses showing mainly calcium and phosphate ions, it was concluded that the inorganic phases of bones and teeth are basically a calcium hydroxyapatite. Based on mineral apatites containing carbonate it was speculated that apatites of dental enamel and bone are carbonate apatites similar to carbonate apatite minerals. Therefore, we can describe the term apatite as a family of calcium phosphate compounds which have similar structures with different compositions [5].

The family of calcium phosphates and their properties can be characterized according to the proportion of calcium to phosphorus ions in its structure. Due to its chemical similarities to the inorganic component of hard tissues, hydroxyapatite is one of the most widely used synthetic calcium phosphate ceramics [29, 42, 43]. Hydroxyapatite has a chemical formula of 39.68 wt. % Ca and 18.45 wt. % P with a Ca/P ratio of 2.151 and Ca/P molar ratio of 1.667. It has higher stability in aqueous media than other calcium phosphate ceramics within a pH range of 4.2 to 8.0 [29, 44].

In certain circumstances it might be desirable for an implant to assist in bone repair and then be slowly resorbed and replaced by natural tissue. However, it is necessary to match the rate of resorption with that of the expected bone tissue regeneration. When the solubility of a calcium phosphate is higher than the rate of tissue regeneration, it will only be of limited use in bone cavity and defect filling. Tricalcium phosphate (TCP) with a molar Ca/P ratio of 1.5 is more rapidly resorbed than hydroxyapatite. Mixtures of hydroxyapatite and TCP, known as biphasic calcium phosphate (BCP), have been investigated as bone substitutes and the higher the TCP content in BCP, the higher dissolution rate achieved.

TCP is a biodegradable bioceramic with the chemical formula, $Ca_3(PO_4)_2$. In addition, it dissolves in physiological media and can be replaced by bone during implantation. TCP has four polymorphs, the most common ones are α and β forms. The stoichiometry of hydroxyapatite is highly significant where thermal processing of the material is required. Slight imbalance in the ratio of Ca/P can lead to appearance of extraneous phases. If the Ca/P ratio is lower than 1.67, then α or β-TCP tricalcium phosphate may be present after processing. If the Ca/P is higher than 1.67, calcium oxide (CaO) may be present along with the hydroxyapatite phase. These irrelevant phases may adversely affect the biological response to the implant in-vivo [29].

Calcium phosphates are now used for a variety of different applications covering all areas of the skeleton including spinal fusion, cranio-maxillofacial reconstruction, treatment of bone defects, fracture treatment, total joint replacement (bone augmentation), and revision surgery. However, only certain compounds are useful for implantation in the body. For instance, compounds with Ca/P ratio less than 1 are not suitable for biological implantation due to their high solubility. Calcium phosphate implants (hydroxyapatite in particular) are used in the form of coatings on metallic implants [45-47], as fillers in polymer matrices [48-50], as self setting bone cements [51-53], as granules[54, 55] or as larger shaped structures [29].

Hydroxyapatite has a specific crystallographic structure in hexagonal system, space group, $P6_{3/m}$. There may be various substitutions in the apatite structure such as Sr for Va, Mg for Ca, F for OH, Cl for OH, CO_3 for PO_4 or CO_3 for OH. All these substitutions affect hydroxyapatite properties such as lattice parameters, spectral properties, crystal size and morphology, which in turn, affects its chemical stability and thermal stability. The crystal structure of hydroxyapatite can accommodate substitutions by various cationic and anionic ions for Ca^{2+}, PO_4^{3-}, and/or OH^- groups. The ionic substitutions can affect the lattice parameters, crystal morphology, crystallinity, solubility, and thermal stability of hydroxyapatite. Cationic substitutions occur in the sites normally occupied by the calcium atoms and include sodium, magnesium, potassium, strontium, and manganese. Imbalances in the charges of the substituting ion can cause disorder within the

17

crystal structure of hydroxyapatite [29]. The difference in valency caused by such a substitution requires a reduction in anionic charge to maintain charge balance. Anionic substitutions can either occur in the PO_4^{3-} or OH^- positions. Fluorapatite and chlorapatite are common examples of anionically substituted hydroxyapatite. They display a similar structure to hydroxyapatite, but the F^- and Cl^- ions substitute for OH^- [29].

Synthetic or biologic hydroxyapatite has also diverse non-medical applications including protein chromatography, water defluoridation, components of dental products (as abrasive or mineralizing agent), and abrasives for orthopedic and dental implants. Biologic apatites constitute the inorganic or mineral phases of normal calcified tissues such as teeth and bones and are also found in some pathologic calcifications such as dental calculus, heart calcifications, urinary stones, soft-tissue calcifications, etc. Biological apatites, unlike pure hydroxyapatite, contain important minor substitutents such as CO_3^{2-}, Na^+, Mg^{2+}, and are more accurately described as carbonated apatite or carbonate apatite approximately by the formula $(Ca,Mg,Na)_{10}(PO_4HPO_4,CO_3(OH)_2)$. Other biologic apatites such as shark and other fish enameloids contain both fluoride (F^-) and carbonate (CO_3^{2-}). Biological apatite from coral, bovine bone or marine algae or synthetic Hydoxyapatite is currently used for bone repair and bone regeneration in the form of granules, blocks, or scaffolds, by itself or as composite with polymers or other ceramics or as coatings on orthopedic or dental implants. Its similarity in composition to natural bone mineral is the basic motivation for development of hydroxyapatite as a bone substitute material.

XRD profile and Fourier transform infrared (FT-IR) spectrum of synthetic hydroxyapatite compared with enamel, dentine, bone apatites show similarities and differences in crystallinity and composition such as presence of carbonate in bone apatite, or the XRD profile of enamel indicates larger crystals than those of dentine or bone. For many years, the mineral phases of calcified tissues have been idealized as hydroxyapatite. However, based on studies on synthetic carbonate apatite and biologic apatites, and using a combination of analytical methods such as

18

XRD, IR spectroscopy, transmission electron microscopy, and chemical analysis it is demonstrated for the first time that biologic apatite is not pure hydroxyapatite. It is a carbonate apatite similar to synthetic apatite with the CO_3 substitution of PO_4 groups, providing experimental evidence to speculate of the similarity of biologic apatite to mineral carbonate apatite [5].

The characterization of carbonate substitute hydroxyapatite (CHA) for biomedical applications was first studied by Raquel LeGeros in 1960s. Since then, due to carbonate is the most abundant substitution in bone mineral (3 – 8 wt. %), CHA has become the most extensively studied synthetic hydroxyapatite. Two types of carbonate substitution proposed in the literature; the substitution of CO_3^{2-} for OH^- (type A) and CO_3^{2-} for PO_4^{3-} (type B) and both of these substitutions influence the crystallographic lattice parameters of the material. Carbonate ion substitution has been shown to increase rates of bone apposition around dense hydroxyapatite implants as compared to pure hydroxyapatite. The increased bioactivity of CHA has been attributed to be due to the greater solubility of the CHA. More recently work has been performed to optimize the production and sintering behavior of CHA for biomedical applications [29].

The first successful repair of a boney defect as a clinical application of calcium phosphate ceramics was reported in 1920 [56]. Five decades later, this technology has progressed by some researches that described a method of preparing ceramic apatite and suggested its use in medicine and dentistry. Finally, the independent studies of many researchers led to commercialization of synthetic hydroxyapatite. All these developments on synthetic hydroxyapatite and other calcium phosphates were motivated by the need to develop synthetic biomaterials for bone repair, substitution, and augmentation that will replace autografts and allografts. Autografts and allografts have definite advantages; however, they also have serious disadvantages such as having limited supply, being expensive, needing additional surgery, possibility to cause trauma morbidity and potential disease transmission. Synthetic hydroxyapatite for bone repair, augmentation or regeneration was developed to provide less expensive and safer alternatives to autografts and allografts [5].

19

2.5 Hydroxyapatite/Bioglass Bioceramics

Phosphate ceramics and different bioglass compositions have been used as sintering aids to assist in sintering of hydroxyapatite or as a component of composite to enhance material properties including bioactivity in order to overcome the limitations of hydroxyapatite [23]. Hydroxyapatite is the main inorganic portion of bone [57], and synthetically produced hydroxyapatite is considered as a bone substitute material that will not cause any defensive bodily reactions [8]. Glasses composed of less than 60mol% SiO_2, high Na_2O and CaO, and high CaO/P_2O_5 ratio are recognized as bioactive glasses that have highly reactive surface for fast bone bonding [11]. The sodium phosphates have also been found to be effective sintering aids for hydroxyapatite, and resulting products were found to be bioactive [58]. The surface reactions happen in any silicate containing bioactive glasses allow the subsequent crystallization of apatite which further allows cell adhesion and collagen formation [59]. So, it is believed to silicon is an essential element in skeleton development due to its participation in early stage of bone calcification [60]. It is also reported that silicate substitute-hydroxyapatite ceramics up to 1.5 wt% addition significantly enhance the bioactivity of hydroxyapatite [61]. In another study, a calcium phosphate phase was formed on the surface of calcium phosphate invert glasses of a $60CaO.30P_2O_57Na_2O_3TiO_2$ when immersed in simulated body fluid (SBF) [62]. Tricalcium phosphate is (TCP, $Ca_3(PO_4)_2$) a crystalline bioactive ceramic that also degrades to calcium and phosphate salts both *in-vivo* and *in-vitro*, and also results in the precipitation of hydroxyapatite on the surface of an implant [63]. Among all the calcium phosphates used in biological applications only two calcium phosphates are stable when they are in contact with aqueous media: At pH<4.2 the stable phase is $CaHPO4.2H_2O$ (DCP) while at pH>4.3 the stable phase is hydroxyapatite [34]. Furthermore, different calcium phosphates have different induction times for the formation of carbonated apatite with some of the calcium deficient hydroxyapatite exhibiting poor bioactivity while TCP and calcium pyro phosphates exhibiting very good bioactivity [34]. In a bioglass bioactivity study, an increased cytotoxic response was shown for glasses with very high sodium

oxide (Na_2O) contents. This increase in cytotoxic response was attributes to the increase in local pH due to ion change reaction occurring at the surface of the bioglass [64].

Among all bioglass compositions Bioglass®45S5 is proven to be the most bioactive glass composition [20]. In addition, the bioactivity of Bioglass®45S5 was shown to be insensitive to the level of crystallization with the 100% crystalline material exhibiting the same level of bioactivity as the amorphous material [65]. Due to the rapid resorption, the bone formation produced by Bioglass®45S5 is greater than that produced by synthetic hydroxyapatite. The rate of bone formation correlates with the dissolution of the particles and the provision of soluble silica to the osteoblasts in the growing bone [66]. When a bioceramic implant placed within the body, the new bone tends to grow on the substrate or into the pores if it is porous enough. A process promotes healing and bone restoration as the calcium-phosphate dissolves and subsequently resorbed. The interaction results in a calcium-phosphate rich hydroxyapatite layer on the surface of bioactive ceramic with dissolution, precipitation, and ion exchange process followed by adsorption and incorporation of biological molecules. However, bone apposes and integrates with hydroxyapatite relatively in slower rates than various bioactive glasses [61]. Therefore, the low resorbability of hydroxyapatite is considered as a limiting factor because the bone conductive effect is restricted [67].

The primary advantage of hydroxyapatite – Bioglass®45S5 mixtures is the combination of their different dissolution behaviors. Synthetic hydroxyapatite will be the stable phase while Bioglass®45S5 is the resorbable accelerating apatite layer formation thus enhancing the initial new bone formation at the implant site [68]. For instance, Chatzistavrou et. al. found that sintered hydroxyapatite composites containing different amounts of bioglass lead to increased bioactivity [23]. It has been also shown by several researchers that Bioglass®45S5 addition to hydroxyapatite increases biological activities of hydroxyapatite [69, 70]. Another study demonstrated that osteoblast like cells divide more rapidly on bioactive glass substrates than they do on synthetic hydroxyapatite [71]. Therefore syntheses of hydroxyapatite – Bioglass®45S5

21

blends are expected to yield forming new bioceramic compositions that have higher bioactivity to form relatively faster apatite layers similar to natural bone and promote cell attachment, proliferation, and bone cell differentiation.

<div align="center">2.6 The Bone: Structure and Properties</div>

Bone is composed of two types of bone; compact (or cortical) and cancellous (trabecular). The hard outer layer of bone is composed of compact bone tissue that has minimal gaps and spaces which may be also referred to dense bone. This tissue gives bones their smooth, white, and solid appearance, and is found in the shafts of the long bones and on the outer surface of the smaller bones which contributes 80% of the weight of a human skeleton [72]. Compact bone has a compressive strength in the longitudinal direction (parallel to the long axis) ranging from 131-224 MPa, and a Young's modulus between 14-20 GPa. It also exhibits good fracture toughness, which is much higher in the transverse direction than in the longitudinal one [72-74].

Trabecular bone is less dense and is made up of an array of rods and struts that form open-cell foam, the pores of which are filled in by marrow and accommodate blood vessels. This type of bone is found at the ends of the long bones and inside the smaller bones such as ribs and spine. Trabecular bone tissue fills the interior of the organs and makes up the bulk of the interior of most bones. The mechanical properties of trabecular bone are highly dependent on its density. Compressive strength and Young's modulus values for trabecular bone ranges between 5-10 MPa and 50-100 MPa, respectively [72]. It can be concluded that the two bones are intrinsically different. Additionally, the elastic modulus values that are given cannot be thought as definite values because these values depend on parameters such as location, microstructure and density [75].

Bone is an extremely hierarchical living composite organism that composes of mineral substances, tissues such as collagen, non-collagenous proteins, other organics, and water. Bone can also be defined as a set of vertebrate tissues that uses some version of calcium phosphates

22

as their mineral. Bone by weight contains about 60% mineral, 30% matrix and 10% water [76]. Although the properties of bone vary from point to point and the proportion of the diverse substances varies according to the different parts of skeleton, bone tissue contains about two-thirds inorganic and one-third organic substances in average [5, 77]. It has three types of tissues: First, principle organic component type I collagen which is bone itself that composed of dentine and enameloid (highly mineralized collagen based tissue). The matrix of bone is comprised primarily of Type I collagen that is highly aligned, yielding a very anisotropic structure. This organic component of bone is predominantly responsible for its tensile strength [72]. Second is calcified cartilage which is found in two places: *(i)* temporary calcified of type II collagen-based cartilage-metaphyses of growing long bones and soon replaced by bone and *(ii)* in permanent skeletal structures of well-mineralised type II collagen-based cartilage structures. The third is the enamel which is highly mineralized, and its organic component is not collagen at all. Organic materials in bone are about 90% by mass collagen type I [5].

One of the functions of bone in the body is acting as a calcium reservoir [72]. The mineral component of bone is a form of calcium phosphate known as hydroxyapatite whose unit cell is $Ca_{10}(PO_4)_6(OH)_2$. Stoichiometric hydroxyapatite adopts a hexagonal geometry with the unit cell crystal dimensions being 9.42 Å in the a and b directions, and 6.88 Å along the c-axis [78]. However, the bone mineral is rarely stoichiometric and the crystal is not pure containing many substitutions such as magnesium, sodium, potassium, fluorine, chlorine, and carbonate ions as also mentioned in section 2.4. Specifically it has about 4-6% of carbonate replaced the phosphate making the mineral a carbonate apatite. The apatitic mineral in bone is closely associated with the collagen fibers and is made up of long, flat, plate-like nano-crystals that are approximately 40 nm long, 10 nm wide and 1-3 nm thick. This mineral component gives rise to the compressive strength of bone [5, 72].

2.7 Bone Marrow Stromal Cells and Bone Mineralization

The marrow is a complex tissue composed of two distinct compartments: the hematopoietic system and the bone marrow stromal. Only bone marrow stromal is in scope of this research. Bone marrow stromal consists of a heterogeneous population of cells that provide the structural and physiological support for hematopoietic cells. In addition, bone marrow stromal contains cells with a stem-cell-like character that allows them to differentiate into bone, cartilage, adipocyte (fat-storing cell), and hematopoietic supporting tissues. In biomedical applications regardless where they are isolated from under appropriate conditions bone marrow stromal cells are capable of forming new bone after *in vivo* transplantation. [79].

The bone fracture healing is a complex process that can be simplified into three stages: inflammation, repair, and remodeling which results in formation of new bone that has properties very similar to the bone before fracture [80]. In the first stage, the normal wound healing response occurs. A fibrin clot is formed when ruptured blood vessels flood the region, resulting in creation of a tunnel by cells called osteoclasts that digest the old damaged bone tissue releasing acids and enzymes with growth factors and signaling molecules [80]. The bone formation starts during the repair stage. The bone-making cells, osteoblast, start being surrounded by groups of collagen fibres forming a callus, and cemented together to produce the cartilage-like bone matrix which eventually mineralizes through deposition of a calcium deficient hydroxyapatite that is known as hydroxyl carbonated apatite [72]. The mineralized collagen fibril is the building block of all the members of the bone family of materials. It has a highly anisotropic structure, due mainly to the layers of tiny plate-shaped crystals of carbonated apatite that span the fibril [81]. In minutes crystals of calcium phosphate are deposited in osteoids in concentric shells with spheroidal, ellipsoidal, or ovoidal shape [77]. The mineralization process in bone is rapid at the beginning, but then slows down while approaching its final state, because as the bone becomes mineralized the rate of diffusion of ions through the tissue of the bones certainly declines [5]. Therefore, osteoblasts play a predominant role in calcification process of bone matrix. That is suggested by

24

their constant presence in osteogenesis areas and by their close relation with bone matrix. Osteoblasts also characterize by a considerable phosphatase activity, both acid and alkaline. The presence of alkaline phosphatase enzyme confirms that cells of the osteoblast type intervene in the calcification process. In fact, this enzyme is contained in matrix vesicles, which are organelles of cellular origin (present between the collagen fibres of the bone matrix border) representing areas of early stage calcification [77]. The final stage is the longest stage where the bone remodels through a process of resorption and deposition that enhances the bone resistance to the applied environmental stresses [72].

<div align="center">2.8 Bioactivity</div>

Two classes of bioactivity for bioactive materials are accepted after it has been reported that there is a large difference in rates of *in vivo* bone regeneration and extend of bone repair for different glasses [5].

Class B bioactivity occurs when only osteoconduction is present such as bone migration along an interface [5], so allows the bone growth along the bone-implant interface [29]. Osteoconduction is usually referred to bone graft healing process that provides scaffolding by protein matrix or mineral phase of bone graft for the in-growth of vessels and osteoprogenitor cells for graft incorporation by the host tissue. Osteoconduction is essential for stable long term orthopedic and dental implants [5]. Hence, osteoconductive implant simply provides a biocompatible interface along which bone migrates, and it elicits only extracellular response at its interface [34]. Bioactive materials including Bioglass®45S5, hydroxyapatite, other calcium phosphate-based biomaterials and glass ceramics which can bond to living bone directly can also generally possess high osteoconductivity [5]. Briefly the mechanism of osteoconduction can be explain as when a bioactive material is implanted, bone appears to grow or spread on the surface of the implant or in to the deeper pores if it is a porous material. However, the bone matrix has no inherent capacity to grow or to spread. What grow or spread is a population of migratory capillaries, fibrovascular tissues, and osteogenetic cells, and this process is followed by the

<div align="center">25</div>

development of new bone formation. Osteogenetic cells, which work much better when they have a matrix or scaffold to attach, may originate either in pre-existing pre-osteoblasts or osteoblasts that are activated by trauma, or in cells recruited from primitive mesenchymal cells by osteoinduction [5].

Class A bioactivity stimulates both osteoconduction and osteoinduction as a result of the rapid reactions on the implant surface [29]. This type of biomaterial elicits both intracellular and extracellular response at its interface, and it can bond to both hard and soft tissues. Osteoinduction is defined as "The process whereby a bioactive surface is colonized by osteogenic stem cells free in the defect environment as a result of surgical intervention" [82]. Osteoinduction is as opposed to osteoconduction is a biological process that induces local mesenchymal cells to differentiate into bone-producing cells. When some osteoconductive biomaterials have a specific porous structure they are known to become also osteoinductive in soft tissues without the addition of osteogenetic cells or bone morphogenic protein [5].

2.9 Mechanism of Bioactive Bonding

With bioactive ceramics solution mediated surface reactions take place after immersion in biological fluids. These reactions include dissolution, reprecipitation, and ion exchange phenomena in combination with protein adsorption events occurring at the bioactive ceramic surface [5]. The sequence of eleven reactions which occur on the surface of a bioactive glasses is summarized in Figure 2.3 [34]. The first five reaction stages that occur on the glass side of the interface do not depend on the presence of tissues. These reactions result in a hydroxyl carbonated apatite crystal layer forming on the implant surface which bone can bond.
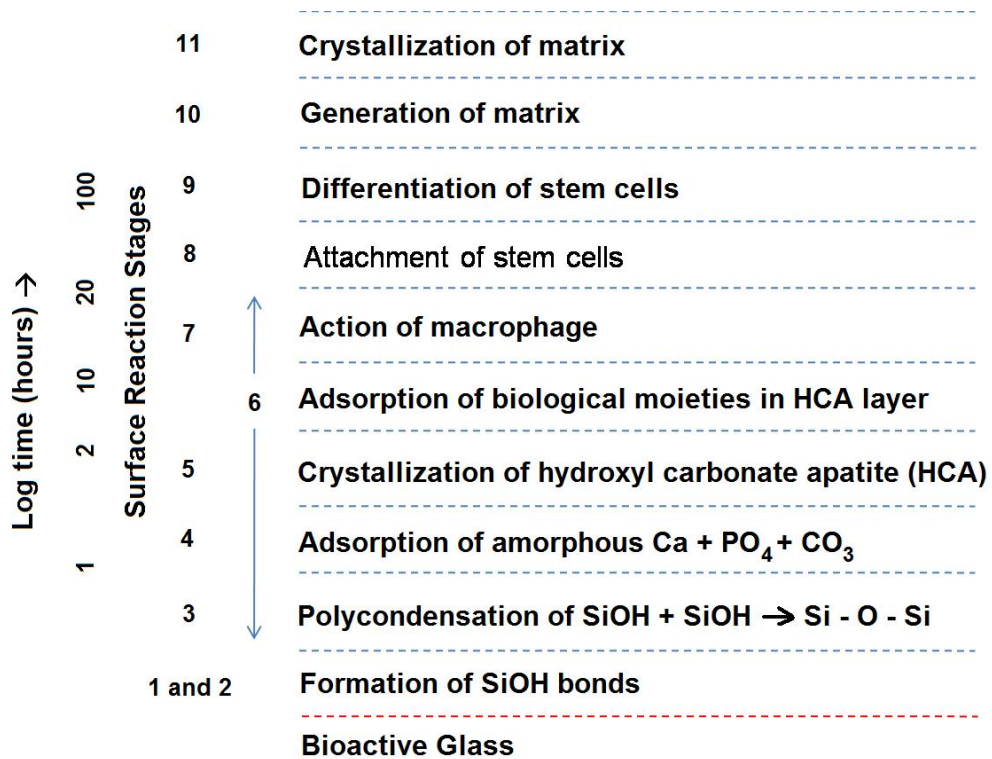
Figure 2.3: Sequence of interfacial reactions involved in forming a bond between tissue and bioactive glasses [34].

The mechanism of hydroxyl carbonated apatite layer formation in silicate containing bioactive implants proposed by Hench and coworkers [28] occurs in three general process: Leaching, dissolution, and precipitation which are given in more detail below.

1.   Surface de-alkalization by rapid cation (Na^+ or K^+) exchange with H^+ or H_3O^+, leading to a high pH local environment. This stage is usually controlled by diffusion. Such as;

$$Si - O - Na^+ + H^+ + OH^- \rightarrow Si - OH^+ + Na^+ \text{ (Solution)} + OH^-$$

2.   Loss of soluble silica in the form of $Si(OH)_4$ to the solution, resulting from breaking of Si-O-Si bonds and formation of Si-OH (silanols) at the interface. This stage is usually controlled by interfacial reaction.

3. Condensation and repolymerization of $Si(OH)_4$ in form a SiO_2-rich layer on the surface depleted in alkalis and alkaline-earth cations.

$$O-Si-OH \;+\; OH-Si-O \;\rightarrow\; O-Si-O-Si-O \;+\; H_2O$$

(with O and O substituents on the Si atoms, as drawn)
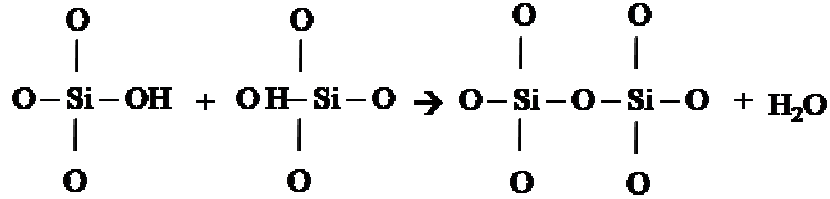
4. Migration and precipitation of Ca^{2+} and PO_4^{3-} groups to the surface through the SiO_2-rich layer forming an amorphous CaO-P_2O_5-rich film on top of the SiO_2-rich layer which is followed by growth of the amorphous CaO-P_2O_5-rich film by incorporation of soluble calcium and phosphate from solution.

5. Crystallization of the amorphous CaO-P_2O_5-rich film by incorporation of OH^- or CO_3^{2-} anions from the solution to form a hydroxyl carbonated apatite.

Exchange of cations in solution such as H^+ and $H3O^+$ of alkali or alkaline earth elements happen in leaching process (Stage 1). This ion exchange is relatively easy, because the alkali and alkaline earth elements are only modify the glass network but not a part of glass network. This happens rapidly in bioactive glasses that are in Figure 2.2 region A. After leaching, dissolution of O-Si-O bonds break and release Si in solution, and OH^- in the solution breaks down the Si bonds and forms $Si(OH_4)$ (Stage 2). There are many bridging oxygens involved in bioactive glasses that have more than 60 mol% of SiO_2; therefore, this dissolution happens harder and slowly in such glasses. The hydrated silica (SiOH) forms on the surface of glass by these reactions and undergoes rearrangement by polycondensation of neighboring silanols resulting in silica rich gel layer formation on the bioactive glass surface (Stage 3). Finally calcium and phosphate ions released from glass surface and those from solution form a calcium-phosphate rich (CaP) layer on the surface (Stage 4). The only difference between the reactions happen *in vivo* and *in vitro* is this layer forms on top of silica gel layer *in vitro* while it forms within the silica gel layer *in vivo*. This calcium phosphate layer formed is initially amorphous, and later crystallizes

28

to a hydroxyl carbonate apatite (HCA) structure by incorporating carbonate ions from solution (Stage 5). This nucleation and growth process is exactly same *in vivo* and *in vitro* and accelerated by hydrated silica which is a nucleation site for HCA.

In order to form a bond with bone this HCA layer must form. Therefore the rate of tissue bonding depends on the rate of HCA formation. In other words, if the stages of 4 and 5 are delayed for too long time the implant material will no longer be bioactive. The rest of the biological steps appear to be Stages 6 through 11. These steps are necessary for the implant to bond to tissue [5, 28].

Rapid growth of HCA incorporates collagen fibrils *in vitro*, without presence of cells, enzymes, or biological growth factors. The stages 8 through 10 can be investigated using cell culture methods which will give better understanding the tissue – implant interaction. Within a week mineralizing bone appears at the interface of the reactive bioactive glasses (Stage 11). In four weeks the interface is completely bonded to bone without any fibrous tissue [1].

The bioactive bonding to bone mechanism for hydroxyapatite is similar to bioactive glasses. When hydroxyapatite is immersed in a simulated body fluid or a similar solution the negatively charged ions on its surface combines with positively charged Ca^{2+} ions in the surrounding. As a result, Ca-rich amorphous calcium phosphate is formed on the surface of hydroxyapatite. As the Ca^{2+} ions accumulate, the hydroxyapatite becomes positively charged on its surface and reacts with negatively charged phosphate ions. As a result Ca-poor amorphous phosphate is formed which is eventually transformed into the more stable submicron sized crystalline bone-like apatite [83]. Afterwards, the bonding happens due to the attachment of osteogenically-competent stem cells on the hydroxyapatite surface those differentiate into osteoblasts. Then a cellular bone matrix is formed at the surface of hydroxyapatite and an amorphous layer containing thin apatite crystals develops on the surface. While the growth is taking place, this bonding area shrinks and hydroxyapatite becomes attached to the bone through a thin epitaxial layer which results in a strong interface between the bone and hydroxyapatite that

has no fibrous tissue layer interposed. Finally the bone formation progresses from the surface of hydroxyapatite [44].

There are two types of cellular interaction between the implant material and the tissue; extracellular and intracellular interactions. Extracellular interaction is determined by the materials surface for adsorption of proteins and collagen. Protein adsorption is followed by coagulation and activation of the complement system and cellular adhesion. It is also known that the hydroxyl carbonated apatite crystallinity on the bioactive material surface may have an effect on stem cell differentiation. Intracellular interaction may be caused by the soluble silicon release from bioceramic glass surface [34]. Studies showed that soluble silicon was a potent mitogen for human osteoblast-like cells, increased DNA synthesis and enhanced alkaline phosphatase activity and osteocalcin release [84].

In order to understand and characterize the apatite formation process and behavior of various bioactive ceramic materials such as calcium phosphates [63, 85, 7], bioactive glasses [7, 23, 86], and their composites [14, 17, 87] numerous in-vitro studies have been carried out using different techniques such as scanning electron microscopy (SEM) coupled with energy dispersive X-ray (EDX) spectroscopy [14, 23], thin film X-ray diffraction (TF-XRD) [87] as well as X-ray absorption near edge spectroscopy (XANES) [88, 89]

CHAPTER 3

EXPERIMENTAL APPROACH AND TECHNIQUES

In order to characterize a bioceramic material it is necessary to evaluate its composition, structure, and surface sufficiently that the material and its properties can be reproduced. There are five major classes of characterization which are chemical composition, size shape and surface of particulates, phase state and structure, microstructure, and surface. Once the information on these features is obtained the reproducibility of properties can be achieved. In order to establish the physical origin of properties and ensure its reproducibility it is necessary to determine not only the specifics of manufacturing process used but also the composition and the structure of the product. Further, characterization will process to property.

The most concerned property for bioceramic materials is its bioactivity, and least is the mechanical, because the implant will be buried in the body and it will only be subjected to a small compressive load. The mechanical and surface properties important for biomedical applications of ceramics depend on all these features explained above; therefore, the micro-structural and surface characteristics are especially critical [1].

In this study a series of experiments have been completed and as a result characterization has been done in order to optimize the material properties and process. This chapter will give an overview of experimental procedures and the material analysis and characterization techniques followed hinterher. First, the chemical compositions formed by sintering hydroxyapatite and Bioglass®45S5 were identified by X-ray diffraction (XRD) and X-ray near edge structure (XANES) spectroscopy. In addition, compression tests were performed to display mechanical property of the bioceramic blends. Second, physical and microstructural properties of the blends were explored by scanning electron microscope coupled with energy

dispersive x-ray spectroscopy (SEM-EDS). After bioactivity tests, surface characteristics of bioceramic blends were observed under SEM-EDS, XANES, as well as thin film X-ray diffraction (TF-XRD) in order to characterize the apatite formation ability of the samples. Third, alkaline phosphatase (ALP) Activity and DNA concentrations were calculated from bone marrow stromal cell culture study to illustrate the tissue attachment and in-growth behavior of the bioceramic blends. Finally, nano-indentation tests were used to measure the reduced elastic modulus and hardness of the bioceramic blends before bioactivity tests and compared with the mechanical characteristics of apatite layers formed by immersion in simulated body fluid.

3.1 Powder and Sample Preparation

A bioactive glass powder consisting of 45 wt% SiO_2, 6 wt% P_2O_5, 24.5 wt% Na_2O, and 24.5 wt% CaO also known as Bioglass®45S5 was acquired from US Biomaterials with a less than 90μm average particle size. The synthetic hydroxyapatite used in this research with a chemical composition of $Ca_{10}(PO_4)_6OH_2$ was acquired from Alfa Aesar, and it has an average particle size of less than 44μm. By using these two precursors five different mixtures were prepared with 1, 2.5, 5, 10, and 25% by weight Bioglass®45S5 addition to hydroxyapatite in polyethylene bottles, and ball milled for 30 hours with zirconia balls (particle size of 5mm) in acetone to ensure homogeneous mixture. Subsequent to ball milling, the mixtures were dried in the oven at 80℃ for 24 hours. The dried powder mix tures were sieved until the particles were separated from each other. Afterwards, the powders were pressed uniaxially in a die with a diameter of 12.7 mm to a pressure of 105.5 MPa, and sintered at 1200℃ for 4 hours with a heating rate of 4℃/minute. The sintering was follo wed by cooling at 10℃/minute down to room temperature in the furnace.

Another set of ceramic compositions were prepared for further analysis. In addition to Bioglass®45S5 and synthetic hydroxyapatite, CaO powder was acquired from Alfa Aesar, and P_2O_5 and SiO_2 powder was obtained from Sigma-Aldrich. As a Na_2O source baking soda ($NaHCO_3$) was used. Five different ceramic compositions were prepared. The first three are pure

synthetic hydroxyapatite, pure Bioglass®45S5, and 25 wt. % Bioglass®45S5 added hydroxyapatite. The last two blends were prepared by using *(i)* 45 wt. % SiO_2, 6 wt. % P_2O_5, 24.5 wt. % Na_2O, and 24.5 wt. % CaO which are Bioglass®45S5 precursors that add up to 25 wt. % Bioglass®45S5 mixed with 75 wt. % pure hydroxyapatite. *(ii)* Same precursors as *(i)* excluding SiO_2. The ceramic powders were mixed in proper amounts, balled milled, dried in oven, and pressed uniaxially as hydroxyapatite – Bioglass®45S5 blends were done. The sintering time and temperatures were chosen depending on the best feasible structure obtained. Pure hydroxyapatite, 25 wt. % Bioglass®45S5 added hydroxyapatite blend and 25 wt. % Bioglass®45S5 precursors added 75 wt. % hydroxyapatite are sintered at 1200℃ for 1 hour. Pure Bioglass®45S5 and Bioglass®45S5 precursors without SiO_2 with hydroxyapatite were sintered at 900ºC for 2 and 1 hour, respectively. A heating rate of 4℃/minute and cooling rate of 10℃/minute was used for all sintering processes.

3.2 Material Characterization

3.2.1 Density and Porosity Measurements

Density of the sintered products was estimated by a simple calculation of the mass of the bioceramic compositions divided by the volume of the bioceramic samples before and after sintering process.

3.2.2 Compression Test

The compression tests were performed on five different (1, 2.5, 5, 10, and 25 wt. %) Bioglass®45S5 added hydroxyapatite cylindrical bioceramic samples were prepared according to ASTM C773-88 (2006) Standards with a length to diameter ratio of approximately 2. For each group the number of specimens tested was not less than 3 and more than 6.

3.2.3 X-ray Diffraction (XRD) and Thin Film X-ray Diffraction (TF-XRD) Analyses

X-ray diffraction (XRD) is one the most widely and frequently used techniques for common crystalline material characterization [90]. The scattering of X-rays from crystalline materials leads to diffraction patterns which provide information about the structure and chemical

composition of crystalline materials. Since the XRD pattern is unique for each crystalline material it can be used to identify the crystalline phases in a mixture. The identification of the phases from XRD patterns usually requires some standard patterns such as JCPDS (powder diffraction file of organic or inorganic phases) which is available in the software of X-ray powder diffraction [5]. It is also possible to determine the relative amounts of phases in a mixture from diffraction peak intensities if the crystal structure of the phases is known by using integrated area method. Precisely, the theoretical diffraction patterns and the integrated area under these peaks are computed. Afterwards, the ratio of the strongest first peaks of each phase is calculated and a relation is found between them. The difference between the theoretical and observed data is compared to obtain the amounts of phases in a mixture. Although XRD is a very useful technique to evaluate and identify chemical compositions of materials, if there is an additional layer on the surface; however, the interfering effect of the substrate may cause less accuracy on information of the upper part. Thin film X-ray diffraction (TF-XRD) provides accurate throughput of the material up to a specific depth by using a low angle incidence of X-ray [91]. As all the beneficial gains of XRD, it has been used widely to examine bioceramic materials [27, 86, 87, 92-94, 94].

Specifically in this research XRD was used to identify the crystalline phases formed after sintering process of bioceramic pellets. Also, it was useful to compute the amount of some phases formed in multiphase compositions, and to find the preferred orientation in apatite layers formed on the surface of bioceramic pellets immersed in SBF. In addition to XRD analysis TF-XRD was performed to accurately identify the hydroxyl carbonate apatite layer formed on the surface of the bioceramic samples after bioactivity tests.

3.2.4 Scanning Electron Microscopy (SEM)-Energy Dispersive Spectroscopy (EDS) Analyses

Scanning Electron Microscopy (SEM) technique have great resolution and depth of field with a three dimensional quality of the surface. There are few different types of signals that can be produced in SEM, and each of them requires a specific detector for detection. In this research mainly secondary electron and energy dispersive X-ray was used. The low energy secondary

34

electrons are emitted from each spot where the focused electron beam impacts and according to the measured intensity of secondary electron emission the atomic composition of the sample and geometry of the features can be observed. In addition to secondary electrons incident electrons may also cause the emission of X-rays from the sample, and the measurement of the energy and intensity of these X-rays can provide for elemental composition mapping across the specimen which is called energy dispersive X-ray spectroscopy (EDS) [95].

SEM is one the most widely used instrument for a rapid characterization of surfaces and interfaces. It is an important advantage that SEM allows to observe micro-structural and surface features of solid materials down to the sub-micrometer scale. In addition, composition of the surface and micro-structural features formed on bioceramic materials can be chemically analyzed by coupling SEM with EDS [1, 5]. The development of microstructures of bioceramic samples after sintering and subsequent to *in vitro* bioactivity tests were investigated.

3.3 *In Vitro* Bioactivity Test and Characterization

3.3.1 Simulated Body Fluid (SBF) Test

Most of the bioactive materials developed so far form a hydroxyl carbonated apatite layer on their surfaces in the living body and then bond to bone through this apatite layer. Therefore, it is widely excepted that the essential requirement for a material to bond to living bone is the formation of this apatite layer on its surface [4]. This *in vivo* formation can be imitated in a simulated physiologic solution, namely simulated body fluid (SBF) with ion concentrations nearly equal to those of human blood plasma [96]. Therefore, this method can be used as screening to identify bone bioactive materials before animal testing, and the duration and the number of animals used in the experiments can be remarkably reduced which can assist in the efficient development of new types of bioactive materials. Hence, in this research it is considered useful to examine this physicochemical analysis of apatite formation on the bioceramic blends synthesized in SBF as a preliminary to *in vivo* animal experiments in order to find whether they are bone-bonding materials [5, 85, 97].

35

Since it was found that hydroxyl carbonated apatite layer reproduction is possible in a solution buffered at 7.4 pH by Tris(hyroxymethyl)amine and hydrochloric acid (Tris buffer solution) [98] a number of SBF solutions has been developed and proposed [5]. Table 3.1 gives a list of SBF solutions that have been proposed up to now. The most recent version of SBF named newly improved SBF was compared with the corrected SBF in stability as well as reproducibility of apatite formation on synthetic materials by 10 research institutes, and resulted that there was not any difference between them. Therefore, corrected SBF has been submitted as the solution for the *in vitro* evaluation of apatite-forming ability of implant materials to International Organization of Standardization and approved as ISO 23317 June 2007 [5]. Hence, it is frequently used by many researches for predicting *in vivo* bone bioactivity of materials which will ensure reduction in the number of animals used in and the duration of animal experiments [5, 97].

Table 3.1: Ion concentrations for SBFs and human blood plasma [97].

	Ion Concentration (mM)							
	Na^+	K^+	Mg^{2+}	Ca^{2+}	Cl^-	HCO_3^-	HPO_4^{2-}	SO_4^{2-}
Human Blood Plasma	142	5.0	1.5	2.5	103.0	27.0	1.0	0.5
Original SBF	142	5.0	1.5	2.5	148.8	4.2	1.0	0
Corrected SBF	142	5.0	1.5	2.5	147.8	4.2	1.0	0.5
Revised SBF	142	5.0	1.5	2.5	103.0	27.0	1.0	0.5
Newly Improved SBF	142	5.0	1.5	2.5	103.0	4.2	1.0	0.5

Most of the calcium phosphate ceramics and bioactive glass compositions, such as hydroxyapatite, bioglass-type Na_2O-CaO-SiO_2-P_2O_5 with or without Al_2O_3 and B_2O_3, CaO-SiO_2 glasses, β-tricalcium phosphate, biphasic ceramics, calcite, etc. are proven to bond to living bone through a layer of apatite or calcium phosphate also by animal experiments except β-tricalcium phosphate and calcite. These two bioceramics even though bond to bone do not form a layer of apatite of calcium phosphate.

36

3.3.2 Bone-like Apatite Formation in SBF

SBF is a highly supersaturated solution with respect to hydroxyl carbonated apatite; therefore, it is not easy to prepare clear SBF with no precipitation. For this reason, a preparation of SBF was adopted from the protocol developed by Kokubo et al [99] with few modifications. In order to prepare 1000 ml of SBF, first of all 700 ml of ion-exchanged and distilled water with a stirring bar into 1000 ml glass beaker is set on a hot plate covering with a watch glass maintaining the temperature at $36.5 \pm 2^{\circ}C$ under stirring. The first 8 order reagents given in Table 3.2 are dissolved in water one by one. The 9th and 10th order reagents are dissolved to adjust pH to 7.4. After the pH adjustment, the solution is cooled down to $20^{\circ}C$ and enough ion-exchange and distilled water is added to complete the solution to 1000ml. After the SBF preparation, the bioceramic pellets sintered at various temperatures and times were immersed in 25mL glass veils of SBF, and the glass veils placed on a rotating mixer in an incubator maintaining human body temperature at $37^{\circ}C$ and pH 7.4. Also, as a reference, Table 3.3 shows the nominal ion concentrations of SBF in comparison with those in human blood plasma.

Table 3.2: Reagents used to prepare the SBF (pH 7.40, 1L) [97]

ORDER NO.	REAGENT	CONTENT
1	NaCl	7,996 g
2	$NaHCO_3$	0,350 g
3	KCl	0,224 g
4	$K_2HPO_4.3H_2O$	0,228 g
5	$MgCl_2.6H_2O$	0,305 g
6	1N-HCl	40 ml
7	$CaCl_2$	0,278 g
8	Na_2SO_4	0,071 g
9	$NH_2C(CH_2OH)_3$	6,057 g
10	1 N-HCl	0-5 ml

Table 3.3: Nominal ion concentrations of SBF in comparison with those in human blood plasma [97].

Ion	Ion concentrations (mM)	
	Blood plasma	SBF
Na^+	142.0	142.0
K^+	5.0	5.0
Mg^{2+}	1.5	1.5
Ca^{2+}	2.5	2.5
Cl^-	103.0	147.8
$HCO3^-$	27.0	4.2
HPO_4^{2-}	1.0	1.0
SO_4^{2-}	0.5	0.5
pH	7.2 – 7.4	7.40

3.3.3 Bone Marrow Stromal Cell (BMSC) Culture Test

Even though SBF is a very useful *in vitro* technique to evaluate bone bonding bioactivity of new materials and investigate the mechanism of apatite formation on bone bonding materials [83], it will still not give any information on how the material will interact with the surrounding tissue in the body. The first 5 steps in bioactive bonding explained in Chapter 2 section 2.4 do not depend on tissue presence; they can occur in simulated body fluids or any similar solutions. On the other hand, bonding to tissue requires an additional series of events (Stage 6 – 11) [1]. The large bone losses cause drastic problems in orthopedics because of their frequency and difficulty in reconstruction. Therefore using biomaterial implants with knowledge of their ability to grow and differentiate into osteogenetic cells on them results in solutions in complete functional recovery of the largely damaged bone tissues.

Stem cells are characterized by the ability to renew and reproduce themselves for long period of times through mitogenic cell division and differentiation into a diverse range of cell types

of the body tissues and organs. Osteoblasts are the cells that form bone which arise from progenitor stem cells in a multistep lineage cascade. The osteoblast progenitors are recruited from outside or inside the bone. Bone marrow stromal cells (BMSCs) that have the capability to differentiate into osteogenic cell types [100] are originated from inside the bone. The injured bony sites induce the chemo-attraction of multi-potent mesenchymal progenitor cells that originated in the bone marrow become osteoblasts through a series of controlled differentiation steps. BMSCs can be isolated from different sources such as human or animals' bone marrow and expanded *in vitro*, which makes them a promising source for tissue engineering and clinical applications. [101].

Skeletal development, normal bone remodeling, and calcium homeostasis are processes that require the coordinated regulation and integration of bone formation by osteoblasts and bone resorption by multinucleated osteoclasts. It has been reported that alterations in osteoclast numbers and/or bone resorptive activity causes orthopedic implant difficulties. Therefore, numerous biomedical investigators interested in basic and clinical aspects of the cellular and molecular biology of bone development and remodeling in order to develop useful models to cope with these issues. In this research we focused on rat osteoclast-like cell culture. Osteoclasts are known to originate from hematopoietic precursors related to monocytic cells either found in the circulation or resident in the bone marrow (BM). Generally, it has been more successful for the *in vitro* formation of osteoclast-like cells, involves the use of primary cultures of BM cells. Originally, feline, rabbit, and avian long-term BM cultures were often used to generate *in vitro* formed multinucleated osteoclast-like cells for study. In recent years, conditions have become well established to also generate osteoclast-like cells from BM of murine, porcine, rat, and human species [102]. In this research primary bone marrow stromal cells were isolated from Sprague-Dawley rat species.

When a bioceramic material is implanted at the bone defect site, the implant allows cell proliferation and osteoblast differentiation directly on their surfaces [100]. Therefore, a key issue in successful implantation is the response and proliferation and differentiation of BMSCs around

39

the implanted materials which can be assessed by DNA synthesis and ALP activity, respectively [103]. There have been studies on effect of Bioglass®45S5 [103], synthetic hydroxyapatite [104] or their composites [17] on proliferation and differentiation of osteoblast cells as well as comparing the behavior of rat bone cells cultured on Bioglass®45S5 and hydroxyapatite [71]. Silver et al suggested that Bioglass®45S5 had no effect on osteoblast viability and did not affect either proliferation or differentiation under most conditions. Adding that studies of proliferation and differentiation of osteoblast cultured on Class A bioactive materials such as bioactive glasses did not yield consistent results. On the other hand, Vrouwenvelder et al proved that Bioglass®45S5 showed significantly higher DNA concentration and ALP activity than synthetic hydroxyapatite. At last, Eun-Jung Lee et al developed hydroxyapatite – Bioglass®45S5 composites by hot-pressing which also showed significantly enhanced osteoblast cell activity with respect to the pure hydroxyapatite confirming their excellent *in vitro* biocompatibility.

3.3.4 Isolation and Culture of BMSCs

Primary rat bone marrow stromal cells (BMSCs) were isolated from the femurs of Sprague-Dawley rats. The rats were sacrificed with CO_2 and the femurs were excised. Aseptically, the epiphyses were removed and the diaphyses flushed with 5 ml of complete bone media (DMEM: Dulbecco's Modified Eagle Medium) purchased from Invitrogen, Catalog Number: 12800017 and 12800082 which is supplemented with 10% fetal bovine serum (FBS) from Hyclone, 0.28 μM Lascorbic acid from RPI Corp., 10 mM-glycerol phosphate from Sigma, 10 nM dexamethasone from Sigma, 1% penicillin-streptomycin and 0.1% fungizone from Invitrogen using an 18 gauge needle. The complete bone media formulation is given in Table 3.4. Aspirating the pellets up and down using the syringe broke up the bone marrow clusters, and the cells were seeded in T-25 flasks (~1 femur per T-25 flask). The T-25 flasks were incubated overnight at 37℃ in 5% CO_2. After 24 hours non-adherent cells were removed by 4-5 washes with PBS, and the adherent cells were further cultured in complete bone media. Upon confluence, cells were detached from the culture surface with trypsin-EDTA, centrifuged at 1000 G's for 10 minutes, and

resuspended in complete bone media for use in experiments or subculture. For analysis, cells on the ceramic disks were lysed on day 3 and day 6 with 1 ml of 1% Triton X100. For the experiments, cells were seeded on hydroxyapatite and hydroxyapatite – Bioglass®45S5 bioceramic substrates at a density of 1×10^4 cells/cm^2 and incubated at -20°C.

Table 3.4: Dulbecco's Modified Eagle Medium (D-MEM) powder (high glucose) Contains 4500 mg/L D-glucose, L-glutamine and 110 mg/L sodium pyruvate but no sodium bicarbonate.

COMPONENTS	Molecular Weight	Concentration (g/L)	Molarity (mM)
Amino Acids			
Glycine	75	30	0.400
L-Arginine hydrochloride	211	84	0.398
L-Cystine 2HCl	313	63	0.201
L-Glutamine	146	584	4.00
L-Histidine hydrochloride-H$_2$O	210	42	0.200
L-Isoleucine	131	105	0.802
L-Leucine	131	105	0.802
L-Lysine hydrochloride	183	146	0.798
L-Methionine	149	30	0.201
L-Phenylalanine	165	66	0.400
L-Serine	105	42	0.400
L-Threonine	119	95	0.798
L-Tryptophan	204	16	0.0784
L-Tyrosine disodium salt dihydrate	261	104	0.398
L-Valine	117	94	0.803
Vitamins			
Choline chloride	140	4	0.0286
D-Calcium pantothenate	477	4	0.00839
Folic Acid	441	4	0.00907
i-Inositol	180	7.2	0.0400
Niacinamide	122	4	0.0328
Pyridoxine hydrochloride	204	4	0.0196
Riboflavin	376	0.4	0.00106
Thiamine hydrochloride	337	4	0.0119
Inorganic Salts			
Calcium Chloride (CaCl$_2$) (anhyd.)	111	200	1.80

Table 3.4 – *Continued*

Ferric Nitrate (Fe(NO$_3$)$_3$"9H$_2$O)	404	0.1	0.000248
Magnesium Sulfate (MgSO$_4$) (anhyd.)	120	97.67	0.814
Potassium Chloride (KCl)	75	400	5.33
Sodium Chloride (NaCl)	58	6400	110.34
Sodium Phosphate monobasic (NaH$_2$PO$_4$-H$_2$O)	138	125	0.906
Other Components			
D-Glucose (Dextrose)	180	4500	25.00
Phenol Red	376.4	15	0.0399
Sodium Pyruvate	110	110	1.000

*Note: Pyridoxine HCl replaces pyridoxal HCl.

3.3.5 Cell Proliferation (DNA Concentration)

A PicoGreen assay kit (Molecular Probes, Eugene, OR) was used to quantitatively determine the amount of total DNA that is correlated to the number of cells grown on hydroxyapatite and hydroxyapatite – Bioglass®45S5 bioceramic substrates. Following the manufacturer's instruction, 100 μl aliquots of each cell lysate sample were added to 400 μl of 1xTE in a cuvette. PicoGreen Reagent Dye solution (500 μl) were added to each cuvette and incubated at room temperature for 2-5 minutes. A blank sample and standards containing final concentrations of 0 to 25 ng/ml of calf thymus DNA were used to make a DNA standard curve. After the incubation time, readings of samples and standards were taken with a fluorometer (VersaFluor Fluorometer, BioRad) with emission wavelength at 480 nm and excitation wavelength of 520 nm.

3.3.6 Alkaline Phosphatase (ALP) Activity

Alkaline phosphatase is an early marker of osteoblast differentiation that was measured by a previously reported method [105]. The quantification of alkaline phosphatase is achieved by the conversion of p-nitrophenyl phosphate, a colorless substrate, into p-nitrophenol, a yellow-colored substance. 80 μl aliquots from each lysate sample were added to individual wells in a 96-well plate with 100 μl of substrate solution (4 mg/ml) and 20 μl of alkaline buffer (1.5 M 2-amino-2methyl-1-propanol at a pH of 10.3). The plate was then incubated for 1 hr at 37℃, and the

reaction was stopped by adding 100 µl of 0.3 N NaOH. The plate reader (UV max kinetic microplate reader, Molecular Devices) was used to determine the absorbance at 405 nm. Samples were compared to p-nitrophenol standards ranging from 0 to 500 µM.

3.3.7 Inductive Coupled Plasma (ICP) Analyses

ICP analyses were performed by Chemical Solutions Ltd. Calcium, phosphorous, potassium, and magnesium concentrations in the complete bone media that was taken from the original media and 6 day cell culture of hydroxyapatite and hydroxyapatite – Bioglass®45S5 bioceramics were measured in order to determine the ion leaching from the substrate to the solutions.

<u>3.4 X-ray Absorption Near Edge Structure (XANES) Spectroscopy</u>

The characterization techniques such as XRD, TF-XRD, SEM coupled with EDS are very useful techniques to analyze and identify the chemical composition and morphology of the bioceramic surfaces; however, these techniques fail to provide any information on nature of the chemical bonds and the structural environment of the atoms in the compounds present throughout the thickness of the materials. The X-ray absorption near edge structure (XANES) spectroscopy is a technique that is capable of probing the local structural and bonding environment around selected atoms and can determine their formal valence (experimentally difficult to determine in a nondestructive technique); coordination environment (e.g., octahedral, tetrahedral coordination) and subtle geometrical distortions of it [106] by using synchrotron radiation. Synchrotron radiation is an intense source of electromagnetic radiation generated by the acceleration of ultra relativistic (moving near the speed of light) charged particles through magnetic fields in an electron or positron storage ring. It has over a wide range of energies produced much greater than a common x-ray laboratory ensuring much higher sensitivity of element specific spectroscopic analyses [107]. Other than broad spectral range, natural collimation that allows high energy resolution in X-ray region, high intensity that enables fast data collection, and high brightness that ensures examining small samples or small areas are few of

43

many characteristics of synchrotron radiation [108]. Another advantage of XANES is that unlike diffraction-based techniques for studying atomic structure of matter, it does not require crystalline samples and can be used as a powerful analytical technique in the study of amorphous phases form such as describing and characterizing the early stages of hydroxyl carbonated apatite deposition on the surface of bioceramic materials [88] or amorphous phases form by sintering different amounts of Bioglass®45S5 with hydroxyapatite.

XANES spectroscopy has been a useful technique to investigate biomedical materials. For instance, to evaluate the structural environment of calcium atoms in calcium deficient hydroxyapatite powders [109] and calcium compounds where they have importance in artificial bone implants and medical treatments [110], to clarify local structure of phosphorus atom in the hydroxyapatite structure [111], to obtain information on changes in the calcium ion environment of calcium phosphate ceramics such as hydroxyapatite during mineralization [112] and crystallization process [113], and understand the process of hydroxyl carbonated apatite (HCA) formation on the surface of bioactive glasses after immersion in SBF solution [89]. Even though, XANES has been used to probe Si coordination environment in amorphous materials [114], silicate minerals [115-117], and glasses [118], it has not been widely used in bioceramic materials. Therefore, for this research XANES will be a unique tool to evaluate the phases form by blending and sintering Bioglass®45S5 with hydroxyapatite as well as apatite deposition on these bioceramic compositions subsequent to immersion in SBF.

When the incident synchrotron X-ray beam photon energy reaches a sufficient level, it excites a core shell electron (either K-edge or $L_{2,3}$-edge) from its bound inner-shell into the conduction band of the material in examination. This creates a defined and discontinues break in the absorption spectrum of the material, and a spectrum taken of a condensed material exhibits an oscillatory structure right above the absorption threshold also known as absorption edge. The peaks close to the absorption edge can be attributed to transitions to localized electronic states, with the edge position itself being related to the oxidation state of the absorbing atom. The strong

44

oscillations just beyond the absorption edge as in XANES can be explained in terms of the multiple scattering of photoelectrons by the atoms in a local cluster around the absorbing atom [108].

The details of the shape of the spectra will give information of different complexes of the same ion state depending on the symmetry and distance between the ion of interest and its near neighbors. The Figure 3.1 (a) and (b) representatively show how XANES spectra change by local coordination chemistry and the oxidation chemistry, respectively. Figure 3.1 (a) represents how the XANES spectra show differences depending on the local coordination environment. Many edges of many elements shows significant edge shifts with oxidation shifts as shown in Figure 3.1 (b) [119].
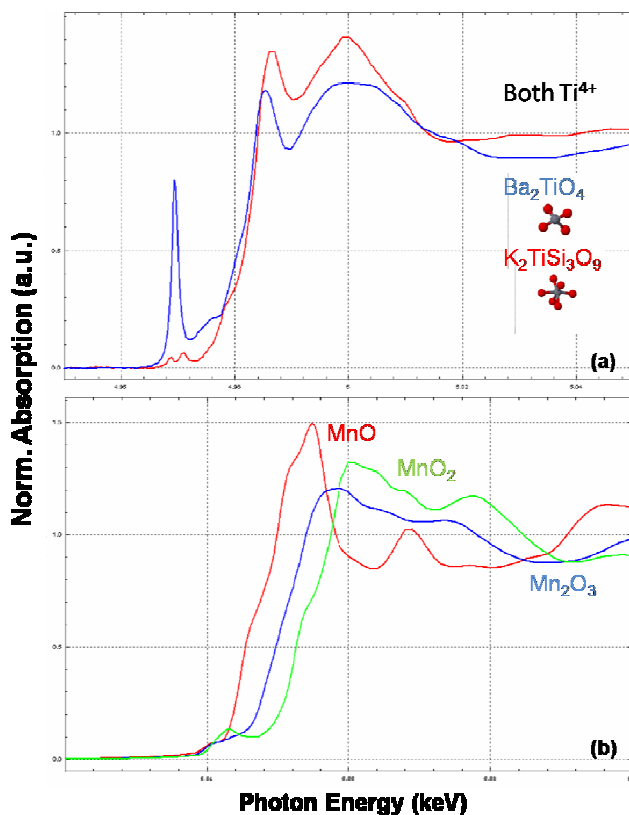
Figure 3.1: (a) Representative XANES spectra shows dependence on the local coordination chemistry, (b) Representative XANES spectra shows edge shifts with oxidation shift.

45

However, it is very hard to conclude any spectra before comparing them with the model compounds. If model compounds consist of the ion of interest are created, one can show the similarities between the model spectra and ion of interest [107]. The absorption peak shape and intensity of the model compounds those are affected by site symmetry, bond angles and distances, and the number of nearest neighbors can be compared to gain information on the structural environment of specific ions in the samples [120]. Therefore, the results can be used as a fingerprint to identify presence of particular chemical species. In this manner, the photon absorption spectra were recorded by using two available modes of XANES which are fluorescent yield and total electron yield to identify both crystalline and amorphous compositional changes of the bulk bioceramics and their surfaces. While total electron yield (TEY) mode allows examine the surface layers up to 5 nm for L-edge and 50 nm for K-edge, Fluorescent yield (FLY) can be used to obtain information from the bulk up to 50 nm for L-edge and 300 nm for K-edge mode [121].

This technique was initially applied to the analysis of model compounds in order to identify the kind of atomic species that can be expected to be present in the bioceramic samples which finger prints the bioceramic compounds through the dependence of the spectral features on the first nearest neighboring atom type and on the oxidation state of the central atom at different absorption edges, with different oxidation states and structures [108]. It was also used to provide information on different oxidation states of element ions and complexes presents in bioceramic compositions and evaluate the main and secondary phases which may have formed during sintering. Particularly, the amorphous portion of these compositions and the effects of these phases on the bioactivity of the compositions were identified by gaining detailed information in molecular level where no crystallinity is required. The distinctive elements present in bioceramic compositions and hydroxyl carbonated apatite layers are silicon (Si), phosphorus (P), and calcium (Ca). Therefore, in this research, Si, P, and Ca K-absorption edge and $L_{2,3}$-absorption edge were used to identify the chemical structure of both crystalline and amorphous phases present in the bioceramic samples as well as model compounds by the support of two

46

Canadian Light Source facilities with two different beamlines, and Table 3.5 summarizes the specifications for these two beamlines:

1. Variable line spacing plane grating monochromator (VLS-PGM) 11ID-2 at the Canadian Light Source (CLS) facility, Saskatoon, Saskatchewan, Canada. The VLS-PGM beamline was used to probe silicon and phosphorus X-ray absorption spectra within the range 5.5 – 250 eV that covers L-absorption edge.

2. The Canadian double crystal monochromator (DCM) at the Synchrotron Radiation Center (SRC) at the University of Wisconsin – Madison in Stoughton, Wisconsin. DCM beamline has an energy range of 1500 – 4000 eV, and was used to probe the X-ray absorption of calcium, phosphorus, and silicon K-absorption edge [106].

Table 3.5: Specifications of the beamlines used in this study [106]

Beamline	DCM	VLS-PGM
Energy Range	1500 – 4000 eV	5.5 – 250 eV
Spot Size (horizontal x vertical)	2mm x 2mm	500µm x 500µm
Resolution	0.5 eV	0.1 eV

3.5 Nano-Indentation Test

Great developments have been made for the past decade in probing mechanical properties of materials under submicron where the force and displacement can be measured as an indentation made. The data derived from indentation load vs. displacement can be used to determine mechanical properties even the indentations are too small to be imaged. Nano-indentation has significant potential to study near surface mechanical properties of solids. It is especially suited to the mechanical characterization of thin film coated systems and surface layers where both low contact loads and high spatial precision can be applied. The use of nano-indentation techniques for coated systems is attractive because smaller test depths than typical thickness can be applied. In addition, the response of the coated system can be measured with

47

the coating in situ on the substrate; tests can be performed at variable displacements so that properties can be determined as a function changing substrate effect. This technique represents one of the only ways of determining the elastic, plastic, and fracture responses of surfaces at real asperity contact [122, 123].

In quasi-static nano-indentation tests, normal force is applied to an indenter tip while measuring tip displacement into the sample. The mechanical properties of the surface can be probed for fine scale and point to point variation which also provides topographic mapping with submicron resolution in the scanning probe microscopy (SPM) mode. Hereby, a quick and an easy imaging can be achieved by using the same tip used for indentation [106]. The most frequently measured mechanical properties using load vs. depth sensing techniques are the elastic modulus, E, and the hardness, H which obtained from one complete cycle of loading and unloading. In this research all bioceramic samples were probed in the SPM mode prior to the indentation test to obtain an undamaged, consistent, uniform, and relatively smooth surface in order to perform a significant test [122, 123].

The three parameters to determine hardness and modulus are the peak load (P_{max}), the depth at peak load (h_{max}), and the initial unloading contact stiffness (S_{max}). During indentation, the applied load force and tip displacement are continually measured, creating a load-displacement curve for each indent. A schematic view of load vs. indenter displacement is shown in Figure 3.2 which can be analyzed according to the Equation 3.1. Equation 3.1 shows the relation between the measured stiffness S, the reduced modulus E_r, and the contact area A. The effect of non-rigid indenters on the load vs. displacement behavior can be effectively accounted for by defining a reduced modulus, E_r, through the Equation 3.2 where E and v are the Young's modulus and Poisson's ratio for the specimen and E_i and v_i are the same parameters for the indenter. The hardness which is defined as the mean pressure the material will support under load is determined by the relation given with Equation 3.3. The contact area can be calculated

48

using the following relation shown in Equation 3.4 where h_c is the contact depth and C is the measured compliance [122, 123].
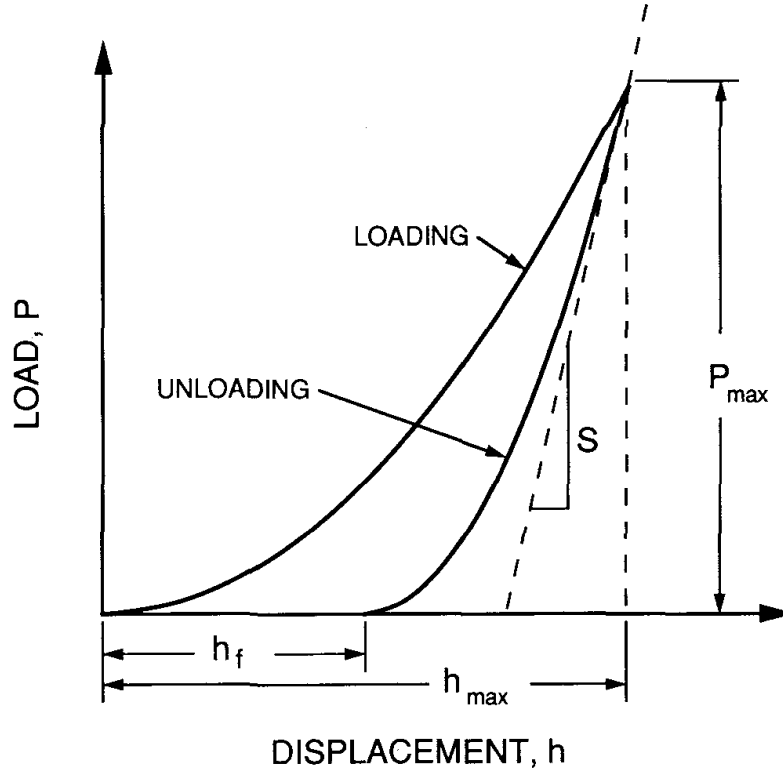
Figure 3.2: A schematic representation of load versus indenter displacement data for an indentation experiment. The quantities shown are P_{max}: the peak indentation load; h_{max}: the indenter displacement at peak load; h_f: the final depth of the contact impression after unloading; and S: the initial unlading stiffness [122].

$$S = \frac{dP}{dh} = \frac{2}{\sqrt{\pi}} E_r \sqrt{A}$$

Equation 3.1

$$\frac{1}{E_r} = \frac{\left(1 - \nu^2\right)}{E} + \frac{\left(1 - \nu_i^2\right)}{E_i}$$

Equation 3.2

$$H = \frac{P_{\max}}{A}$$

Equation 3.3

49

$$A = 24.5h_c{}^2 + \sum_{i=0}^{7} Cih_c{}^{1/2i} \qquad\qquad \text{Equation 3.4}$$

Even though local mechanical properties of various biological tissues [124, 125] as well as bioceramic materials, such as compact sintered bioceramic powders [123, 126], bioceramic coatings [127, 128] and the interfacial properties between the coating and the substrate [129], and bioceramic composites [33, 130, 131], have been evaluated by well established nano-indentation technique, there is very little literature available focusing on the nano-mechanical evaluation of precipitates formed on bioceramic materials by *in vitro* incubation [132, 133]. Since the nano indentation can be conducted at a relatively high resolution across the specimen, and mineralized tissue such as bone has a non-homogenous mineralized structure, the nano-indentation can be very significant for measuring the mechanical properties of very small selected regions [133].

In this research, nano indentation tests were run using two different types of quasi-static load functions; a trapezoidal single loading and a cyclic loading. Both load functions were engaged under the load control mode and the depth dependence by vertical displacement of the indenter tip. The nano-indentation tests by trapezoid single indents were used to measure the reduced elastic modulus (E_r) and the hardness (H) of sintered Bioglass®45S5 added hydroxyapatite bioceramics before and after immersion to SBF solution for 4 weeks to provide information on the mechanical property differences of the precipitated and mineralized layers formed on the bioceramic sample surfaces following *in vitro* incubation.

All nano indentation tests were run at the Hysitron Ubi 1 TriboIndenter® using a Berkovich tip which is a three sided pyramid with a total included angle of 142.3 degrees and a half angle of 65.35 degrees. The elastic modulus of Berkovich tip is 1140 GPa and has a poisson ratio of 0.07.

50

<u>Trapezoidal single indents</u>

Each indentation test with a trapezoidal load function is composed of a 5-second loading segment, a 2-second holding segment (at the maximum load), and a 5-second unloading segment. The reduced modulus is measured during the unloading segment by measuring the slope of the load-displacement curve at the early stages of unloading. The trapezoidal load function is shown in Figure 3.3 (a). The response is the load displacement curve from which the reduced elastic modulus is measured from the unloading segment (Figure 3.3 (b)). Accurate measurement of the displacement of the tip during the indentation process allows the calculation of the hardness and reduced elastic modulus of the bioceramic samples and the hydroxyl carbonated apatite layer formed on them from a load versus displacement curve (Figure 3.3 (b)). The values are calculated from the initial slope of the withdrawal (unloading) as mentioned in an early study [122]. The TriboIndenter® Berkovich tip was calibrated for compliance and tip abnormalities, using the manufacturer's suggested method of measuring a succession of indents into a silica sample at different penetration depths to calculate the tip area function needed for calculating hardness and the reduced elastic modulus (E_r) is defined through the Equation 3.4 given earlier this section [106].
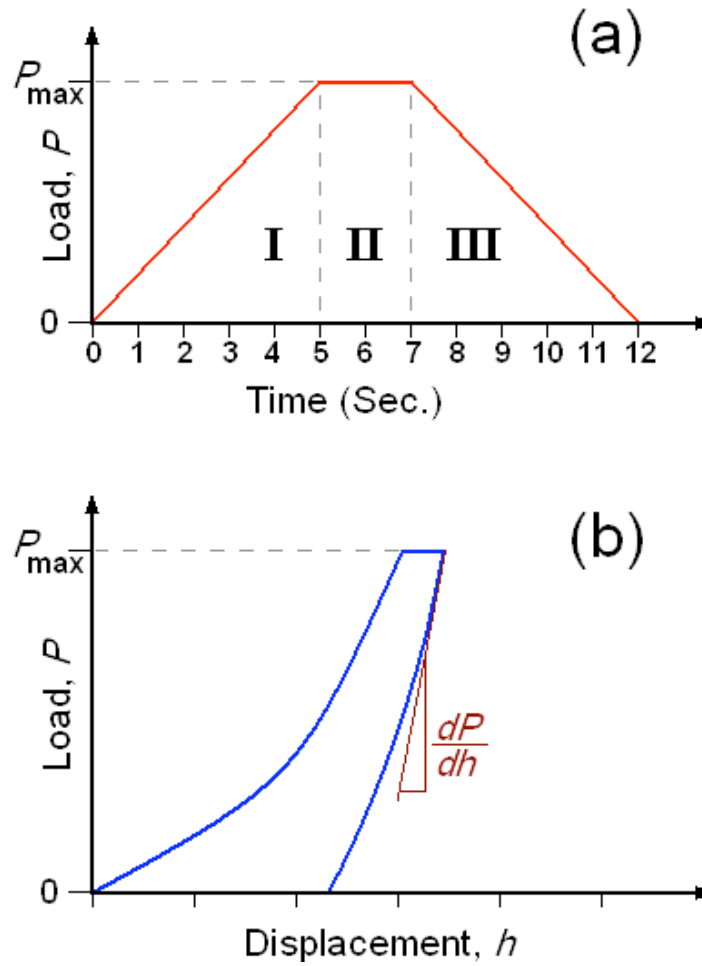
Figure 3.3: (a) Load function of trapezoidal single indentation test with I: Loading, II: Holding, III: Unloading segments, (b) Schematic of load vs. displacement curve [106].

Cyclic loading indents

In cyclic loading indentation, the load function is series of trapezoidal loading cycles with a total of 25 cycles. It consists of a 1-second loading segment, a 1-second holding segment and a 1-second unloading segment. The maximum load for each holding segment is incrementally increased with each loading cycle with the first cycle having a maximum load of 0.25 μN and the final cycles having a maximum load of 10,000 μN. The final load of unloading segment in each cycle is slightly higher than the starting load of the loading segment in that cycle. The load function of cyclic loading indents used in this study is shown in Figure 3.4. The cyclic loading

52

indentation tests were run with the Hysitron Ubi 1 TriboIndenter® with a Berkovich tip. The main advantage of using cyclic indentation is since the tip can penetrates further with each indentation cycles, the measured reduced elastic modulus and hardness values can be plotted against displacement of the tip in the vertical direction (i.e. penetration depth). The resulting modulus and hardness vs. depth data may however differ from data collected from single indents specifically in the case of apatite layers. All biological tissues are highly inhomogeneous and consist of high internal irregularities [134]. Since the hydroxyl carbonated apatite layers formed on the surface of bioceramic samples have similar structure to that of bone, certain differences are expected from the data obtained from cyclic loading of these samples.
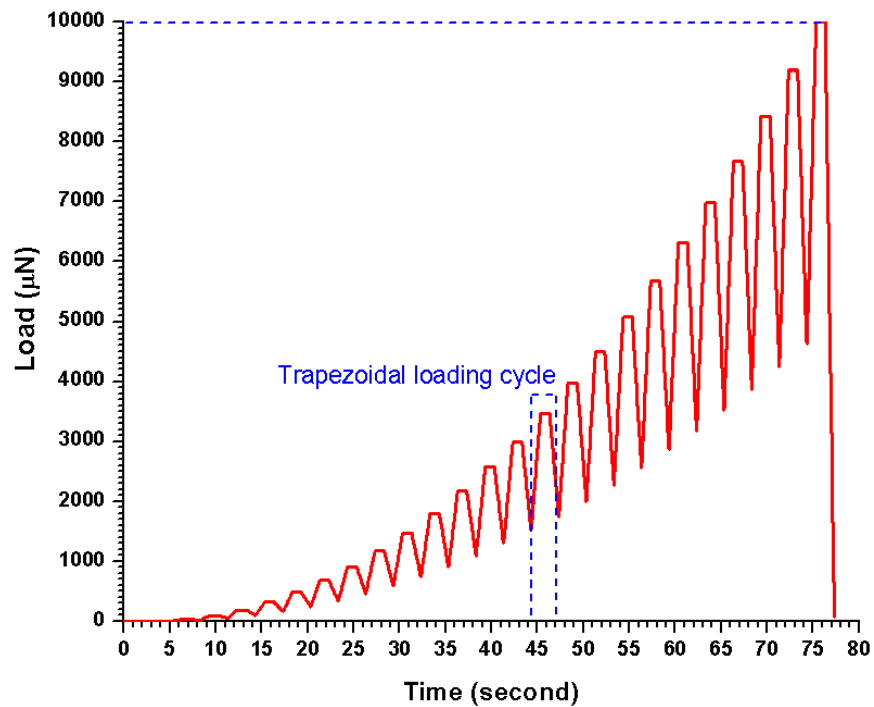
Figure 3.4: Load function of cyclic loading indents.

CHAPTER 4

SYNTHESIS OF NEW BIOCERAMICS AND THEIR BIOACTIVITY

4.1 Introduction

Hydroxyapatite ($Ca_{10}(PO_4)_6(OH)_2$) is one of the most well known phosphates in the biologically active phosphate ceramic family by virtue of its similarity to natural bone mineral. Synthetic and biologically harvested hydroxyapatite finds a variety of biological applications and elicits the formation of an apatite layer at the interface with bone tissue [7-11]. Applications include bone repair in prosthetics [12], and dental applications [13].

Although hydroxyapatite has an osteoconductive nature and supports osteogenic differentiation of marrow stromal cells (MSCs) [18], its bioactivity, while attractive, is not nearly sufficient to actively form apatite layers on surfaces [14-16]. In addition, hydroxyapatite requires longer time and large number of MSC's to differentiate them into osteoblasts [18].

Other materials such as phosphate ceramics and different bioglass compositions have been used as sintering aids to assist in sintering of hydroxyapatite or as a component of composite to enhance material properties including bioactivity. For instance, Chatzistavrou et al found that sintered hydroxyapatite composites containing different amounts of Bioglass®45S5 lead to increased bioactivity [23]. The sodium phosphates have also been found to be effective sintering aids for hydroxyapatite, and resulting products were found to be bioactive [58]. In toxicity studies of silica containing calcium phosphate glasses, it has been shown that the presence of even 5 wt. % SiO_2 in a glass results in significant mortality when injected intraperitoneally into mice [135]. In another study, a calcium phosphate phase was formed on the surface of calcium phosphate invert glasses of composition $60CaO.30P_2O_5 7Na_2O_3 TiO_2$ when immersed in simulated body fluid (SBF) [62]. Tricalcium phosphate (TCP) a crystalline bioactive ceramic also degrades

to calcium and phosphate salts both *in-vivo* and *in-vitro*, and also results in the precipitation of hydroxyapatite on the surface of an implant [63]. Several studies with β-TCP and biphasic HA/β-TCP ceramics have shown that β-TCP behaves in an osteoinductive manner enhancing bone ingrowth around and into implants in animal studies [136, 137]. In a separate study using a mixture of hydroxyapatite with TCP with autogenous cancellous bone it was shown that there was strong callus formation and a strong bony union after four weeks of implantation [138]. Among all the calcium phosphates used in biological applications only two calcium phosphates are stable when they are in contact with aqueous media: At a pH<4.2 the stable phase is $CaHPO_4.2H_2O$ (DCP) while at pH>4.3 the stable phase is hydroxyapatite [34]. Furthermore, different calcium phosphates have different induction times for the formation of carbonated apatite, with some of the calcium deficient hydroxyapatite exhibiting poor bioactivity and the TCP and calcium pyro phosphates exhibiting very good bioactivity [34].

Among all bioglass compositions Bioglass®45S5 developed by Larry L. Hench and co-workers [20] consisting of 45 wt.% SiO_2, 24.5 wt.% Na_2O, 24.5 wt.% CaO, and 6 wt.% P_2O_5 has been found to be one of the most bioactive glasses [16]. Moreover, it has the potential to be used in many more bioactive applications than hydroxyapatite [21]. The bioactivity of Bioglass®45S5 was shown to be insensitive to the level of crystallization with the 100% crystalline material exhibiting the same level of bioactivity as the amorphous material [65]. In a bioactivity study an increased cytotoxic response was shown for glasses with very high sodium oxide (Na_2O) content. This increase in cytotoxic response was attributed to the increase in local pH due to ion exchange reaction occurring at the surface of the bioactive glass [64]..

The Bioglass®45S5 by itself is not structurally viable and as a structural material sintered hydroxyapatite is a very brittle ceramic which is more or less strong in compression and weak in tension [22]. Therefore, Bioglass®45S5 is used in conjunction with hydroxyapatite either as a sintering aid (<5wt %) or second phase (>5wt %) [8, 23, 24] which may also result in improved mechanical properties specifically compressive strength. There have been many attempts to

55

combine hydroxyapatite with bioactive glasses of different compositions in order to produce composites with improved mechanical and biological properties [16, 17, 23, 27] and significant gains in mechanical properties with improved bioactivity have been reported.

Another important concern in bioceramic materials is the porosity. Porous bioceramics have an advantage over dense bioceramics for tissue engineering. Proper sized pores and having enough interconnection to pass through the bioceramics are desirable due to the penetration of cells, blood vessels, and extracellular matrices deep into the bulk. Therefore, the new tissue can regenerate not only around the surface but also inside [25]. It is shown that new compositions formed by sintering hydroxyapatite with different amounts of Bioglass®45S5 at relatively elevated temperatures causes a liquid phase sintering which resumes with a significant improved densification [16]. However, successful tissue in-growth which will furthermore enhance the tissue attachment can only be maintained with an optimum level of porosity [26]. In contrast, substantial porosity will negatively affect the structural viability of the implant. Therefore, it is very crucial to achieve enough porosity while maintaining a viable structure to support the damaged bone.

In the present study, a series of hydroxyapatite – Bioglass®45S5 mixtures were sintered yielding products ranging from sintered hydroxyapatite with β-TCP to new chemistries of ceramics with compositions of calcium phosphate silicate to sodium calcium phosphate in silicate matrices. The structure and porosity of these blended materials were examined by X-ray diffractometer, scanning electron microscopy, and a simple calculation of mass over volume, respectively. The compression tests were performed on sintered bioceramic compositions using a MTS machine. In addition, rat bone marrow stromal cells were cultured on these substrates, and the cell proliferation and osteoblast differentiation after 3 and 6 day cell culture were investigated using Pico Green DNA assays and alkaline phosphatase activity, respectively.

56

<u>4.2 Experimental Procedure</u>

4.2.1 Formulation of Hydroxyapatite – Bioglass®45S5 Blends

 <u>Powder preparation</u> The bioglass powder consisting of 45 wt. % SiO_2, 6 wt. % P_2O_5, 24.5 wt. % Na_2O, and 24.5 wt. % CaO also known as Bioglass®45S5 was acquired from US Biomaterials with a particle size of <90µm, and the hydroxyapatite with a chemical composition of $Ca_{10}(PO_4)_6OH_2$ was acquired from Alfa Aesar with a particle size of <44µm. Five different mixtures were prepared with 1, 2.5, 5, 10, and 25 wt. % Bioglass®45S5 addition to hydroxyapatite.

 <u>Sample Preparation</u> The Bioglass®45S5 powders were mixed with proper amount of hydroxyapatite in 250 ml polyethylene bottles, and ball milled for 30 hours with acetone. After ball milling, the mixtures were dried in the oven at 80°C for 24 hours. The dried powder mixtures were sieved until the particles were separated from each other. The powders were pressed uniaxially in a die with a diameter of 12.7 mm to a pressure 105 MPa, and sintered at 1200°C for 4 hours with a heating rate of 4°C/minute. The sintering was fol lowed by cooling at 10°C/minute down to room temperature.

4.2.2 Material Characterization

 <u>Density and Porosity Measurements</u> The apparent densities of the green and sintered bioceramic samples were determined by a simple geometric weight over volume method. Eight to ten samples were used to determine the average density for each group. The theoretical densities of each group were calculated by rule of mixtures. The porosity of the sintered product was measured by mercury porosimetry using a Quantachrome Instruments Poremaster Mercury Porosimeter.

 <u>XRD Analyses</u> X-ray diffraction studies of sintered Bioglass®45S5, hydroxyapatite, and hydroxyapatite – Bioglass®45S5 mixtures were examined using a Siemens Kristalloflex 810 Powder Diffractometer using CuKα radiation. The data were recorded over the 2θ range of 20-60° with a 0.01° step size and a count time of 0.1 seco nd.

SEM Analyses The development of microstructures in the bioceramic samples after sintering and subsequent cell culture studies was investigated using Hitachi S-300N and Zeiss Supra 55VP scanning electron microscopes operated in secondary electron mode.

Compression Test The compression test was performed with MTS Q-Test150 with a 150kN capacity. Five different (1, 2.5, 5, 10, and 25 wt. %) hydroxyapatite – Bioglass®45S5 cylindrical bioceramic samples were prepared according to ASTM C773-88 (2006) Standards with approximately 2.0 mean diameter/height ratio. The tests were run at a crosshead speed of 0.5 mm/minute. Compressive strength of cylindrical samples was measured reporting load to failure divided by the cross-sectional area of the samples. The number of specimens tested for each group was at least 3.

4.2.3 Bioactivity (In vitro) Characterization

Isolation and Culture of BMSCs Primary rat bone marrow stromal cells (BMSC's) were isolated from the femurs of Sprague-Dawley rats. The rats were sacrificed with CO_2 and the femurs were excised. Aseptically, the epiphyses were removed and the diaphyses flushed with 5 ml of complete bone media (DMEM) from Invitrogen, supplemented with 10% fetal bovine serum (FBS) from Hyclone, 0.28 µM L-ascorbic acid from RPI Corp., 10 mM β-glycerol phosphate from Sigma, 10 nM dexamethasone from Sigma, 1% penicillin-streptomycin and 0.1% fungizone from Invitrogen using an 18 gauge needle. Aspirating the pellets up and down using the syringe broke up the bone marrow pellets, and the cells were seeded in T-25 flasks (~1 femur per T-25 flask). The T-25 flasks were incubated overnight at 37°C in 5% CO_2. After 24 hours non-adherent cells were removed by 4-5 washes with phosphate buffer solution (PBS) and the adherent cells were further cultured in complete bone media. Upon confluence, cells were detached from the culture surface with trypsin-EDTA, centrifuged at 1000 G's for 10 minutes, and re-suspended in complete bone media for use in experiments or subculture. For analysis, cells on the ceramic disks were lysed on day 3 and day 6 with 1 ml of 1% Triton X100. The experiments were performed on triplicate samples for each group, and cells were seeded on the samples at a density of

58

1×10^4 cells/cm^2 and incubated at 37°C.

Cell Proliferation A Pico Green DNA assay kit (Molecular Probes, Eugene, OR) was used to quantitatively determine the amount of total DNA that is correlated to the number of cells grown on the hydroxyapatite – Bioglass®45S5 substrates. Following the manufacturer's instruction, 100 μl aliquots of each cell lysate sample were added to 400 μl of 1xTE in a cuvette. PicoGreen Reagent Dye solution (500 μl) were added to each cuvette and incubated at room temperature for 2-5 minutes. A blank sample and standards containing final concentrations of 0 to 25 ng/ml of calf thymus DNA were used to make a DNA standard curve. After the incubation time, readings of samples and standards were taken with a fluorometer (VersaFluor Fluorometer, BioRad) with emission wavelength at 480 nm and excitation wavelength of 520 nm.

Alkaline Phosphatase Activity Alkaline phosphatase is an early marker of osteoblast differentiation that was measured by a previously reported method [105]. The quantification of alkaline phosphatase is achieved by the conversion of p-nitrophenyl phosphate, a colorless substrate, into p-nitrophenol, a yellow-colored substance. 80 μl aliquots from each lysate sample were added to individual wells in a 96-well plate with 100 μl of substrate solution (4 mg/ml) and 20 μl of alkaline buffer (1.5 M 2-amino2methyl-1-propanol at a pH of 10.3). The plate was then incubated for 1 hour at 37°C, and the reaction was stopped by adding 100 μl of 0.3 N NaOH. The plate reader (UV max kinetic microplate reader, Molecular Devices) was used to determine the absorbance at 405 nm. Samples were compared to p-nitrophenol standards ranging from 0 to 500 μM.

ICP Analyses ICP analysis were performed by Chemical Solutions Ltd. Calcium, phosphorous, potassium, and magnesium concentrations in the complete bone media that was taken from the original media and 6 day cell culture of hydroxyapatite and 1, 2.5, 5, 10, and 25 wt. % Bioglass®45S5 added hydroxyapatite bioceramics were measured in order to determine the ion leaching from the substrate to the solutions.

4.2.4 Statistics

The *in-vitro* bone marrow stromal cell proliferation and differentiation tests were performed on triplicate samples for each group of bioceramic compositions. The data represented as mean ± SD (Standard Deviation). Statistical difference was analyzed using one-way ANOVA variance analysis, and *p* value of less than 0.05 was considered significant.

<u>4.3 Results</u>

4.3.1 Physical and Chemical Characterization

Five different compositions of ranging from hydroxyapatite with 1 wt. % Bioglass®45S5 to a composition with 75 wt. % hydroxyapatite and 25 wt. % Bioglass®45S5 were sintered at 1200°C for a period of 4 hours. The structural chan ges and new phase formation associated with the reaction between the hydroxyapatite and Bioglass®45S5 after the sintering process were probed using powder X-ray diffraction (XRD). Shown in Figure 4.1 are the XRD patterns of the five different products. Analyses of the diffraction peaks resulted in the identifications of the products that are listed in Table 4.1. The primary ceramic present when 1, 2.5 and 5 wt. % Bioglass® was sintered with hydroxyapatite is hydroxyapatite itself (JCPDF#09-0432) with β-TCP ($Ca_3(PO_4)_2$, JCPDF#09-0169) as the secondary phase. There is no evidence of any crystalline silicate phase formed using X-ray diffraction. This indicates that the Bioglass®45S5 behaves more as a sintering aid and promotes the conversion of HA to β-TCP.
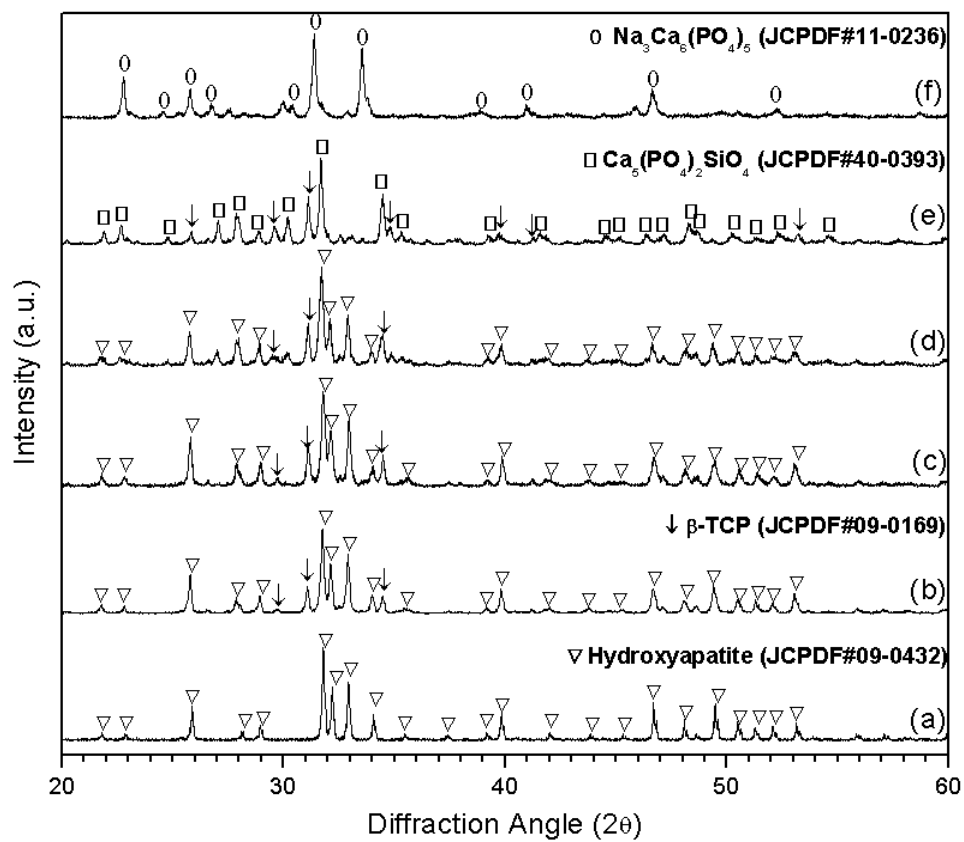
Figure 4.1: Powder X-ray diffraction spectra of bioceramics formed by sintering hydroxyapatite with (a) 1, (b) 2.5, (c) 5, (d) 10, and (e) 25 wt. % Bioglass®45S5 at 1200°C for 4 hours. ∇: $(Ca_{10}(PO_4)_6(OH)_2)$, $\downarrow$: β-$Ca_3(PO_4)_2$, $\square$: $Ca_5(PO_4)_2SiO_4$, and 0: $Na_3Ca_6(PO_4)_5$.

Table 4.1: Bioceramic compositions formed by sintering hydroxyapatite with 1, 2.5, 5, 10, and 25 wt. % Bioglass®45S5 at 1200°C for 4 hours.

Bioglass®45S5 content (wt. %)	Composition of Phases Present
0	Synthetic Hydroxyapatite $(Ca_{10}(PO_4)_6OH_2)$
1	Synthetic Hydroxyapatite + β-TCP $(β-Ca_3(PO_4)_2)$
2.5	Synthetic Hydroxyapatite + β-TCP
5	Synthetic Hydroxyapatite + β-TCP
10	Calcium Phosphate Silicate $(Ca_5(PO_4)_2SiO_4)$ + β-TCP + Amorphous Silicate Phase
25	Sodium Calcium Phosphate $(Na_3Ca_6(PO_4)_5)$ + Amorphous Silicate phase

In order to estimate the extent of conversion of HA to β-TCP quantitative X-ray diffraction techniques were used. Reference samples of known amounts of hydroxyapatite and β-TCP (up to 60% β-TCP) were prepared and homogenized and their powder x-ray patterns were determined. The dominant peaks in hydroxyapatite, the (2,1,1) peak and the (0,2,10) peak in β-TCP were used as reference for quantitative analysis. The ratio of integrated intensity of the (0,2,10) β-TCP peak to the (2,1,1) hydroxyapatite peak to the wt.% of β-TCP is shown in Figure 4.2 and is mathematically represented in Equation 4.1.

$$\left. I_{β-TCP(0,2,10)} \middle/ I_{HA(2,1,1)} \right. = 0.0174W_{β-TCP} - 0.0976 \qquad \text{Equation 4.1}$$
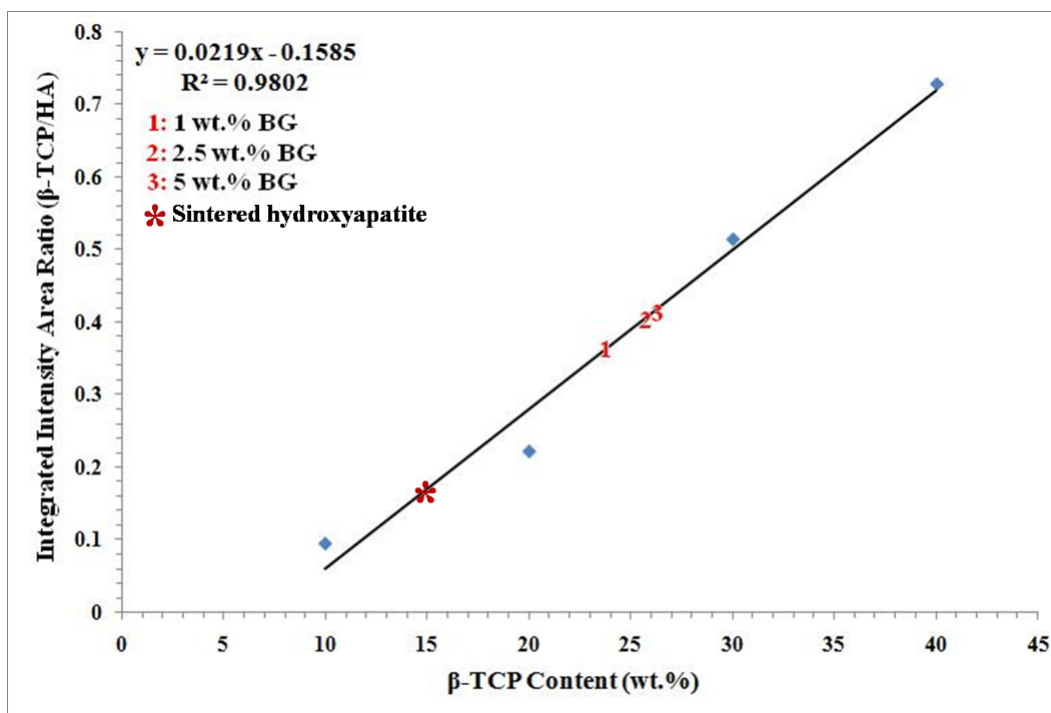
Figure 4.2: Calibration plot of ratio of measured integrated intensities of peaks of β-TCP and hydroxyapatite. Superimposed are the measured ratios of the integrated intensities for sintered hydroxyapatite and the compositions with up to 5 wt. % Bioglass®45S5.

The ratio was used in each case to determine the ratio of crystalline phases β-TCP to hydroxyapatite in the sintered composites and superimposed on the calibration curve are the actual ratios for the ceramics with up to 5 wt. % Bioglass®45S5. It is evident from Figure 4.2 that as the extent of Bioglass®45S5 is increased the extent of conversion of hydroxyapatite to β-TCP increases till it reaches 35% at a composition of 5 wt. % Bioglass®45S5.

However, when 10 and 25 wt. % Bioglass®45S5 are added to the hydroxyapatite and sintered, the main crystalline phase present in the sintered product is no longer hydroxyapatite. It is calcium phosphate silicate ($Ca_5(PO_4)_2SiO_4$, JCPDF#40-0393) when 10 wt. % Bioglass®45S5 is added, and sodium calcium phosphate ($Na_3Ca_6(PO4)_5$, JCPDF#11-0236) when 25 wt. % Bioglass®45S5 is used. In the case of 10 wt. % Bioglass®45S5, there is still some β-TCP present as indicated by the arrows. On the other hand, the 25 wt. % Bioglass®45S5 added hydroxyapatite bioceramic has very little evidence of the presence of any other crystalline phase

other than $Na_3Ca_6(PO_4)_5$. As Bioglass®45S5 contains 45 wt. % SiO_2, it can be presumed that the bioceramics formed with 10 and 25 wt. % Bioglass® have their crystalline phases embedded within an amorphous silicate matrix.

The X-ray diffraction (XRD) analyses of un-sintered Bioglass®45S5 and Bioglass®45S5 sintered at 1200ºC for 4 hours are shown in Figure 4.3. In the case of un-sintered Bioglass®45S5 no characteristic diffraction peaks were observed which indicates that all Bioglass®45S5 was amorphous prior to sintering. On the other hand, peaks observed for sintered Bioglass®45S5 are indexed as $Na_2CaSi_3O_8$ (JCPDF#12-0671).
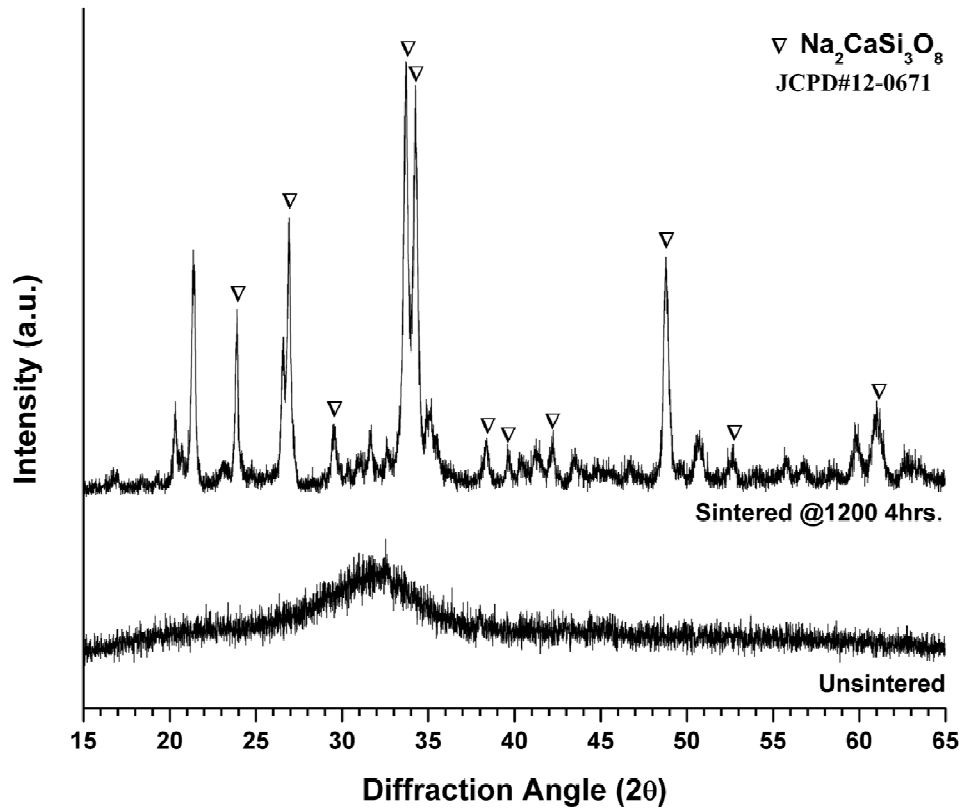
Figure 4.3: Powder X-ray diffraction spectra of un-sintered and sintered Bioglass®45S5 at 1200℃ for 4 hours showing the formation of crystal line phases of $Na_2CaSi_3O_8$.

XRD patterns of un-sintered hydroxyapatite, hydroxyapatite sintered at 1100℃ for 1 hour; α-TCP, un-sintered β-TCP and β-TCP sintered for 1 hour at 1200℃ are shown in Fig ure 4.4. An interesting observation is that the powder diffraction patterns of the un-sintered HA and β-

TCP are very similar. However, on sintering their respective crystalline structures are revealed. The sintered hydroxyapatite has approximately 14% β-TCP formed by decomposition of hydroxyapatite.
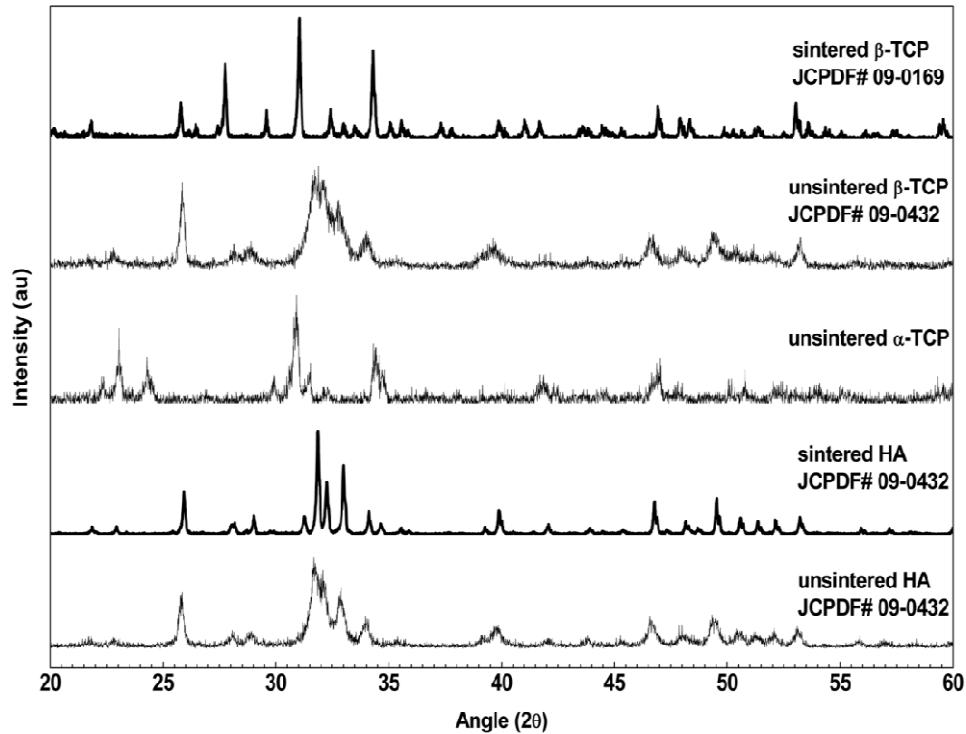
Figure 4.4: Powder XRD spectra of as received $Ca_{10}(PO4)_6(OH)_2$ (HA), the $Ca_{10}(PO_4)_6(OH)_2$ sintered for 4 hours yielding synthetic HA with small amounts of β-TCP, α-TCP, as-received β-TCP and β-TCP sintered for 4 hours at 1200°C showing the development of sharp peaks of β-TCP.

The theoretical, green, and sintered densities of the bioceramic compositions are shown in Figure 4.5(a) and the porosity content measured by mercury porosimetry of the sample cross section is shown in Figure 4.5(b). The theoretical density is based on a simple rule of mixtures with the assumption that constituents used in the mix remain unchanged on sintering, which is certainly not the case here, but yet provide a first estimate of the density of the ceramic product. Bioglass®45S5 has lower density compared to synthetic hydroxyapatite, and as expected the density of the mixtures increases after sintering and decreases with an increase in Bioglass®45S5 content. However, the observed decrease in density is larger than that predicted

65

by simple rule of mixtures. In compositions with up to 5 wt. % Bioglass®45S5 up to 35 % of the hydroxyapatite is decomposed to β-TCP, the theoretical density of hydroxyapatite is 3.16 g/cm^3 and that of β-TCP is 3.07 g/cm^3. The lower density of β-TCP compared to hydroxyapatite partly accounts for the decrease in density of compositions with up to 5 % Bioglass®45S5 but does not completely explain it. The porosity content of the ceramics with up to 5 wt. % Bioglass®45S5 as measured by mercury porosimetry is close to 0 % (Figure 4.5(b)) which indicates that there is some closed porosity in the sintered product resulting in final densities ranging between 85 to 90 % of theoretically calculated values.

Compositions with higher amounts of Bioglass®45S5 of 10 and 25% exhibited higher levels of porosity (14 and 10% porosity after sintering respectively) and lower levels of densification indicating the presence of glassy phases that retarded the densification process. This also explains the fact that the measured density of the finished ceramic in the compositions with 10 and 25 wt. % Bioglass®45S5 is significantly lower than the theoretical density.
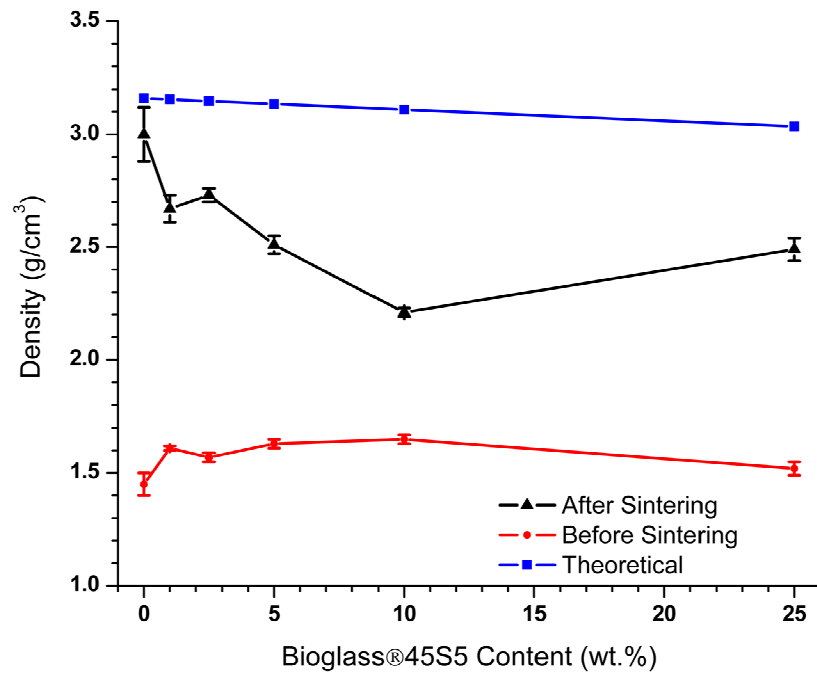
(a)
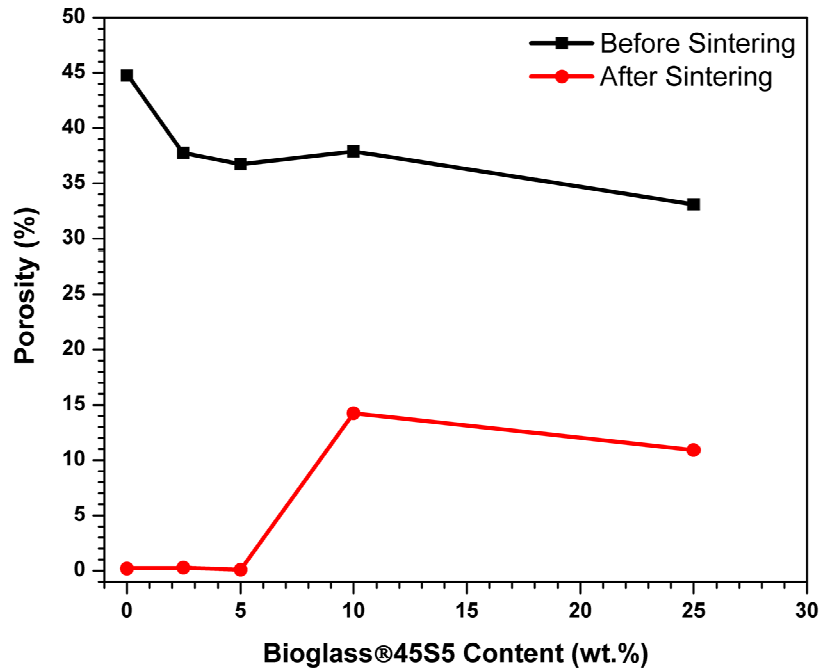
(b)

Figure 4.5: (a) Theoretical density of the bioceramics and the measured density of the green and sintered bioceramics. (b) Porosity of the green and sintered bioceramics.

67

4.3.2 Microstructural Characterization

The secondary electron scanning electron micrographs (SEM) of hydroxyapatite, and hydroxyapatite with 1, 2.5, 5, 10 and 25 wt. % Bioglass®45S5 after sintering are shown in Figure 4.6(a-f), respectively. Figure 4.6(a) shows the microstructure of pure hydroxyapatite and indicates a well sintered microstructure with a typical grain size of 1-2 μm. When 1 and 2.5 wt. % Bioglass®45S5 is used, the microstructures are quite similar with good densification and little evidence of any second phase along the grain boundary. On the other hand, when 5 wt. % Bioglass®45S5 is used as shown in Figure 4.6(d), some regions are covered with glassy phase and there is evidence of larger porosity in the microstructure. The grain size in all compositions with less than 5 wt. % Bioglass®45S5 are in the range of 1-2 μm. On the other hand, the compositions with 10 and 25 wt. % Bioglass®45S5 (Figure 6 (e and f)) exhibit an amorphous glassy matrix with the composition with 10 wt. % Bioglass®45S5 embedded with $Ca_5(PO_4)_2SiO_4$ whiskers and the composition with 25 wt.% has $Na_3Ca_6(PO_4)_5$, crystalline particles within a glassy matrix.
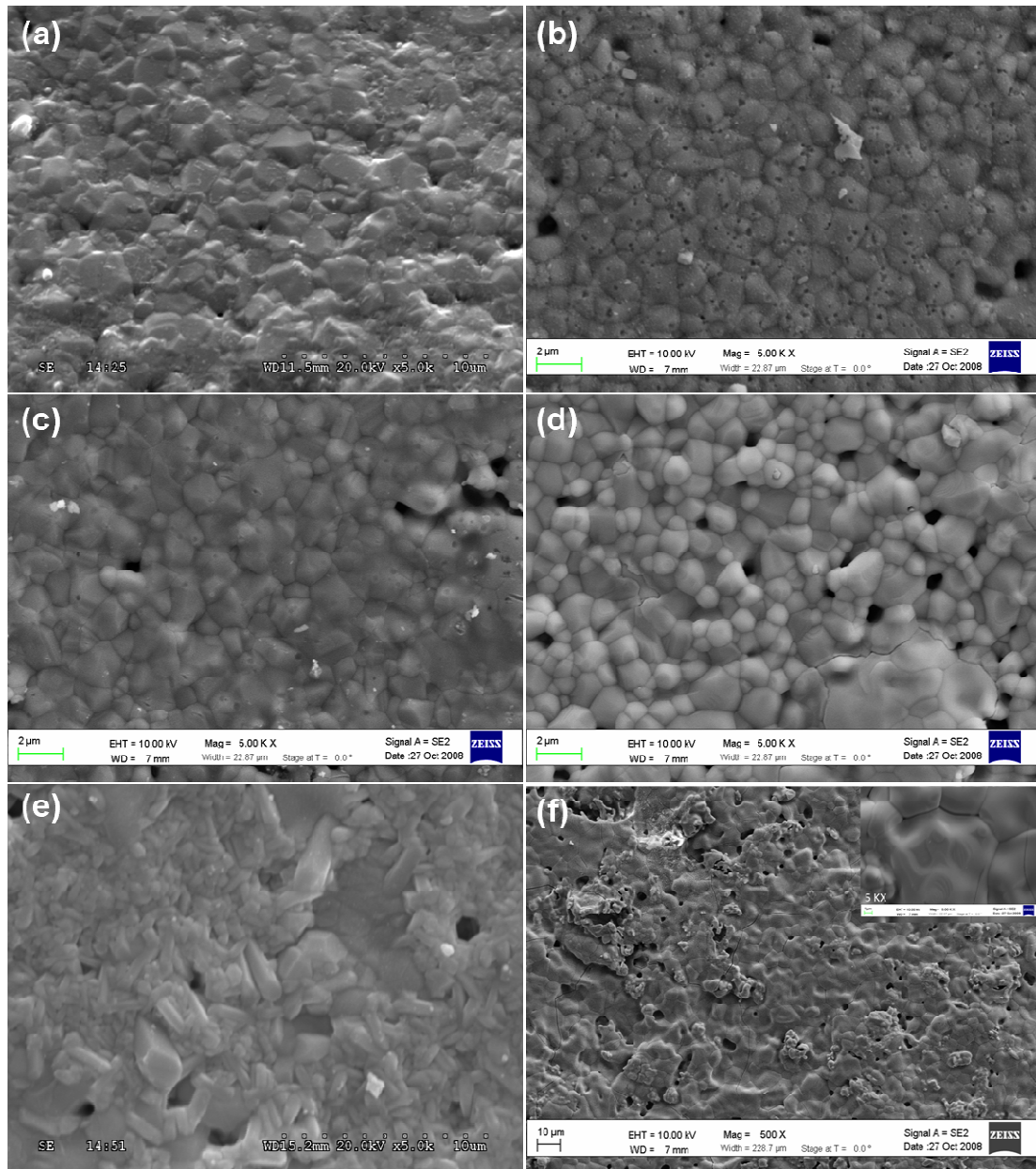
Figure 4.6: Scanning electron micrographs (at 5 KX) of as sintered bioceramics with HA and (a) 0, (b) 1, (c) 2.5, (d) 5, (e) 10, and (f) 25 wt. % Bioglass®45S5. All bioceramic compositions were sintered at 1200°C for 4 hours. The bioceramic compositions with 10 wt. % Bioglass®45S5 has $Ca_5(PO_4)_2SiO_4$ in a silicate matrix, and the bioceramic compositions with 25 wt. % Bioglass®45S5 is made up of $Na_3Ca_6(PO_4)_5$ in a silicate matrix.

In order to differentiate the mineralization behavior in the presence of bone marrow stromal cells and in its absence, the different ceramic chemistries were placed in media with and without bone marrow stromal cells. The secondary electron micrographs of hydroxyapatite and compositions with 1, 2.5, 5, 10, and 25 wt. % Bioglass®45S5 added hydroxyapatite bioceramics after 6 day culture in media **without** bone marrow stromal cells (BMSC) are shown in Figure 4.7(a-f). Hydroxyapatite and compositions of hydroxyapatite with up to 5 wt. % Bioglass®45S5 shown in Figure 4.7(a-d) indicate some amounts of dissolution followed by reprecipitation in other regions. The dissolution results in the formation of micro porosity. On the other hand compositions with $Ca_5(PO_4)_2SiO_4$ and $Na_3Ca_6(PO_4)_5$ in a silicate matrix shown in Figure 4.7(e, f) formed an apatite layer with the latter composition showing the largest levels of apatite formation.
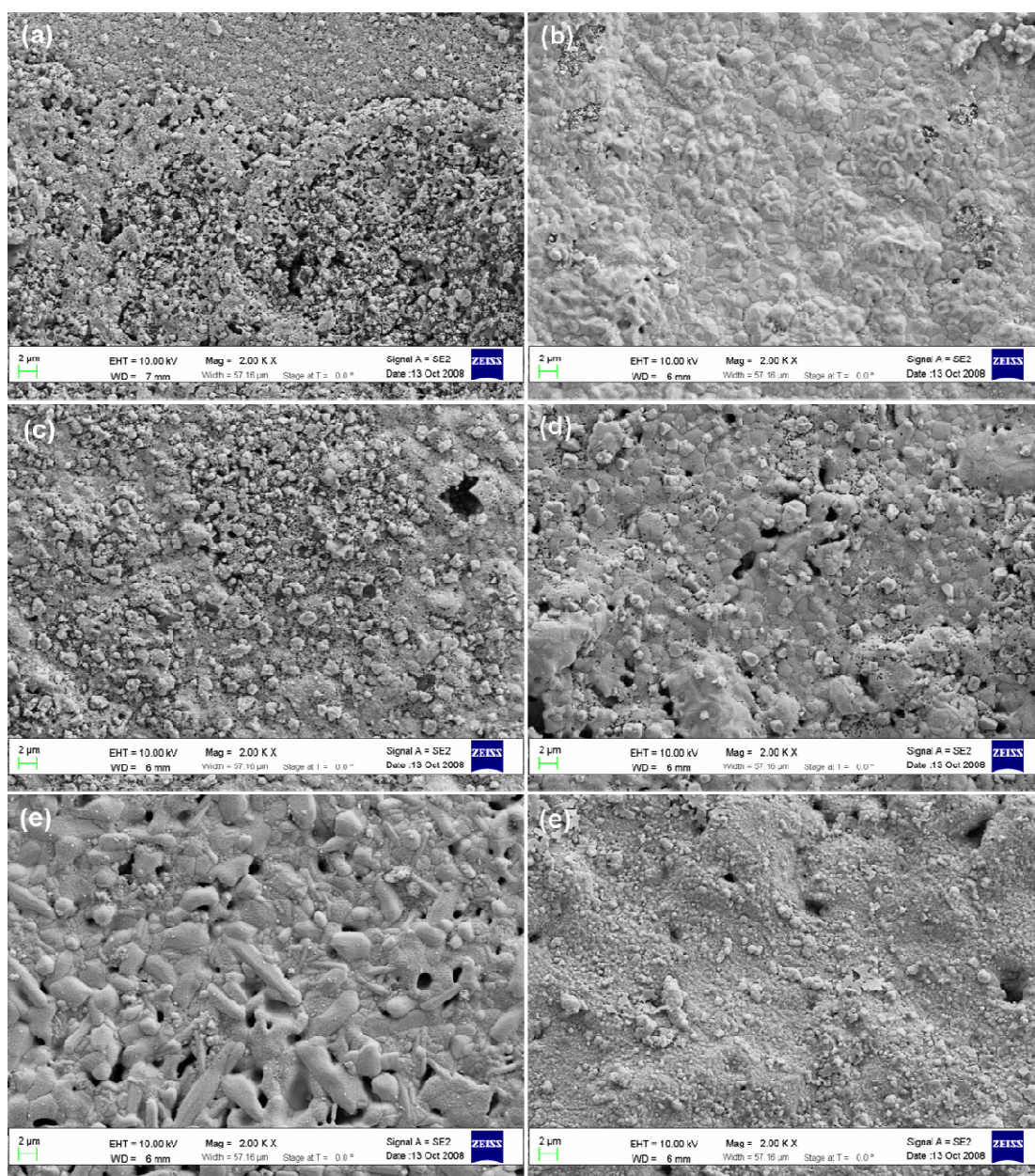
Figure 4.7: Scanning electron micrographs of the bioceramic compositions with (a) 0, (b) 1, (c) 2.5, (d) 5, (e) 10, and (f) 25 wt. % Bioglass®45S5 incubated 6 days in DMEM without cells.
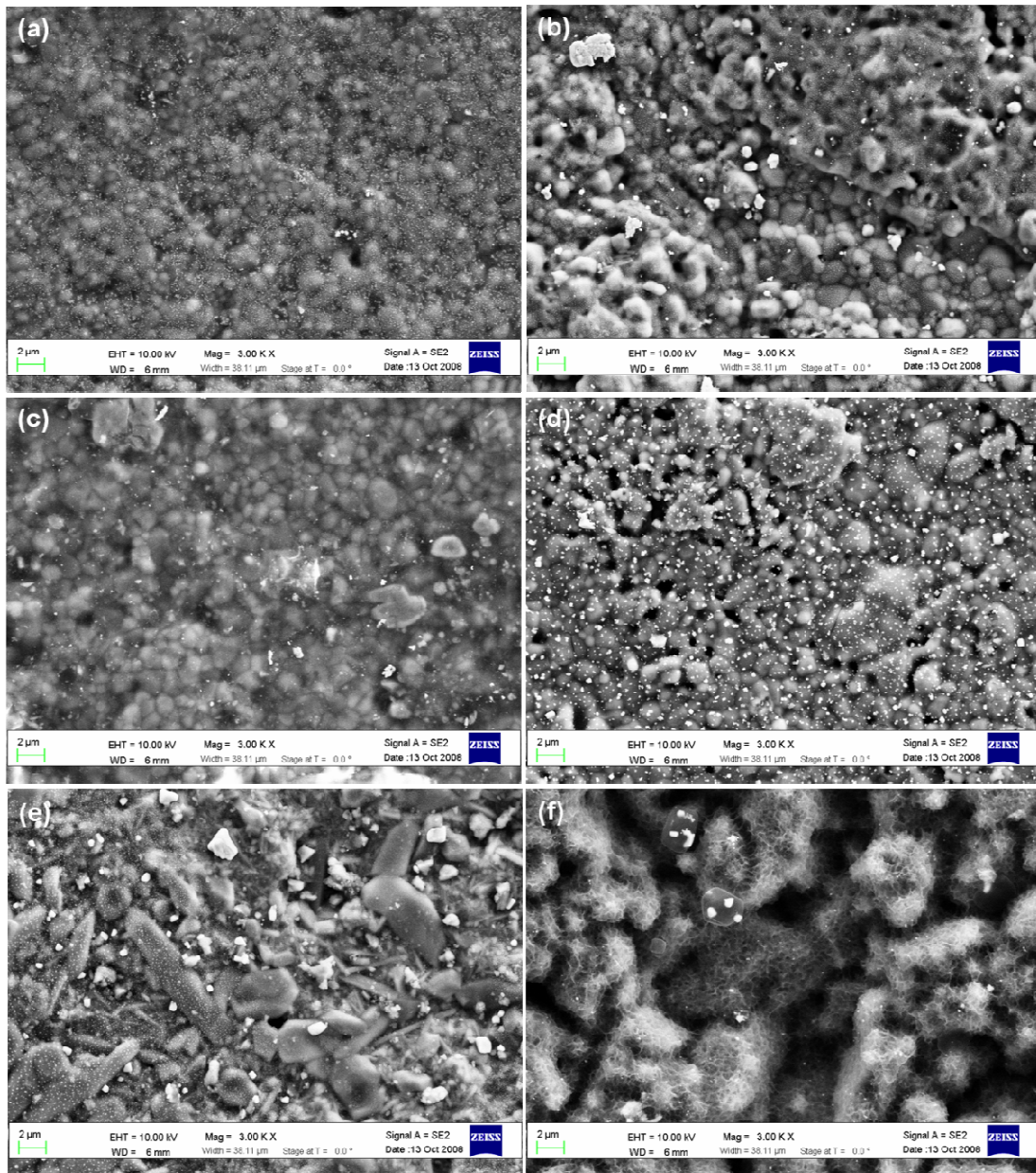
Figure 4.8: Scanning electron micrographs of the ceramics with (a) 0, (b) 1, (c) 2.5, (d) 5, (e) 10, and (f) 25 wt. % Bioglass®45S5 incubated 6 days in DMEM with bone marrow stromal cells.

The secondary electron micrographs of HA and compositions with 1, 2.5, 5, 10, and 25 wt. % Bioglass® added HA bioceramics that were cultured for 6 days in bone media **with** BMSC are shown in Figure 4.8 (a-f). All samples exhibited an apatite layer formation on their surfaces. The highest amount of apatite formation was seen in the bioceramic with $Na_3Ca_6(PO_4)_5$ in a

silicate matrix.

4.3.3 Mechanical Characterization

The variation of the compressive strength of hydroxyapatite and the bioceramics with different amounts (1, 2.5, 5, 10, and 25 wt. %) of Bioglass®45S5 addition to hydroxyapatite and sintered at 1200ºC for 4 hours are shown in Table 4.2. Compressive strength of cylindrical samples was measured reporting load to failure divided by the cross-sectional area of the samples. The average compressive strength achieved for sintered hydroxyapatite is similar or better when compared to literatures as given in Table 4.3.

Table 4.2: Average values of compressive strength for hydroxyapatite and five different hydroxyapatite – Bioglass®45S5 bioceramic compositions sintered at 1200°C for 4 hours.

Composition	Compressive Strength (MPa)
Hydroxyapatite (0 wt. % Bioglass®) (HA)	64±18
1 wt. % Bioglass®45S5 added HA	26±2
2.5 wt. % Bioglass®45S5 added HA	34±5
5 wt. % Bioglass®45S5 added HA	79±15
10 wt. % Bioglass®45S5 added HA	74±8
25 wt. % Bioglass®45S5 added HA	131±14

Table 4.3: Compressive strength values for hydroxyapatite, dentine hydroxyapatite, bovine hydroxyapatite, cortical bone, and cancellous bone from various literatures.

Synthetic Hydroxyapatite [22, 139]	
Sintering Temperature	1140 – 1340 ºC
Compressive Strength	5.26 – 13.81 MPa
Sintering Temperature	1000 – 1300 ºC
Compressive Strength	25.22 MPa in average
Dentine Hydroxyapatite [140]	
Sintering Temperature	1000 – 1300 ºC
Compressive Strength	9.83 – 56.77 MPa
Enamel Hydroxyapatite [141]	
Sintering Temperature	1000 – 1300
Compressive Strength	27.60 – 61.27 MPa
Bovine Hydroxyapatite [140]	
Sintering Temperature	1000 – 1300 ºC
Compressive Strength	12 – 65 MPa
Cortical Bone [1, 72-74]	
Compressive Strength	100 – 230 MPa
Cancellous Bone [1, 28, 72]	
Compressive Strength	2 – 12 MPa

4.3.4 In-vitro Characterization

The inductive couple plasma (ICP) analysis for calcium, phosphorous, potassium, and magnesium concentrations in the complete bone media that was taken from the original media and 6 day cell culture of BMSC on the surface of hydroxyapatite, and hydroxyapatite with 1, 2.5, 5 wt. % Bioglass®45S5 and bioceramics with $Ca_5(PO_4)_2SiO_4$ and $Na_3Ca_6(PO_4)_5$ in a silicate matrix are shown in Figure 4.9. The most significant deviation in the chemistry of the solution was found

74

when the bioceramic with $Na_3Ca_6(PO_4)_5$ was immersed for 6 days in media containing BMSC

with higher levels of Ca and lower levels of P in the media.
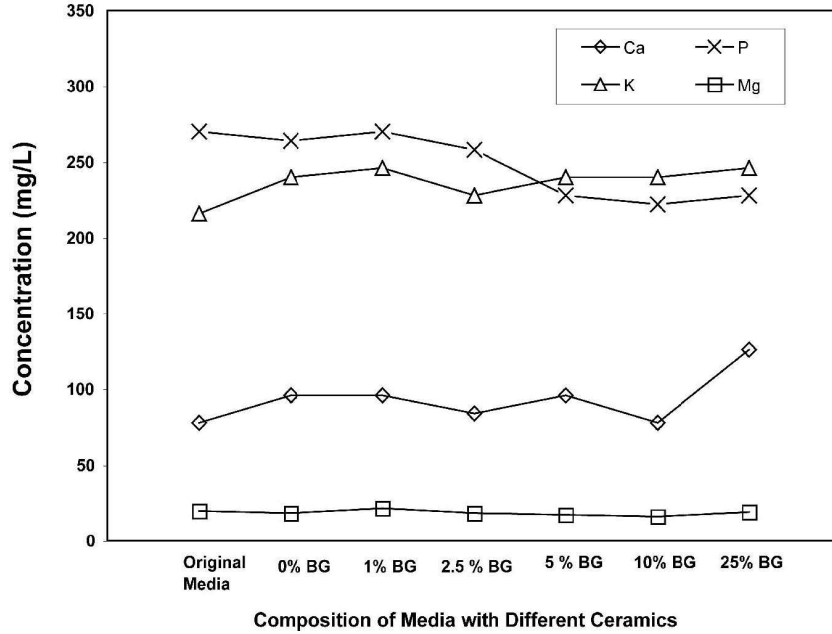
Figure 4.9: Inductive couple plasma (ICP) analysis for calcium, phosphorous, potassium, and magnesium concentrations in the DMEM that was taken from the original media and media where samples of pure HA and bioceramics with mixtures of 1, 2.5, 5, 10, and 25 wt.% Bioglass® with HA were immersed in the DMEM and BMSC and cultured for 6 days.

The proliferation of rat BMSC on hydroxyapatite and compositions with 1, 2.5 and 5 wt. %

Bioglass®45S5 as well as bioceramics $Ca_5(PO_4)_2SiO_4$ and $Na_3Ca_6(PO_4)_5$ in a silicate matrix after

3 and 6 day cell culture are shown in Figure 4.10. Pico Green DNA assay was used to compare

the DNA concentration on the bioceramic substrates that correlates to the number of cells on the

substrates. All Bioglass® added HA bioceramics exhibited more cell proliferation compared to

pure synthetic HA samples, in a silicate matrix both after 3 and 6 day incubation (except the

composition with $Na_3Ca_6(PO_4)_5$ that showed a marginal decrease after 6 days). However, One-

way analysis of variance (ANOVA) showed statistically significant difference only in pure HA in

comparison to compositions with 2.5 and 5 wt. % Bioglass® ($p < 0.05$) and compositions with 2.5

wt. % Bioglass® in comparison to compositions with 10 and 25wt. % Bioglass® ($p < 0.05$) after 3

day cell culture. The composition with $Ca_5(PO_4)_2SiO_4$ in a silicate matrix exhibited the maximum proliferation of the rat BMSC after 6 day cell culture showing statistically significance over all bioceramic compositions ($p < 0.05$).
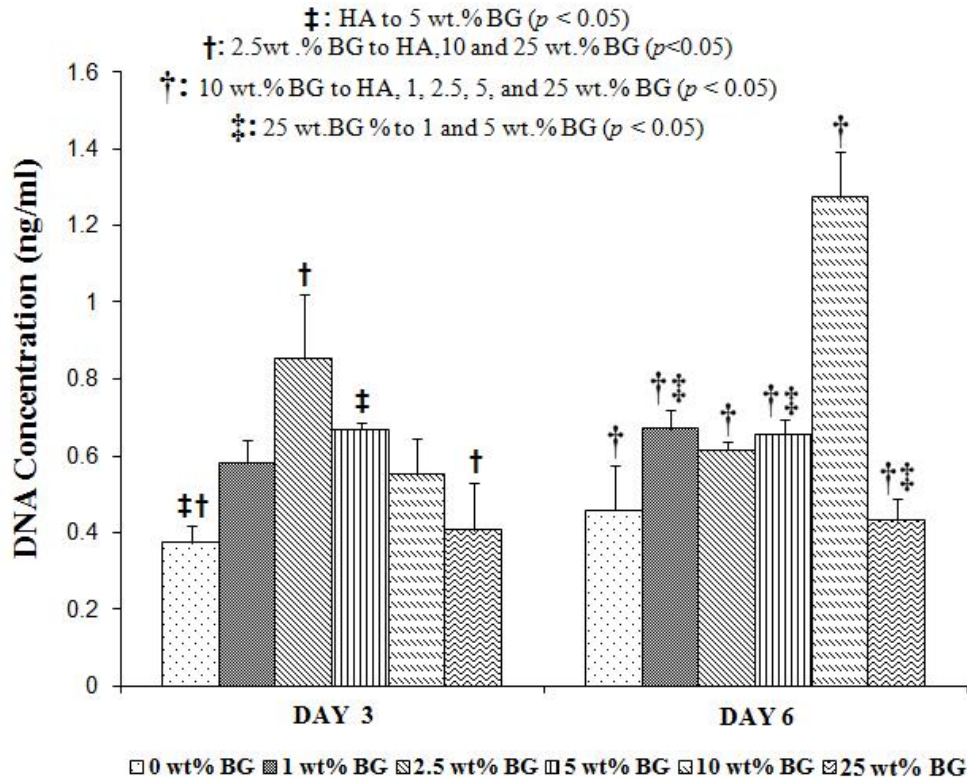
Figure 4.10: Pico Green DNA assay of rat BMSC cultured in DMEM for 3 and 6 day on the surface of the pure HA and bioceramic compositions with different amounts of Bioglass®. The data represents mean ±SD.

The Alkaline Phosphatase (ALP) activity of rat BMSC cultured on HA and bioceramic compositions with 1, 2.5 and 5 wt. % Bioglass® as well as bioceramics with $Ca_5(PO_4)_2SiO_4$ and $Na_3Ca_6(PO_4)_5$ in a silicate matrix in complete bone media for 3 and 6 day are shown in Figure 4.11. The ALP activity, which was normalized on the basis of DNA concentration per sample, was found to be the most in the samples that contain $Na_3Ca_6(PO_4)_5$ compared to the other compositions. The one-way analysis of variance (ANOVA) showed statistically significant difference between HA and bioceramic composition with $Na_3Ca_6(PO_4)_5$ in a silicate matrix ($p <$

0.05) after 3 day cell culture, and except compositions with 1 wt. % Bioglass® compared to composition with 10 wt. % Bioglass® (*p* > 0.05) and composition with 2.5 wt. % Bioglass® compared to composition with 5 wt.% Bioglass® (*p* > 0.05), all bioceramic compositions have statistically significant difference between them (p < 0.05).
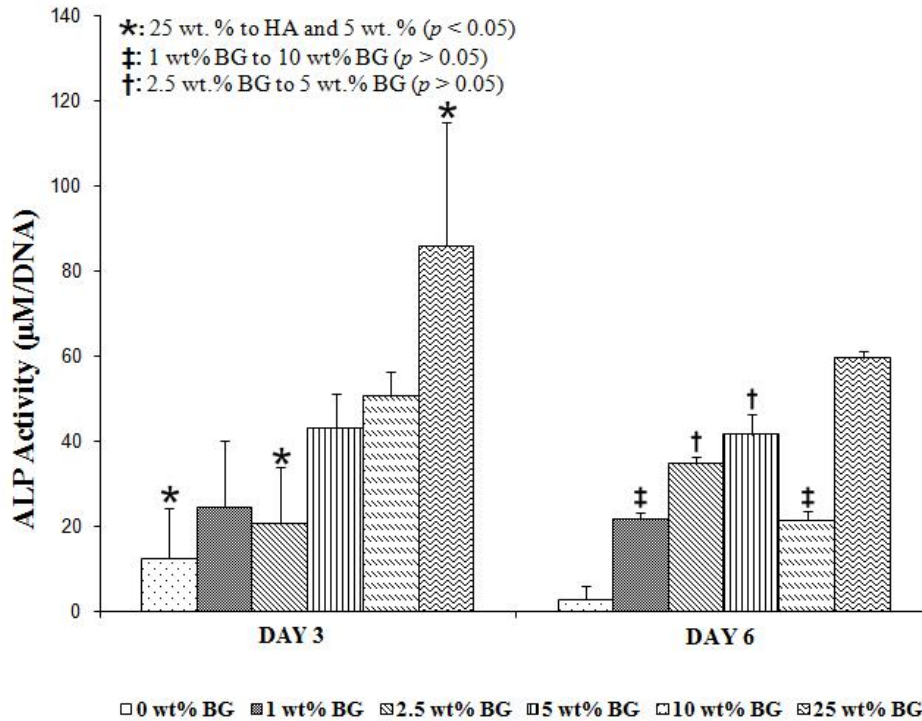
Figure 4.11: ALP activity of the rat BMSC for 3 and 6 day measured with p-NPP assay and normalized on the basis of DNA content per sample. Data represents mean ±SD.

4.4 Discussion

In this study bioceramics with different amounts of hydroxyapatite and Bioglass®45S5 were blended and sintered together. The bioceramic products were characterized for their structure and physical and mechanical characteristics and were examined for biocompatibility and feasibility as substrates for differentiation and proliferation of bone marrow stromal cells.

In order to evaluate the stability and structure of the individual components, they were sintered at 1200°C for a period of 4 hours. Powder XRD patterns for pure hydroxyapatite, 1, 2.5,

5, 10, and 25 wt. % Bioglass®45S5 added hydroxyapatite bioceramics are shown in Figure 4.1. Powder XRD indicates that pure hydroxyapatite retains its structure after sintering with no increase in β-TCP content. In compositions with 1 and 2.5 wt. % Bioglass®, β-TCP is the only new phase detected. On increasing the content of Bioglass®45S5 to 5 wt. % the amount of β-TCP increases (Figure 4.2), indicating the decomposition of hydroxyapatite. Other studies of pure hydroxyapatite have indicated decomposition of hydroxyapatite occurs in the presence of moisture resulting in the formation of β-TCP and CaO at temperature above 1200°C [142]. On the other hand it had also been shown that Ca deficient hydroxyapatite when sintered at temperatures between 700-850°C decompose to yield stoichiometric hydroxyapatite and β-TCP [143]. In a study of decomposition of hydroxyapatite in an air environment at temperatures of 1500°C it has been shown that commercial hydroxyapatite decomposes to tetracalcium phosphate and β-TCP [144]. In thermal decomposition studies of carbonated hydroxyapatite it has been shown that the environment plays an important role in determining the nature of the decomposition products with wet and dry CO_2 encouraging the formation of β-TCP at 1500 and 1300°C while the presence of wet and dry N_2 resulting in the formation of β-TCP at 1200 and 1400°C [145]. In a study where decomposition of hydroxyapatite was examined in the presence of SiO_2 it was shown that a structure similar to β-TCP was formed that contained Si within it and is known as Si-TCP to indicate a Si-stabilized TCP where P in the structure is replaced by Si [146]. This structure has been shown by others to be of great biological interest as it is osteoconductive [147].

There is clear evidence here that indicates that in the absence of Bioglass®45S5 there is very little decomposition of hydroxyapatite on sintering at 1200°C for 4 hours but in the presence of as little as 1 % hydroxyapatite up to 25 % of the hydroxyapatite decomposes to form β-TCP and the β-TCP content increase to 35% as the amount of Bioglass®45S5 is increased to 5 wt. %. The Bioglass®45S5 appears to play the role of a trigger or nucleus that accelerates the decomposition of hydroxyapatite to β-TCP. While the presence of SiO_2 was essential for the

78

formation of Si-TCP, the presence of P already in the Bioglass®45S5 precluded the formation of Si-TCP and forced the decomposition of hydroxyapatite to β-TCP.

On the other hand, in compositions with 10 and 25 wt. % Bioglass®45S5, hydroxyapatite reacts with the Bioglass®45S5 yielding new phases. The composition with 10 wt. % Bioglass®45S5 results in the formation of calcium phosphate silicate ($Ca_5(PO_4)_2SiO_4$) and a limited amount of β-TCP, and the composition with 25 wt. % Bioglass®45S5 yields a sodium calcium phosphate ($Na_3Ca_6(PO_4)_5$) with no evidence of β-TCP. Bioglass®45S5 is a mixture of 45 wt. % SiO_2, 24.5 wt. % Na_2O, 24.5 wt. % CaO, and 6 wt. % P_2O_5. This indicates that in composition with hydroxyapatite that have 10 wt. % Bioglass®45S5 in addition to the crystalline phase $Ca_5(PO_4)_2SiO_4$ there is an amorphous phase rich in Na, P, O with some Si present. The scanning electron micrograph shown in Figure 4.6(e) of the microstructure indicates the presence of whiskers of $Ca_5(PO_4)_2SiO_4$ embedded within a glassy matrix. The formation of calcium phosphate silicate by adding Bioglass®45S5 to hydroxyapatite has been observed by other investigators as well [8, 27]. In addition, in the current study the composition with hydroxyapatite with 25 wt. % Bioglass®45S5 exhibits the formation of a new phase with stoichiometry of sodium calcium phosphate ($Na_3Ca_6(PO_4)_5$) with the complete absence of Si in the crystalline phases. This indicates that the crystalline $Na_3Ca_6(PO_4)_5$ is embedded within an amorphous silicate matrix. The microstructure shown in Figure 6.6(f) indicates that the amorphous silicate matrix is the continuous phase and is present as a glassy phase on the surface.

The XRD diffraction patterns for Bioglass®45S5 before and after sintering are shown in Figure 4.3. Bioglass®45S5 is amorphous in its un-sintered state and crystallizes after sintering at 1200℃ for 4 hours. Crystallization of Bioglass®45S 5 is in agreement with other studies [32] that also show formation of $Na_2CaSi_3O_8$ on sintering Bioglass®45S5. However, some studies [65, 148] have also indicated the possible formation of $Na_2Ca_2Si_3O_9$ that is absent in this study.

The density of theoretical, green, and sintered bioceramic compositions formed by sintering 1, 2.5, 5, 10, and 25 wt. % Bioglass®45S5 added hydroxyapatite were given in Figure

4.5(a). Hydroxyapatite has a theoretical density of 3.16 g/cm^3 [6], Bioglass® 2.66 g/cm^3 [6], and β-TCP 3.07 g/cm^3 [149]. The density of the bioceramics decreases as the Bioglass®45S5 content increases up to 10 wt. % Bioglass®45S5 addition and including the 25 wt. % Bioglass®45S5 added bioceramics all mixtures have lower density levels than the theoretical densities. This would be a proper approach for only up to 5 wt. % Bioglass®45S5 additions, because the rule of mixtures only applies to these bioceramics. 10 and 25 wt. % Bioglass®45S5 added hydroxyapatite bioceramics have traces of neither hydroxyapatite nor Bioglass®45S5 after sintering at 1200ºC for 4 hours. Therefore, the presence of low porosity in compositions with up to 5 wt. % Bioglass® may be associated with the complete reaction of hydroxyapatite with Bioglass®45S5 as suggested by Tancred et al [16]. The gradual density decrease may be contributed from the formation of new phases such as tricalcium phosphate (TCP: $Ca_3(PO_4)_2$) and/or higher porosity levels in composites containing more glass phase.

The porosity of the green bodies was measured prior to sintering and is shown in Figure 4.5(b) indicated that the porosity ranged between 35 and 45% consistent with the particles that arrange themselves on uniaxial cold pressing. On sintering, the density of the pure hydroxyapatite and hydroxyapatite with up to 5 wt. % Bioglass®45S5 indicated very good densification with almost no porosity, this is consistent with the Bioglass®45S5 acting as a sintering aid. Compositions with higher amounts of Bioglass®45S5 of 10 and 25 wt. % exhibited higher levels of porosity (14 and 10% porosity after sintering respectively) and lower levels of densification indicating the presence of glassy phases retarded the densification process. The densities for these compositions can be attributed to the fact that while Bioglass®45S5 by itself has a lower density than hydroxyapatite the composition with 10 wt. % bioglass has a higher porosity that the composition with 25 wt. % Bioglass®45S5, hence the latter composition has a higher density.

Scanning electron microscopy (SEM) of the sintered bioceramics shown in Figure 4.6 (a-f) indicates that the pure hydroxyapatite sintered as a typical ceramic with the presence of micro-porosity at grain boundary triple points. Compositions with 1 wt. % Bioglass®45S5 also have

some microporosity on the surface while compositions with 2.5 and 5 wt. % Bioglass®45S5 have fewer of these microporosities. Compositions with 5 wt. % Bioglass®45S5 also exhibit regions with glassy phase on the surface. In all compositions with up to 5 wt. % Bioglass®45S5 the grain size of the ceramic is in the 1-2 μm range indicating minimal grain growth. Composition with 10 wt. % Bioglass®45S5 exhibits rod shaped crystals of $Ca_5(PO_4)_2SiO_4$ embedded in an amorphous matrix, the presence of the larger Bioglass®45S5 content also results in an increased porosity as evidences by the large number of micro-porosity (1-2 μm) dispersed throughout the surface. Composition with 25 wt. % Bioglass®45S5 exhibits an equiaxed distribution of $Na_3Ca_6(PO_4)_5$ within a silicate matrix. In this composition as well the larger bioglass content results in a higher level of micro-porosity (1-2μm) distributed evenly over the surface.

The compression tests were performed on 5 different Bioglass®45S5 added hydroxyapatite bioceramic compositions sintered at 1200°C for 4 hours to evaluate the variations in mechanical properties. The results are compared to hydroxyapatite sintered at 1200°C for 4 hours as shown in Table 4.2. In addition, all results are compared to various hydroxyapatite and cortical and cancellous bone compressive strength values reported earlier as shown in Table 4.3. The average compressive strength achieved for sintered hydroxyapatite is similar or better when compared to the reported values given in Table 4.3. The hydroxyapatite – Bioglass®45S5 bioceramic compositions with 1 and 2.5 wt. % displays the lowest compressive strength values while 25 wt. % Bioglass®45S5 added hydroxyapatite bioceramics exhibit the highest value indicating that high amounts of Bioglass®45S5 addition significantly improve the compressive strength of bioceramic samples. Bone is composed of two types of bone; cortical and cancellous. The hard outer layer of bone is composed of cortical bone tissue that has minimal gaps and spaces which may be also referred to dense bone skeleton. On the other hand, cancellous bone is less dense and is made up of an array of rods and struts that form open-cell foam, the pores of which are filled in by marrow and accommodate blood vessels [72]. All the bioceramic samples show higher compressive strength than cancellous bone; however, only compressive strength

81

values achieved for 25 wt. % Bioglass®45S5 added hydroxyapatite bioceramic sample with a crystalline $Na_3Ca_6(PO_4)_5$ phase in a glassy silicate matrix falls within the range required for human cortical bone (100-230 MPa) [1, 72-74].

In order to isolate the mineralization ability of each of these sintered bioceramics in the absence of BMSC's, the samples were immersed in DMEM for 3 and 6 days **without** the BMSC. Figure 4.7(a-f) are SEM images of the surfaces after the 6 day immersion. All surfaces exhibited dissolution coupled with mineralization with the composition with $Na_3Ca_6(PO_4)_5$ in a silicate matrix (HA- Bioglass® bioceramic blend with 25 wt. % Bioglass®45S5 and 75 wt. % HA) exhibiting the highest levels of mineralization, and the sintered HA without any Bioglass® showed the lowest levels of mineralization. There are some important distinctions in the nature of dissolution and mineralization on the bioceramic surfaces. The pure hydroxyapatite surface exhibited the least level of activity with the surface exhibiting some dissolution, on the other hand the composition with 1 wt.% Bioglass®45S5 exhibited a fine layer of mineralization on the surface coupled with some dissolution. The composition with 2.5 and 5 wt. % Bioglass®45S5 exhibit larger levels of mineralization coupled with large dissolution of the glassy phase. The level of mineralization in these three chemistries increases with the amount of β-TCP and amount of glassy phase. The composition with 10 wt. % Bioglass®45S5 ($Ca_5(PO_4)_2SiO_4$ in a silicate matrix) exhibited very fine deposits with a uniform layer deposited throughout. The composition with 25 wt. % Bioglass®45S5 that yielding $Na_3Ca_6(PO_4)_5$ within a silicate matrix exhibited the largest bioactivity with extensive mineralization on the surface. This indicates that even in the absence of BMSC the bioceramic sample with a composition of $Na_3Ca_6(PO_4)_5$ in a silicate matrix exhibits significant capacity for mineralization. It is now very well known that calcium to phosphorus molar ratio plays an important role in the dissolution rate of calcium phosphate bioceramics in body fluids [150]. The calcium phosphate bioceramics with Ca/P molar ratio greater than 1.67 are too stable and they are bio-inert; on the other hand, the Ca/P molar ratio lower than 1.5 increases the dissolution rate of the bioceramics in body fluids. Calcium phosphate silicate crystals in

bioceramic compositions formed with 10 w. % Bioglass®45S5 addition have a Ca/P molar ratio of 2.5 which is too high and this may be the reason for this composition does not show much dissolution but does have mineralization. On the contrary, 25 wt. % Bioglass®45S5 added compositions have a Ca/P molar ratio of 1.5 which boosts the dissolution of this composition in DMEM and result in higher mineralization [150]. Also, studies with Bioglass®45S5 have been shown to exhibit faster bone production compared to HA when implanted in rats [66]. In these studies it has been shown that the several reaction layers are formed in the surface of Bioglass®45S5 together with osteoblast proliferation and differentiation that explained the enhanced mineralization on the bioceramic surface [20]. This mechanism suggests that bone bonding and bone tissue in-growth enhancement is the result of these multiple, parallel, and sequential reactions at the bioceramic-tissue interface. In addition, it has shown that these interactions are related to either to physicochemical phenomena that occur in the presence or absence of cells, or reactions affected by cellular activity [5].

The SEM images of surfaces after 6 day cell culture are shown in Figure 4.8(a-f). The bioceramic compositions with larger amounts of Bioglass®45S5 exhibited higher levels of mineralization compared to compositions of pure hydroxyapatite, and the bioceramic compositions with lower levels of Bioglass® (1, 2.5, and 5 wt. % Bioglass®45S5) when cultured for 6 days **with** bone marrow stromal cells in DMEM. This indicates that the formation of the new chemistries of calcium phosphate silicate and sodium calcium phosphate significantly influence the mineralization on the surface in the presence of BMSC. On the other hand, all the bioceramic compositions placed in DMEM without the BMSC showed dissolution on the surface after 6 day incubation. Of all the bioceramic compositions, the 25 wt. % Bioglass®45S5 with 75 wt. % hydroxyapatite that yielded $Na_3Ca_6(PO_4)_5$ in a silicate matrix had the highest bioactivity both in the presence and absence of BMSC. In Figures 4.7(f) and 4.8(f) we can see extensive mineralization on the surface. In an earlier study with Bioglass®45S5 it has been shown that in the first stages the ions dissolve and go into solution, after which a silica gel layer is formed. This

layer is believed to enhance the proliferation and differentiation of cells and mineralization [20].

ICP analysis of the DMEM solution extracted after 6 days immersion of the bioceramic substrates and BMSC was conducted. The data shown in Figure 4.9 indicates that there is not much of a change in the concentration of Mg and K in all the cases. However, the concentration of P in the solution is the lowest in the compositions with 5, 10 and 25 wt. % Bioglass®45S5 and appears to be related to the larger amounts of apatite deposited on the bioceramic surfaces. In addition, the solution in contact with the bioceramic that has a crystalline phase of $Na_3Ca_6(PO_4)_5$ in a silicate matrix (25 wt. % Bioglass®45S5) shows an increase in the concentration of Ca. This indicates that the particles of $Na_3Ca_6(PO_4)_5$ embedded in a silicate matrix leaches out more Ca^{2+} ions into the DMEM in the presence of BMSC. However, the lower P concentration in the DMEM coupled with the significantly higher concentration of apatite formation on the surface indicates a rapid dissolution – reprecipitation process for the mineralization. The extent of mineralization is significantly higher in the presence of BMSC and supports the conclusion of Jie Tue et al [151] who reported that up to a certain range, higher Si concentration in the scaffolds is mitogenic for osteoblasts.

The DNA concentration in the lysate after 6 days immersion in DMEM with BMSC indicate that the scaffold with 10 wt. % Bioglass®45S5 that contains $Ca_5(PO_4)_2SiO_4$ in a silicate matrix has the largest concentration of DNA as shown in Figure 4.10. Figure 4.11 shows the ALP activity normalized by the DNA concentration. The DNA concentration is associated with osteoblastic proliferation, and it is clearly evident that the substrate that contains $Ca_5(PO_4)_2SiO_4$ in a silicate matrix promotes osteoblastic proliferation better than other substrates. However, it has been reported that extensive proliferation affects BMSC differentiation capability and replicative potential of bioceramic substrates [101]. From Figure 4.11 it can be seen that bioceramics formed when 10 wt. % Bioglass® is sintered with hydroxyapatite ($Ca_5(PO_4)_2SiO_4$ in a silicate matrix) did not shown a significant amount of ALP activity. On the other hand, the level of ALP activity in the lysate after 6 days immersion in DMEM with BMSC indicates that the

84

scaffold with 25 wt. % Bioglass®45S5 that contains $Na_3Ca_6(PO_4)_5$ in a silicate matrix has the highest level of activity as shown in Figure 4.11. ALP expression is associated with osteoblastic differentiation, and the level of ALP activity indicates the early stage of osteoblastic differentiation [104]. The higher ALP expression on the $Na_3Ca_6(PO_4)_5$ in silicate matrix indicates that this bioceramic composition promotes osteoblastic differentiation better than other compositions.

<p style="text-align:center;">4.5 Conclusion</p>

Five different ceramic compositions with different amounts of Bioglass®45S5 in synthetic hydroxyapatite (HA) were synthesized by sintering at 1200°C for four hours. Analysis of the structure of the bioceramics using X-ray diffraction reveals that when small amounts of Bioglass® is added (< 5 wt.%) the Bioglass® performs the role of a sintering aid. Higher levels of Bioglass® addition resulted in new phases formed with the bioceramic with 10 wt. % Bioglass® yielding a $Ca_5(PO_4)_2SiO_4$ phase embedded within a silicate matrix, and the composition with 25 wt. % Bioglass® formed new bioceramic phases with a composition of $Na_3Ca_6(PO_4)_5$ in a silicate matrix. A composition with Na3Ca6(PO4)5 in a silicate matrix elicits the highest levels of mineralization on the surface when immersed in DMEM both in the presence and absence of bone marrow stromal cells. Alkaline Phosphatase activity was the highest in the substrates with $Na_3Ca_6(PO_4)_5$ in a silicate matrix indicating that there is a higher level of osteoblast differentiation in the presence of $Na_3Ca_6(PO_4)_5$ in a silicate matrix. DNA concentration that is a measure of osteoblast proliferation is largest in compositions with $Ca_5(PO_4)_2SiO_4$ in a silicate matrix.

CHAPTER 5

XANES STUDY OF HYDROXYAPATITE – BIOGLASS®45S5 CO-SINTERED BIOCERAMICS

5.1 Introduction

The reactivity of bioceramics is a measure of the rate of formation of an interfacial bond between the bioceramic and the bone when it is implanted. Therefore, bioceramics can be classified in four categories based on their chemical reactivity with physiological environment: Nearly inert, porous, surface reactive, and resorbable. Nearly inert bioceramics like alumina and zirconia do not form a bond with the bone. Porous bioceramics such as porous hydroxyapatite form a mechanical bond via in-growth of bone into the pores. Bioactive ceramics like hydroxyapatite, bioglass and glass ceramics form a chemical bond on the interface, and resorbable bioceramics like bioglass and tricalcium phosphate degrade gradually over time and replace bone [1, 57]

Bioceramics such as hydroxyapatite and bioactive glasses have been frequently used for restoration of damaged hard tissues. Synthetic hydroxyapatite is widely used in biomedical applications due to its chemical and biological similarity to natural bone [17, 42]. However, hydroxyapatite has slower degradation rate and lower bioactivity as compared with the biological form of apatite or bioactive glass [17]. Among many bioglass compositions Bioglass®45S5 developed by Larry L. Hench and co-workers [20] consisting of 45 wt.% SiO_2, 24.5 wt.% Na_2O, 24.5 wt.% CaO, and 6 wt.% P_2O_5 has been found to be one of the most bioactive glasses [16]. Bioglass®45S5 has higher bone forming ability than synthetic hydroxyapatite due to having rapid surface reactions within the body [17].

X-ray near edge structure (XANES) spectroscopy has been a useful technique to investigate biomedical materials. For instance, to evaluate the structural environment of calcium

86

(Ca) atoms in calcium deficient hydroxyapatite powders [109] and Ca compounds where they have importance in artificial bone implants and medical treatments [110], to clarify the local structure of phosphorus (P) atom in the hydroxyapatite structure [111], to obtain information on changes in the Ca ion environment of calcium phosphate ceramics such as hydroxyapatite including its mineralization [112] and crystallization process [113]. Even though, XANES has been used to probe silicon (Si) coordination environment in amorphous materials [114], silicate minerals [115-117], and glasses [118], it has not been widely used in bioceramic materials. Therefore, in this chapter, XANES will be a unique tool to evaluate the crystalline as well as amorphous phases formed by blending and sintering different amounts (1, 2.5, 5, 10, and 25 wt. %) of Bioglass®45S5 with hydroxyapatite at 1200ºC for 4 hours, and compare these compositions with various possible model compounds.

5.2 Experimental Procedure

5.2.1 Powder Preparation

The bioglass powder consisting of 45 wt. % SiO_2, 24.5 wt. % Na_2O, 24.5 wt. % CaO, and 6 wt. % P_2O_5 also known as Bioglass®45S5 was acquired from US Biomaterials with a particle size of <90µm, and the synthetic hydroxyapatite with a chemical composition of $Ca_{10}(PO_4)_6OH_2$ was acquired from Alfa Aesar with a particle size of <44µm. Five different mixtures were prepared with 1, 2.5, 5, 10, and 25 wt. % Bioglass®45S5 addition to synthetic hydroxyapatite.

5.2.2 Sample Preparation

The Bioglass®45S5 powders were mixed with proper amounts of hydroxyapatite in 250ml polyethylene bottles, and ball milled for 30 hours with acetone. After ball milling, the mixtures were dried in the oven at 80ºC for 24 hours. The dried powder mixtures were sieved until the particles were separated from each other. The powders were pressed uniaxially in a die with a diameter of 12.7mm to a pressure 105MPa, and sintered at 1200ºC for 4 hours with a heating rate of 4ºC/minute. The sintering was followed by cooling at 10ºC/minute down to room temperature. The sintered products were ground for XANES analysis.

87

5.2.3 XANES Analyses

In this study, P and Si $L_{2,3}$- and K-edge and Ca K-edge were used to characterize the chemical structure of both the crystalline and amorphous phases. The P and Si $L_{2,3}$-edge spectra were obtained at the 2.9 GeV storage ring at the Canadian Light Source, Saskatoon, Canada using the Variable Line Spacing Plane Grating Monochromator (11ID-2 VLS-PGM) beam line. The step size used in acquiring Si $L_{2,3}$-edge was 0.1 eV with a dwell time of 1 second per point in the energy range of 100 – 120 eV for all samples. The P $L_{2,3}$-edge was acquired in three regions *(1)* 130-135eV, step size: 0.25eV, *(2)* 135-150eV, step size: 0.1, *(3)* 150-155eV, step size: 0.25eV with a constant dwell time of 1 second/point. The P and Si K-edge spectra and Ca K-edge spectra were obtained at the Synchotron Radiation Center in Madison, Wisconsin using the Double Crystal Monochromator Beamline (800 MeV for the Si and P spectra and 1 GeV for the Ca K-edge spectra). The data acquisition for the Si-K edge was acquired using three regions: *(1)* 1830-1835eV, step size: 1eV, *(2)* 1835-1880eV, step size: 0.25eV, *(3)* 1881-1900eV, step size: 1eV with a constant dwell time of 1 second/point. The spectra for the P K-edge were acquired using two regions: *(1)* 2130-2180eV, step size: 0.25eV and *(2)* 2180-2190eV, step size: 1eV with a constant dwell time of 1 second/point. The spectra for the Ca K-edge was acquired using the region 4010 to 4100eV with a 0.5eV step size for bioceramic compositions and 0.5-0.7eV for model compounds with a constant dwell time of 1 second/point.

The backgrounds for all spectra were subtracted and plotted using arbitrary units. The peak intensities were measured by calculating the difference between the peak and the background.

5.3 Results and Discussion

Figure 5.1 illustrates the crystalline phases formed and identified by powder X-ray diffraction as discussed in chapter 4. The crystalline phases present are largely phosphates of calcium suggesting that the Si and Na that are present in the Bioglass®45S5 are present in the form of amorphous glass. These amorphous phases can play an important role in improving

bioactivity of the sintered bioceramic products. XANES spectroscopy is a very useful tool to identify these amorphous phases and characterize the chemical and electronic (bonding) properties of these compositions. In order to identify the crystalline and amorphous phases formed by reacting Bioglass®45S5 and hydroxyapatite, a series of calcium, silicate, and phosphate model compounds were also examined.
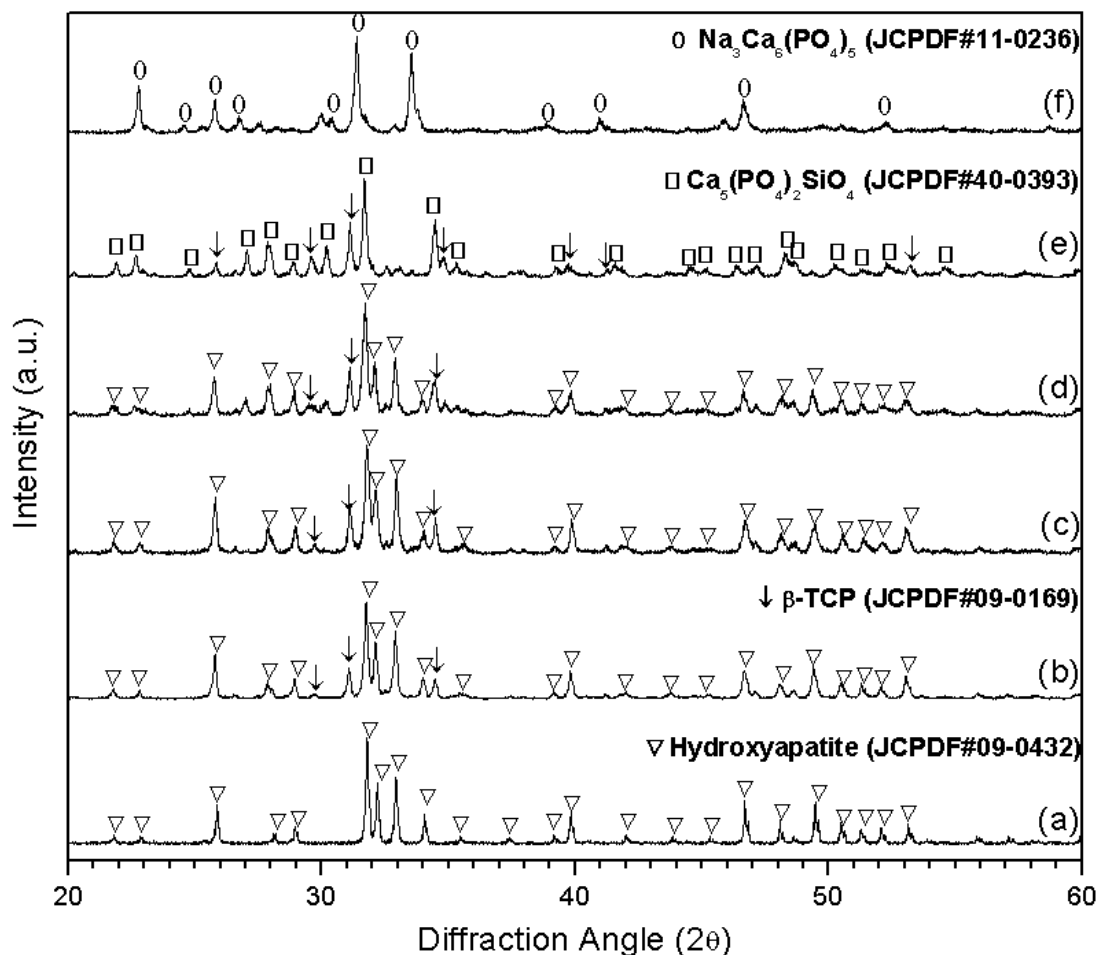
Figure 5.1: XRD spectra for (a) pure hydroxyapatite, (b) 1 wt. %, (c) 2.5 wt. %, (d) 5 wt. %, (e) 10 wt. %, and (f) 25 wt. % Bioglass®45S5 added hydroxyapatite sintered at 1200°C for 4 hours.

XANES spectroscopy was carried out on the model compounds and 5 different HA – Bioglass®45S5 compositions. In both cases, XANES spectra were recorded in fluorescence yield (FLY). The acquired XANES spectra from hydroxyapatite – Bioglass®45S5 compositions are

89

compared with the model compounds in order to understand the chemical nature and the structural environment of silicon (Si), phosphorus (P), and calcium (Ca) atoms. Si and P K- and $L_{2,3}$-edge and Ca K-edge spectra of hydroxyapatite – Bioglass®45S5 compositions were acquired. In addition, SiO_2, Na_4SiO_4, Na_2SiO_3, $CaSiO_3$, sintered Bioglass®45S5 ($Na_2CaSi_3O_8$ is the crystalline phase when Bioglass®45S5 is sintered at 1200ºC for 4 hours) are used as representative model compounds for silicon $L_{2,3}$- and K-edge spectra. $NaHPO_4$, NaH_2PO_4, $CaHPO_4$, $CaHPO_4-H_2O$, $Ca_2P_2O_7$, β-$Ca_3(PO_4)_2$, α-$Ca_3(PO_4)_2$, sintered Bioglass®45S5, and hydroxyapatite are used as the model compounds for P $L_{2,3}$-edge, and $CaHPO_4$, $CaHPO_4-H_2O$, $Ca_2P_2O_7$, β-$Ca_3(PO_4)_2$, α-$Ca_3(PO_4)_2$, and hydroxyapatite for P K-edge spectra. At last, $CaOH_2$, CaO, $CaCO_3$, $Ca_2P_2O_7$, β-$Ca_3(PO_4)_2$, $CaHPO_4$, $CaHPO_4-H_2O$, Bioglass®45S5, and hydroxyapatite are used as representative model compounds for Ca K-edge spectra. All the model compounds chosen are representing the possible silicates, phosphates, and calcium compounds formed in hydroxyapatite – Bioglass®45S5 compositions.

All the model compounds and bioceramic compositions were ground into powder and a thin layer of powder deposited on carbon tape and placed in the vacuum chamber of the beamline. And all K- and $L_{2,3}$-edge XANES spectra of model compounds and bioceramic compositions in this chapter were obtained by measurement of the fluorescence yield (FLY) as a function of incident photon energy.

5.3.1 Silicon $L_{2,3}$-edge XANES

Figures 5.2 and 5.3 are the silicon (Si) $L_{2,3}$-edge spectra for various possible silicate model compounds and 5 different hydroxyapatite – Bioglass®45S5 bioceramic compositions after sintering at 1200ºC for 4 hours, respectively. In Figure 5.2 the basic spectral features for sodium orthosilicate (Na_4SiO_4), sodium metasilicate (Na_2SiO_3), and sintered Bioglass®45S5 ($Na_2CaSi_3O_8$) are similar but differ from those of $CaSiO_3$ and SiO_2. On the other hand Bioglass®45S5 has a spectrum that is similar to the sodium orthosilicate and sodium metasilicate with an additional weak pre-edge peak **d** at around 104.2eV which also appears in $CaSiO_3$ at

around 104.5eV. The strong peak **c** is the main Si $L_{2,3}$-edge peak and peak **a** and **b** are the pre-edge peaks. Peak **c** can be attributed to the transition of Si 2p electrons to 3s- or 3d-like orbitals [115]. Previously it has been mentioned that the Si $L_{2,3}$-edge spectra can be used as a structural fingerprint to distinguish [4]Si and [6]Si in silicate glasses [115, 152]. The strong peak for all silicate model compounds and hydroxyapatite – Bioglass®45S5 compositions, peak **c**, at 107.9±0.2eV, also characterizes the [4]Si atoms in the Si $L_{2,3}$-edge XANES which is evident in both Figure 5.2 and 5.3 indicating that Si is fourfold coordinated in all model compounds as well as in the hydroxyapatite – Bioglass®45S5 bioceramic compositions [87]. In the case of [6]Si, another predominant peak appears around 106.7±0.2eV which is absent in the Si $L_{2,3}$-edge spectra of either model compounds or hydroxyapatite – Bioglass®45S5 compositions. The two pre-edge peaks right above 105eV (105.5±0.1eV and 106.1±0.1eV) are the characteristic of native SiO_2 are a result of the formation of tetrahedron bonds of silicon atoms with oxygen [153]. The four pre-edge features below 105eV between 100 and 104eV can only be seen in amorphous and single crystalline silicon Si $L_{2,3}$-edge. The Si $L_{2,3}$-edge of SiO_2 model compound reveals both characteristic of silicon elementary (between 100 and 104eV) and SiO_2 at 105.5±0.1eV and 106.1±0.1eV indicating that the model sample used to obtain Si $L_{2,3}$-edge has a thin layer of oxide on its surface. All other silicate compositions show only the pre-edge peaks after 105eV except calcium silicates which also have an additional peak at 104.5eV.
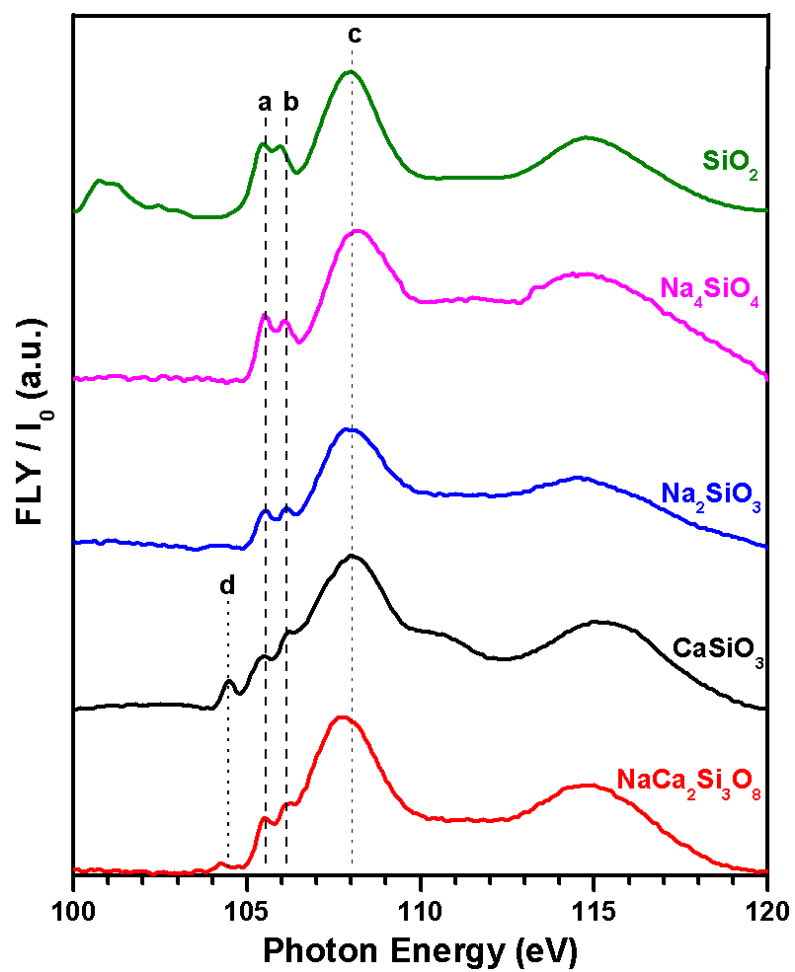
Figure 5.2: Silicon L$_{2,3}$-edge XANES spectra for various possible silicate model compounds.
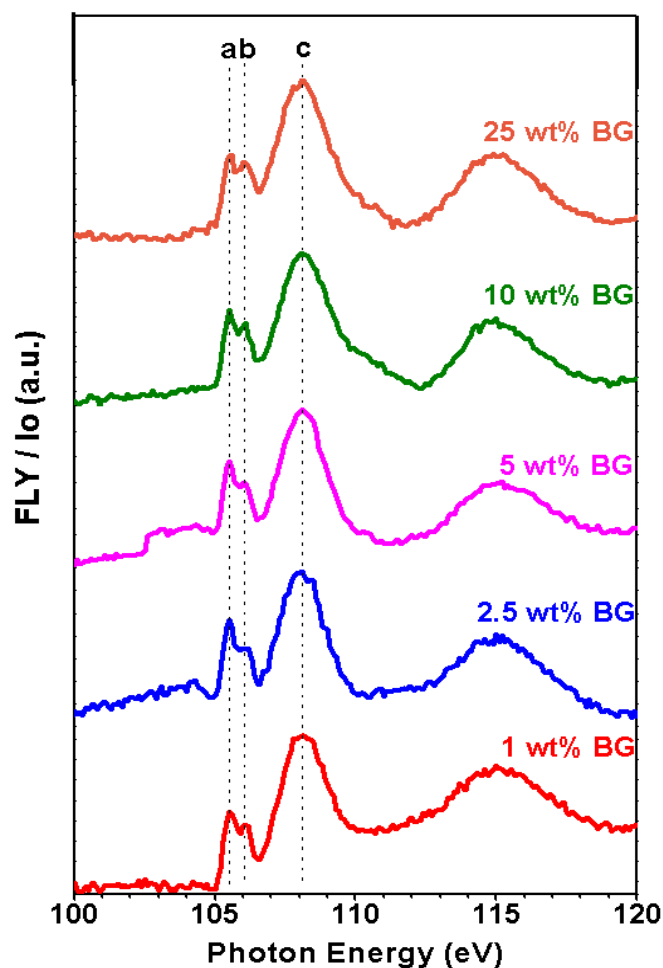
Figure 5.3: Silicon $L_{2,3}$-edge XANES spectra for 5 different hydroxyapatite – Bioglass®45S5 bioceramic compositions after sintering at 1200ºC for 4 hours.

An outcome from comparison of Si $L_{2,3}$-edge spectra of model compounds and hydroxyapatite – Bioglass®45S5 bioceramic compositions is that none of the bioceramic compositions contains calcium silicates. Both Bioglass®45S5 (that has a crystalline $Na_2CaSi_3O_8$ when sintered at 1200ºC for 4 hours) and $CaSiO_3$ have a pre-edge peak **d** at around 104.5eV near peaks **a** and **b**. Neither sodium silicates nor any bioceramic compositions have a peak at that energy which indicates that the peak at 104.5 eV is a distinguishing peak for calcium silicates. In addition, there is a broad post-edge shoulder peak at around 111eV that is only visible in $CaSiO_3$. On the other hand, all bioceramic compositions show pre-edge peaks **a** and **b**

93

at around 105.5±01eV and 106.1±01eV, respectively. The peaks **a** and **b** can be attributed to transitions from 2p electrons to unoccupied 3d orbitals which were split (~0.6 eV) by the 2p spin-orbit splitting [115, 152]. The third pre-edge peak **d** only seen in calcium silicates, is probably a so called dipole forbidden pre-edge peak (Si 2p to Ca 3d empty orbitals). The 3d orbital in sodium is so far away that it is rational that there is no pre-edge peak for sodium in the glass.

Since all the **a** and **b** peak positions are similar in Si $L_{2,3}$-edge XANES spectra of bioceramic compositions, one way to differentiate them is to calculate the ratio of intensity of peak **a** to peak **b**. However, as an atomic property, 2p spin orbit splitting causes $2p_{3/2}$ and $2p_{1/2}$ splitting where $2p_{3/2}$ has 4 and $2p_{1/2}$ has 2 electrons making the ratio 2:1. In another words the peaks **a** and **b** are the spin-orbit pair indicating their energy separation and relative intensity should be constant, 2:1, unless the samples are a mixture. Therefore, the integrated areas for the peaks **a** and **b** in bioceramic compositions as well as all model compounds are derived and the ratios are calculated and tabulated in Table 5.1. It is evident that from the integrated areas of the peaks the primary silicates that are present are sodium silicates in the amorphous phase and the data does not match with calcium silicates.

Table 5.1: Integrated peak area ratios for peak **a** to peak **b** in Si $L_{2,3}$-edge of HA – Bioglass®45S5 bioceramic compositions and silicate model compounds.

Si $L_{2,3}$-edge Bioceramics		Si $L_{2,3}$-edge Model Compounds	
Composition	Ratio (**a/b**)	Composition	Ratio (**a/b**)
1wt.% Bioglass®45S5	1.54	SiO_2	1.023
2.5wt.% Bioglass®45S5	1.76	Na_4SiO_4	1.51
5wt.% Bioglass®45S5	1.55	Na_2SiO_3	1.55
10wt.% Bioglass®45S5	1.42	$CaSiO_3$	1.20
25wt.% Bioglass®45S5	1.42	$BG(Na_2CaSi_3O_8)$	1.88

5.3.2 Silicon K-edge XANES

Figure 5.4 and 5.5 show silicon K-edge spectra for various possible silicate model compounds and 5 different hydroxyapatite – Bioglass®45S5 bioceramic compositions after sintering at 1200ºC for 4 hours, respectively. The features (peaks) in both model compounds and bioceramic composition spectra are labeled as **a**, **b**, and **c**. Both Si K-edge XANES spectra of both model compounds and bioceramic compositions have very similar white line peak positions indicating that Si is in a similar structural environment throughout the bioceramic compositions [120]. One apparent difference in bioceramic compositions is the Si K-edge white line peak increases with respect to P K-edge white line peak as the amount of Bioglass®45S5 increases as calculated and shown in Table 5.2.
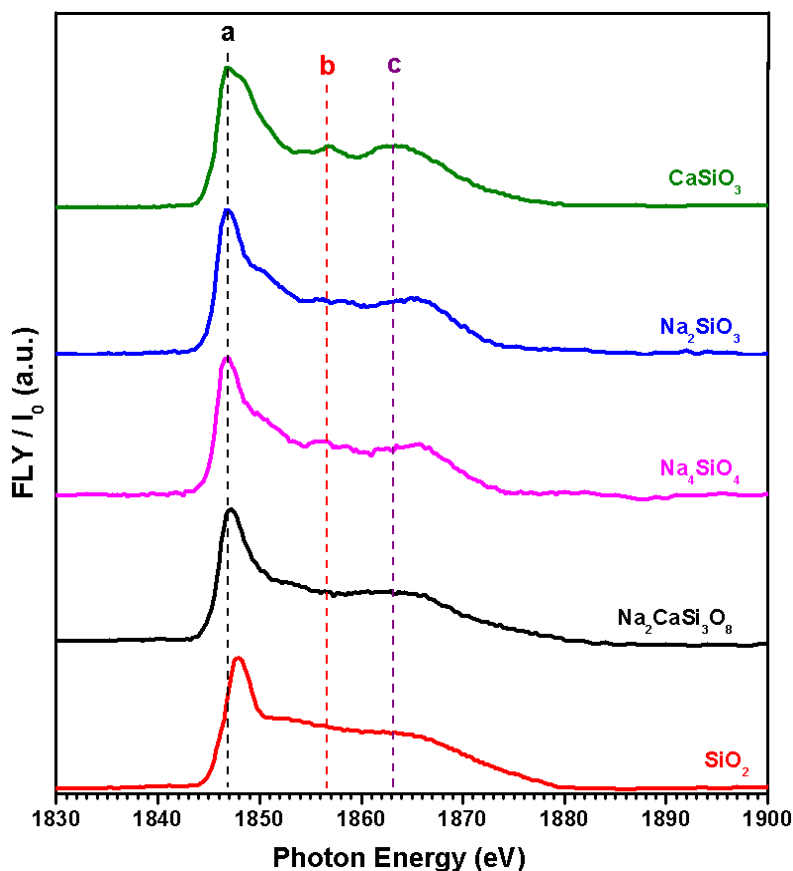
Figure 5.4: Silicon K-edge XANES spectra for various possible silicate model compounds.
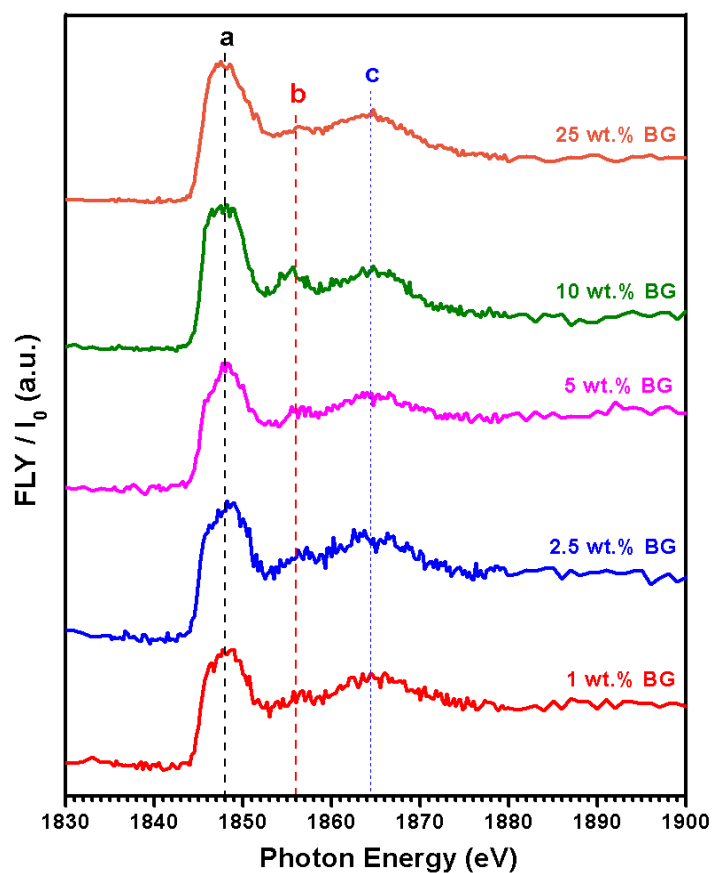
Figure 5.5: Silicon K-edge XANES spectra for 5 different hydroxyapatite – Bioglass®45S5 bioceramic compositions after sintering at 1200ºC for 4 hours.

Table 5.2: Integrated peak ratios of phosphorus K-edge to silicon K-edge in HA – Bioglass®45S5 bioceramic compositions

Integrated Peak Area Ratio of main P K-edge to main Si K-edge	
Composition	P K-edge / Si K-edge
1 wt.% Bioglass®45S5	157.22
2.5 wt. % Bioglass®45S5	133.56
5 wt. % Bioglass®45S5	120.00
10 wt. % Bioglass®45S5	30.30
25 wt. % Bioglass®45S5	19.60

It has also been shown that Si K-edge XANES that it is a very useful technique to distinguish between 4- and 6-coordinated Si in crystalline and amorphous materials [116, 152]. In general, the strongest peak at about 1846.8eV is defined as the Si K-edge which characterizes the [4]Si, and the strongest peak at about 1848.9eV characterizes the [6]Si with O in the Si K-edge XANES [118, 152]. The peak **a** in Figure 5.4 and 5.5 is assigned to the transition of Si 1s electrons to the unoccupied 3p- or 3s-like state (majority 3p-like) [115, 152]. This transition is allowed by selection rules; therefore, peak **a** is the strongest and called Si K-edge. It is apparent that there is not any peak at about 1848.9eV in either Figure 5.4 or 5.5. On the other hand, the sharper absorption peak that is labeled as **a** is located at 1847.25±0.25eV in model compounds except SiO_2 which is shifted to a higher energy by 1.5eV, and 1847.5±0.25eV in bioceramic compositions which are closer to the peak that characterizes [4]Si. Therefore, we can conclude that all the bioceramic compositions have four-coordinated Si in their structure. These findings are also good agreement with the Si $L_{2,3}$-edge XANES spectra discussed in the previous section 5.3.1. However, the white line peaks in all the bioceramic compositions are much broader than the model compounds indicating that the origin of these peaks is from an amorphous matrix with different coordination of Si and possible differences in glassy structure.

In addition there are two weak peaks observed in the post-edge area at around 1856.5eV and 1864eV in Si K-edge of bioceramic compositions (Figure 5.5) marked as peak **b** and **c**, respectively. The peaks **b** and **c** in Figures 5.4 and 5.5 are attributed to the transition of Si 1s electrons to the 3d-like states [116]. In the Si K-edge spectra of sodium silicate model compounds peak **b** is separated into two absorption peaks at about 1856eV and 1859eV. The split of peak **b** is distinctively visible upon enlargement of the absorption area. Even though this separation is an expected outcome for most glasses [120], it is only visible in sodium silicate model compounds and not in the calcium silicates.

In a XANES study of amorphous silica and alkali silicate glasses it has been shown that all spectra have similar peaks and positions. However, the addition of Na_2O to SiO_2 causes a shift

of the peaks to lower energies [120]. The Si K-edge spectra of hydroxyapatite – Bioglass®45S5 bioceramic compositions are also similar to SiO_2 glasses [154] except for less defined due to the disorder of glasses [120]. Therefore, addition of Na and Ca to silica causes a shift in the Si K-edge peaks of model compounds. On the other hand, this shift is hard to distinguish in hydroxyapatite – Bioglass®45S5 bioceramic compositions due to the peak broadening caused by disorder of glass structure.

5.3.3 Phosphorus $L_{2,3}$-edge XANES

Figures 5.6 (a, b, and c) and 5.7 show the phosphorus $L_{2,3}$-edge spectra for various possible phosphate model compounds and 5 different hydroxyapatite – Bioglass®45S5 bioceramic compositions after sintering at 1200ºC for 4 hours, respectively.

(a)

(b)

(c)
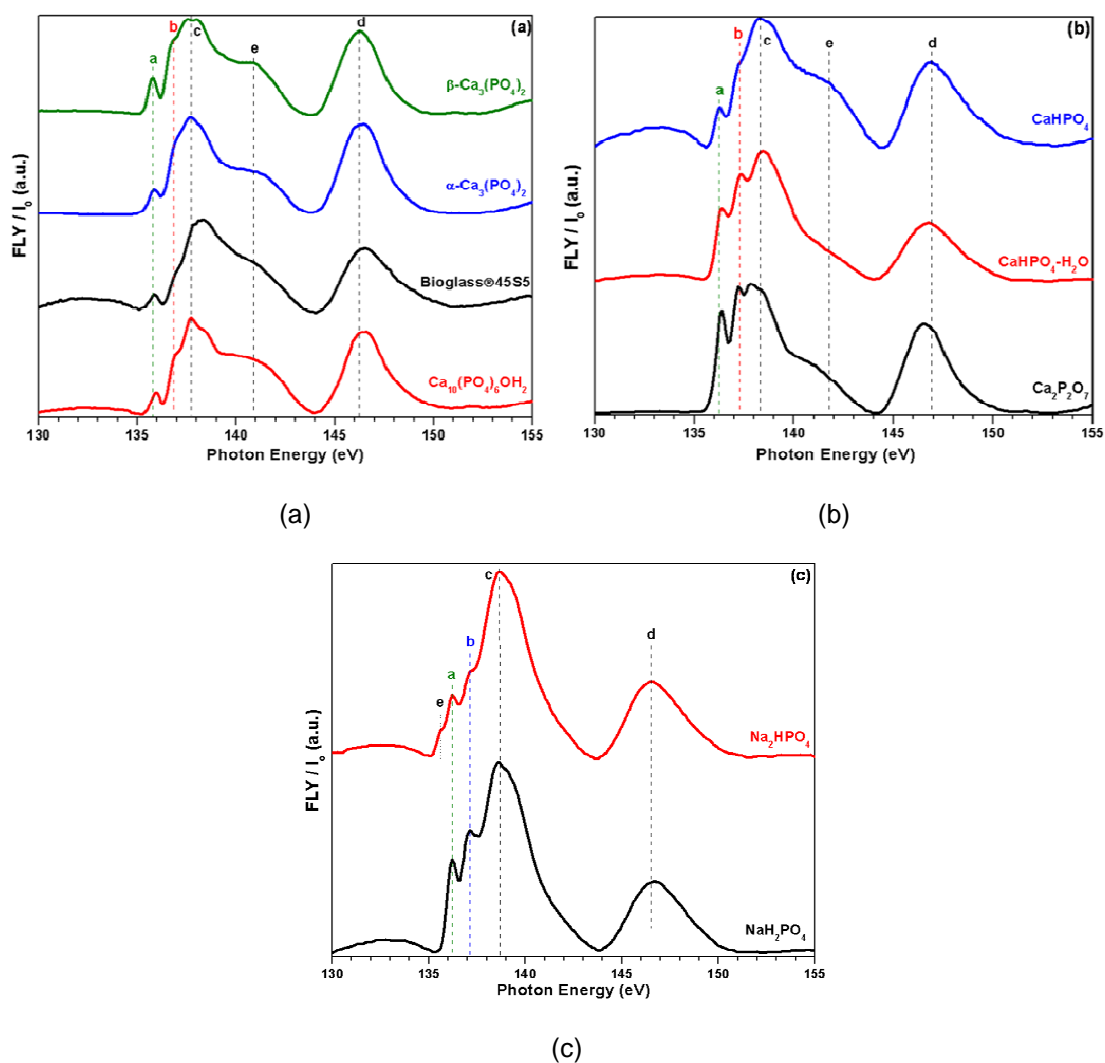
Figure 5.6: Phosphorus $L_{2,3}$-edge XANES spectra for (a) Hydroxyapatite, sintered Bioglass®45S5, α- and β-TCP, (b) $CaHPO_4$, $CaHPO_4$-H_2O, and $Ca_2P_2O_7$, and (c) Na_2HPO_4 and NaH_2PO_4 model compounds.
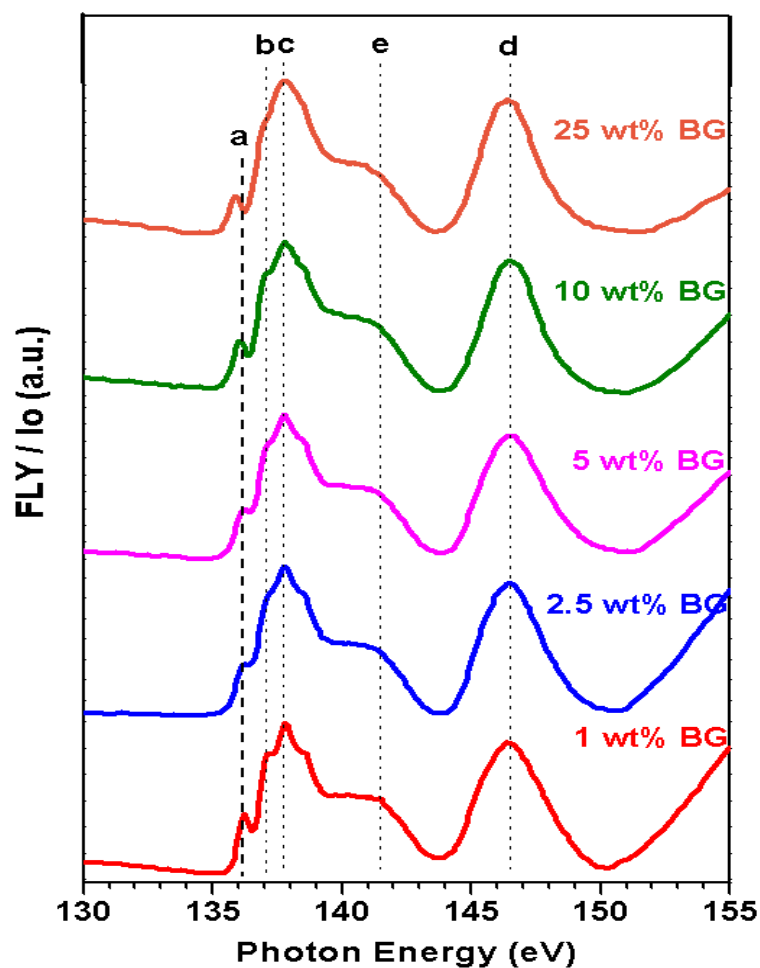
Figure 5.7: P L$_{2,3}$-edge XANES spectra for 5 different hydroxyapatite – Bioglass®45S5 bioceramic compositions after sintering at 1200ºC for 4 hours.

Hydroxyapatite, α-, and β-TCP P L$_{2,3}$-edge spectra demonstrate similar peaks and peak positions with main P L$_{2,3}$-edge peak **c** at 137.8eV, one pre-edge peak **a** at around 135.8eV, and a pre-edge **b** at around 137.9eV and post-edge at **b'** at 138.3eV, respectively in figure 5.6(a). In addition there is a shoulder **e** at 141eV and a secondary peak at **d** at 146.2eV. The peaks **a** and **b** at the low energy side are generally separated by approximately by 1eV and arise from spin orbit split 2p electron into the 2p$_{3/2}$ and 2p$_{1/2}$ levels, i.e. L$_3$ and L$_2$ edges. This spin-orbit splitting is an atomic property and is insensitive to the chemical environment. The main peak **c** has been attributed to transitions to 3p orbitals which are made possible due to the presence of other

100

elements such as oxygen and other cationic species such as Si and Ca. The peak **e** at higher energies that appears as a shoulder is characteristic of Ca-phosphates and possibly arises from transitions from P 2p to empty Ca 3d orbitals {{535 Kruse, Jens 2009}}. Peak **d** that appears in all the phosphates is due to transitions from the 2p to 3d orbital in phosphorous.

Comparison of peak position **c** in the different sintered chemistries shows certain distinctive differences. The peak **c** in hydroxyapatite is very distinctive at 137.8eV with a pre-edge shoulder at 136.9eV and post edge shoulder at 138.4eV, in comparison the dominant peak in Bioglass®45S5 is shifted 0.5eV to the right at **c'** at 138.4eV, there is a small pre-edge shoulder at 137.8eV but no post edge shoulder. On the other hand the α-TCP and β-TCP have distinctive differences as well; the main peak **c** in the β-TCP is actually a doublet while the main peak **c** in α-TCP is a singlet.

Comparison of Figure 5.6(b) for compounds $CaHPO_4$, $CaHPO_4.H_2O$ and $Ca_2P_2O_7$ with the other Ca-phosphates in Figure 5.6(a) yields some distinctive differences. The $CaHPO_4$ in Figure 5.6(b) is very similar to hydroxyapatite but its hydrated version $CaHPO_4.H_2O$ exhibits much larger intensities of peaks **a** and **b** relative to the un-hydrated version. The shoulder at location **e** is almost absent in the hydrated version in comparison to the un-hydrated $CaHPO_4$. On the other hand $Ca_2P_2O_7$ is distinctively different with peak **b** having the same intensity as peak **c**.

The phosphorus $L_{2,3}$-edge spectra for sodium phosphate model compounds demonstrate the strongest peak (the P $L_{2,3}$-edge peak) at 138.8eV (peak c) and 2 pre-edge peaks at around 136.2eV (peak a) and 137.1eV(peak b) in addition to a very weak pre-edge shoulder at 135.5eV (peak **a'**) in only Na_2HPO_4 shown in Figure 5.6(b). The pre-edge peaks **a** and **b** are called the a-b spin orbit doublet which is assigned to the transition of $2p_{3/2,1/2}$ electrons to molecular orbit $a_{1,}$ and the change in the intensity of the doublet is likely due to the distortion of the phosphate tetrahedral [155]. Comparison of Figure 5.6(c) with 5(a) and (b) show some distinctive differences arise between the Ca-phosphates and Na-phosphates. To begin with the broad shoulder located at 141.9 eV in the Ca-phosphates that is associated with the transition of the 2p electrons in

phosphorous to the empty 3d orbitals in Ca is completely absent in the Na-phosphates indicating the transition is not possible in Na as the 3d orbitals in Na are very far out. Secondly, the peaks **a** and **b** that correspond to transitions from spin orbit split 2p electrons are located at the same energy levels in both Ca and Na phosphates, however, the relative intensities of the peaks in the Na phosphates are much higher.

Figure 5.7 is the P $L_{2,3}$-edge spectra of all the sintered hydroxyapatite – Bioglass®45S5 compositions. All the compositions exhibit sharp shoulder at location **e** indicating that the compositions are all dominated by Ca-phosphates. A careful examination of the spectra indicates that they all follow the general pattern of the hydroxyapatite spectra; however, the intensity of the pre-edge peaks **a** and **b** relative to the peak **c** decreases with increasing Bioglass®45S5 content and moves to slightly lower energies as well. This indicates that as the hydroxyapatite and β-TCP content decrease with increasing Bioglass®45S5 content new chemistries form that includes amorphous silicates resulting in a decrease in intensity of peak **a.** This observation is in good agreement with the XRD spectra of hydroxyapatite – Bioglass®45S5 bioceramic compositions in Figure 5.1 that shows formation of crystalline $Na_3Ca_6(PO_4)_5$ and $Ca_5(PO_4)_2SiO_4$ phases in an amorphous silicate matrix when the amount of Bioglass®45S5 is increased to 10 and 25 wt.%, respectively. Additionally, the spectra for $CaHPO_4$-H_2O and $Ca_2P_2O_7$ in Figure 5.6(b) are distinctively different in comparison to the sintered bioceramic compositions indicating they are not present in bioceramic compositions.

Although, it is difficult to conclude the exact structures of the phosphate phases as they are made up of a mixture of different phosphates, it is clearly seen that there is no evidence of sodium phosphate present in the sintered bioceramic compositions. In order to establish the exact nature of the Ca-phosphate, the ratio of peak **c** to peak **a** is calculated to find the compound that is closer to the bioceramic compositions. Table 5.3 gives the ratio of intensity of peak **c** to peak **a** in Figures 5.6(a, b, and c) and 5.7 for the P $L_{2,3}$-edge. From this table it is clear that for compositions with up to 5 wt. % Bioglass®45S5 the primary phosphate is either HA or β-TCP.

102

This outcome is also verified by the powder X-ray diffraction of these bioceramics which indicates that as the extent of Bioglass®45S5 is increased it results in increased decomposition of hydroxyapatite yield forming β-TCP. On the other hand as the Bioglass®45S5 content reaches 10 wt. % and increases to 25 wt. %, new silicate chemistries are created resulting in a larger **c/a** ratio that does not match that of either hydroxyapatite or β-TCP.

Table 5.3: Integrated peak area ratios for peak c and a in P $L_{2,3}$-edge of HA – Bioglass®45S5 bioceramic compositions and phosphate model compounds

P $L_{2,3}$-edge Bioceramics		P $L_{2,3}$-edge Model Compounds	
Composition	Ratio (c/a)	Composition	Ratio **(c/a)**
1wt.% Bioglass®45S5	2.925	$Ca_{10}(PO_4)_5OH_2$	2.779
2.5wt.% Bioglass®45S5	2.901	Bioglass®45S5	5.563
5wt.% Bioglass®45S5	2.579	$Ca_2P_2O_7$	1.559
10wt.% Bioglass®45S5	3.896	$CaHPO_4$	3.736
25wt.% Bioglass®45S5	4.814	$CaHPO_4\text{-}H_2O$	2.175
		Na_2HPO_4	3.646
		NaH_2PO_4	2.416
		$\alpha\text{-}Ca_3(PO_4)_2$	4.329
		$\beta\text{-}Ca_3(PO_4)_2$	2.631

5.3.4 Phosphorus K-edge XANES

Figure 5.8 (a and b) and 5.9 illustrate the P K-edge spectra for various possible calcium and sodium phosphate compounds and 5 different HA – Bioglass®45S5 bioceramic compositions after sintering at 1200ºC for 4 hours, respectively.
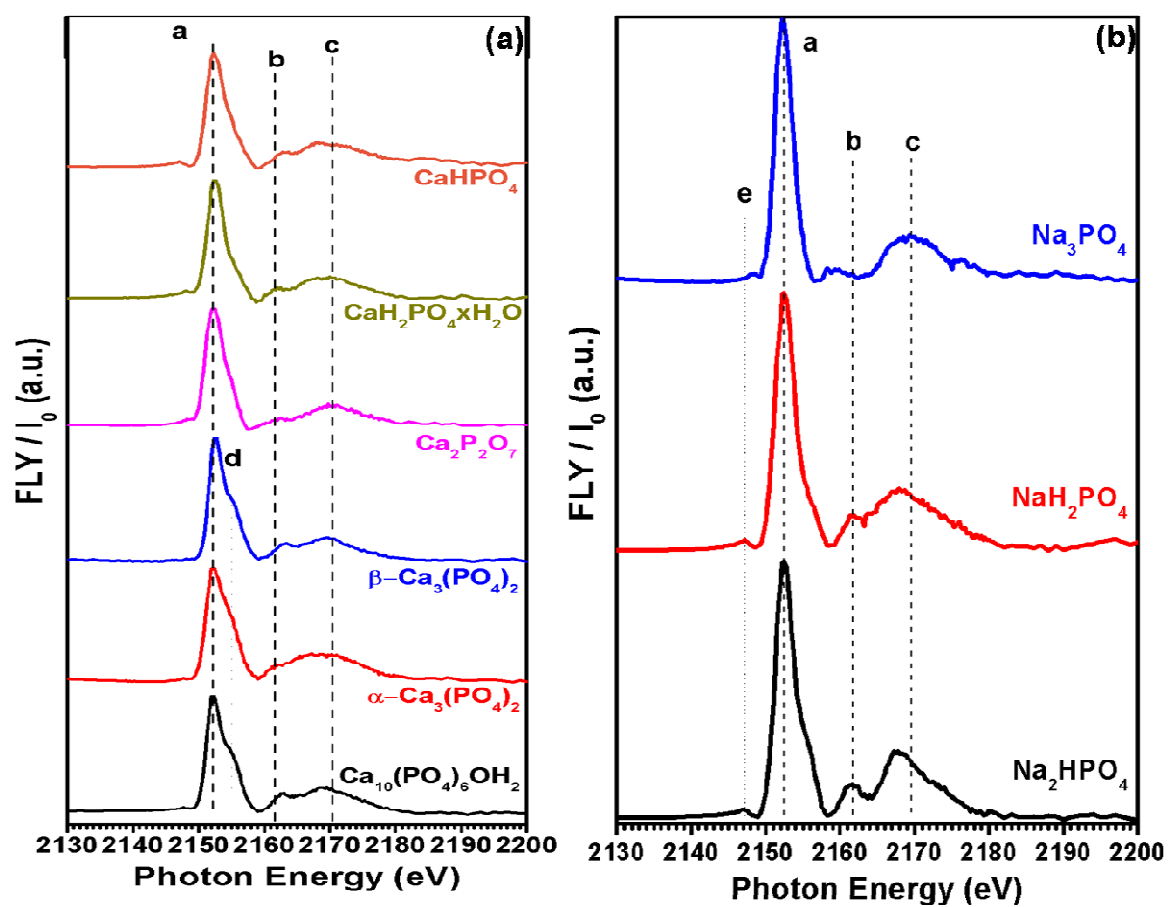
Figure 5.8: P K-edge XANES spectra for (a) various calcium-phosphate and (b) sodium-phosphate model compounds.
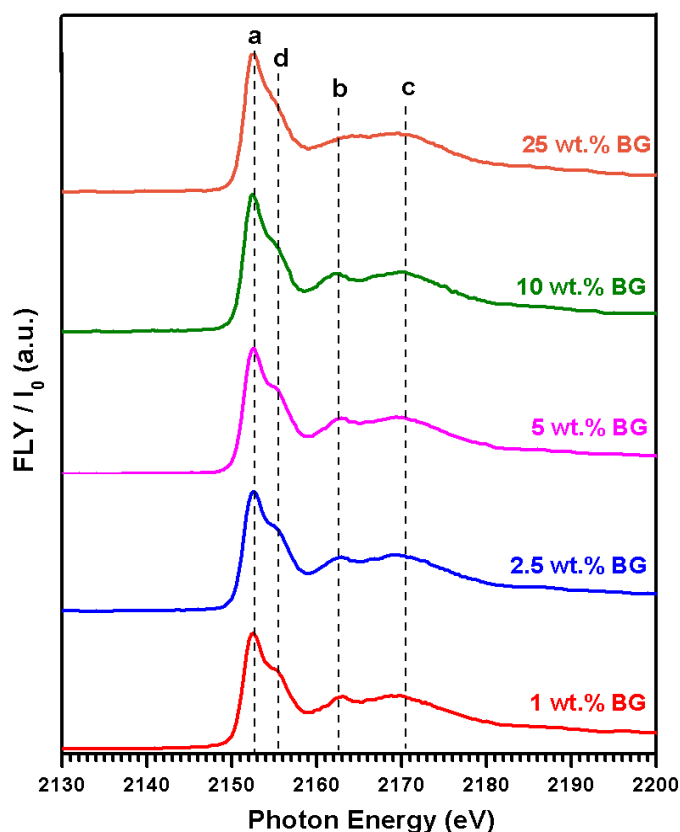
Figure 5.9: P K-edge XANES spectra for 5 different hydroxyapatite – Bioglass®45S5 bioceramic compositions after sintering at 1200ºC for 4 hours.

All calcium phosphate model compounds in Figure 5.8 (a) have two post edge peaks at around 2163eV (peak **b**) and 2169eV (peak **c**) in addition to the main P K-edge peak **a** at around 2152eV. In addition to these 3 peaks β-TCP (β-$Ca_3(PO_4)_2$) and HA ($Ca_{10}(PO_4)_6OH_2$) have a post-edge shoulder peak at around 2155eV, this shoulder corresponds to a transition of 1s P to the 3d calcium orbital. All bioceramic compositions in Figure 5.9 also show these four peaks indicating that the P structure environment in hydroxyapatite – Bioglass®45S5 bioceramic compositions are similar to hydroxyapatite and β-TCP. However, the post-edge shoulder peaks get less noticeable as the Bioglass®45S5 content increases from 1 wt. % to 25 wt. % indicating that fewer of these transitions are occurring. A closer observation of the post-edge shoulder peak at around 2155eV discloses this shoulder to be more defined for calcium phosphate compounds with decreasing solubility and increasing thermodynamic stability [156]. This shoulder peak is more noticeable in

105

hydroxyapatite and β-TCP, and none of the rest calcium phosphate model compounds show a distinctive post-edge peak. P K-edge spectra of various calcium phosphate compounds [157] show that only DCPA (dicalcium phosphate anhydrous) does not have a noticeable post-edge shoulder. The reason behind was suggested that while the stability of calcium phosphate phase increases, the spectral features such as post-edge shoulder peak may appear more distinctive. In Figure 5.9 the only spectra that does not show a noticeable post edge shoulder peak is 25 wt. % Bioglass®45S5 added hydroxyapatite bioceramic composition indicating that it is more soluble compared to the other compositions. Also, Table 5.4 gives the ratio of intensity of peak **a** to peak **d** in Figure 5.9 for the P K-edge confirming that peak **a** to peak **d** ratio is smaller in 25 wt. % Bioglass®45S5 addition than up to 10 wt. % Bioglass®45S5 addition. This finding also explains increased bioactivity of this bioceramic composition. It is well excepted that even though synthetic hydroxyapatite is similar to natural bone mineral, hydroxyl carbonated apatite formation is relatively slow which is attributable to its slow degradation rate that leads to low bioactivity compared to the biological form of apatite [14-17]. Therefore, it can be concluded that the bioceramic composition with higher solubility rate may induce faster hydroxyl carbonated apatite formation leading to higher bioactivity.

Table 5.4: Integrated peak area ratios for peak a to d in P K-edge of HA – Bioglass®45S5 bioceramic compositions

Phosphorus K-edge of HA – Bioglass®45S5 Bioceramic Compositions	
Composition	Ratio (a/d)
1 wt. % Bioglass®45S5	1.05
2.5 wt. % Bioglass®45S5	1.08
5 wt. % Bioglass®45S5	1.04
10 wt. % Bioglass®45S5	1.06
25 wt. % Bioglass®45S5	0.70

All sodium phosphate phosphorus K-edge spectra shown in Figure 5.8(b) consist of one sharp main P K-edge peak **a** due to the transition of 1s electrons to p-like anti-bonding orbital in addition to two weaker post edge peaks (peak **b** and **c**) that most likely corresponding to shape resonance or multiple scattering [155] and one pre-edge peak. The phosphorus K-edge spectra of sodium phosphate model compounds have similar features at close photon energies as phosphorus K-edge of calcium phosphate model compounds. However, the sodium phosphate model compounds have a more visible pre-edge peak **e** (at 2147eV for Na_3PO_4 and 2148eV for NaH_2PO_4 and NaH_2PO_4) than calcium phosphate compounds (at 2147eV for $CaHPO_4$ and 2148eV for the rest of the calcium phosphate compounds). Another distinctive difference between calcium phosphates and the sodium phosphates is the absence of the shoulder at location **d**, which is a signature of the calcium phosphates. All of the sintered bioceramic compositions exhibit this distinctive shoulder indicating that the primary phosphate present is one of calcium not sodium.

5.3.5 Calcium K-edge XANES

Figure 5.10(a, b, and c) and 5.11 show Ca K-edge spectra for a variety of possible calcium oxide, calcium phosphate, calcium silicate model compounds, and 5 different HA – Bioglass®45S5 bioceramic compositions after sintering 1200ºC for 4 hours, respectively.
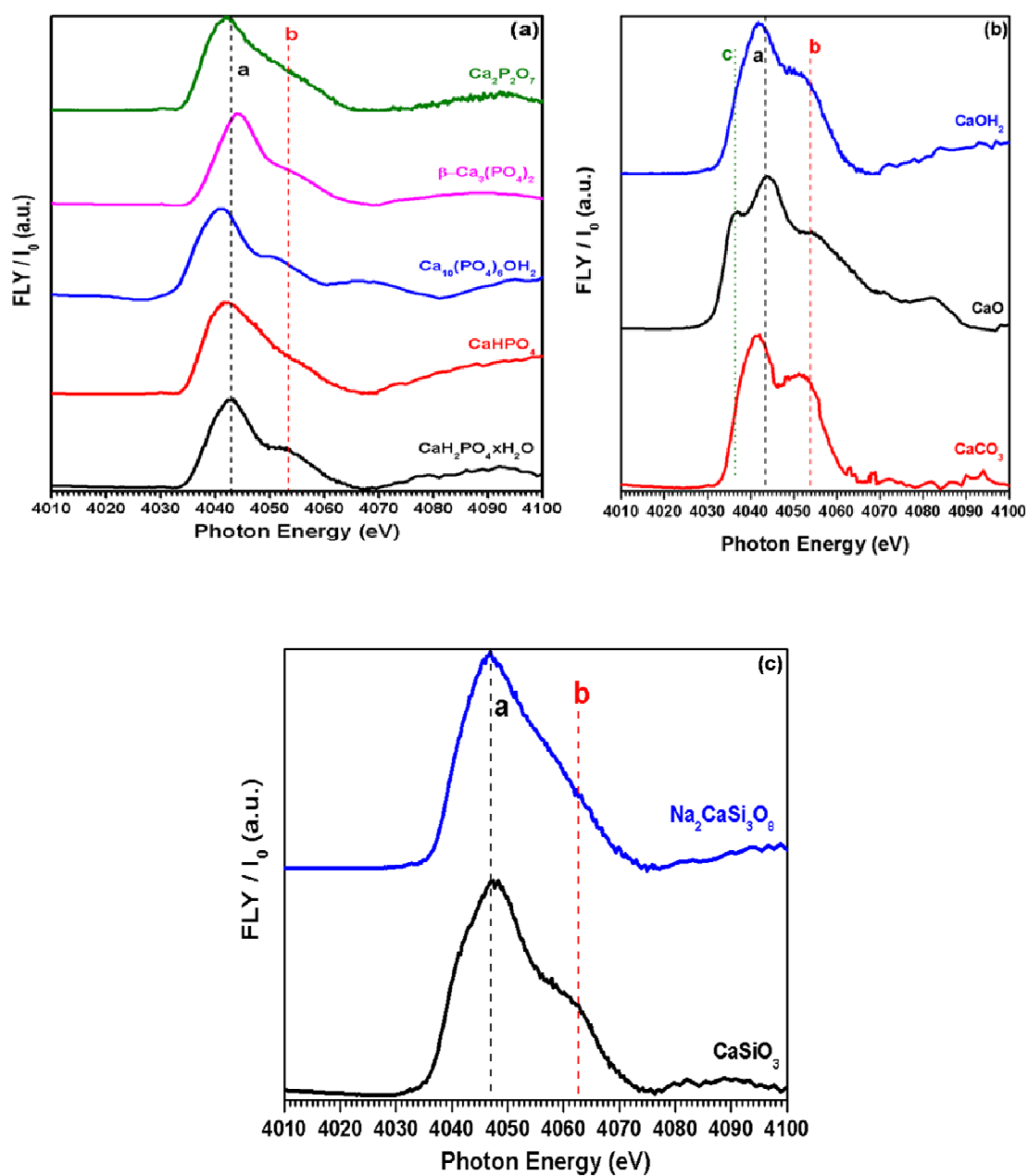
Figure 5.10: Ca K-edge XANES spectra for (a) calcium phosphate, (b) calcium oxide, and (c) calcium silicate model compounds.
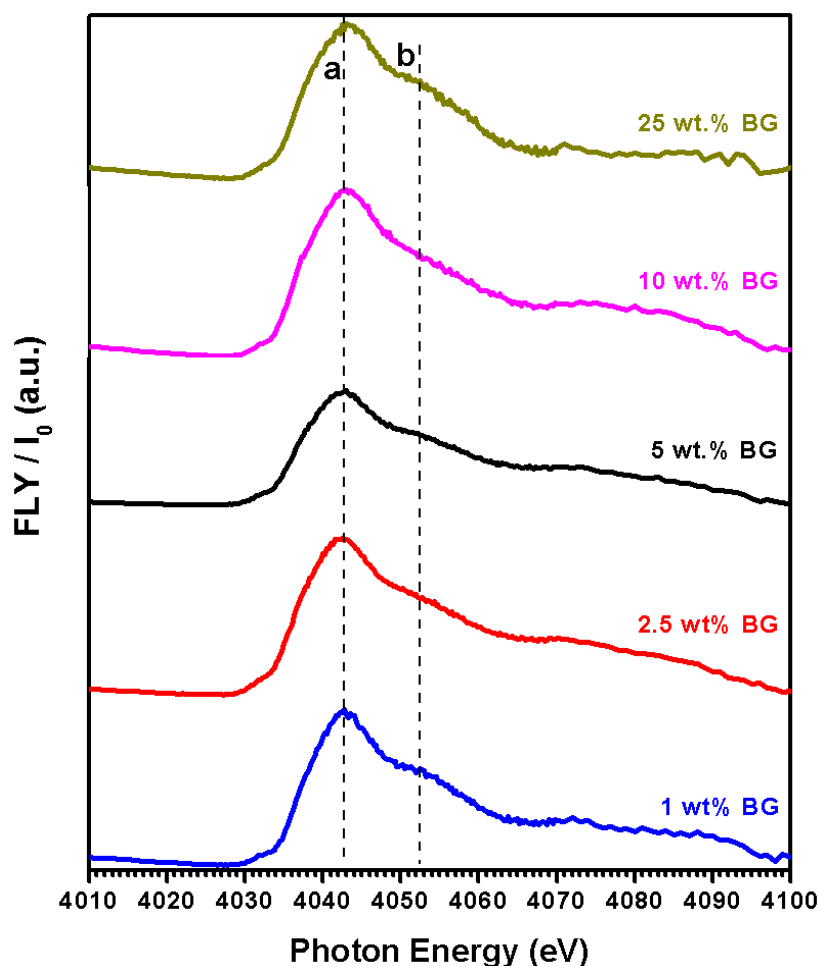
Figure 5.11: Ca K-edge XANES spectra for 5 different hydroxyapatite – Bioglass®45S5 bioceramic compositions after sintering at 1200ºC for 4 hours.

The main Ca K-edge peaks are labeled as **a** and **b** in all model compounds and bioceramic compositions except an additional peak **c** in calcium oxide (CaO) model compound. None of the bioceramic compositions display this pre-edge peak **c** indicating that CaO is not present in the bioceramic compositions. The post edge peak **b** is more distinctive in $CaOH_2$, CaO, $CaCO_3$, HA ($Ca_{10}(PO_4)_6OH_2$), $CaH_2PO_4xH_2O$, and $CaSiO_3$ and gets wider in all model compounds which is similar to the hydroxyapatite – Bioglass®45S5 bioceramic compositions. The post-edge shoulder peak **b** corresponds to transition to unoccupied states mainly from 5s states [158].

The white line Ca K-edge peak at 4038eV [159] is assigned to 1s to 4p transition [158]. This peak is shifted to about 4043eV for calcium silicates, 4044eV for CaO, 4051eV for $CaCO_3$

and CaOH, and about 4043eV for bioceramic compositions which may be due to different scan times. In addition to those 3 peaks most of the calcium compounds show one small pre-edge peak, one pre-edge shoulder and 4 small post-edge peaks [158] which are not present in any of the spectra in this research. This may be caused by the energy range that is used during the scan. The spectra in this research are taken at energy range between 1500 – 4000eV at 1 GeV which barely makes it possible to collect Ca K-edge spectra, because the flux decreases as it approaches to 4000eV and the energy and the current used is not high enough to catch all peaks due to the low resolution as seen in Figure 5.12. On the other hand, higher energy ranges makes it possible to identify even smaller XANES structures as found in reference [158].
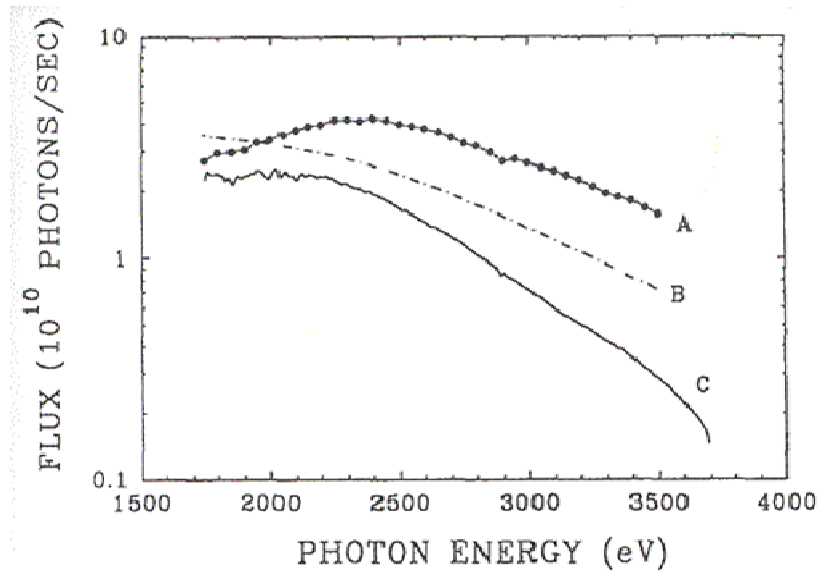
Figure 5.12: Beam line photon flux as a function of energy. (A) Measured value while Aladdin is at 1 GeV, 100mA. (B) Calculated (shadow) value for Aladdin at 800MeV, 100mA, (C) Measured value while Aladdin is at 800MeV, 100mA

5.4 Conclusion

Sintering different amounts (1, 2.5, 5, 10, and 25 wt. %) of Bioglass®45S5 with hydroxyapatite at 1200ºC for 4 hours yield forming new crystalline phases. The crystalline phases formed were identified by X-ray diffraction. In addition to the crystalline phases some amorphous

110

phases were also present in the sintered bioceramic compositions. In this chapter, silicon (Si) and phosphorus (P) K- and $L_{2,3}$-edge and calcium (Ca) K-edge of possible model compounds and bioceramic compositions were obtained to identify the crystalline and amorphous phases formed as a result of sintering. Si $L_{2,3}$-edge of bioceramic compositions showed that none of the compositions contains calcium silicates, and the primary silicates that are present in these compositions are sodium silicates in amorphous phase. It is also shown that Si in the sodium silicates are 4-fold coordinated. From Si K-edge it can be interpreted that the silicates are in a similar structural environment throughout the bioceramic compositions. In Si K-edge spectra the white line peaks in all the bioceramic compositions are much broader than the model compounds indicating that the origin of these peaks is from an amorphous matrix with different coordination of Si and possible differences in glassy structure. Although, it is difficult to conclude the exact structures of the phosphate phases in P $L_{2,3}$-edge as they are made up of a mixture of different phosphates, it is clearly shown that there is no evidence of sodium phosphate present in the sintered bioceramic compositions. Compositions with up to 5 wt.% Bioglass®45S5 the primary phosphate is either hydroxyapatite or β-TCP which is verified by the powder X-ray diffraction of these bioceramics indicating that as the Bioglass®45S5 addition increases decomposition of hydroxyapatite which yield β-TCP increases. On the other hand, as the Bioglass®45S5 content reaches 10 wt. % increased to 25 wt. %, new silicate chemistries are created. P K-edge the post-edge shoulder peak at around 2155eV discloses this shoulder to be more defined for calcium phosphate compounds with decreasing solubility and increasing thermodynamic stability. This shoulder peak is more noticeable in hydroxyapatite and β-TCP suggesting while the stability of calcium phosphate phase increases, the spectral features such as post-edge shoulder peak may appear more distinctive. The only spectra that does not show a noticeable peak is 25 wt. % Bioglass®45S5 added hydroxyapatite bioceramic composition indicating that it is more soluble compared to the other compositions. Another distinctive difference between calcium phosphates and the sodium phosphates is the absence of the shoulder at location **d**, which is a signature of

111

the calcium phosphates. All of the sintered bioceramic compositions exhibit this distinctive shoulder indicating that the primary phosphate present is one of calcium not sodium.

The Ca K-edge spectra of the model compounds and hydroxyapatite – Bioglass®45S5 bioceramic compositions show common features except an additional feature in CaO. The only conclusion that could be made from Ca K-edge spectra is that the calcium environment in hydroxyapatite – Bioglass®45S5 bioceramic compositions is much closer to $Ca_2P_2O_7$, β-TCP, and $CaHPO_4$ than the other model compounds.

Finally, the increased bioactivity of newly formed $Na_3Ca_6(PO_4)_5$ crystalline phase in a mixture of sodium silicate and calcium phosphate amorphous glassy matrix can be attributed to higher solubility of these phases that induce faster hydroxyl carbonated apatite formation.

CHAPTER 6

APATITE FORMATION BEHAVIOR OF HYDROXYAPATITE – BIOGLASS®45S5 CO-
SINTERED BIOCERAMICS IN SIMULATED BODY FLUID

6.1 Introduction

Human body fluid is supersaturated with respect to apatite. The high activation energy for

the apatite nucleation in human body fluid make apatite formation only occur in bone tissue. If an

artificial material has a functional group such as Si-OH or PO_4H_2, that could be an effective

apatite nucleation site on its surface and easily form apatite nuclei on its surface. Once the

apatite nuclei are formed they spontaneously grow by consuming calcium and phosphate ions

from the surrounding body fluid. The formed apatite is very similar to the bone mineral in its

composition and structure. Therefore, osteoblasts preferentially proliferate and differentiate on

this apatite layer. Consequently, the surrounding bone can come into direct contact with the

surface apatite layer. When this occurs, a strong chemical bond is formed between the bone

minerals and the surface apatite layer to reduce the interface energy between them [5, 31].

The nature of the bioceramics and its surface characteristics play important roles in

determining bone adaption to the implant material. Surface reactivity is the common

characteristics of bone bioactive ceramics. It contributes to their bone bonding ability and their

enhancing effect on bone tissue formation. During implantation, reactions occur at the material-

tissue interface that leads to changes in the surface characteristics of the implant material and the

tissues at the interface which eventually maintains an interfacial bonding between the implant and

the host tissue as describe in the previous paragraph. However, the bonding time, strength,

mechanism, or thickness varies depending on the chemical activity of those bioceramics [1, 32].

A comparison of the relative chemical activity of these different types of bioceramics is shown in

Figure 2.1 in Chapter 2 which is closely correlated with the rate of an interfacial bond formation with the bone. According to the type of bioceramics used and their interaction within the host tissue bioactive ceramics may be resorbable or non-resorbable [29]. There are two distinctive classes of bioactivity defined for bioactive ceramics. While Class A biomaterials are both osteoconductive and osteoinductive, Class B biomaterials are only osteoconductive. Osteoconduction is defined as the growth of bony tissue into the structure of an implant material while osteoinduction is stimulation of cells with the capacity to form bone in the implant site [160]. This classification separates most calcium phosphate ceramics from bioactive glasses [161].

Hydroxyapatite ($Ca_{10}(PO_4)_6OH_2$) is the main inorganic portion of bone [57], and synthetically produced hydroxyapatite is considered as a bone substitute material that will not cause any defensive bodily reactions [8]. Glasses composed of less than 60 mol% SiO_2, high Na_2O and CaO, and high CaO/P_2O_5 ratio are recognized as bioactive glasses that have highly reactive surface for fast bone bonding [11]. In certain circumstances it might be desirable for an implant to assist in bone repair and then be slowly resorbed and replaced by natural tissue. However, it is necessary to match the rate of resorption with that of the expected bone tissue regeneration. When the solubility of a bioceramic material is higher than the rate of tissue regeneration, it will only be of limited use in bone cavity and defect filling [29].

Among all bioglass compositions Bioglass® 45S5 is proven to be the most bioactive glass composition [20]. Due to the rapid resorption of Bbioglass®45S5 the bone formation is greater than that produced by synthetic hydroxyapatite. The rate of bone formation correlates with the dissolution of the particles and the provision of soluble silica to the osteoblasts in the growing bone [66]. When a bioceramic implant placed within the body a process promotes healing and bone restoration as the calcium-phosphate dissolves and subsequently resorbed. The interaction results in a calcium-phosphate rich hydroxyapatite layer on the surface of bioactive ceramic with dissolution, precipitation, and ion exchange process followed by adsorption and incorporation of biological molecules. However, bone apposes and integrates with hydroxyapatite relatively in

114

slower rates than some bioactive glasses [61]. Therefore, the low resorbability of hydroxyapatite is considered as a limiting factor because the bone conductive effect is restricted [67].

The primary advantage of hydroxyapatite – Bioglass®45S5 mixtures is the combination of their different dissolution behaviors. Synthetic hydroxyapatite will be the stable phase while Bioglass®45S5 is the resorbable accelerating apatite layer formation thus enhancing the initial new bone formation at the implant site [68]. For instance, Chatzistavrou et. al. found that sintered hydroxyapatite composites containing different amounts of bioglass lead to increased bioactivity [23]. It has been also shown by several researchers that bioglass addition to hydroxyapatite increases biological activities of hydroxyapatite [69, 70].

In order to understand and characterize the apatite formation process and behavior of various bioactive ceramic materials such as calcium phosphates [63, 85][7], bioactive glasses [7, 7, 23, 23, 86, 86], and their composites [14, 17, 87], numerous in-vitro studies have been carried out. Different techniques such as scanning electron microscopy (SEM) coupled with energy dispersive X-ray (EDX) spectroscopy [14, 23], thin film X-ray diffraction (TF-XRD) [87] as well as X-ray absorption near edge spectroscopy (XANES) [88, 89] have been employed to examine the surface structural changes.

In this chapter, the syntheses of hydroxyapatite – Bioglass®45S5 blends are expected to yield forming new bioceramic compositions that have higher bioactivity to form relatively faster apatite layers similar to natural bone which further promotes cell attachment, proliferation, and bone cell differentiation. In this manner, to characterize and understand the apatite formation process and compare the structural changes before and after *in vitro* SBF test on hydroxyapatite – Bioglass®45S5 bioceramic compositions different techniques such as scanning electron microscopy (SEM) coupled with energy dispersive X-ray (EDX) spectroscopy, thin film X-ray diffraction (TF-XRD), and X-ray absorption near edge structure (XANES) spectroscopy are employed.

115

<u>6.2 Experimental Procedure</u>

6.2.1 Powder Preparation

        The bioglass powder consisting of 45 wt. % SiO_2, 24.5 wt. % Na_2O, 24.5 wt. % CaO, and 6 wt. % P_2O_5 also known as Bioglass®45S5 was acquired from US Biomaterials with a particle size of <90μm, and the hydroxyapatite with a chemical composition of $Ca_{10}(PO_4)_6OH_2$ was acquired from Alfa Aesar with a particle size of <44μm. Five different mixtures were prepared with 1, 2.5, 5, 10, and 25 wt. % Bioglass®45S5 addition to hydroxyapatite.

6.2.2 Sample Preparation

        The Bioglass®45S5 powders were mixed with proper amount of hydroxyapatite in 250ml polyethylene bottles, and ball milled for 30 hours with acetone. After ball milling, the mixtures were dried in the oven at 80ºC for 24 hours. The dried powder mixtures were sieved until the particles were separated from each other. The powders were pressed uniaxially in a die with a diameter of 12.7mm to a pressure 105MPa, and sintered at 1200ºC for 4 hours with a heating rate of 4ºC/minute and cooled down to room temperature with a cooling rate of 10ºC/minute.

6.2.3 Immersion in SBF Behavior Test

        The preparation of SBF was adopted from the protocol developed by Kokubo et al [99] with few modifications. In order to prepare 1000 ml of SBF, first of all 700 ml of ion-exchanged and distilled water with a stirring bar into 1000 ml glass beaker is set on a hot plate covering with a watch glass maintaining the temperature at 36.5±2ºC under stirring. The first 8 order reagents given in Table 6.1 are dissolved in water one by one. The 9th and 10th order reagents are dissolved to adjust pH to 7.4. After the pH adjustment, the solution is cooled down to 20ºC and enough ion-exchange and distilled water is added to complete the solution to 1000ml.

        After the SBF solution preparation, the sintered bioceramic pellets were immersed in 25mL glass veils of SBF solution, and the glass veils placed on a rotating mixer in an incubator maintaining human body temperature at 37ºC and pH 7.4 for various time. Also as a reference,

116

Table 6.2 shows the nominal ion concentrations of SBF in comparison with those in human blood plasma.

Table 6.1: Reagents used to prepare the SBF (pH7.40, 1L) [97]

ORDER NO.	REAGENT	CONTENT
1	NaCl	7,996 g
2	$NaHCO_3$	0,350 g
3	KCl	0,224 g
4	$K_2HPO_4.3H_2O$	0,228 g
5	$MgCl_2.6H_2O$	0,305 g
6	1N-HCl	40 ml
7	$CaCl_2$	0,278 g
8	Na_2SO_4	0,071 g
9	$NH_2C(CH_2OH)_3$	6,057 g
10	1 N-HCl	0-5 ml

Table 6.2: Nominal ion concentrations of SBF in comparison with those in human blood plasma [97].

Ion	Ion concentrations (mM)	
	Blood plasma	SBF
Na^+	142.0	142.0
K^+	5.0	5.0
Mg^{2+}	1.5	1.5
Ca^{2+}	2.5	2.5
Cl^-	103.0	147.8
$HCO3^-$	27.0	4.2
HPO_4^{2-}	1.0	1.0
SO_4^{2-}	0.5	0.5
pH	7.2 – 7.4	7.40

The immersed bioceramic samples were removed from the SBF solution and dried at room temperature after 1, 2, 4, and 10 weeks. The samples before and after soaking in SBF were analyzed by X-ray diffraction (XRD) and thin film X-ray diffraction (TF-XRD), respectively to identify phases formed before and after immersion in SBF solution. XRD experiments performed on the Siemens Kristalloflex 810 Powder Diffractometer using Cu Kα radiation. The data were recorded over the 2θ range of 20-60° with a 0.01° step size and a count time of 0.1 second. The TF-XRD was carried out on Philips PW 1830 Thin Film X-Ray Diffractometer with Cu of Kα. The samples were set at theta position of (incident beam) 0.5º and fixed; the detector was scanned between 20 and 60º with a step size of 0.02º and 1 second dwell time. The development of microstructures in the bioceramic samples after sintering before immersion in SBF solution were investigated using Hitachi S-3000N VP and Zeiss Supra 55VP scanning electron microscopes. The top and cross section microstructures of bioceramic compositions immersed in SBF solution were characterized using Jeol JSM 7000F Field Emission scanning electron microscope and

Zeiss Supra 55VP scanning electron microscope coupled with energy dispersive X-ray (EDX) spectroscopy, respectively. All SEMs were operated in secondary electron mode.

6.2.4 XANES Analyses

XANES spectroscopy was carried out on the model compounds and 5 different hydroxyapatite – Bioglass®45S5 compositions after sintering at 1200°C for 4 hours before and after immersion in SBF solution. The acquired XANES spectra from hydroxyapatite – Bioglass®45S5 compositions before and after immersion are compared with the model compounds in order to understand the chemical nature and the structural environment of silicon (Si), phosphorus (P), and calcium (Ca) atoms.

Si, P, and Ca K-edge XANES spectra of hydroxyapatite – Bioglass®45S5 compositions before and after 1, 4, and 10 week immersion in SBF solution and Si and P $L_{2,3}$-edge XANES spectra before and after 10 week immersion in SBF solution were acquired. The P and Si $L_{2,3}$-edge XANES spectra were obtained at the 2.9 GeV storage ring at the Canadian Light Source, Saskatoon, Canada using the Variable Line Spacing Plane Grating Monochromator (11ID-2 VLS-PGM) beam line. The step size used in acquiring Si $L_{2,3}$-edge was 0.1 eV with a dwell time of 1 second per point in the energy range of 100 – 120 eV for all samples. The P $L_{2,3}$-edge for model compounds and sintered bioceramic compositions before immersion in SBF solution was acquired in three regions *(1)* 130-135eV, step size: 0.25eV, *(2)* 135-150eV, step size: 0.1eV, *(3)* 150-155eV, step size: 0.25eV with a constant dwell time of 1 second per point. The step size used in acquiring P $L_{2,3}$-edge was 0.1eV with a dwell time of 1 second per point in the energy range of 130 – 155eV for apatite layers formed after immersion in SBF solution. The P and Si K-edge spectra and Ca K-edge spectra were obtained at the Synchotron Radiation Center in Madison, Wisconsin using the Double Crystal Monochromator Beamline (800 MeV for the Si and P spectra and 1 GeV for the Ca K-edge spectra). The data acquisition for the Si K-edge was acquired using three regions: *(1)* 1830-1835eV, step size: 1eV, *(2)* 1835-1880eV, step size: 0.25eV, *(3)* 1881-1900eV, step size: 1eV with a constant dwell time of 1 second per point for all

119

samples. The spectra for the P K-edge were acquired using two regions: *(1)* 2130-2180eV, step size: 0.25eV and *(2)* 2180-2190eV, step size: 1eV with a constant dwell time of 1 second per point for model compounds and sintered bioceramic samples before *in vitro* SBF tests. The P K-edge XANES spectra for apatite layers formed after immersion in SBF solution were acquired in three regions: *(1)* 2130-2138eV, step size: 1eV, *(2)* 2138-2180eV, step size: 0.3eV, and 2181-2200eV, step size: 1eV with a constant dwell time of 1 second per point. The spectra for the Ca K-edge was acquired using the region 4010 to 4100eV with a 0.5eV step size for bioceramic compositions and 0.5-0.7eV for model compounds with a constant dwell time of 1 second per point. The spectra for the Ca K-edge of apatite layers formed after immersion in SBF solution was acquired using three regions: *(1)* 4010-4020eV, step size: 1eV, *(2)* 4020-4070eV, step size: 0.25eV, and *(3)* 4070-4100eV, step size: 1eV with a constant dwell time of 1 second per point.

SiO_2, Na_4SiO_4, Na_2SiO_3, $CaSiO_3$, sintered Bioglass®45S5 ($Na_2CaSi_3O_8$ is the crystalline phase when Bioglass®45S5 is sintered at 1200ºC for 4 hours) are used as representative model compounds for Si $L_{2,3}$- and K-edge spectra. $NaHPO_4$, NaH_2PO_4, $CaHPO_4$, $CaHPO_4$-H_2O, $Ca_2P_2O_7$, β-$Ca_3(PO_4)_2$, α-$Ca_3(PO_4)_2$, sintered Bioglass®45S5, and hydroxyapatite are used as the model compounds for P $L_{2,3}$-edge, and $CaHPO_4$, $CaHPO_4$-H_2O, $Ca_2P_2O_7$, β-$Ca_3(PO_4)_2$, α-$Ca_3(PO_4)_2$, and hydroxyapatite for P K-edge spectra. At last, $CaOH_2$, CaO, $CaCO_3$, $Ca_2P_2O_7$, β-$Ca_3(PO_4)_2$, $CaHPO_4$, $CaHPO_4$-H_2O, Bioglass®45S5, and hydroxyapatite are used as representative model compounds for Ca K-edge spectra. All the model compounds chosen are representing the possible silicates, phosphates, and calcium compounds formed in hydroxyapatite – Bioglass®45S5 bioceramic compositions. All the model compounds and bioceramic compositions before immersion in SBF solution were ground into powder and a thin layer of powder deposited on carbon tape and all bioceramic samples after immersion in SBF solution were attached on carbon tape and placed in the vacuum chamber of the beamline. All XANES spectra of model compounds and bioceramic compositions after sintering were obtained by measurement of the fluorescence yield (FLY) as a function of incident photon energy. The

backgrounds for all spectra were subtracted and plotted using arbitrary units. The peak intensities were measured by calculating the difference between the peak and the background.

<div align="center">6.3 Results and Discussion</div>

6.3.1 Immersion in SBF Behavior

In order to evaluate the stability and structure of 5 different Bioglass®45S5 added hydroxyapatite bioceramic compositions and identify the crystalline phases formed, they were sintered at 1200℃ for a period of 4 hours and X-ray diffraction was performed on pure hydroxyapatite, 1, 2.5, 5, 10, and 25 wt. % Bioglass®45S5 added hydroxyapatite bioceramics (Figure 6.1).

The secondary electron scanning electron (SEM) micrographs of hydroxyapatite, and hydroxyapatite – Bioglass®45S5 bioceramic compositions after sintering are observed to evaluate the surface microstructures as shown in Figure 6.2 (a – f). The XRD and SEM results of pure hydroxyapatite and hydroxyapatite – Bioglass®45S5 bioceramic compositions are discussed in detail in Chapter 4. The crystalline phases present are largely phosphates of calcium suggesting that the Si and Na that are present in the Bioglass®45S5 are present in the form of amorphous glass. The HA – Bioglass®45S5 bioceramic compositions that have up to 5 wt. % Bioglass®45S5 (Figure 6.2 (b – d)) show similar microstructures with fine distribution of hydroxyapatite grains with a grain size of approximately 1-3μm. On the other hand, the compositions with 10 and 25 wt. % Bioglass®45S5 (Figure 6.2 (e and f)) show an amorphous glassy matrix with embedded $Ca_5(PO_4)_2SiO_4$ and $Na_3Ca_6(PO_4)_5$, respectively. The bioactivity of the bioceramic compositions can be highly depending on these amorphous phases as widely discussed in Chapter 5.
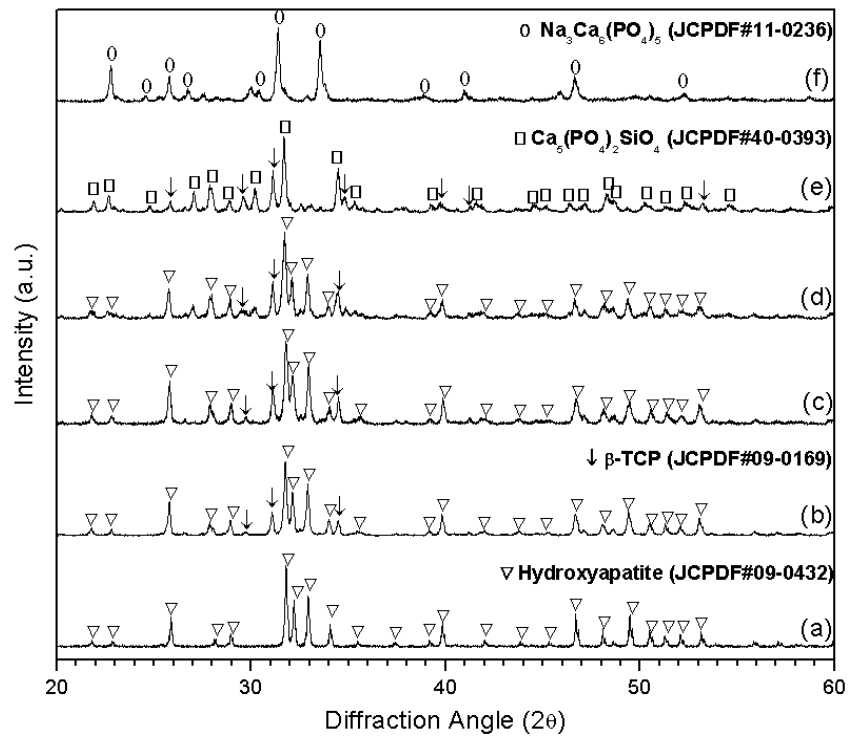
Figure 6.1: XRD spectra for (a) pure hydroxyapatite, (b) 1 wt. %, (c) 2.5 wt. %, (d) 5 wt. %, (e) 10 wt. %, and (f) 25 wt. % Bioglass®45S5 added hydroxyapatite sintered at 1200°C for 4 hours.
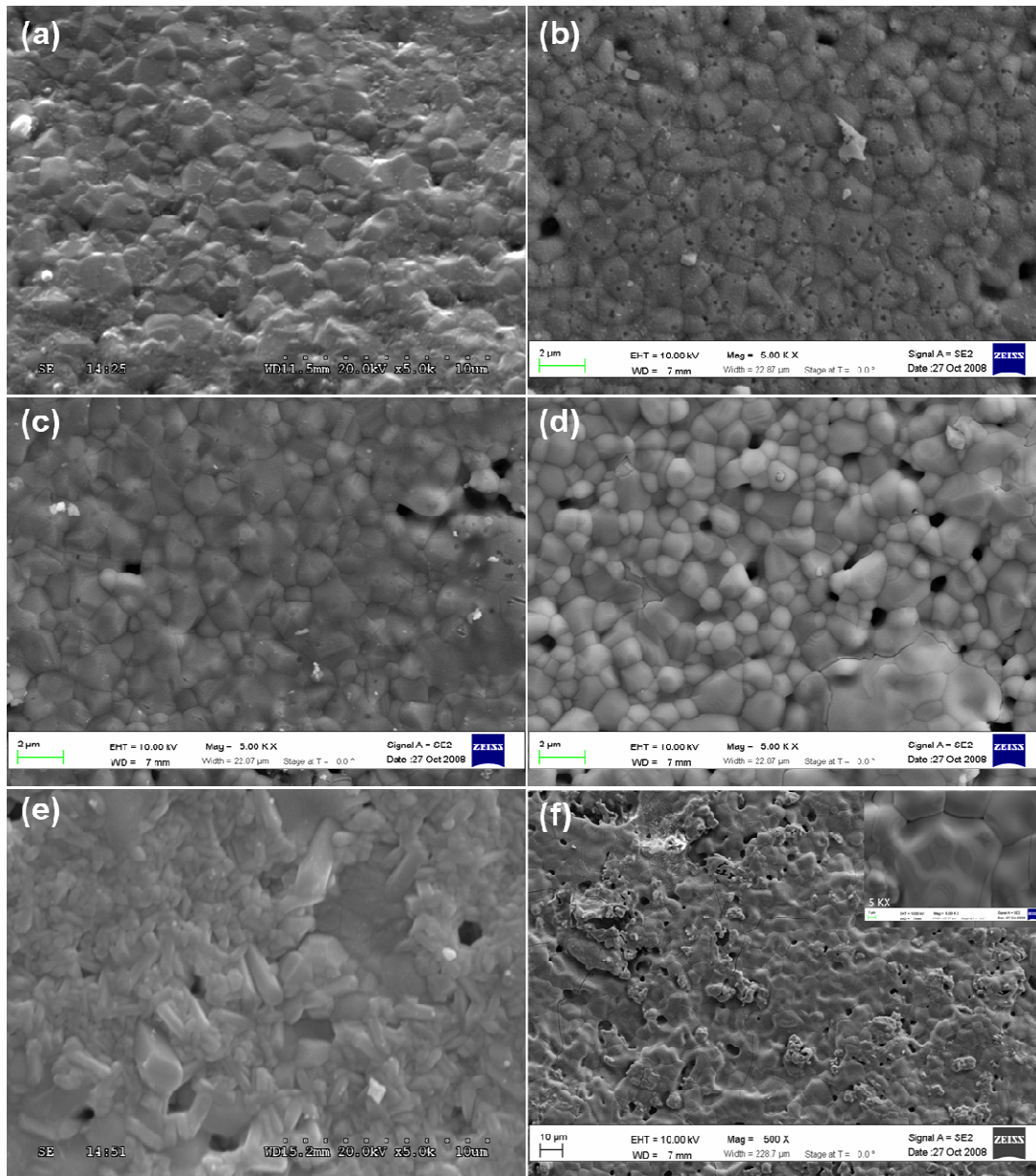
Figure 6.2: SEM micrographs of (a) 1 wt. %, (b) 2.5 wt. %, (c) 5 wt. %, (d) 10 wt. %, (e) 25 wt. % Bioglass®45S5 added hydroxyapatite bioceramic compositions sintered at 1200C for 4 hours.

This chapter mainly focuses on the apatite formation ability of hydroxyapatite – Bioglass®45S5 bioceramic compositions when immersed in SBF solution for various time periods by using scanning electron microscope coupled with energy dispersive X-ray spectroscopy, thin film X-ray diffraction, and X-ray adsorption near edge spectroscopy. In addition, the surface

123

chemistries formed after immersion in SBF solution were evaluated and compared to model compounds and sintered bioceramic compositions by X-ray adsorption near edge spectroscopy. The main and secondary phases formed and surface microstructures after sintering of up to 5 wt% Bioglass®45S5 added hydroxyapatite bioceramic compositions are very similar to pure hydroxyapatite (Figure 6.1 and 6.2(a – f)); therefore, the immersion behavior of 1 wt. % Bioglass®45S5 added hydroxyapatite will be compared to 10 and 25 wt. % Bioglass®45S5 added hydroxyapatite bioceramic compositions those have a crystalline main phase of $Ca_5(PO_4)_2SiO_4$ and $Na_3Ca_6(PO_4)_5$ in an amorphous glassy matrix, respectively.

The formation of an apatite layer is a very common indication for the bioactivity of bioceramics [4, 96, 97, 162-164]. This process could be reproduced in simulated body fluid (SBF), which later on can be used to predict the *in vivo* bioactivity of those biomaterials [165].

The surface microstructures of 1, 10, and 25 wt.% Bioglass®45S5 added hydroxyapatite bioceramic compositions soaked in SBF solution for 1, 2, and 4 weeks are shown in Figures 6.3 – 6.5 (a – c). It is apparent that the formation of apatite layer on the bioceramic samples is closely related with their distinctive compositions. After 1 week immersion of 1, 10, and 25 wt. % Bioglass®45S5 added hydroxyapatite bioceramic compositions are shown in Figures 6.3 – 6.5 (a). It can be seen from the figures that tiny particles formed on the surface of 1 wt. % Bioglass®45S5 added bioceramic composition which has a main crystalline phase of hydroxyapatite, and the surface before immersion can be seen beneath the particles. Figure 6.4 (a) shows the surface of 10 wt. % Bioglass®45S5 added hydroxyapatite bioceramic composition. Basically similar surface features were found for 10 wt. % Bioglass®45S5 added hydroxyapatite bioceramic composition except that the particles formed are agglomerated and the number of them are more than 1 wt. % Bioglass®45S5 added hydroxyapatite composition, but not enough to cover the total surface. On the other hand, the SEM micrograph of 25 wt. % Bioglass®45S5 added hydroxyapatite composition surface after 1 week immersion in SBF solution shows that it is completely covered with the apatite layer and thus the original surface before immersion in SBF

124

solution disappeared thoroughly. It has been shown that the solubility of the bioactive ceramics plays an imported role in the formation of apatite layer [27]. This indicates that even after 1 week of SBF immersion 25 wt. % Bioglasss®45S5 added hydroxyapatite bioceramic composition forms a thick and uniform layer of apatite on its surface confirming that has a higher dissolution rate. The SEM micrographs for 1, 10, and 25 wt. % Bioglass®45S5 added hydroxyapatite bioceramic compositions after 2 weeks immersion in SBF solution are given in Figures 6.3 – 6.5 (b). In the case of 1 wt. % Bioglass®45S5 added hydroxyapatite bioceramic composition the size and the number of the particles increased with increased soaking time, yet still not covered the whole surface (Figure 6.3(b)). Figure 6.4 (b) shows the surface of 10 wt. % Bioglass®45S5 added hydroxyapatite bioceramic composition with a relatively thicker and more uniform layer of apatite formation than 1wt. % Bioglass®45S5 added hydroxyapatite bioceramic composition. The SEM micrograph of 25 wt. % Bioglass®45S5 added hydroxyapatite bioceramic composition after 2 weeks immersion in SBF solution shows that there is an obvious change in the surface features on the entire surface of the sample. These features started to transform into needle-like apatite indicating that the crystalline apatite already started to grow. On top of these needle-like features some spherical particles are seen showing that the apatite nucleation is also continuing. After 4 weeks immersion in SBF solution for 1, 10, and 25 wt.% Bioglass®45S5 added hydroxyapatite bioceramic compositions are shown in Figures 6.3 – 6.5 (c). In Figure 6.3 (c) it can be clearly seen that the particles that formed during the first and second week transformed into needle-like apatites that cover almost the entire surface pointing out that the apatite layer become more uniform and crystalline apatite started to grow by the fourth week of immersion in SBF solution. The surface microstructure of 10 wt. % Bioglass®45S5 added hydroxyapatite bioceramic composition after 4 weeks immersion in SBF solution is given in Figure 6.4 (c) showing similar results to 1 wt. % Bioglass®45S5 added hydroxyapatite bioceramic sample. This indicates that even though the apatite formation on 10 wt. % Bioglass®45S5 added hydroxyapatite bioceramic composition started and progressed better than 1 wt. % Bioglass®45S5 added hydroxyapatite

125

sample, it slows down by week 4 showing that 1 and 10 wt. % Bioglass®45S5 added hydroxyapatite samples have similar immersion behaviors while 25 wt. % Bioglass®45S5 added hydroxyapatite bioceramic compositions have noticeably improved immersion behavior which can be attributed to higher solubility property that induce faster dissolution thus apatite formation on its surface [87, 166].
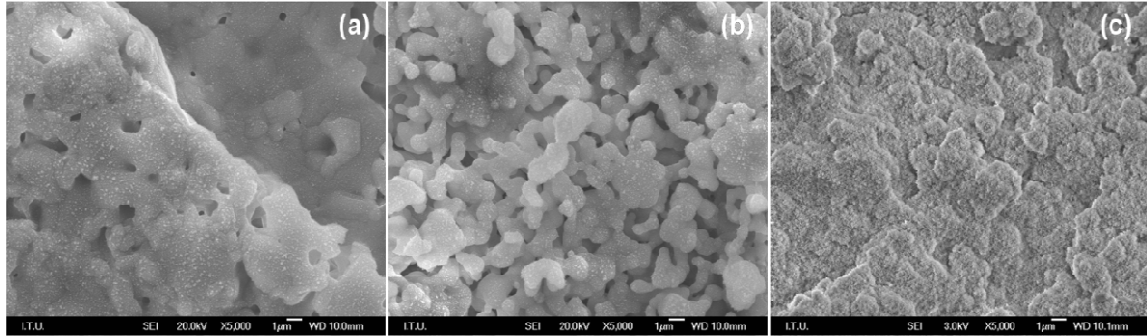
Figure 6.3: SEM micrographs (at 5KX) of 1 wt. % Bioglass®45S5 added hydroxyapatite bioceramic composition after (a) 1, (b) 2, and (c) 4 weeks immersion in SBF solution.
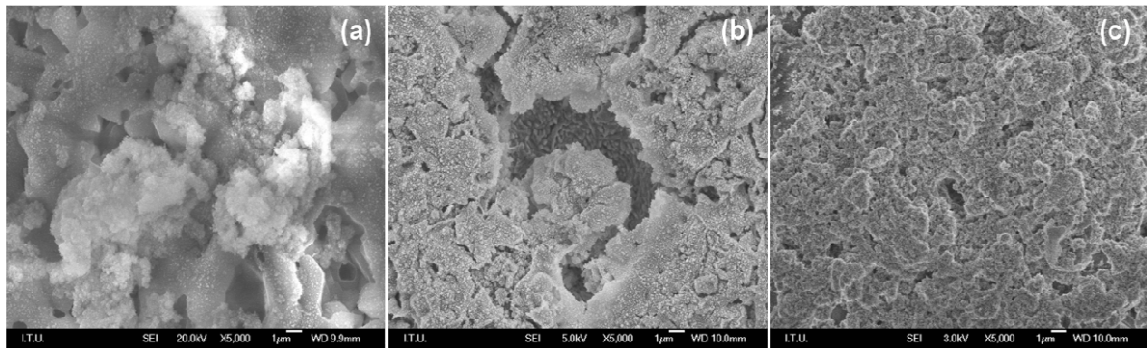
Figure 6.4: SEM micrographs (at 5KX) of 10 wt. % Bioglass®45S5 added hydroxyapatite bioceramic composition after (a) 1, (b) 2, and (c) 4 weeks immersion in SBF solution.
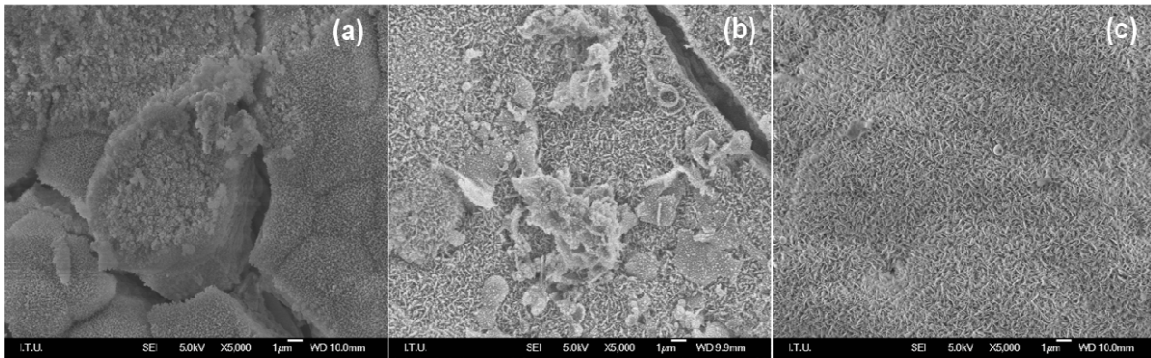
Figure 6.5: SEM micrographs (at 5KX) of 25 wt. % Bioglass®45S5 added hydroxyapatite bioceramic composition after (a) 1, (b) 2, and (c) 4 weeks immersion in SBF solution.

Figure 6.6 – 6.8 shows the characteristic cross section micrographs of 1, 10, and 25 wt. % Bioglass®45S5 added hydroxyapatite bioceramic compositions after 4 weeks immersion in SBF solution. These SEM micrographs are coupled with energy dispersive X-ray spectra taken from the substrate and the top layer as seen in Figures 6.9 and 6.10, respectively. The crystalline $Ca-P_2O_5$-rich layers formed in all three samples are more or less homogeneous and continues, and covers completely the underlying silicate-rich layer as interpreted from the EDX spectra shown in Figure 6.9 and 6.10. In Figure 6.9 relative Si, Ca, and P amounts from the substrates after 4 week immersion in SBF are shown. It can be clearly seen that as the Bioglass®45S5 amount increases the relative Si amount in the bioceramic compositions increases with respect to the amount of Ca and P. Figure 6.10 shows no traces of Si in 10 and 25 wt. % Bioglass®45S5 added hydroxyapatite compositions and little amount of Si in 1 wt. % Bgiolass®45S5 added hydroxyapatite bioceramic composition indicating that the layers formed on 10 and 25 wt. % Bioglass®45S5 added samples are rich in Ca and P which is known as $Ca-P_2O_5$-rich apatite layer while Si is still incorporated in the apatite formed on 1 wt. % Bioglass®45S5 added hydroxyapatite sample. In addition, the apatite layers formed on the surface of 1, 10, and 25 wt. % Bioglass®45S5 added hydroxyapatite bioceramic compositions are well connected to the substrates. However, while the thickness of the apatite layer formed in 1 wt. % Bioglass®45S5 added hydroxyapatite bioceramic composition is approximately 10µm (Figure 6.6), the apatite

127

layer formed on 10 ad 25 wt. % Bioglass®45S5 added hydroxyapatite bioceramic compositions display twice as thick layer on their surfaces indicating that addition to the high dissolution rate of 25 wt. % Bioglass®45S5 added hydroxyapatite bioceramics, the apatite nucleation and growth is faster in 10 and 25 wt. % Bioglass®45S5 added hydroxyapatite bioceramic compositions than 1 wt. % Bioglass®45S5 added hydroxyapatite samples. This can be accredited to the high amount of SiO_2 in those two bioceramic compositions since the prerequisite for apatite formation on an implant material in a living body is the presence of some types of functional groups [31] which is silanol (Si-OH) in this case. This functional group is known as a promising candidate for supplying effective sites for the apatite nucleation [167]. Once the apatite nuclei have been formed, they spontaneously grow by consuming Ca^{2+} and $PO4^{3-}$ from the surrounding fluid and form an amorphous $CaO-P_2O_5-$ rich film, because SBF is already supersaturated with respect to the apatite [5, 86]. Eventually, this amorphous layer crystallizes to hydroxyl carbonated apatite by incorporation of OH^- and CO^{3-} ions from the surrounding [86, 168].
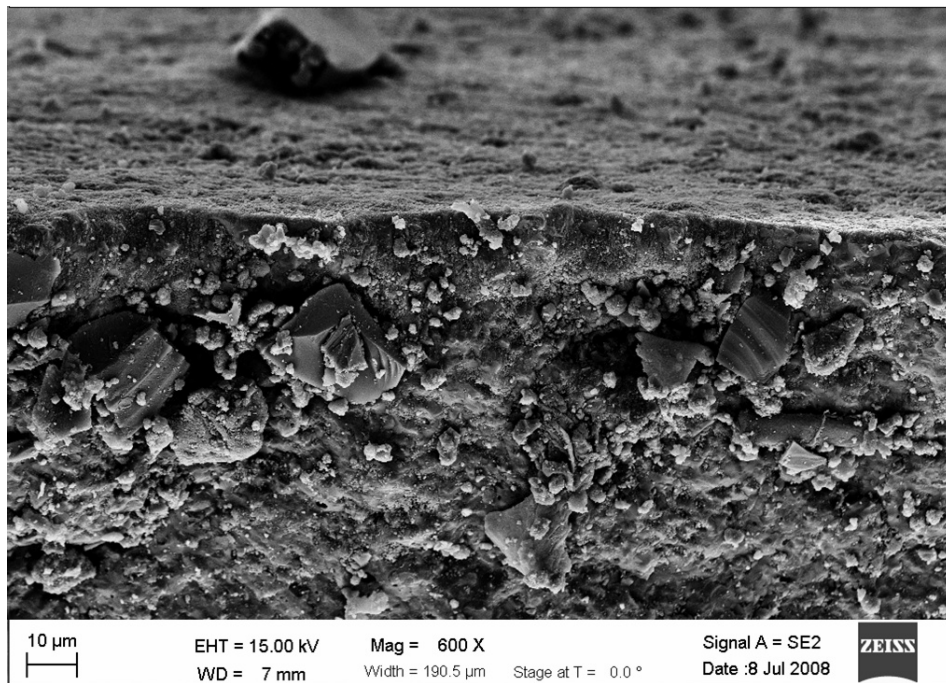
Figure 6.6: SEM micrograph for 1 wt. % Bioglass®45S5 added hydroxyapatite bioceramic composition after 4 weeks immersion in SBF solution.

128
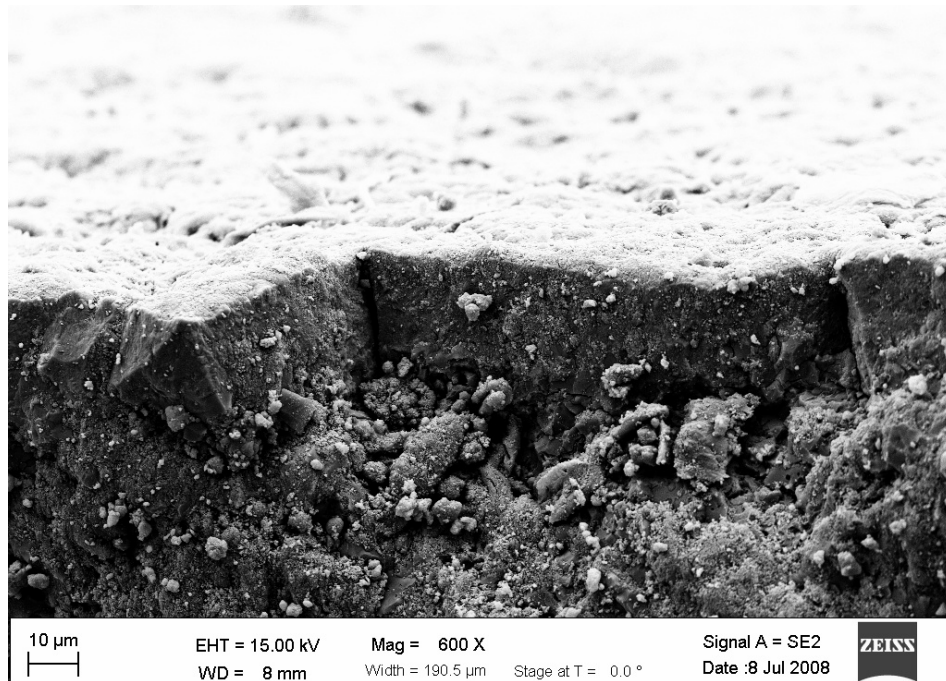
Figure 6.7: SEM micrograph for 10 wt. % Bioglass®45S5 added hydroxyapatite bioceramic composition after 4 weeks immersion in SBF solution.
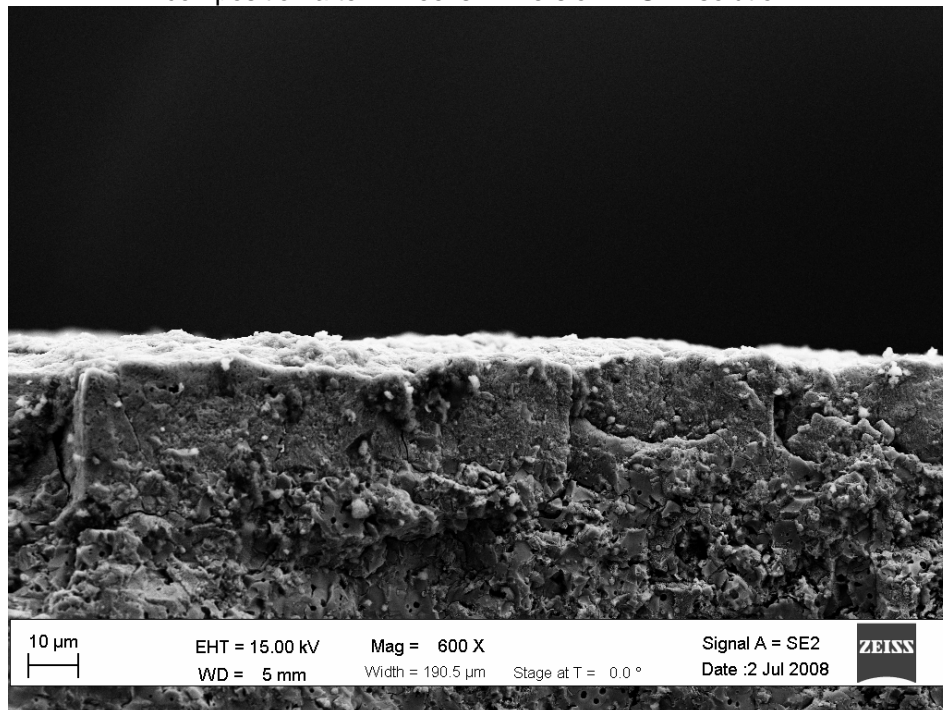
Figure 6.8: SEM micrograph for 25 wt. % Bioglass®45S5 added hydroxyapatite bioceramic composition after 4 weeks immersion in SBF solution.
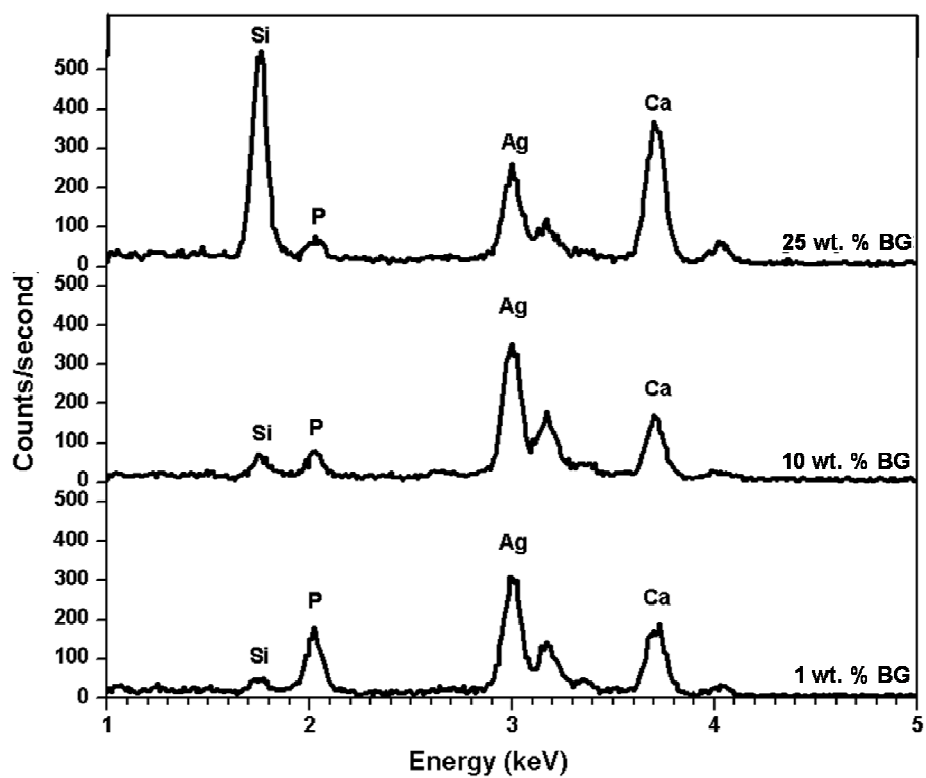
Figure 6.9: EDX spectra taken from 1, 10 and 25 wt. % Bioglass®45S5 added hydroxyapatite substrates after 4 weeks immersion in SBF solution.
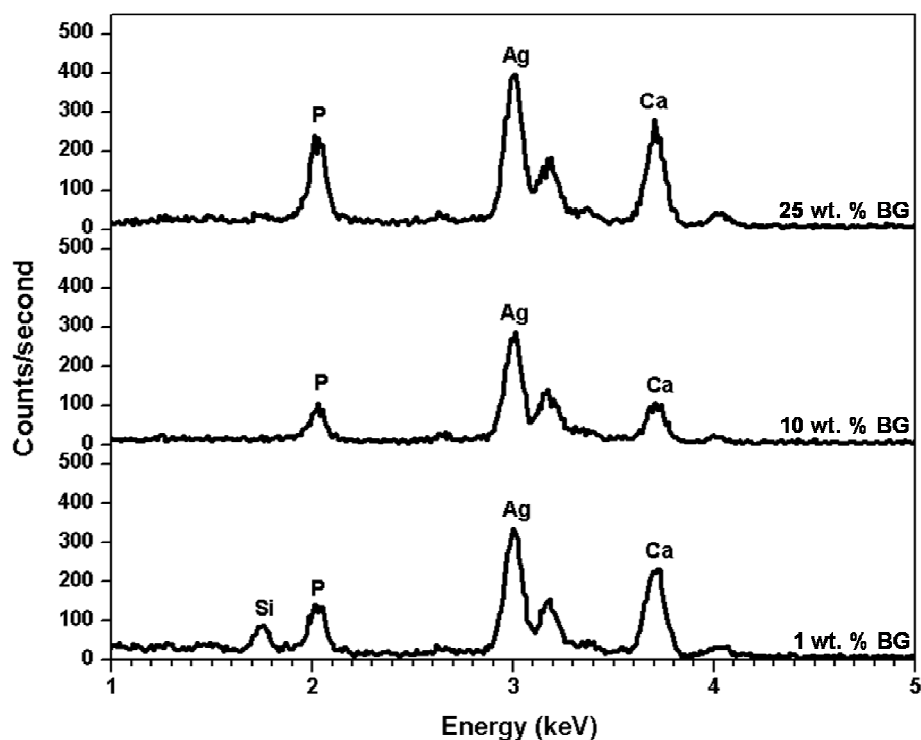
Figure 6.10: EDX spectra taken apatite layers formed on 1, 10 and 25 wt. % Bioglass®45S5 added hydroxyapatite bioceramic compositions after 4 weeks immersion in SBF solution.

This apatite layer formation and transformation from amorphous to crystalline hydroxyl carbonated apatite which is similar in composition and structure to bone apatite is also demonstrated by TF-XRD patterns of 1, 10, and 25 wt. % Bioglass®45S5 added HA bioceramic compositions after 0, 1, 2, 4, and 10 weeks immersion in SBF solution shown in Figure 6.11 – 6.13. The Figure 6.11 shows the TF-XRD patterns of 1 wt. % Bioglass®45S5 added hydroxyapatite bioceramic samples before and after soaking in SBF solution for 0, 1, 2, 4, and 10 weeks. Firstly, it should be mentioned that the intensity count ranges for after SBF tests are all same ranging from -25 to 500 differ from as sintered sample which is between -25 and 1300. The peak intensities of hydroxyapatite and β-tricalcium phosphate decreased gradually whereas new peaks due to apatite (JCPDF# 09-0432) gradually increased in intensity with the increase of soaking time. However, it is very hard to distinguish the main apatite peaks from main hydroxyapatite peaks due to the peak overlapping. One important observable fact is from week 1

131

to week 10 the intensity of one of the main peaks assigned for (211) miller indices of apatite decreases while (300) splits and becomes more visible. This signifies that at the beginning of the calcium phosphate layer formation on the surface of 1 wt. % Bioglass®45S5 is not entirely crystalline and not covers the whole surface of the sample so that both peaks of hydroxyapatite and apatite peaks are visible. When it reaches week 10, the crystalline hydroxyapatite and β-tricalcium phosphate phases are almost disappearing and a crystalline apatite forms on the entire surface.   The Figure 6.12 shows the TF-XRD patterns of 10 wt. % Bioglass®45S5 added hydroxyapatite bioceramic samples before and after soaking in SBF solution for 0, 1, 2, 4, and 10 weeks. The intensity counts for after SBF tests are all same ranging from -25 to 400 and differ from as sintered sample which is between -25 and 600. The peak intensity of $Ca_5(PO_4)_2SiO_4$ (JCPDF# 40-0393) decreases gradually whereas new peaks due to apatite (JCPDF# 09-0432) gradually increases with the longer soaking time. The peak overlapping can be also seen in these samples up to week 2. Starting from week 4 the crystalline $Ca_5(PO_4)_2SiO_4$ peaks barely visible while the main apatite peaks assigned for (211) and (300) miller indices start to be much apparent. And after 10 week immersion in SBF, the entire surface of 10 wt. % Bioglass®45S5 added hydroxyapatite bioceramic composition has a crystalline apatite layer on its surface. In the case of 25 wt. % Bioglass®45S5 added hydroxyapatite bioceramic samples the apatite formation and crystallization is much faster as can be easily seen in Figure 6.13. The intensity count range for after SBF tests are all same ranging from 0 to 175 and differ from as sintered sample which is between -10 and 500. The apatite layer formed on this bioceramic compositions can be detected as early as 1 week of immersion which also shows an increase in the intensity as the immersion time increases. Even after 1 week immersion there is not any visible $Na_3Ca_6(PO_4)_5$ (JCPDF#11-0236) peaks seen. In addition, the main peaks of apatite assigned for (300) and (202) miller indices are much distinguished by the increase in intensity and also by resolution of the peaks indicating that a thick layer of crystalline hydroxyapatite is already formed by the end of first week.

132

All these TF-XRD results support the SEM micrographs and EDX spectroscopy of these bioceramic compositions before and after soaking in SBF solution.
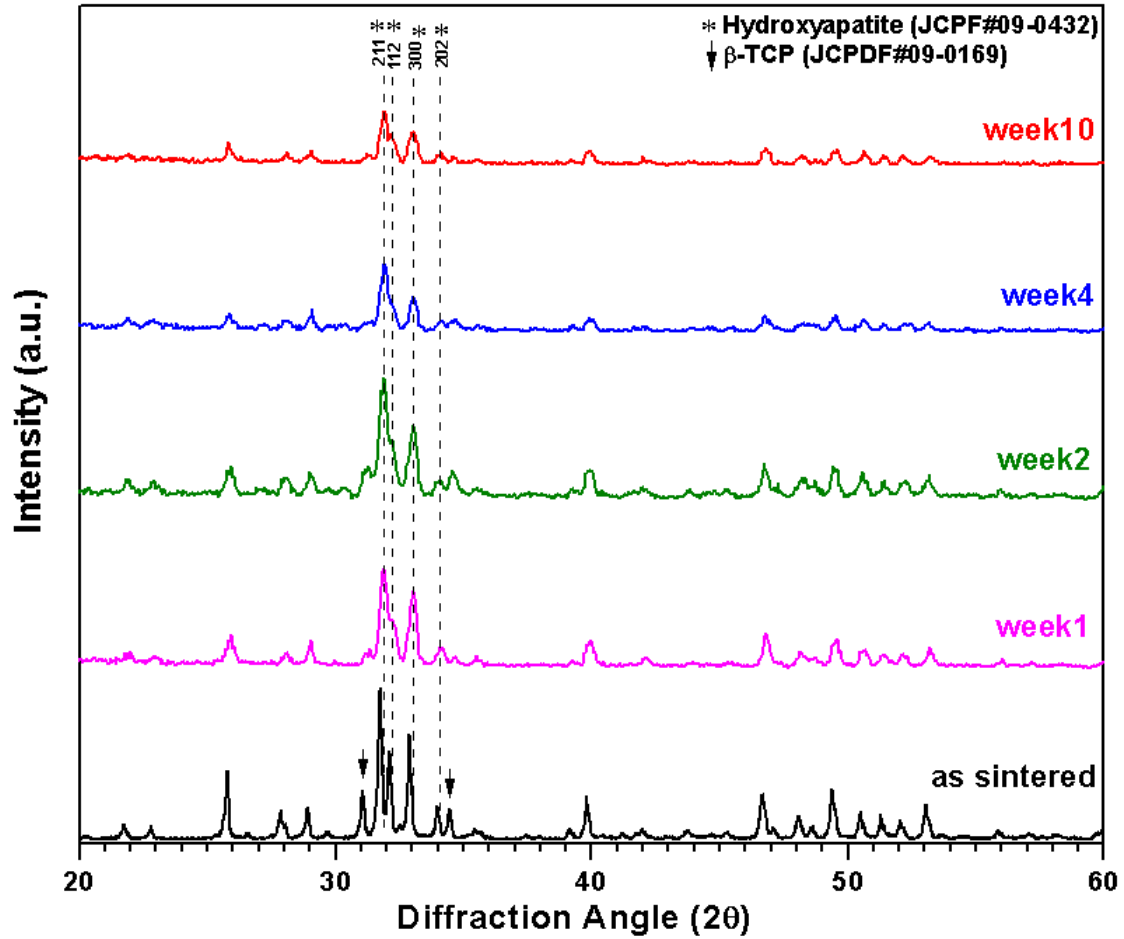
Figure 6.11: TF-XRD patterns obtained from 1 wt. % Bioglass®45S5 added hydroxyapatite bioceramic compositions after 0, 1, 2, 4, and 10 weeks immersion in SBF solution.
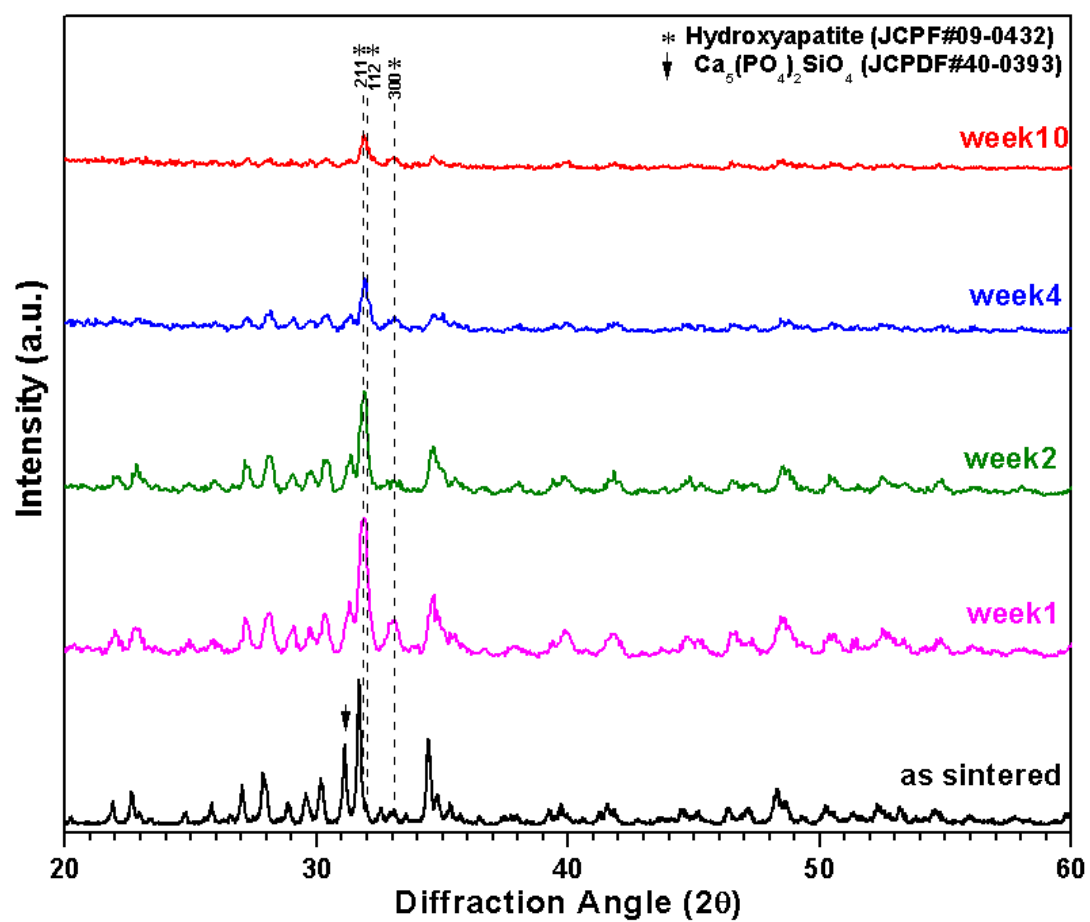
Figure 6.12: TF-XRD patterns obtained from 10 wt. % Bioglass®45S5 added hydroxyapatite bioceramic compositions after 0, 1, 2, 4, and 10 weeks immersion in SBF solution.
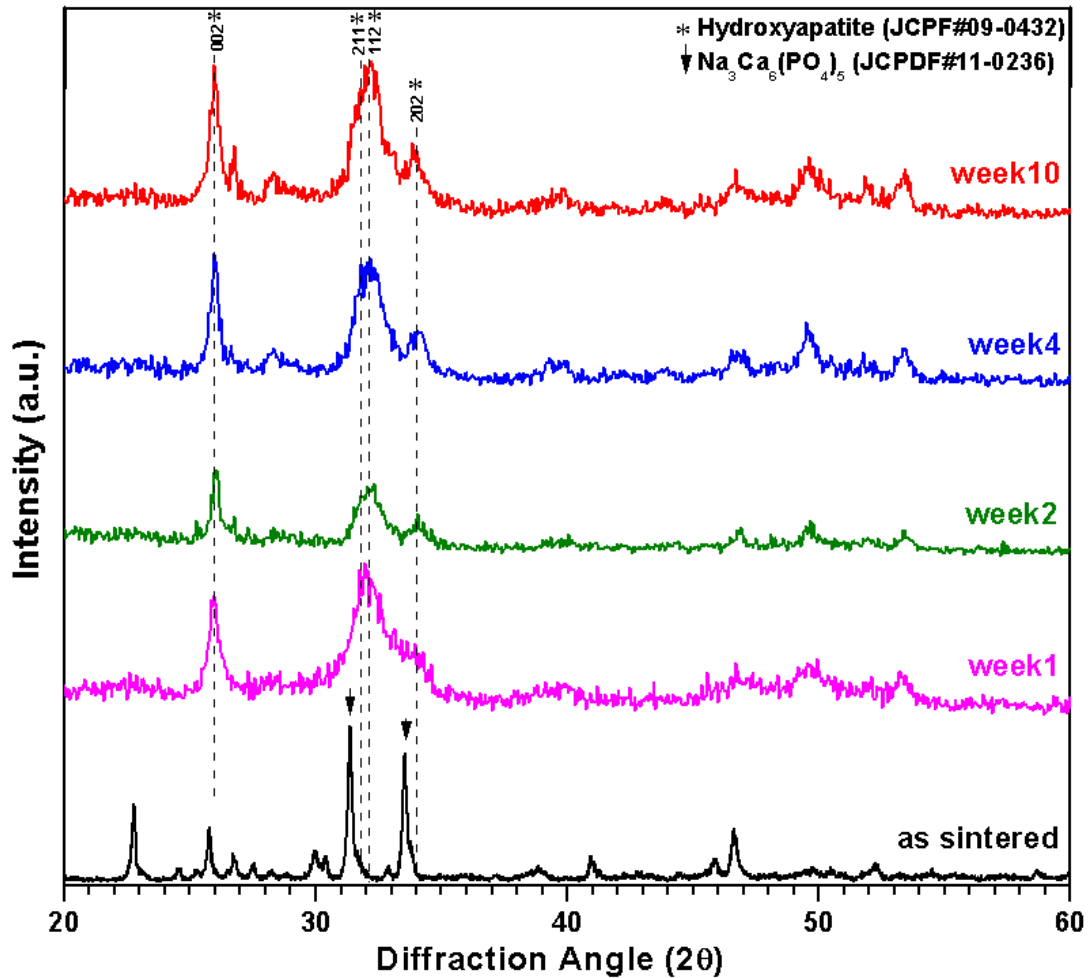
Figure 6.13: TF-XRD patterns obtained from 25 wt. % Bioglass®45S5 added hydroxyapatite bioceramic compositions after 0, 1, 2, 4, and 10 weeks immersion in SBF solution.

It can be concluded that the addition of significant amounts of Bioglass®45S5 to hydroxyapatite and sintering at 1200ºC for 4 hours lead forming new crystalline phases embedded in amorphous glassy matrix while small amounts only cause decomposition of hydroxyapatite. These newly formed phases enhance the apatite layer forming ability due to having increased dissolution rates. In addition, adding high amounts of Bioglass®45S5 which is the main source of SiO_2 to hydroxyapatite would raise the opportunity for the formation of the Si-OH groups [19] that act as nucleation site for a calcium-phosphate rich layer formation that later crystallizes as hydroxyl carbonated apatite that has a similar structure as bone apatite. Therefore,

135

these findings strongly demonstrated that the addition of 25 wt. % Bioglass®45S5 to hydroxyapatite yield forming new bioceramic composition that has been able to enhance markedly the *in vitro* bone like apatite forming ability of synthetic hydroxyapatite.

6.3.2 XANES Analyses

Figure 6.14 (a, b, and c) shows the Si K-edge XANES spectra of apatite layers formed on 5 different (1, 2.5, 5, 10, and 25 wt. % Bioglass®45S5 added hydroxyapatite) bioceramic compositions after immersed in SBF solution for 1, 4, and 10 weeks, respectively. Figure 6.15 shows the Si K-edge XANES spectra of 5 different bioceramic compositions after sintering prior to SBF solution immersion. Figure 6.16 shows Si $L_{2,3}$-edge XANES spectra of apatite layers formed on 5 different (1, 2.5, 5, 10, and 25 wt. % Bioglass®45S5 added hydroxyapatite) bioceramic compositions after immersed in SBF solution for 10 weeks. Figure 6.17 shows Si $L_{2,3}$-edge XANES spectra for as sintered bioceramic compositions before immersion in SBF solution. Si K- and $L_{2,3}$-edge XANES spectra for model compounds are given in Chapter 5 in Figures 5.4 and 5.2, respectively. All the details from these graphs are discussed in the related chapter.

The peak **a** in figures 6.14 (a-c) and 6.15 is assigned to the transition of Si 1s electrons to the unoccupied 3p- or 3s-like state (majority 3p-like) [115, 152]. This transition is allowed by selection rules; therefore, peak **a** is the strongest and called Si K-edge white line peak which characterizes the [4]Si with O in the Si K-edge XANES. There are two additional weak peaks are observed in the post-edge area at around 1856.5eV and 1864eV which are marked as peak **b** and **c**, respectively. The peaks **b** and **c** are attributed to the transition of Si 1s electrons to the 3d-like states [116]. In addition, it is reported that some silicate compositions may have the strongest peak at about 1848.9eV which characterizes the [6]Si with O in the Si K-edge XANES [118, 152]. The Si K-edge white lines in Figures 6.14 (a) through (c) show very sharp peaks only in the apatite layers formed after 1, 4, and 10 weeks of SBF immersion for 25 wt. % Bioglass®45S5 added bioceramic composition, and all the apatite layers formed on other bioceramic compositions (1 – 10 wt. % Bioglass®45S5) follow similar paths from week 1 to week 10

136

immersion with a significantly broader white line peaks which may be due to having a silicate compound of combination of 4- and 6- coordinated Si in their structure. The other possibility for broadening of the white lines in Si may be located in two different places. In one case it may be present as a silicate glass while in the other it may be incorporated into the apatite structure.

The P to Si integrated peak area ratios calculated from Si and P K-edge XANES spectra of apatite layers formed on 1, 10, and 25 wt. % Bioglass®45S5 added hydroxyapatite bioceramic samples after 1, 4, and 10 weeks immersion in SBF solution which is shown in Table 6.3 clearly shows that the Si to P ratio in apatite layers formed on 1 and 25 wt. % Bioglass®45S5 added hydroxyapatite samples decrease as the immersion period increases indicating that thicker apatite layers are forming. This finding is also in good agreement with EDX analysis obtained from apatite layers formed on 1, 10, and 25 wt. % Bioglass®45S5 added hydroxyapatite bioceramic samples after 4 weeks immersion in SBF solution (Figure 6.10) which do not show any evidence of Si in the apatite layers formed on 10 and 25 wt. % Bioglass®45S5 added hydroxyapatite bioceramic samples. On the other hand, 1 wt. % Bioglass®45S5 added hydroxyapatite bioceramic sample exhibits Si to some extent which can be attributed to the thinner apatite layer formed on it and the influence of the substrate. However, the resolution of an EDX system is typically 1-2 wt. % indicating the amount of Si present in the apatite layer is relatively low. The Si K -edge XANES spectra in fluorescence yield for Si provides information over a thickness between 2-3 μm, indicating that in the composition with 1 wt. % Bioglass®45S5 and 25 wt. % Bioglass®45S5 as the apatite layer grows the amount of Si incorporated into it decreases. On the other hand, in case of apatite layer grows on 10 wt. % Bioglass®45S5 added hydroxyapatite do not follow the same P to Si ratio trend indicating that the amount of Si incorporated to the apatite layer is more than 1 and 25 wt. % Bioglass®45S5 addition.

Table 6.3: P to Si integrated peak area ratios calculated from Si and P K-edge XANES spectra of apatite layers formed on 1, 10 ,and 25 wt. % Bioglass®45S5 added hydroxyapatite bioceramic samples after immersion in SBF solution for 1, 4, and 10 weeks.

	P to Si integrated peak area ratio		
Apatite layers formed on:	Week 1	Week 4	Week 10
1 wt. % Bioglass®45S5	12.54	20.12	39.18
10 wt. % Bioglass®45S5	14.46	15.37	12.25
25 wt. % Bioglass®45S5	12.21	65.51	76.44

The location, shape, and position of the Si $L_{2,3}$-edge XANES spectra (Figure 6.16) of apatite layers formed after 10 weeks immersion in SBF solution do not differ from the substrate XANES spectra. The Si $L_{2,3}$-edge provides information on the top 50 nm of the surface and indicates that chemically the structure has Si incorporated into the apatite layer. The P to Si integrated peak area ratios calculated from Si and P $L_{2,3}$-edge XANES spectra of apatite layers formed on 1, 10, and 25 wt. % Bioglass®45S5 added hydroxyapatite bioceramic samples after 10 weeks immersion in SBF solution is given in Table 6.4. It clearly shows that while the Si amount is more than P in apatite layers formed on 1 and 25 wt. % Bioglass®45S5 added hydroxyapatite samples, the Si amount in apatite layer formed on 10 wt. % Bioglass®45S5 is less than P. This indicates that 1 and 25 wt. % Bioglass®45S5 added hydroxyapatite samples exhibits more incorporation of Si into CaO-P_2O_5- rich films (apatite layers) closer to the surface. The reason behind this may be while the apatite layer grows; also Si incorporated to the apatite layer continues migrating towards the surface. In addition, the Si to P ratio of surface of the apatite layer formed on 25 wt. % Bioglass®45S5 is more than the surface of the apatite layer formed on 1 wt. % bioglass®45S5 added hydroxyapatite sample. This may be due to 25 wt. % Bioglass®45S5 bioceramic composition having larger amount of SiO2 in the composition. On the other hand, the apatite layer formed on 10 wt. % Bioglass®45S5 added hydroxyapatite sample do not follow the same P to Si ratio trend which shows bigger amount of P compared to Si

amount indicating that in this composition Si incorporated into apatite does not move towards the surface and rather stays in the bulk which is also in good agreement with the Si K-edge spectra.

Figure 6.14: Silicon K-edge XANES spectra of 5 different (1, 2.5, 5, 10, and 25 wt. % Bioglass®45S5 added hydroxyapatite) bioceramic compositions after immersed in SBF solution for (a) 1, (b) 4, and (c) 10 weeks.

Figure 6.15: Silicon K-edge XANES spectra for as sintered bioceramic compositions (1 – 25 wt. % Bioglass®45S5 added hydroxyapatite) before immersion in SBF solution.
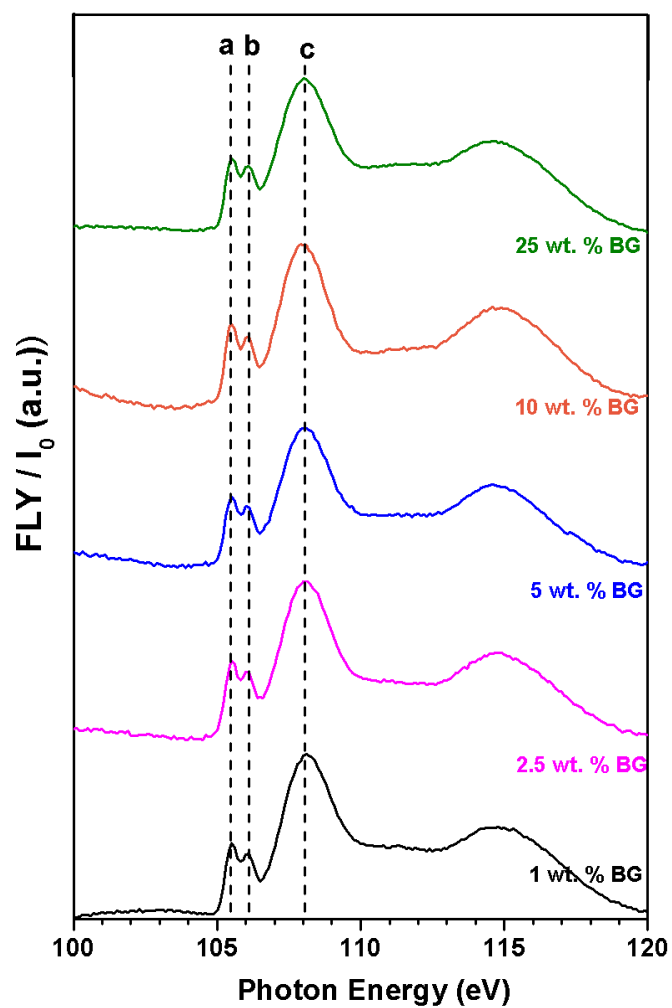
Figure 6.16: Silicon $L_{2,3}$-edge XANES spectra of 5 different (1, 2.5, 5, 10, and 25 wt. % Bioglass®45S5 added hydroxyapatite) bioceramic compositions after immersed in SBF solution for 10 weeks.
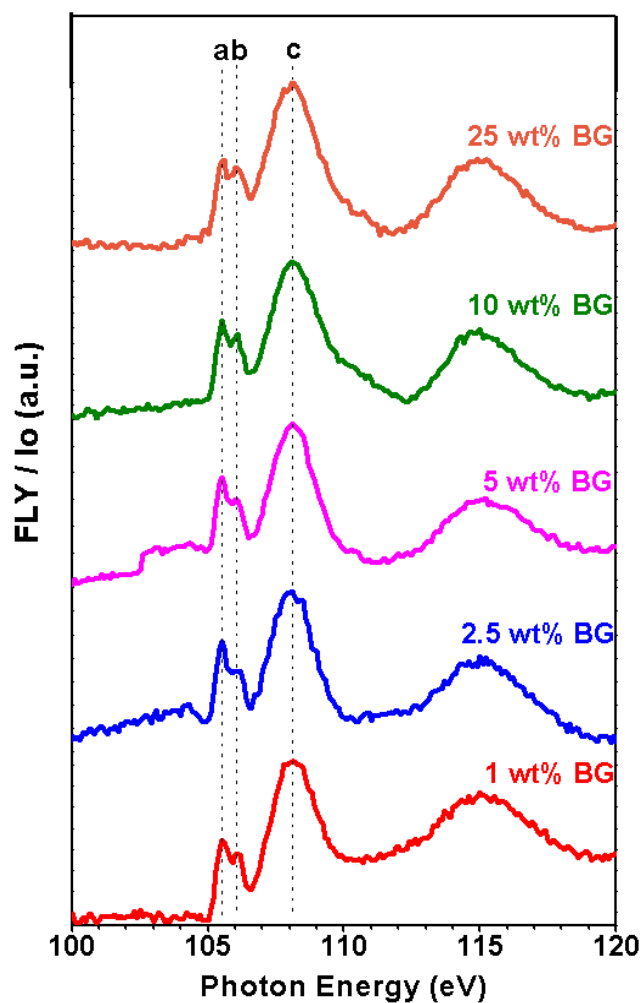
Figure 6.17: Silicon $L_{2,3}$-edge XANES spectra of as sintered bioceramic compositions (1 – 25 wt. % Bioglass®45S5 added hydroxyapatite) before immersion in SBF solution

Table 6.4: Si to P integrated peak area ratios calculated from Si and P $L_{2,3}$-edge XANES spectra of apatite layers formed on 1, 10 ,and 25 wt. % Bioglass®45S5 added hydroxyapatite bioceramic samples after immersion in SBF solution for 4 weeks.

Apatite layers formed on	Integrated peak area		Si to P integrated peak area ratio
	Si	P	
1 wt. % Bioglass®45S5	23.99091	17.41807	1.377
10 wt. % Bioglass®45S5	9.48371	11.48371	0.825
25 wt. % Bioglass®45S5	8.56063	3.2096	2.667

Figure 6.18 (a, b, and c) shows the P K-edge spectra of 5 different bioceramic compositions after immersion in SBF solution for 1, 4, and 10 weeks, respectively. Followed by P K-edge XANES spectra of as sintered bioceramic compositions before *in vitro* SBF tests in Figure 6.19. Figure 6.20 shows P $L_{2,3}$-edge XANES spectra for apatite layers formed on 5 different bioceramic compositions subsequent to 10 week immersion in SBF solution. P $L_{2,3}$-edge XANES spectra for as sintered bioceramic compositions before immersion in SBF solution are given in Figure 6.21. P K- and $L_{2,3}$-edge XANES spectra for various model compounds are given in Chapter 5 in Figures 5.8 (a-b) and 5.6 (a-c), respectively and widely discussed in the related chapter.

All P K-edge XANES spectra obtained from apatite layers formed on hydroxyapatite – Bioglass®45S5 bioceramic samples in Figure 6.18 (a - c) show two post edge peaks at around 2163eV (peak **b**) and 2169eV (peak **c**) in addition to the main P K-edge peak **a** at around 2152eV. In addition to these 3 peaks there is also a post-edge shoulder peak at around 2155eV, this shoulder corresponds to a transition of 1s phosphorus to the 3d calcium orbital. All hydroxyapatite – Bioglass®45S5 bioceramic compositions subsequent to sintering in Figure 6.19 also shows these four peaks indicating that the P structure environment in hydroxyapatite – Bioglass®45S5 bioceramic compositions are similar to the apatite layers formed. On the other

143

hand, a closer look to P L$_{2,3}$-edge XANES spectra of apatite layers formed after 10 week immersion in SBF solution indicates that the largest changes in the P structure occurs in the case of apatite layers formed on 1 and 25 wt. % Bioglass®45S5 added bioceramic samples. In case of apatite layer formed on 1 wt. % Bioglass®45S5 addition the white line P L$_{2,3}$-edge peak has shifted to a higher energy about 1eV, and the post- and pre-edges formed after sintering have disappeared. In case of 25 wt. % Bioglass®45S5 added hydroxyapatite bioceramic composition while the pre-edge and white line peaks have faded away, the post-edge peak has become more dominant. These findings imply that after 10 week immersion in SBF solution the P structural environment may only considerably changed in the apatite layer formed on 25 wt. % Bioglass®45S5 added hydroxyapatite bioceramic sample.
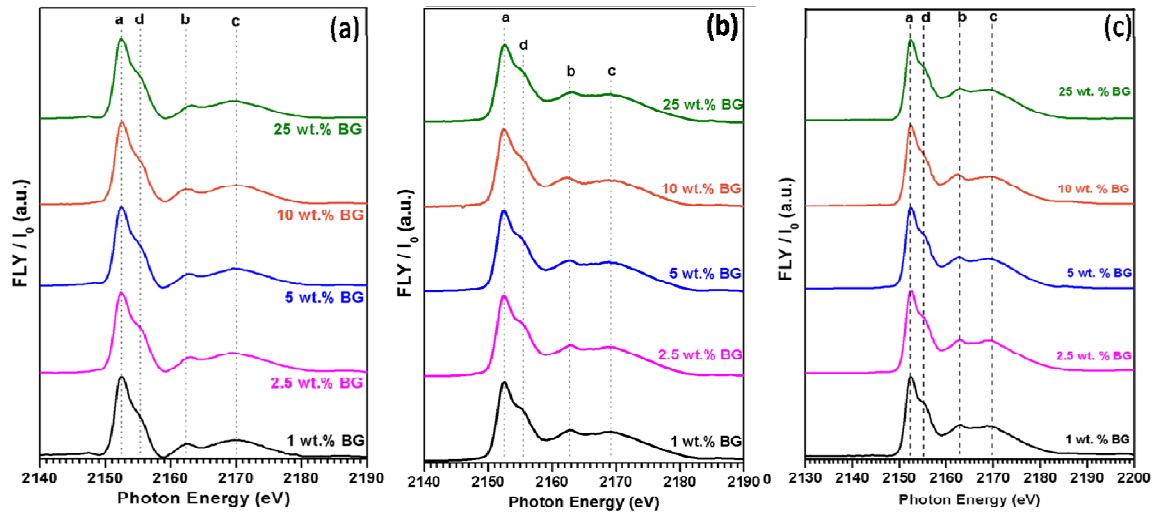
Figure 6.18: Phosphorus K-edge XANES spectra of 5 different (1, 2.5, 5, 10, and 25 wt. % Bioglass®45S5 added hydroxyapatite) bioceramic compositions after immersed in SBF solution for (a) 1, (b) 4, and (c) 10 weeks.
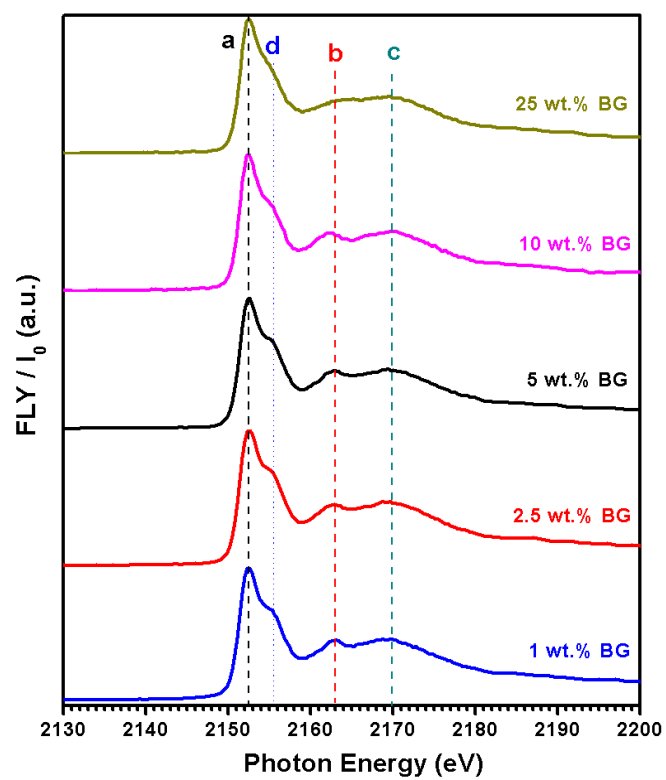
Figure 6.19: Phosphorus K-edge XANES spectra for as sintered bioceramic compositions (1 – 25 wt. % Bioglass®45S5 added hydroxyapatite) before immersion in SBF solution.
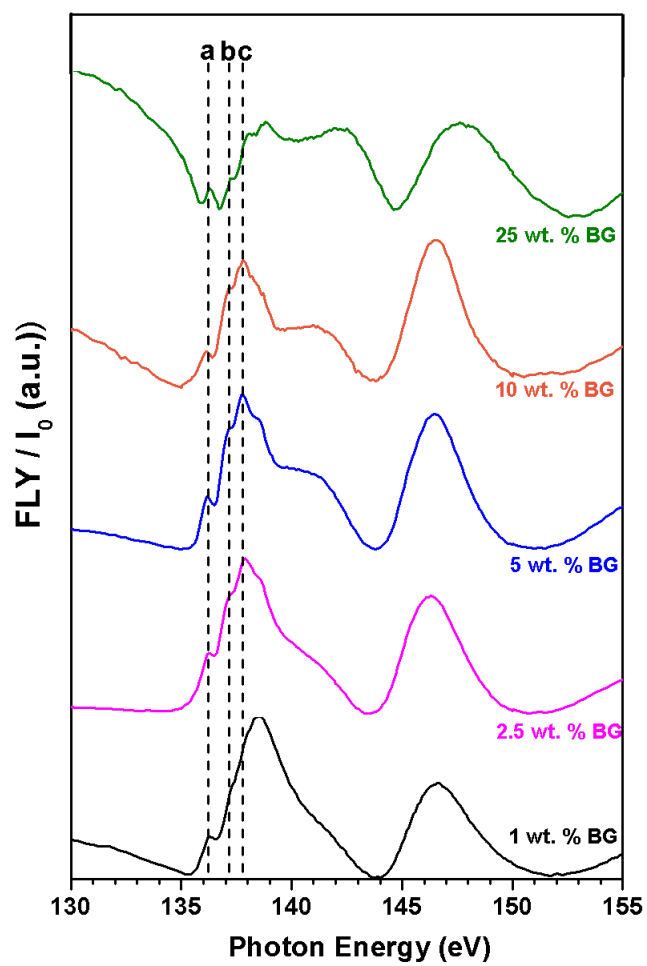
Figure 6.20: Phosphorus $L_{2,3}$-edge XANES spectra of 5 different (1, 2.5, 5, 10, and 25 wt. % Bioglass®45S5 added hydroxyapatite) bioceramic compositions after immersed in SBF solution for 10 weeks.

146
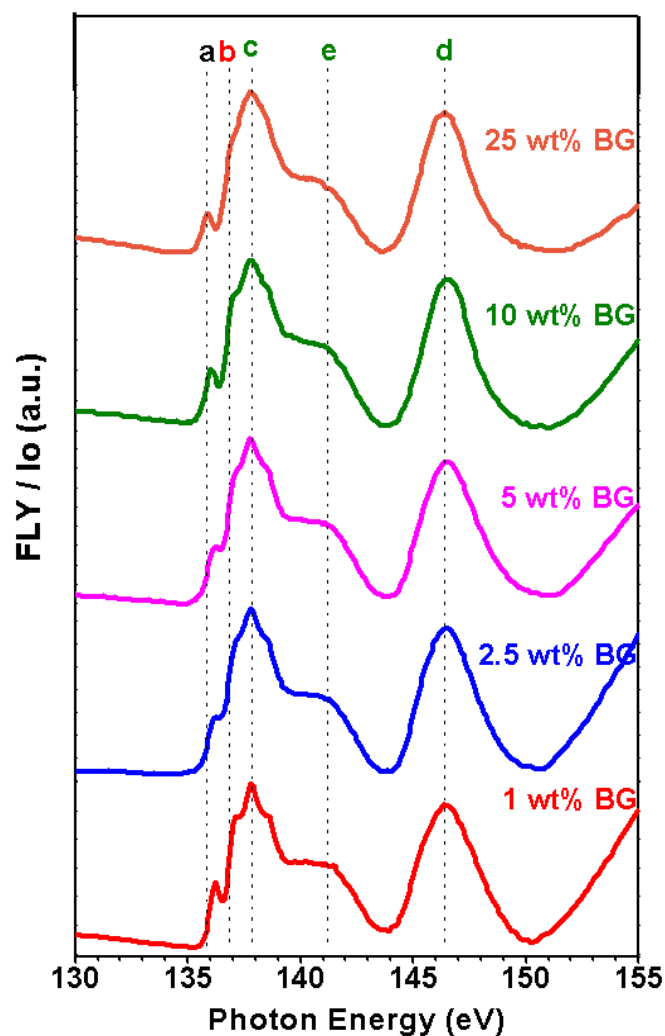
Figure 6.21: Phosphorus $L_{2,3}$-edge XANES spectra of as sintered bioceramic compositions (1 – 25 wt. % Bioglass®45S5 added hydroxyapatite) before immersion in SBF solution

Figure 6.22 (a and b) illustrates the Ca K-edge spectra for 5 different bioceramic compositions after immersed in SBF solution for 1 and 10 weeks, respectively. Ca K-edge XANES spectra for different bioceramic compositions (1 – 25 wt. % Bioglass®45S5 added hydroxyapatite) after sintering before immersion in SBF solution are provided in Figure 6.23. Ca K-edge XANES spectra for calcium compound model compounds are given and discussed in Figure 5.10 (a-c) in Chapter 5.

147

The most intense peak (peak **a**) of the spectra of as sintered bioceramic compositions (1 – 25 wt. % Bioglass®45S5 added hydroxyapatite) before immersion in SBF solution (Figure 6.23) corresponds to the main 1s to 3p transition. The Ca K-edge white line peak in Figure 6.23 has only a post edge peak at around 4052eV. On the other hand, the Ca K-edge XANES spectra for apatite layers formed after 1 and 10 weeks shown in Figures 6.22 (a) and (b) exhibits small features pre- and post edge regions. In addition, the white line peaks for apatite layers formed on 1 and 2.5 wt. % Bioglass®45S5 added hydroxyapatite bioceramic compositions in Figure 6.22 (b) composed of two peaks. The splitting of these Ca K-edge white line peaks (specifically in apatitic materials) can be assigned to the existence of two calcium sites with different coordination spheres [158]. Additionally, as the Bioglass®45S5 content increases the splited peaks start to combine to be one main peak and the peak intensity relative to peak **a** gradually decreases. Finally when the Bioglass®45S5 amount reaches 25 wt. %, it almost disappears. This finding suggests that the composition of the crystalline phase and silicate matrix plays an important role in the structural environment of calcium in apatite layers formed. The Si is most probably incorporating with Ca in $CaO-P_2O_5$ apatite layers since P K- and $L_{2,3}$-edges do not show very significant changes compared to Si and Ca K-edge XANES spectra. On the other hand, the same effect is not visible in Figure 6.22 (a) where the Ca K-edge XANES spectra for apatite layers formed on bioceramic compositions after 1 week immersion in SBF solution is shown.
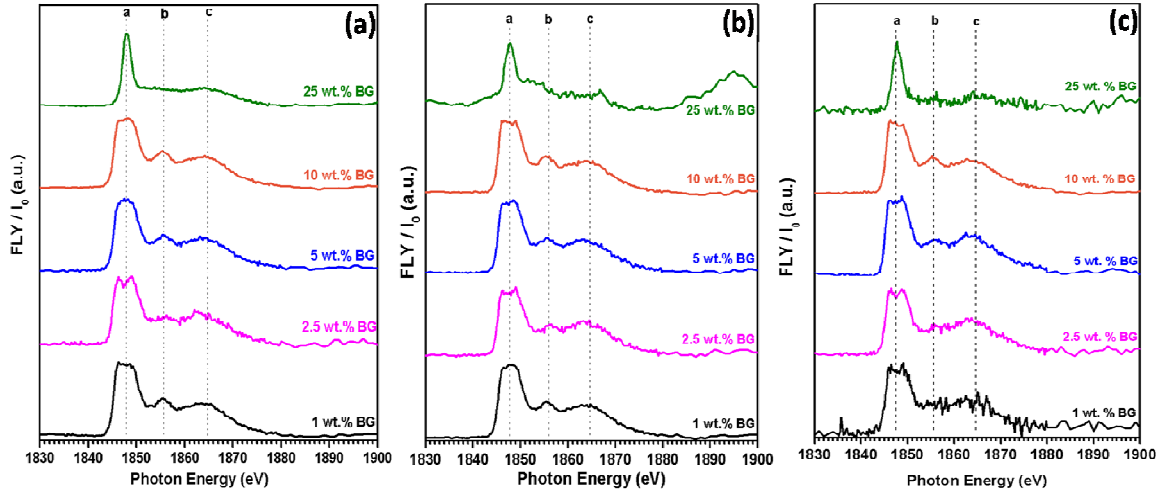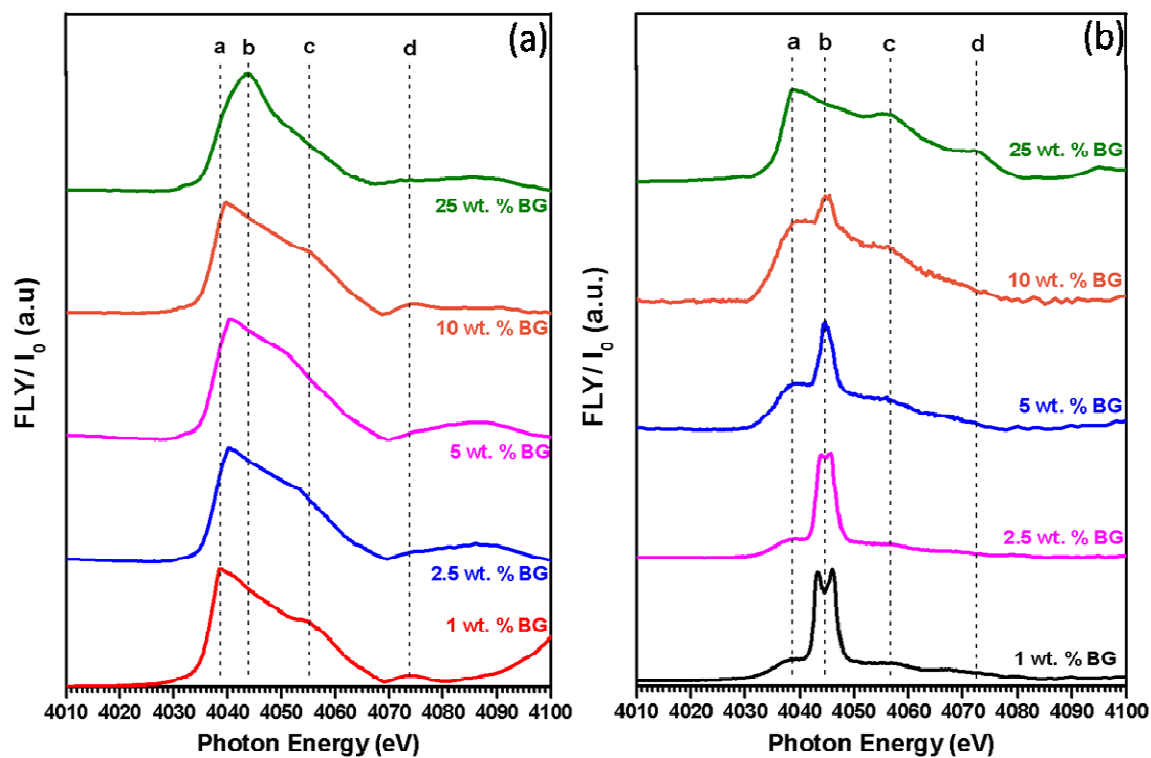
Figure 6.22: Calcium K-edge XANES spectra of 5 different (1, 2.5, 5, 10, and 25 wt. % Bioglass®45S5 added hydroxyapatite) bioceramic compositions after immersed in SBF solution for (a) 1 and (c) 10 weeks.

149
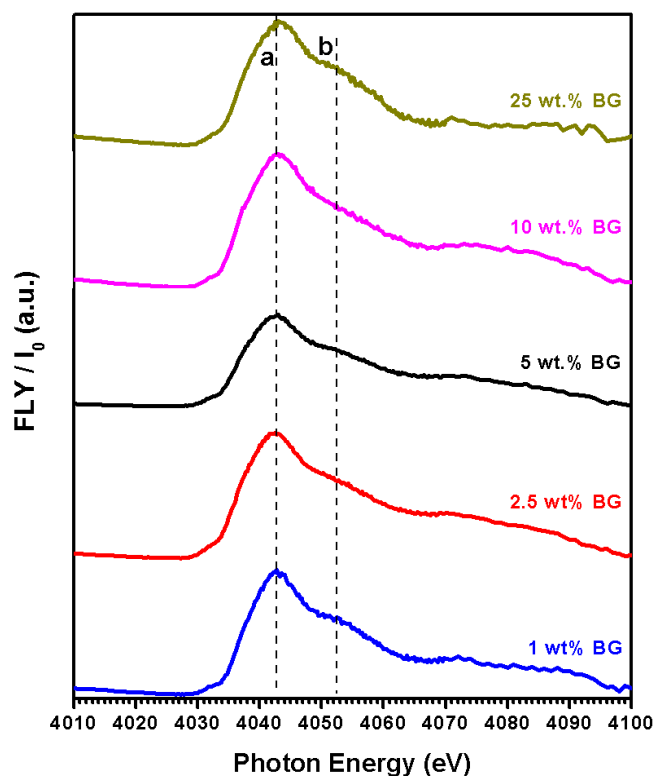
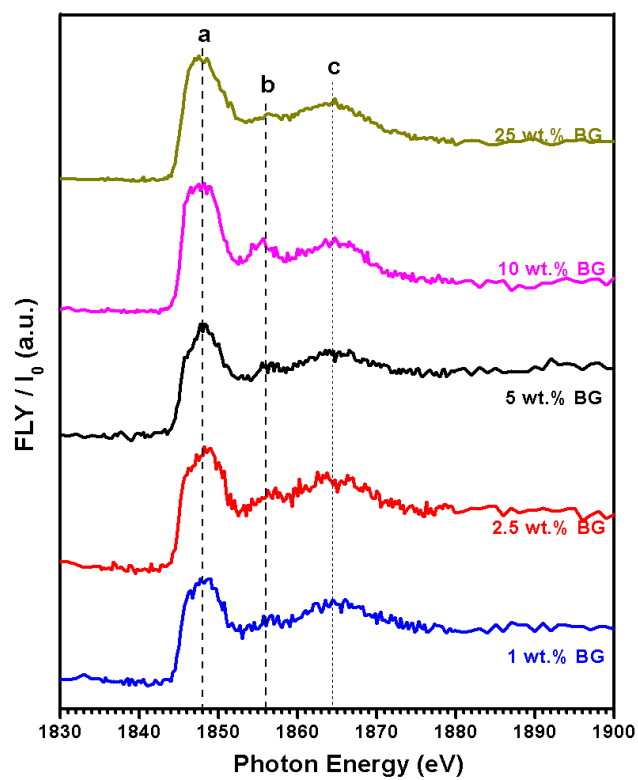Figure 6.23: Calcium K-edge XANES spectra of as sintered bioceramic compositions (1 – 25 wt. % Bioglass®45S5 added hydroxyapatite) before immersion in SBF solution

6.4 Conclusion

In order to evaluate apatite formation ability that is closely related to the bioactivity of materials, apatite formation mechanism, the structural variations in the apatite layers five different amounts of Bioglass®45S5 were blended with hydroxyapatite and sintered at 1200ºC for 4 hours. The X-ray diffraction analyses after sintering resulted that up to 5 wt. % Bioglass®45S5 addition certain amount of hydroxyapatite decomposed to β-tricalcium phosphate. 10 and 25 wt. % Bioglass® addition yielded new chemistries with $Ca_5(PO_4)_2SiO_4$ and $Na_3Ca_6(PO_4)_5$ crystalline phases in silicate matrices, respectively. 1 wt. % Bioglass®45S5 added hydroxyapatite is compared to 10 and 25 wt. % Bioglass®45S5 added hydroxyapatite bioceramic compositions in order to distinguish bone forming ability of these bioceramics. Even though all bioceramic compositions formed an apatite layer after various (1, 2, 4, and 10 weeks) immersion periods in

150

simulated body fluid (SBF) solution, a thicker and more uniform layer of apatite formation even after 1 week of immersion in SBF solution was observed only for $Na_3Ca_6(PO_4)_5$ crystalline phases in silicate matrix (25 wt. % Bioglass®45S5 added hydroxyapatite) bioceramic sample indicates that this composition has a higher solubility leading to a higher rate of apatite formation thus higher bioactivity than other compositions.

Si K-edge XANES spectra for all apatite layers formed except 25 wt. % Bioglass®45S5 showed broader white line peaks than the model compounds indicates that the origin of these peaks may be from Si incorporated to $CaO-P_2O_5$- rich (apatite) layers formed even though the TF-XRD patterns show same crystalline phase forming (hydroxyapatite). This finding is also in good agreement with EDX analysis obtained from apatite layers formed on 1, 10, and 25 wt. % Bioglass®45S5 added hydroxyapatite bioceramic samples after 4 weeks immersion in SBF solution. However, XANES spectroscopy has over a wide range of energies produced much greater than a common X-ray technique ensuring much higher sensitivity of element specific spectroscopic analyses [107]. This may be the reason why as all thin film XRD patterns from all samples after 4 week immersion displays same crystalline phases (apatite), the spectra obtained by XANES gives much detailed information and is able to pick the differences between the apatite layers. It is found that while Si K-edge spectra for apatite layers formed on 1 and 25 wt. % Bioglass®45S5 added hydroxyapatite bioceramics show increasing P to Si ratio, apatite layers formed on 10 wt. % Bioglass®45S5 added hydroxyapatite bioceramic composition remains more or less same following 1, 4, and 10 weeks immersion in SBF solution. This indicates that while the Si incorporated in apatite layers formed on 1 and 25 wt. % added hydroxyapatite bioceramic compositions decreasing in the bulk of apatite layer, it remains same for 10 wt. % Bioglass®45S5 added hydroxyapatite sample. In addition, the Si $L_{2,3}$-edge spectra for 1 and 25 wt. % Bioglass®45S5 added hydroxyapatite bioceramic samples showed that the Si is migrating towards the surface which gives a rise in the relative Si to P amount after 10 weeks immersion. On the contrary, the P amount was found larger than the Si amount on the surface of apatite layer

formed on 10 wt. % Bioglass®45S5 added hydroxyapatite bioceramic sample. This indicates that while the Si in apatite layers formed on 1 and 25 wt. % Bioglass®45S5 added hydroxyapatite samples migrates from bulk to surface of apatite layers, it does not diffuse through the apatite layer formed on 10 wt. % Bioglass®45S5 added hydroxyapatite bioceramic composition. The P structure environment in hydroxyapatite – Bioglass®45S5 bioceramic compositions are similar to the apatite layers formed. On the other hand, a closer look to P $L_{2,3}$-edge XANES spectra of apatite layers formed after 10 week immersion in SBF solution indicates that the largest changes in the P structure occurs in the case of apatite layers formed on only 1 and 25 wt. % Bioglass®45S5 added bioceramic samples may be due to incorporation of Si into the apatite layer closer to the surface of it after 10 weeks immersion in SBF solution. The Ca K-edge XANES spectra of apatite layers formed after 10 week immersion in SBF solution on bioceramic compositions shows splitting of Ca K-edge white line peaks (specifically in apatitic materials) which can be assigned to the existence of two calcium sites with different coordination spheres [158]. Additionally, as the Bioglass®45S5 content increases these peaks start to combine to be one main peak and the peak intensity relative to peak **a** gradually decreases. Finally when the Bioglass®45S5 amount reaches 25 wt. %, it almost disappears. This finding suggests that the Bioglass®45S5 content in hydroxyapatite closely related to the structural environment of calcium in apatite layers formed. In addition, the Si is incorporating with both P and Ca in CaO-P_2O_5-rich layers (apatite layers). However, further analyses including XANES spectroscopy are required to identify these Si incorporated compositions much in detail.

152

CHAPTER 7

NANO SCALE PROPERTIES OF HYROXYAPATITE – BIOGLASS®45S5 CO-SINTERED
BIOCERAMICS BEFORE AND AFTER *IN VITRO* BIOACTIVITY TESTS

7.1 Introduction

Bioceramic materials such as Bioglass®45S5 and hydroxyapatite have been clinically

used in orthopedic applications to repair damaged bone tissues [168, 169]. Both Bioglass®45S5

[86, 170, 171] and hydroxyapatite [86, 170, 172] bioceramics have affinity to form an apatite

layer on their surface when they get in contact with physiological fluids *in vitro* and *in vivo* via

chemical reactions which provoke development of an interfacial bond between the bone and the

implant [1]. Therefore, the bioactivity level of these bioceramics can be defined by their ability to

form apatite layer [173, 174], because the formation of this biologically active bone-like apatite on

the surface is an essential requirement for a bioactive material to bond to living bone [168].

However, bonding time, strength, mechanism, or thickness varies depending on the chemical

activity they exhibit [1, 32]. The two distinctive bioactive behavior described earlier suggests that

there are two main classes of bioactivity. While Class A biomaterials are both osteoconductive

and osteoinductive, class B biomaterials are only osteoconductive. This classification separates

most calcium phosphate ceramics from bioactive glasses [161].

Calcium phosphate ceramics especially hydroxyapatite has been proven to be ideal

bioceramic material used clinically to repair bone defects due to their chemical and

crystallographic structure being similar to that of bone mineral [175]. However, the medical

applications of hydroxyapatite are limited, because even though it can form an apatite layer and

bond to bone, it is too stable *in vivo* to be absorbed and substituted by a new bone which limits its

bone conductive effect [19]. Fortunately, the bioactivity, physical, and chemical stability of

153

hydroxyapatite can be modified by mixing hydroxyapatite with another bioactive material and improve its both biological and material properties [17, 176, 177]. In this manner, different amounts (1, 2.5, 5, 10, 25 wt. %) of Bioglass®45S5 were blended with hydroxyapatite and sintered at 1200ºC for 4 hours to form new compositions that can potentially replace hydroxyapatite and Bioglass®45S5 as a bone substitute.

The conventional microhardness measurement methods such as Vickers or Knoop use indentation loads such as 10 – 500 grams which are relatively too large to measure mechanical properties of calcium phosphate ceramics such as hydroxyapatite due to their brittle and fragile properties [178]. In addition, the surface mechanical properties such as hardness could be grain-size dependent in bioceramic materials. From this point of view nano-indentation has been proven to be a powerful technique for measuring mechanical properties at nano scale level [131]. Even though local mechanical properties of various biological tissues [124, 125] as well as bioceramic materials, such as compact sintered bioceramic powders of hydroxyapatite and hydroxyapatite/α-tricalcium phosphate [123, 126], bioceramic coatings [127, 128] and the interfacial properties between the coating and the substrate [129], and bioceramic composites [33, 130, 131], have been evaluated by well established nano-indentation technique, there is very little literature available focusing on the nano-mechanical evaluation of precipitates formed on bioceramic materials by *in vitro* incubation [132, 133]. However, since the nano indentation can be conducted at a relatively high resolution across the specimen and mineralized tissue such as bone which has a non-homogenous structure, the nano-indentation can be very significant for measuring the mechanical properties of very small selected regions [133].

In this research, the nano-indentation tests by trapezoid single indents were used to measure the reduced elastic modulus (E_r) and the hardness (H) of Bioglass®45S5 added hydroxyapatite bioceramic compositions aiming to understand, characterize, and compare the nano-mechanical properties after sintering and formation of an apatite layer on these substrates due to immersion in SBF solution for 4 weeks. In addition, cyclic trapezoid indentation (or

154

incremental load with periodic unloading) is used to identify the hardness and elastic modulus values for the bioceramic materials and apatite layers formed on them to obtain nano mechanical properties as a function of thickness. While single indentation is performed on different spots on the surface, the cyclic indentation is applied on same location applying incremental loadings. Therefore, this research will enlighten nano mechanical behaviors of newly formed bioceramic compositions by sintering different amounts of Bioglass®45S5 with hydroxyapatite at 1200℃ for 4 hours and the apatite layers formed on the surface of these compositions after 4 week immersion in SBF solution which will give an idea on whether the bioceramic compositions formed are suitable for biomedical applications.

7.2 Experimental Procedure

7.2.1 Bioceramic Syntheses

Pure Hydroxyapatite powder (Alfa Aesar) was mixed with 1, 10, and 25 wt% Bioglass®45S5 (US Biomaterials) in 250ml polyethylene bottles with zirconia balls (5µm in diameter) for 30 hours in order to have a homogenous mixture. The powder mixtures were dried at 80℃ for 24 hours and sieved to mechanically separate the particles, and manually uniaxially pressed with 105 MPa pressure in a die to achieve 12.7mm in diameter pellets. Compressed pellets were sintered at 1200ºC for 4 hours with a heating and cooling rate of 4ºC/minute and 10C/minute, respectively to prevent cracking.

7.2.2 In Vitro Bioactivity Tests in SBF

The preparation of SBF was adopted from the protocol developed by Kokubo et al [99] with few modifications. In order to prepare 1000 ml of SBF, first of all 700 ml of ion-exchanged and distilled water with a stirring bar into 1000 ml glass beaker is set on a hot plate covering with a watch glass maintaining the temperature at 36.5±2ºC under stirring. The first 8 order reagents given in Table 7.1 are dissolved in water one by one. The 9th and 10th order reagents are dissolved to adjust pH to 7.4. After the pH adjustment, the solution is cooled down to 20ºC and

155

enough ion-exchange and distilled water is added to complete the solution to 1000ml. A more detailed SBF preparation protocol is given in reference [97].

After the SBF solution preparation, the sintered bioceramic pellets were immersed in 25mL glass veils of SBF solution, and the glass veils placed on a rotating mixer in an incubator maintaining human body temperature at 37°C and pH 7.4 for various times. Also as a reference, Table 7.2 shows the nominal ion concentrations of SBF in comparison with those in human blood plasma. 1, 10, and 25wt% Bioglass®45S5 added hydroxyapatite bioceramic compositions were removed from the SBF solution and dried at room temperature after 4 weeks.

Table 7.1: Reagents used to prepare the SBF (pH7.40, 1L)

ORDER NO.	REAGENT	CONTENT
1	NaCl	7,996 g
2	$NaHCO_3$	0,350 g
3	KCl	0,224 g
4	$K_2HPO_4.3H_2O$	0,228 g
5	$MgCl_2.6H_2O$	0,305 g
6	1N-HCl	40 ml
7	$CaCl_2$	0,278 g
8	Na_2SO_4	0,071 g
9	$NH_2C(CH_2OH)_3$	6,057 g

Table 7.2: Nominal ion concentrations of SBF in comparison with those in human blood plasma [97].

Ion	Ion concentrations (mM)	
	Blood plasma	SBF
Na^+	142.0	142.0
K^+	5.0	5.0
Mg^{2+}	1.5	1.5
Ca^{2+}	2.5	2.5
Cl^-	103.0	147.8
$HCO3^-$	27.0	4.2
HPO_4^{2-}	1.0	1.0
SO_4^{2-}	0.5	0.5
pH	7.2 – 7.4	7.40

7.2.3 TF-XRD Analyses

The *in vitro* reaction layers formed after 4 weeks immersion in SBF solution were examined using a Philips PW 1830 Thin Film X-Ray Diffractometer with copper radiation of Kα. The samples were set at theta position of (incident beam) 0.5⁰ and fixed; the detector was scanned between 20 and 60⁰ with a step size of 0.02⁰ and 1 second dwell time.

7.2.4 SEM-EDX Analyses

The surface morphology of 1, 10, and 25 wt% Bioglass®45S5 added hydroxyapatite bioceramic pellets after sintering with and without polishing the surface and after immersion in SBF solution for 4 weeks were examined by Zeiss Supra 55VP, JEOL JSM – 6360 LV, and JEOL JSM 7000F Field Emission Scanning Electron Microscopes, respectively. In addition, the cross section views of these bioceramic samples were taken and coupled with EDX analyses for relative silicon, calcium, and phosphorus amounts to confirm apatite formation on their surfaces by using Zeiss Supra 55VP Scanning Electron Microscope.

7.2.5 Nano-Indentation Tests

As sintered polished 1, 10, and 25 wt. % Bioglass®45S5 added hydroxyapatite before bioactivity tests and the unpolished as sintered samples after bioactivity tests were mounted in the sample holder for nano-indentation studies. The nano-indentation tests were performed by using two different techniques: Trapezoidal single indents and cyclic loading indents. The single indentation was carried out at 10,000 µN and the cycling the load from 0 to 10,000 µN in 25 steps shown schematically in Figure 7.1 and 7.2, respectively.

Each indentation test with a trapezoidal load function is composed of a 5-second loading segment, a 2-second holding segment (at the maximum load), and a 5-second unloading segment. The reduced modulus is measured during the unloading segment by measuring the slope of the load-displacement curve at the early stages of unloading. All the nano indentation tests were run using a Hysitron Ubi 1 TriboIndenter® using a Berkovich tip that is a three sided pyramid with a total included angle of 142.3 degrees and a half angle of 65.35 degrees. The tip has an elastic modulus of 1140 GPa and a Poisson ratio of 0.07. Accurate measurement of the displacement of the tip during the indentation process allows for the calculation of the hardness and reduced elastic modulus of the bioceramic surfaces before and after bioactivity tests from a load–displacement curve. The values are calculated from the initial slope of the withdrawal (unloading) as mentioned in an early study [122]. A silica sample was used as the standard calibration material to determine the nano indenter TriboIndenter® Berkavich tip area function and instrument compliance as manufacturer's suggested method.

In cyclic loading indentation, the load function is series of trapezoidal loading cycles with a total of 25 cycles. It consists of a 1-second loading segment, a 1-second holding segment and a 1-second unloading segment. The maximum load for each holding segment is incrementally increased with each loading cycle with the first cycle having a maximum load of 0.25 µN and the final cycles having a maximum load of 10,000 µN. The final load of unloading segment in each cycle is slightly higher than the starting load of the loading segment in that cycle. The cyclic

158

loading indentation tests were run with the Hysitron Ubi 1 TriboIndenter® with a Berkovich tip. The main advantage of using cyclic indentation is since the tip can penetrates further with each indentation cycles, the measured reduced elastic modulus and hardness values can be plotted against displacement of the tip in the vertical direction (i.e. penetration depth). The resulting modulus and hardness vs. depth data, will however be different from data collected from single indents run at different loads, since in the case of cyclic loading, all indentation cycles are performed on the same location on samples and thus microscopic damage in the form of microcracks will inevitably skew the data to some extent while for single-indentation tests, each data point is collected from a different spot on the surface [106].

Both single and cyclic indentation tests were run at least at three different locations for each sample and the results are found to show similar trends.
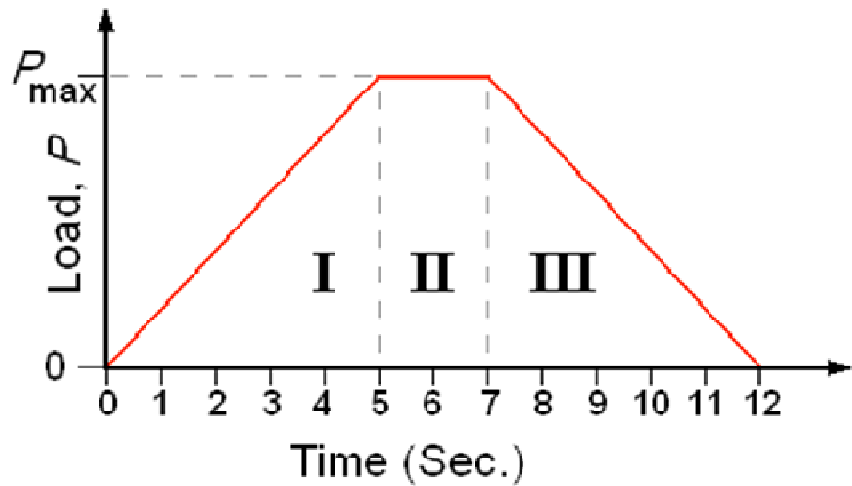
Figure 7.1: Load versus time plot for single indentation measurements
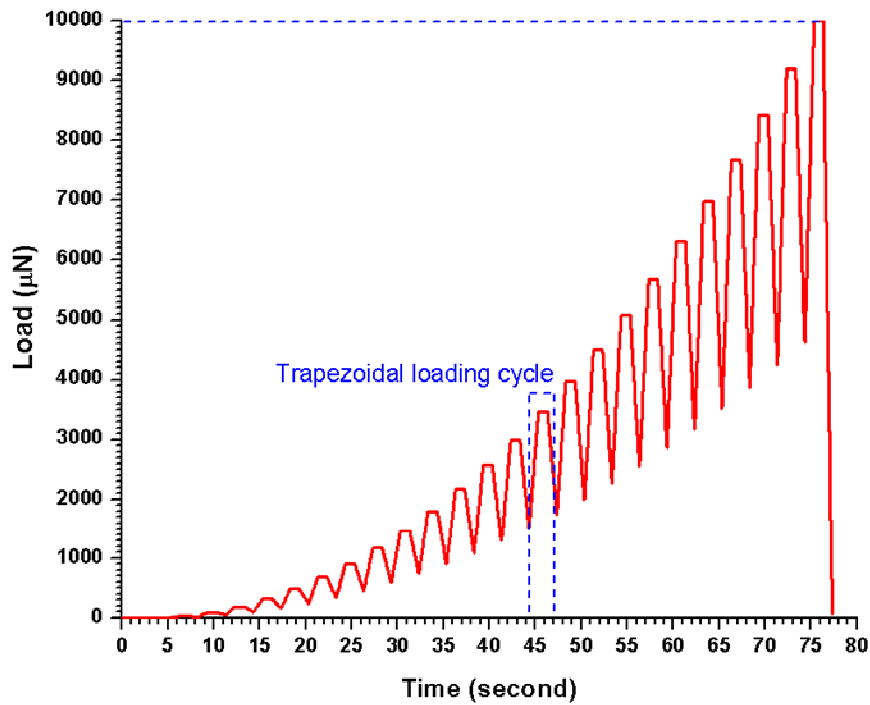
Figure 7.2: Load versus time plot for cyclic loading indentations

7.3 Results and Discussion

The X-ray diffraction pattern for all bioceramic compositions are shown in Figure 7.3. The crystalline and amorphous phases formed in these bioceramic compositions and their bioactivity dependence on these phases formed is discussed in detail in Chapter 4, 5, and 6. When up to 5 wt. % Bioglass®45S5 added to hydroxyapatite, the main phase of bioceramic compositions was a mixture of hydroxyapatite and β-TCP. On the other hand, when 10 and 25 wt. % Bioglass®45S5 were added they yielded new main crystalline phases namely $Ca_5(PO_4)_2SiO_4$ and $Na_3Ca_6(PO_4)_5$ in silicate matrices, respectively. The highest bioactivity has been achieved in 25 wt. % Bioglass®45S5 added hydroxyapatite bioceramic compositions.

160
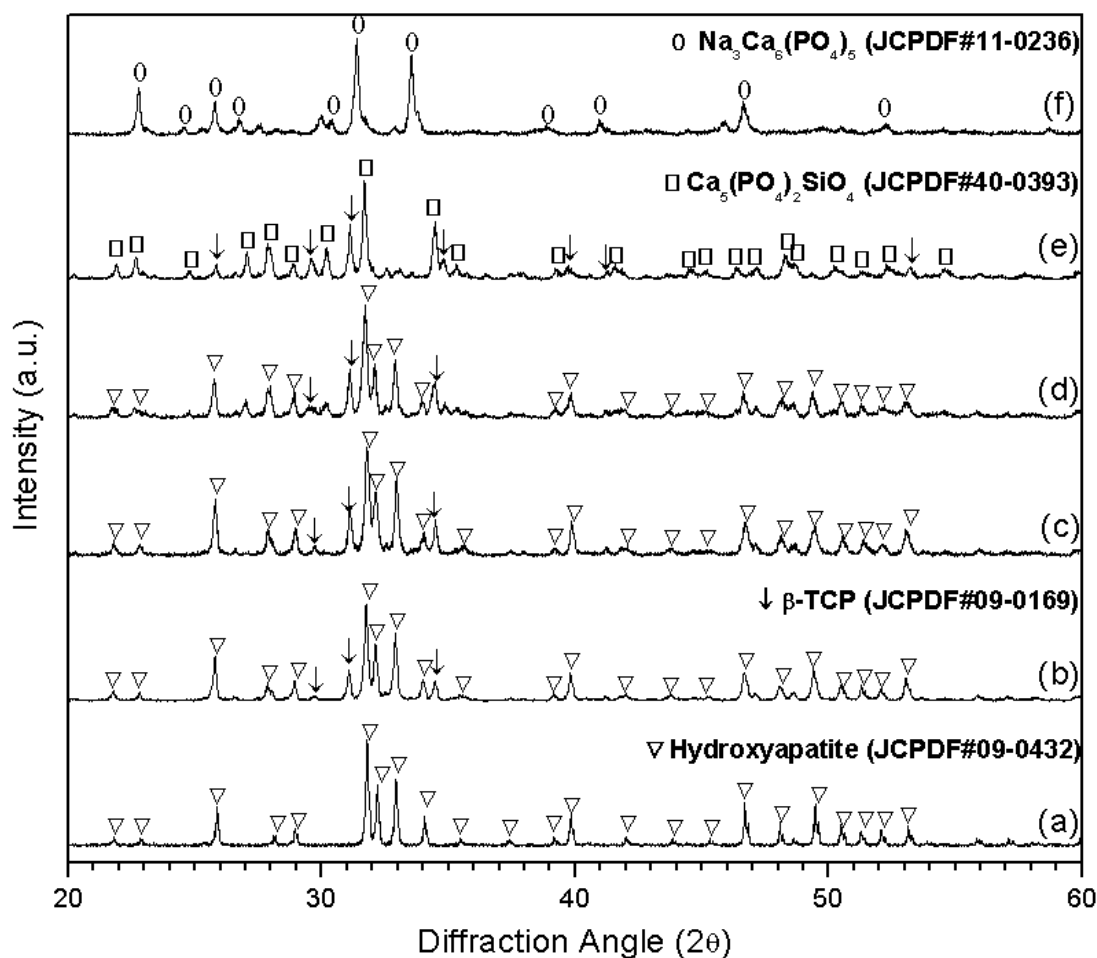
Figure 7.3: X-ray diffraction patterns for 5 different amounts of Bioglass®45S5 added hydroxyapatite bioceramic compositions after sintering at 1200°C for 4 hours.

The difference between 1, 2.5, and 5 wt. % Bioglass®45S5 added hydroxyapatite blends is the amount of β-TCP increases with increase in amount of Bioglass®45S5 addition; however, these three bioceramic compositions exhibit similar cell proliferation and differentiation as synthetic hydroxyapatite as discussed in detail in Chapter 4. Therefore, in this study 1 wt. % Bioglass®45S5 added hydroxyapatite bioceramic blend sintered at 1200°C for 4 hours is used as the base line, and its bioactivity is compared to 10 and 25 wt. % Bioglass®45S5 added hydroxyapatite bioceramic compositions which form very different compositions.

The microstructure of as sintered synthetic hydroxyapatite and 1, 10, and 25 wt. %

161

Bioglass®45S5 bioceramic samples without polishing are shown in Figure 7.4 (a-d). The as sintered synthetic hydroxyapatite SEM micrograph is illustrated to compare it with 1 wt. % Bioglass®45S5 composition. It can be seen that the surface microstructures of synthetic hydroxyapatite and 1 wt. % Bioglass®45S5 added bioceramics are very similar with a rough surface and a finer grain size about 1-3μm. The bioceramic composition with 10 wt. % Bioglass®45S5 exhibits rod shaped crystals of $Ca_5(PO_4)_2SiO_4$ embedded in an amorphous matrix. The bioceramic composition with 25 wt. % Bioglass®45S5 exhibits an equiaxed distribution of crystalline $Na_3Ca_6(PO_4)_5$ within an amorphous silicate matrix. As it is discussed earlier in Chapter 5, these amorphous silicate matrices play an important role in bioactivity of the bioceramic compositions along with the crystalline phases formed. The surface of these bioceramic compositions were polished in order to have a flat and relatively uniform surface prior to nano-indentation to ensure consistent measurements. Figure 7.5 (a-c) shows the surface of as sintered 1, 10, and 25 wt. % Bioglass®45S5 added hydroxyapatite polished bioceramic samples prior to nano-indentation tests.
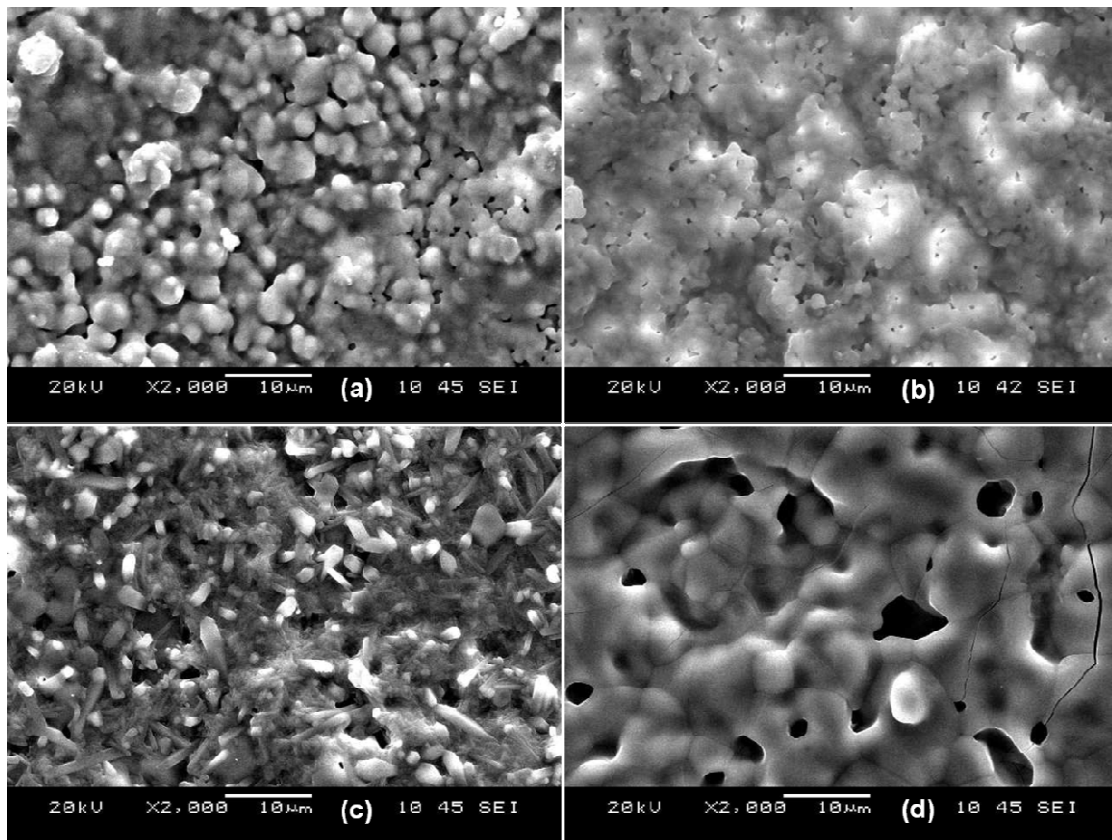
Figure 7.4: The SEM micrographs for the unpolished as sintered (a) synthetic hydroxyapatite and (b) 1 wt. %, (c) 10 wt. %, (d) 25 wt. % Bioglass®45S5 added hydroxyapatite bioceramics.
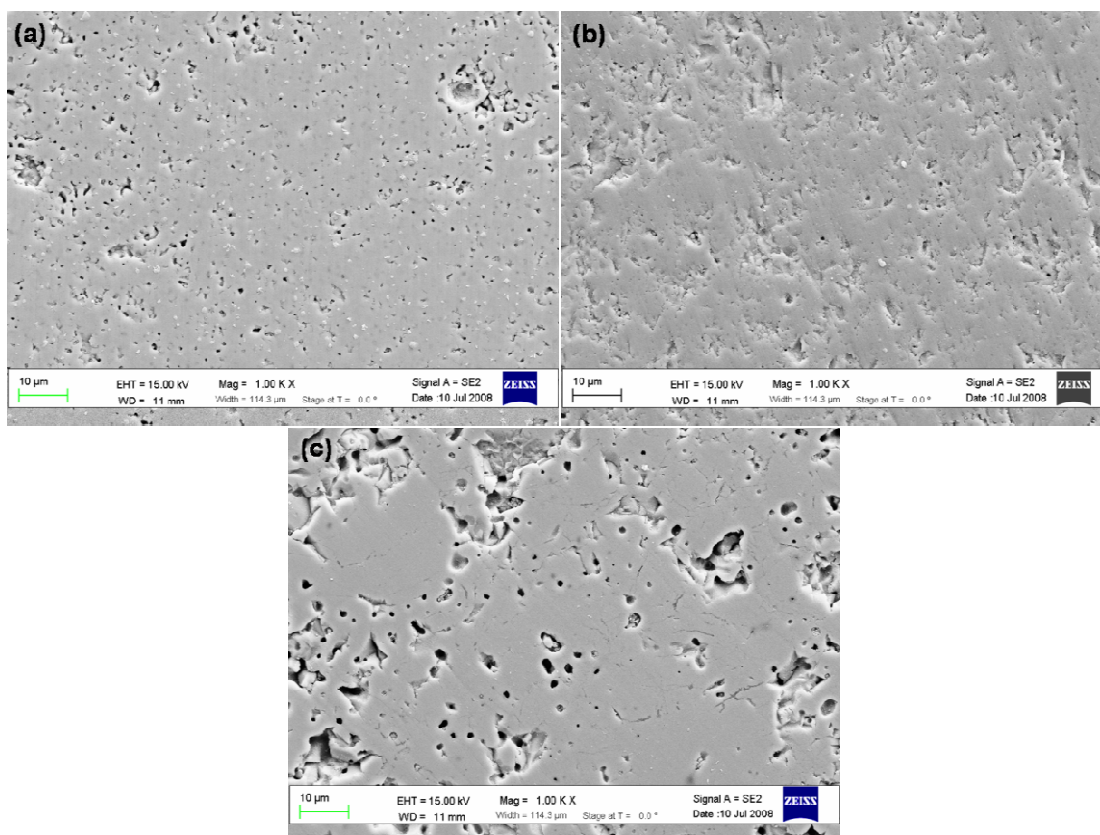
Figure 7.5: The SEM micrographs for polished as sintered (a) 1 wt. %, (b) 10 wt. %, and (c) 25 wt. % Bioglass®45S5 added hydroxyapatite bioceramics.

In order to identify the apatite formation on the surface of 1, 10, and 25 wt. % Bioglass®45S5 added bioceramic compositions, they were immersed in SBF solution. The relatively uniform apatite layer formation with minor differences is observed for all bioceramic compositions after 4 week immersion in SBF solution. The SEM micrographs for the apatite layers formed on these three bioceramic samples after 4 week immersion in SBF solution are shown in Figure 7.6 (a-c). These apatite layers are also identified by thin film X-ray diffraction analyses. The thin film X-ray diffraction patterns for 1, 10, and 25 wt. % Bioglass®45S5 added hydroxyapatite bioceramic compositions as sintered and after soaking in SBF solution for 4 weeks are shown in Figure 7.7 (a-f). It can be clearly seen that after 4 weeks immersion in SBF solution all bioceramic compositions formed a crystalline phase on their surfaces and these are identified as hydroxyapatite which is similar in composition and structure to bone apatite. The

164

mechanism of amorphous apatite formation and transformation into crystalline hydroxyl carbonated apatite on these bioceramic compositions are discussed in Chapter 6.
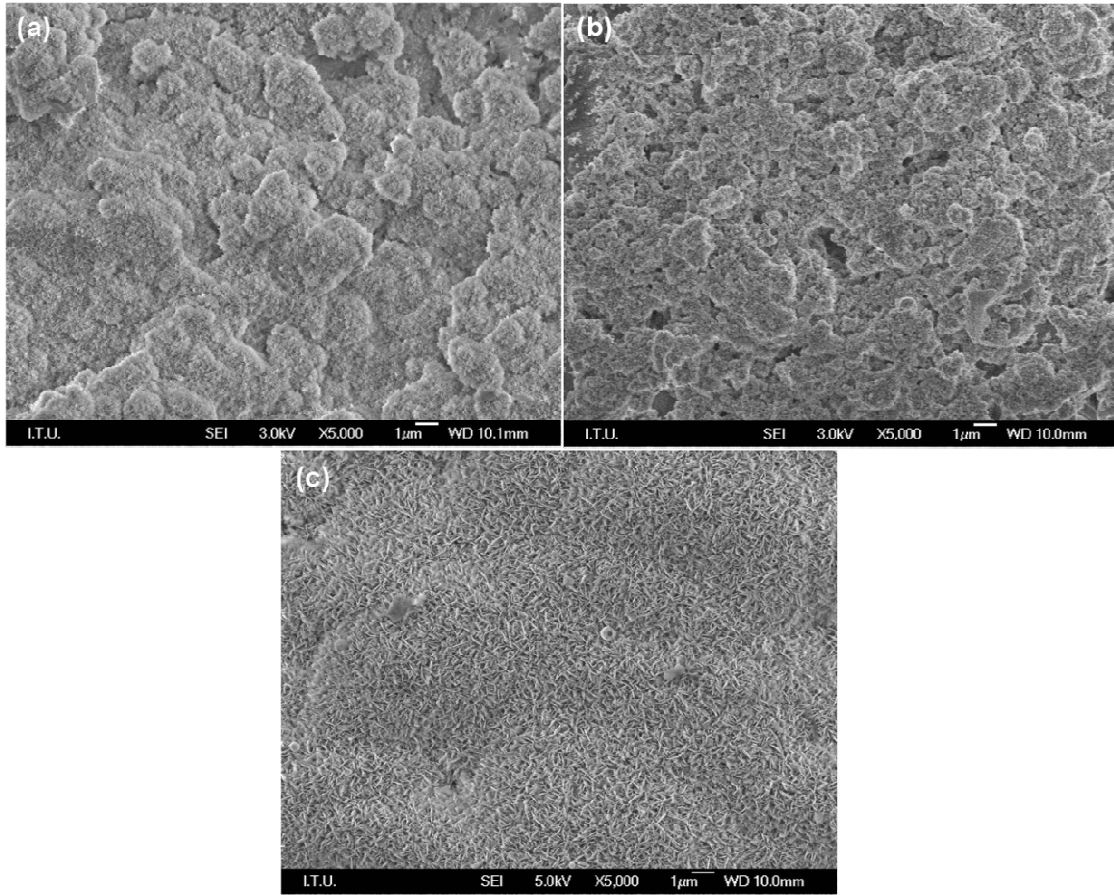
Figure 7.6: The SEM micrographs for apatite layers formed on (a) 1 wt. %, (b) 10 wt. %, and (c) 25 wt. % Bioglass®45S5after 4 week immersion in SBF solution.
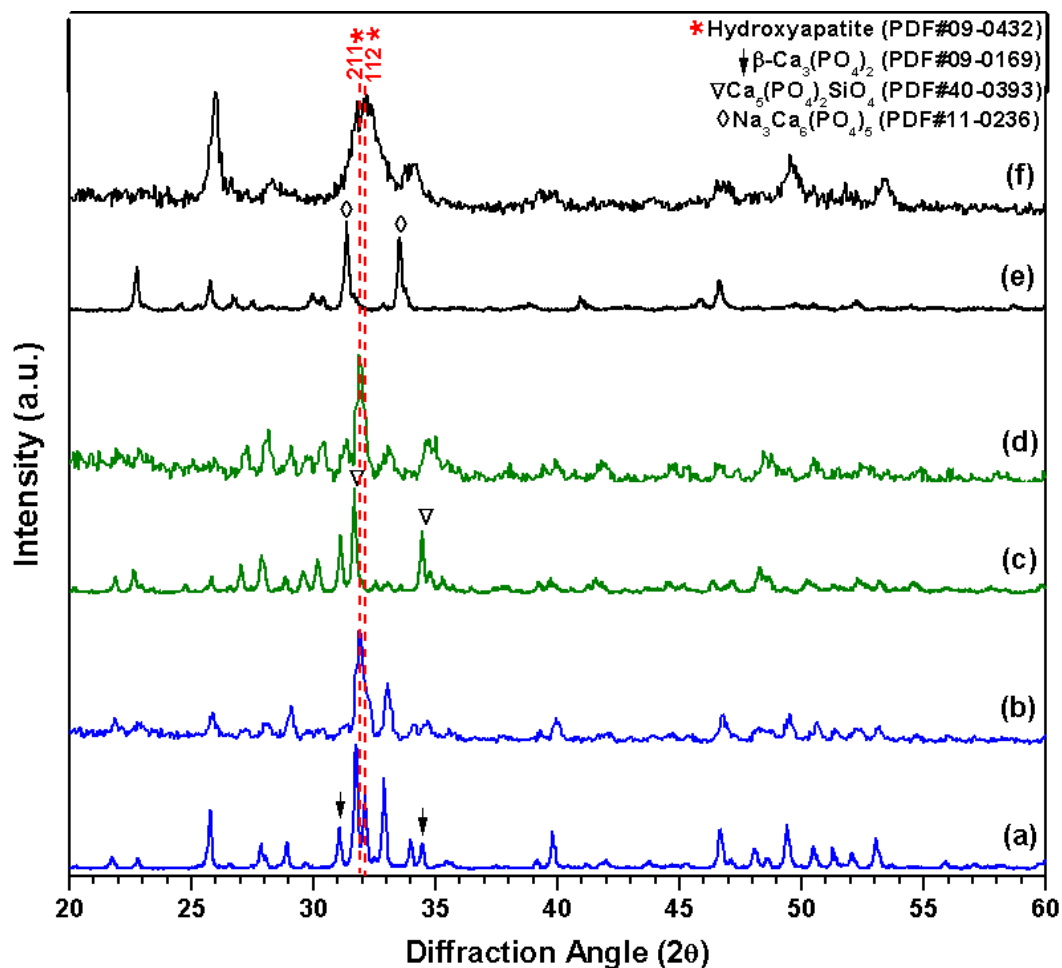
Figure 7.7: Thin film X-ray diffraction patterns of (a) as sintered 1 wt. % (b) 4 weeks after bioactivity test of 1 wt. %, (c) as sintered 10 wt. %, (d) 4 weeks after bioactivity test of 10 wt. %, (e) as sintered 5 wt. %, and (f) 4 weeks after bioactivity of 25 wt. % Bioglass®45S5 added hydroxyapatite compositions.

Finally, the cross section SEM micrographs of bioceramic compositions and related EDX analyses taken from substrates and top layers formed after immersion in SBF solution for 4 weeks are shown in Figure 7.8 (a-c) and 7.9 (a and b), respectively. The crystalline $Ca-P_2O_5$-rich layers formed in all three samples are homogeneous and continues, and completely covers the underlying silicate-rich layer that is also discussed in detailed in Chapter 6.
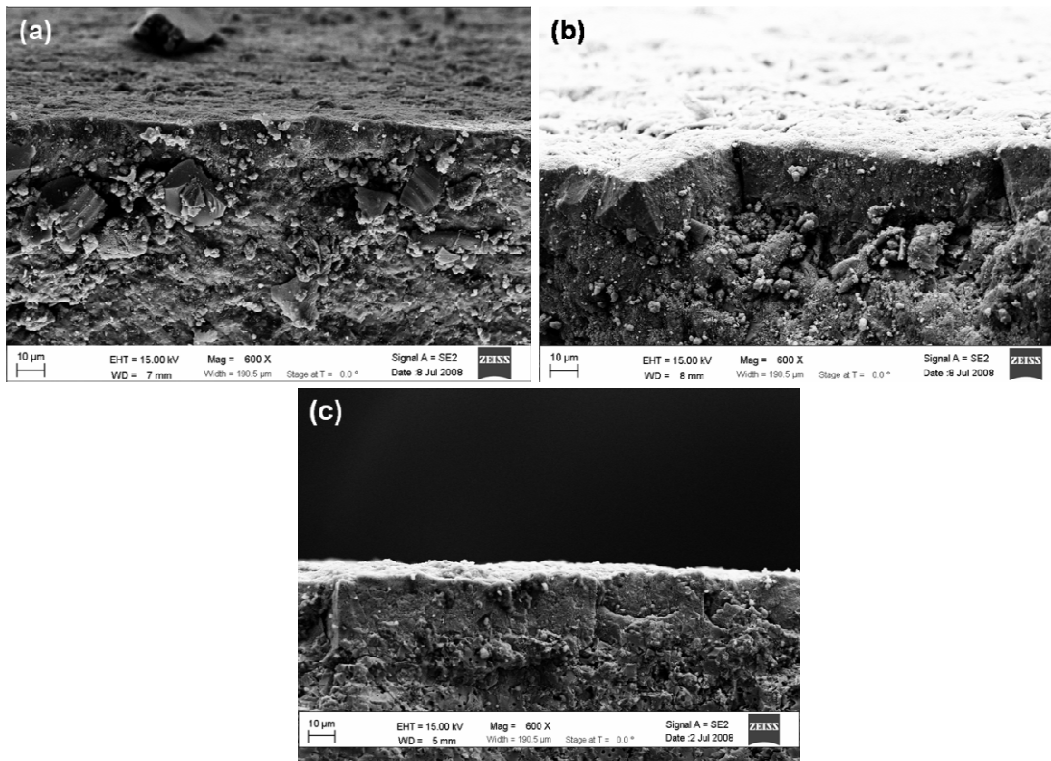
Figure 7.8: The cross section SEM micrographs of (a) 1 wt. %, (b) 10 wt. %, and (c) 25 wt. % Bioglass®45S5 added hydroxyapatite bioceramics after 4 week immersion in SBF solution.
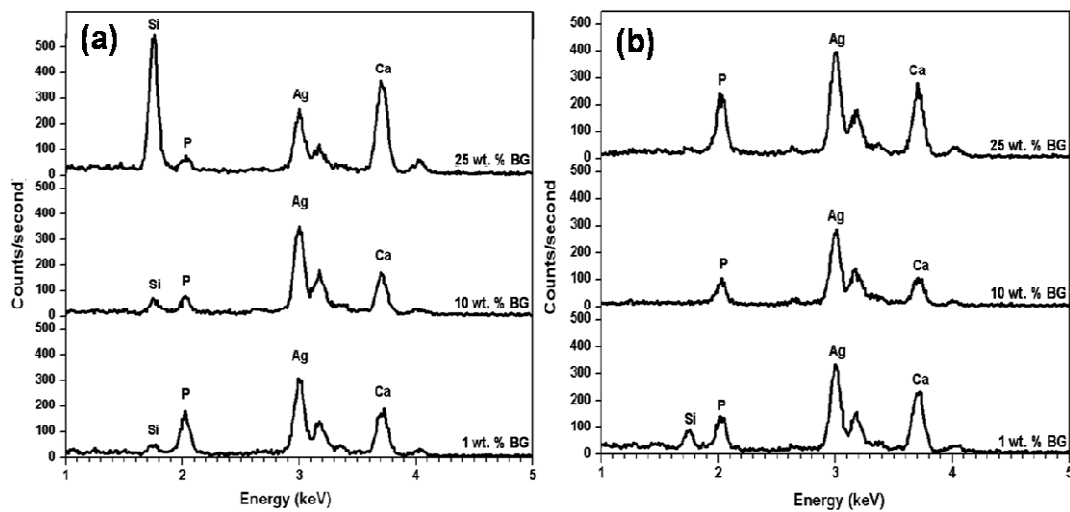
Figure 7.9: The EDS Analyses of (a) substrates and (b) apatite layers formed after 4 week immersion in SBF solution.

In order to investigate the influence of microstructure and phase composition on the nano-mechanical behavior of newly formed bioceramic compositions and identify nano-mechanical properties of apatite layers formed after immersion in SBF solution for 4 weeks single indentation and incremental load cyclic nano indentation tests were performed on 1, 10, and 25 wt. % Bioglass®45S5 added hydroxyapatite bioceramic samples and the apatite layers formed on them, respectively.

Figure 7.10 shows the typical load – displacement curves obtained for 1, 10, and 25 wt. % Bioglass®45S5 added hydroxyapatite compositions at a target load of 10,000μN. The loading curve was rather smooth for all three samples except for a small flaw at around the depth 250nm in 25 wt. % Bioglass added hydroxyapatite composition that may be caused by interference of the tip with porosity or a crack. The differences in hardness of the bioceramic samples are apparent from the differences in the depth attained at the particular load. For an applied load of 10,000μN, peak depths of about 250, 300, and 470nm were obtained for 1, 25, and 10 wt. % Bioglass®45S5 added hydroxyapatite compositions, respectively. Indicating that, 10 wt. % Bioglass®45S added bioceramic composition (3.4±2 GPa) is being the softest and 1 wt. % Bioglass®45S5 added hydroxyapatite sample (7.4±1 GPa) is the hardest. 25 wt. % Bioglass®45S5 added hydroxyapatite sample (5.1±2 GPa) has a lower hardness compared to 1 wt. % Bioglass®45S5 added bioceramic sample. These results are shown in Table 7.3. On the other hand the reduced elastic modulus values are not following the same trend. While 1 wt. % Bioglass®45S5 displays the highest reduced elastic modulus (123.7±1 GPa), 25 wt. % Bioglass®45S5G added hydroxyapatite bioceramic sample shows the lowest value (75±10), but closer to 10 wt. % Bioglass®45S5 added hydroxyapatite bioceramic sample (88.1±13 GPa).

168
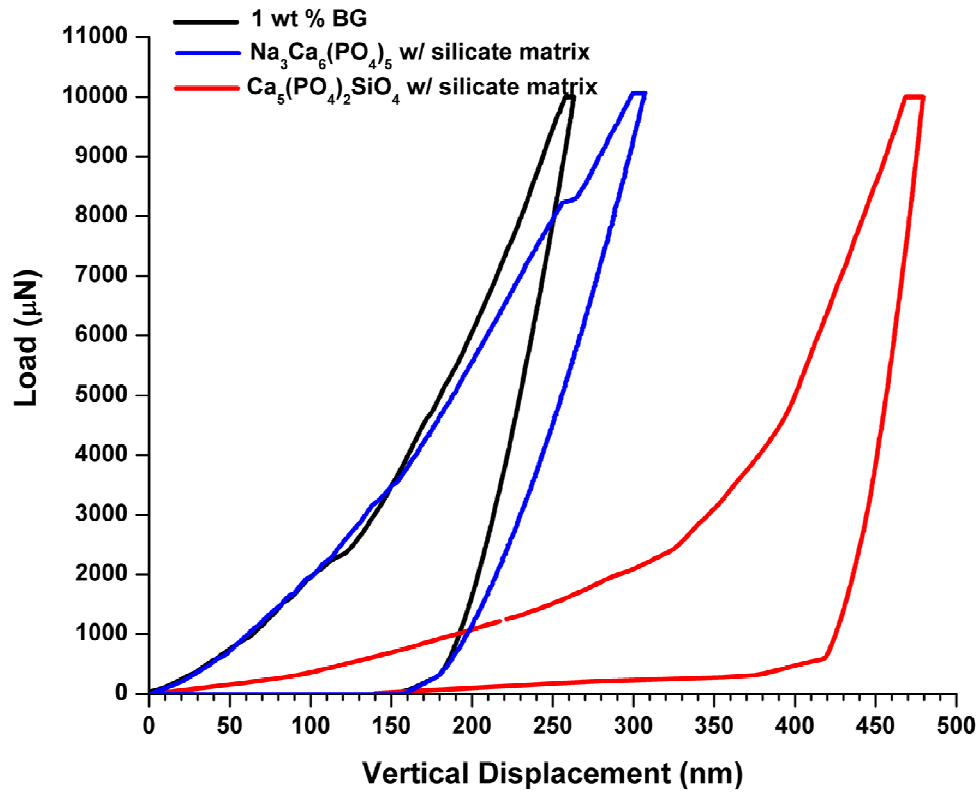
Figure 7.10: Representative load versus displacement curves for 1, 10, and 25 wt. % Bioglass®45S5 added hydroxyapatite bioceramic compositions.

Table 7.3: Reduced Elastic Modulus and Hardness values of 1 wt%, 10 wt. % ($Ca_6(PO_4)_2SiO_4$ in silicate matrix), and 25 wt. % ($Na_3Ca_6(PO_4)_5$ in silicate matrix) Bioglass®45S5 added hydroxyapatite bioceramics by single indentation.

Load (µN)	$Ca_5(PO_4)_2SiO_4$ in silicate matrix		$Na_3Ca_6(PO_4)_5$ in silicate matrix		1 wt. % Bioglass®45S5 added hydroxyapatite	
	E_r (GPa)	H (GPa)	E_r (GPa)	H (GPa)	E_r (GPa)	H (GPa)
10,000	88.1±13	3.4±2	75±10	5.1±2	123±6	7.4±1

The lower nano hardness values achieved for 10 and 25 wt. % Bioglass®45S5 added bioceramic compositions than 1 wt. % Bioglass®45S5 added hydroxyapatite composition can be attributed to the new phases formed in these bioceramic compositions. The amount of

169

amorphous glassy matrix formed in 10 and 25 wt. % Bioglass®45S5 added hydroxyapatite compositions is higher than 1 wt. % Bioglass®45S5 added hydroxyapatite bioceramic sample may also cause a drop in hardness since the amount of Bioglass®45S5 addition is much less. In addition, it has been reported that the amorphous zone supposedly has lower elastic modulus value than crystalline zone of plasma sprayed hydroxyapatite [179]. Relatively higher standard deviations found in 10 and 25 wt. % Bioglass®45S5 added hydroxyapatite samples may be due to inhomogeneous properties of local surface area caused by formation of two different phases after sintering [131].

It has been shown in early studies that the elastic modulus values for hydroxyapatite and tricalcium phosphate (TCP) are 80 – 110 GPa [5] and 18 – 24 GPa, respectively depending on the synthesis method and sintering conditions [123]. Kumar et al found that the nano hardness and reduced elastic modulus of synthetic hydroxyapatite is 6.76 and 122 GPa, respectively [123]. These values are closely matching with the reduced elastic modulus and hardness values of 1 wt. % Bioglass®45S5 added hydroxyapatite composition. In another study it has been shown that pure hydroxyapatite has higher nano hardness and elastic modulus values than β-TCP/hydroxyapatite bioceramics suggesting that containing a second phase (β-TCP) in hydroxyapatite caused a decrease in the nano hardness [131]. However, as the nano hardness and elastic modulus values of 1 wt. % Bioglass®45S5 added hydroxyapatite sample match with pure hydroxyapatite values reported earlier [123], the amount of β-TCP (≈25%) phase is not sufficient enough to effect nano mechanical properties of this bioceramic composition in this study.

The typical load – displacement curves obtained from apatite layers formed on 1, 10, and 25 wt. % Bioglass®45S5 added hydroxyapatite compositions after 4 week immersion in SBF solution at a target load of 10,000μN are shown in Figure 7.11. There are some differences in hardness of the bioceramic samples which can be interpreted from the differences in the depth attained at the particular load. For an applied load of 10,000μN, peak depths of about 300, 395,

and 450nm were obtained for apatite layers formed on 1, 25, and 10 wt. % Bioglass®45S5 added hydroxyapatite compositions, respectively. These results are also confirmed by the calculated hardness values for same hydroxyapatite – Bioglass®45S5 bioceramic samples which are given in Table 7.4. The apatite layers formed on all bioceramic samples show lower hardness values than the as sintered bioceramic samples indicating that the surface compositions have been subjected to a change which is another indication of a layer with a different composition than as sintered samples are formed. The apatite layers formed on 10 and 25 wt. % Bioglass®45S5G added hydroxyapatite bioceramic compositions show relatively closer calculated hardness values being 2.4±0.1 and 3.1±1 GPa, respectively. On the other hand, the hardness for 1 wt. % Bioglass®45S5 added hydroxyapatite bioceramic composition has a relatively higher hardness value of 4.9±1 GPa. The load versus displacement curves for 1 and 25 wt. % Bioglass®45S5 added hydroxyapatite bioceramic samples have formed steps during loading indicating that there have been many discontinuities probably due to inhomogeneous characteristics of the apatite layer. This is more severe in the case of 25 wt. % Bioglass®45S5 added hydroxyapatite bioceramic composition and 10 wt. % Bioglass added hydroxyapatite bioceramic sample did not show same tendency. The multi-asperity porous surface structure with higher thickness may cause greater scatter of the indenter penetration curve of 25 wt. % Bioglass®45S5 [133]. In addition, most biological tissue are highly inhomogeneous with high internal irregularities [134]. Since the structure of the apatite layer formed on surface of the bioceramic samples has similar structure to bone mineral [175], it is greatly expected to have abnormality in the curves. However, this is only very apparent in the case of 25 wt. % Bioglass®45S5 added hydroxyapatite bioceramic sample which indicates that surface microstructure of this bioceramic sample is closely matching with the bone mineral. On the other hand it is known from the SEM micrographs coupled with EDX and TF-XRD patterns of the sample surfaces and cross section views after immersion in SBF solution for 4 weeks that 10 wt. % Bioglass®45S5 added hydroxyapatite bioceramic sample also formed an apatite layer that has

171

approximately same thickness (20~µm) on its surface; however it is not as crystalline as 1 or 25 wt% Bioglass®45S5 added bioceramic compositions. Also, lower reduced elastic modulus can be attributed to the partially amorphous structure of the apatite formed on 10 wt. % Bioglass®45S5 added hydroxyapatite. Therefore, it can be understood that the amount of apatite forms and the structure of the layer (amorphous or crystalline) exhibit different nano mechanical behaviors; higher nano hardness and reduced elastic modulus and irregularities with thicker apatite layer and more crystallinity.
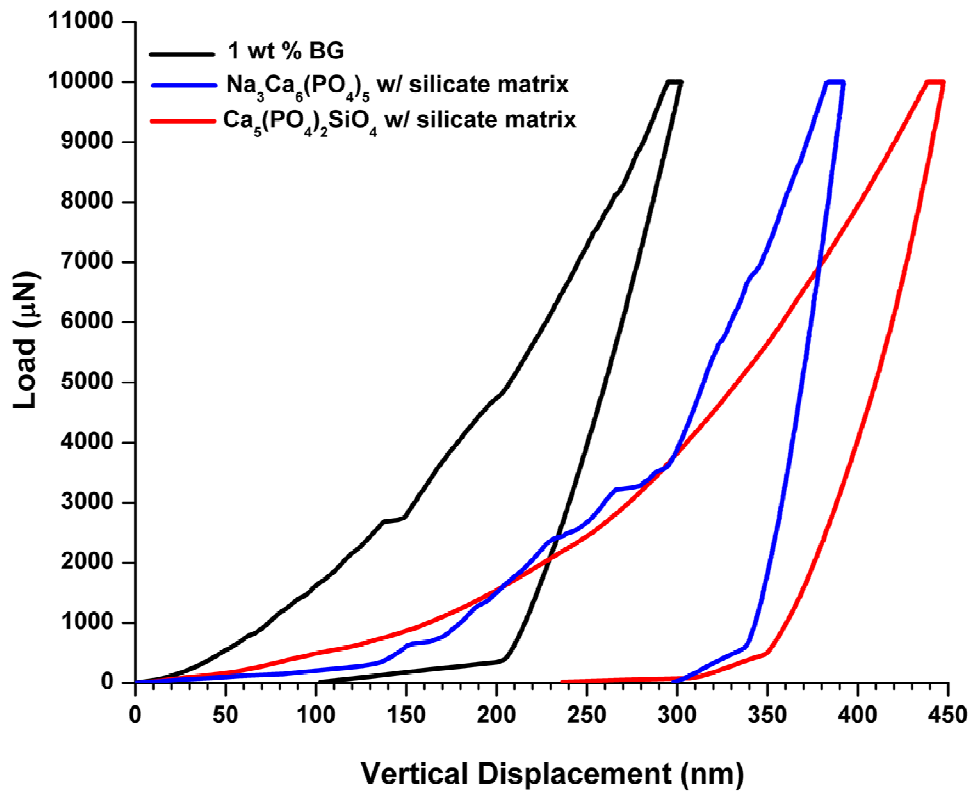
Figure 7.11: Representative load versus displacement curves for apatite layers formed on 1, 10, and 25 wt. % Bioglass®45S5 added hydroxyapatite bioceramic compositions after immersion in SBF solution for 4 weeks.

172

Table 7.4: Reduced Elastic Modulus and Hardness values of apatite layer formed after 4 week immersion of 1 wt%, 10 wt. % ($Ca_6(PO_4)_2SiO_4$ in silicate matrix), and 25 wt. % ($Na_3Ca_6(PO_4)_5$ in silicate matrix) Bioglass®45S5 added hydroxyapatite bioceramics in SBF solution by single indentation.

Load (µN)	$Ca_5(PO_4)_2SiO_4$ in silicate matrix		$Na_3Ca_6(PO_4)_5$ in silicate matrix		1 wt. % Bioglass®45S5 added HA	
	E_r (GPa)	H (GPa)	E_r (GPa)	H (GPa)	E_r (GPa)	H (GPa)
10,000	57.8±11	2.4±0.1	89±10	3.1±1	85.5±0.4	4.9±1

The depth dependence of the nano hardness and elastic modulus of sintered 1, 10, and 25 wt. % Bioglass®45S5 added hydroxyapatite bioceramic samples and apatite layers formed on them after 4 week immersion in SBF solution were measured by cyclic load indentation. Figures 7.12 and 7.13 show the elastic modulus and nano hardness versus cyclic loading curves for 1, 10, and 25 wt. % Bioglass®45S5 added hydroxyapatite bioceramics before and after 4 week immersion in SBF solution, respectively.

Scattered data points in hardness with increasing penetration depth at the early stages of the cyclic indentation measurements may rise from the unknown tip area function at low penetration depths. In addition this effect is more visible for the samples with higher irregularities on their surface. The relative hardness values for all bioceramic samples exhibit similar behavior to single indentation results. 1 wt. % Bioglass®45S5 added hydroxyapatite bioceramic composition have higher hardness (~6GPa) than 10 and 25 wt. % Bioglass®45S5 added hydroxyapatite bioceramic samples. Up to 150 nm depth 10 wt. % Bioglass added hydroxyapatite sample shows higher hardness than 25 wt. % Bioglass®45S5 added hydroxyapatite sample which can be attributed to higher Bioglass®45S5 amount. However, after 150 nm both bioceramic samples reach to a hardness of approximately 4.5GPa which is in standard deviation limits of single indentation results (Table 7.3) found for both bioceramic compositions. Also, the reduced elastic modulus values throughout the depth (up to 400nm) of all bioceramic samples are in agreement with the values obtained from single indentation (Table 7.3). Even though the

values are slightly smaller than the values found in single indentation, they all follow similar trend with 1 wt. % Bioglass®45S5 added hydroxyapatite sample having highest reduced elastic modulus and 25 wt. % Bioglass®45S5 added hydroxyapatite sample has the lowest.

Figure 7.13 illustrates the elastic modulus and nano hardness of apatite layers forms on the surface of 1, 10, and 25 wt. % Bioglass®45S5 added hydroxyapatite bioceramic samples up to 480 nm. It has been previously shown in cross section SEM micrographs of 1, 10, and 25 wt. % Bioglass®45S5 added hydroxyapatite bioceramic samples (Figure 7.8) that the apatite layer formed on their surfaces are about 10μm for 1 wt. % Bioglass®45S5 added hydroxyapatite and 20μm for 10 and 25 wt. % Bioglass®45S5 added hydroxyapatite bioceramic compositions indicating that the cyclic nano indentations performed on these apatite layers are still in the apatite layer and not affected by the substrate. The nano hardness and reduced elastic modulus values obtained from cyclic indentation has similar trend as the values obtained from single indentation with slightly lower values. The apatite layers formed on 1 and 25 wt. % Bioglass®45S5 added hydroxyapatite bioceramics exhibit similar results to each other and show higher values than the apatite layer formed on 10 wt. % Bioglass®45S5 added hydroxyapatite bioceramic sample which can be related to the partial crystal-partial amorphous nature of the apatite layer. An apparent linear increase in nano hardness of the apatite layer formed on 10 wt. % Bioglass®45S5 added hydroxyapatite bioceramic sample can be seen in Figure 7.13 indicating that the apatite layer is more amorphous closer to the surface. It is known that when a bioactive material is immersed in SBF solution initially an amorphous $CaO-P_2O_5$ rich layer forms which later crystallizes to hydroxyl carbonated apatite by incorporation of OH^- and CO_3^{2-} from surrounding [86], however this process is a continues process where the deposited $CaO-P_2O_5$ rich layer crystallizes there is still new $Ca-P_2O_5$ deposition is ongoing . Therefore, this process may cause a difference in the hardness and elastic modulus of apatite layers forming on the surface of bioceramic samples. Clearly, this is seen in much clear in the case of 10 wt. % Bioglass®45S5

174

added hydroxyapatite bioceramic composition. This process is also proven by the TF-XRD patterns up to 10 weeks of SBF immersion shown and discussed in Chapter 6 (Figure 6.11-6.13).

The reduced elastic modulus and hardness values from apatite layers formed on all three samples show that the values are very close to each other indicating that the apatite formed on their surfaces are very similar in structure. On the other hand, the least scattered data has been acquired from 25 wt. % Bioglass®45S5 added hydroxyapatite bioceramic sample shows that the apatite layer formed on this bioceramic sample is more uniform than the other two bioceramic samples. Nevertheless, al bioceramic samples show similar reduced elastic modulus and nano hardness throughout the penetration depth and the values are more or less same as the values achieved from single indentation values.
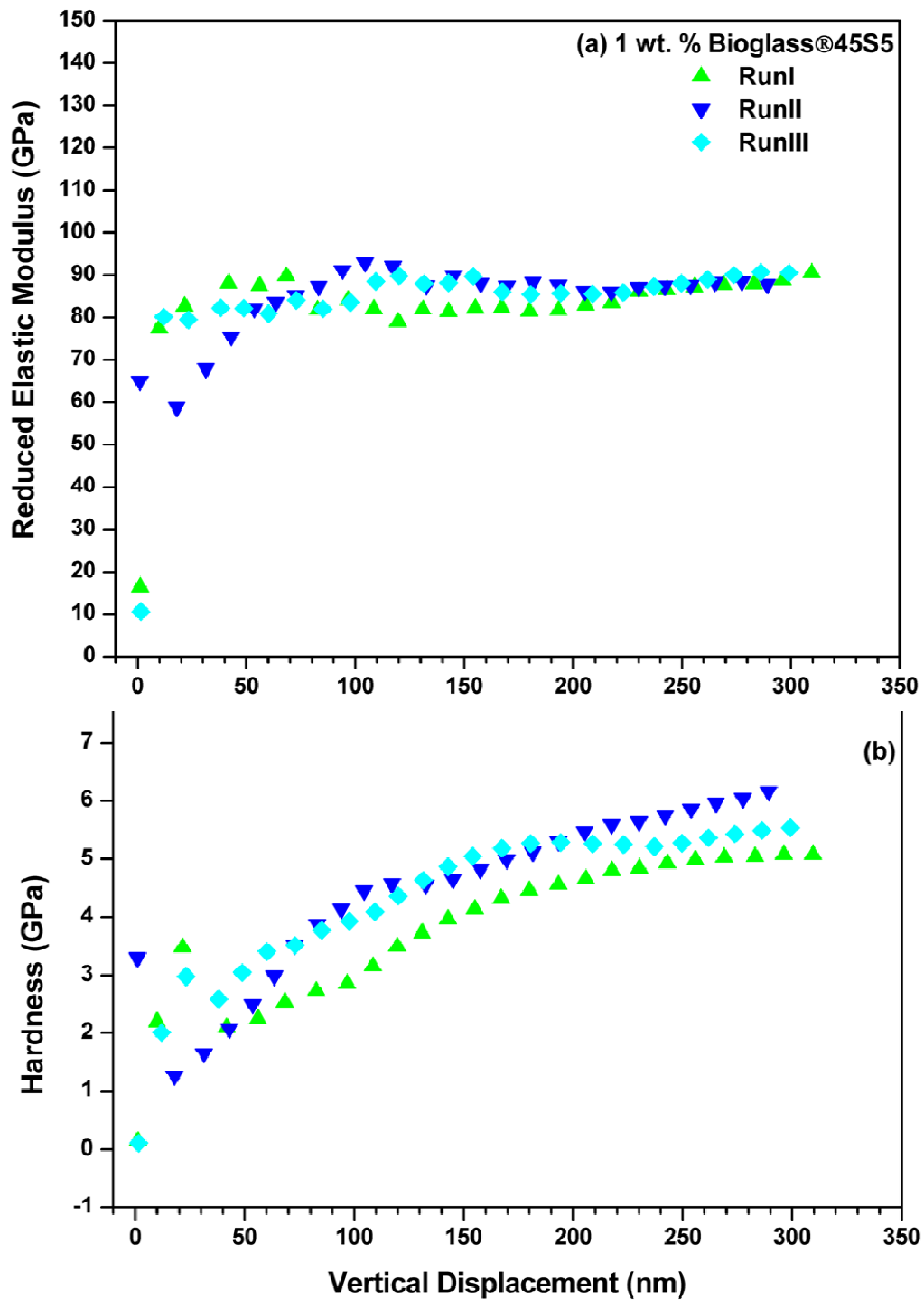
Figure 7.12: (a) Reduced elastic modulus and (b) Nano hardness versus vertical displacement curves attained by cyclic indentation of 1 wt. % Bioglass®45S5 added hydroxyapatite bioceramics sintered at 1200ºC for 4 hours after polishing.
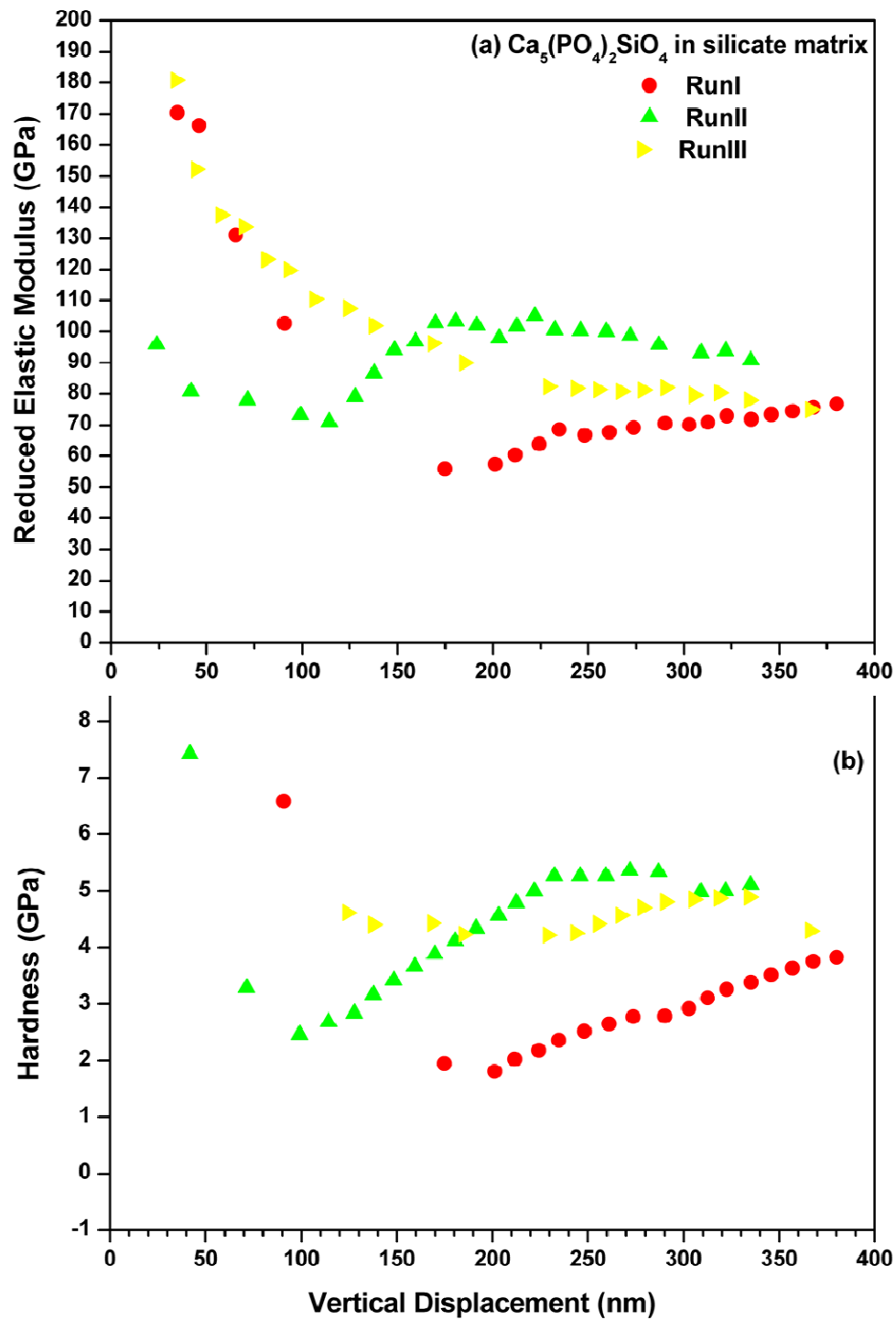
Figure 7.13: (a) Reduced elastic modulus and (b) Nano hardness versus vertical displacement curves attained by cyclic indentation of 10 wt. % Bioglass®45S5 added hydroxyapatite bioceramics sintered at 1200ºC for 4 hours after polishing.
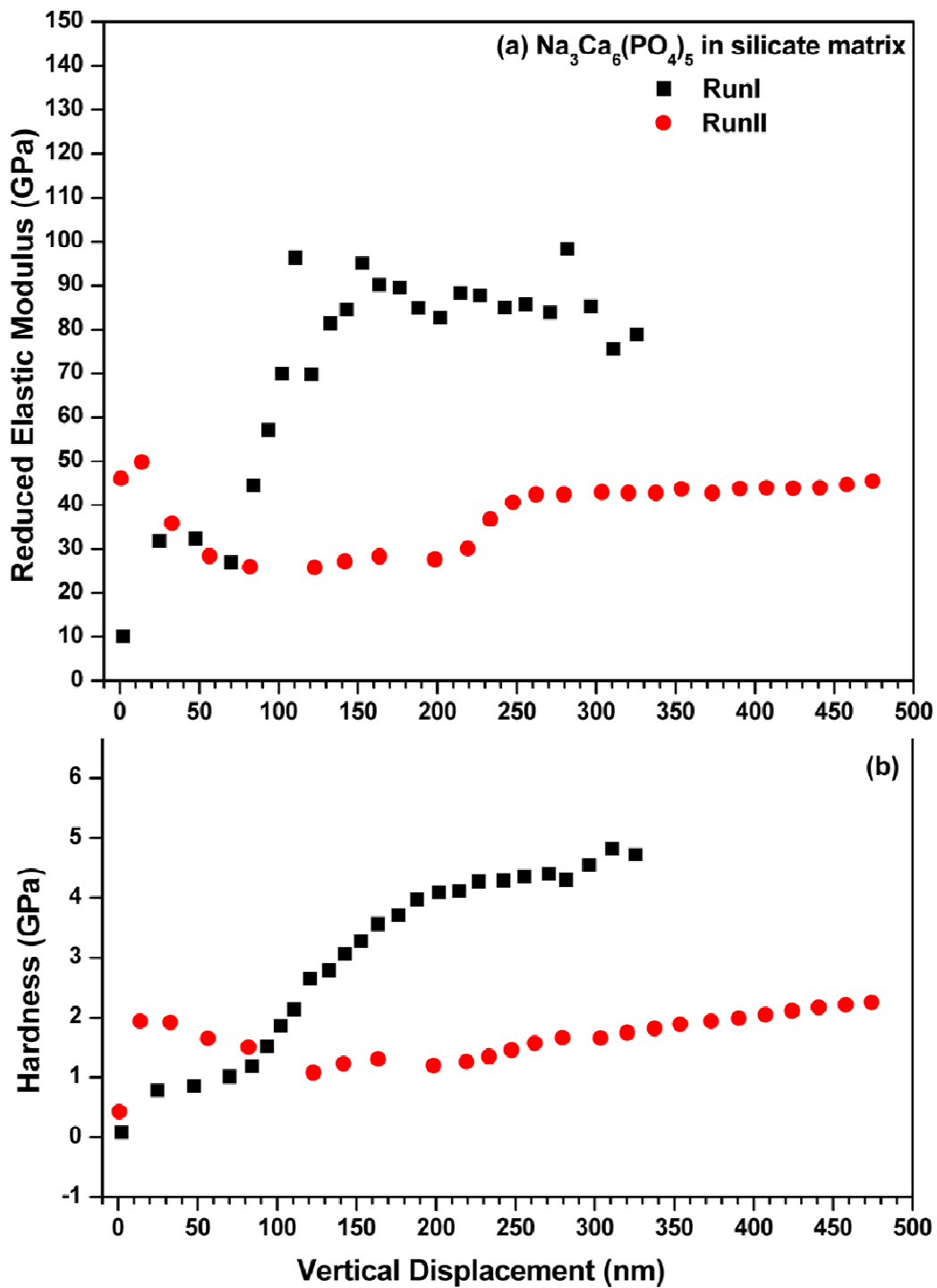
Figure 7.14: (a) Reduced elastic modulus and (b) Nano hardness versus vertical displacement curves attained by cyclic indentation of 25 wt. % Bioglass®45S5 added hydroxyapatite bioceramics sintered at 1200ºC for 4 hours after polishing.
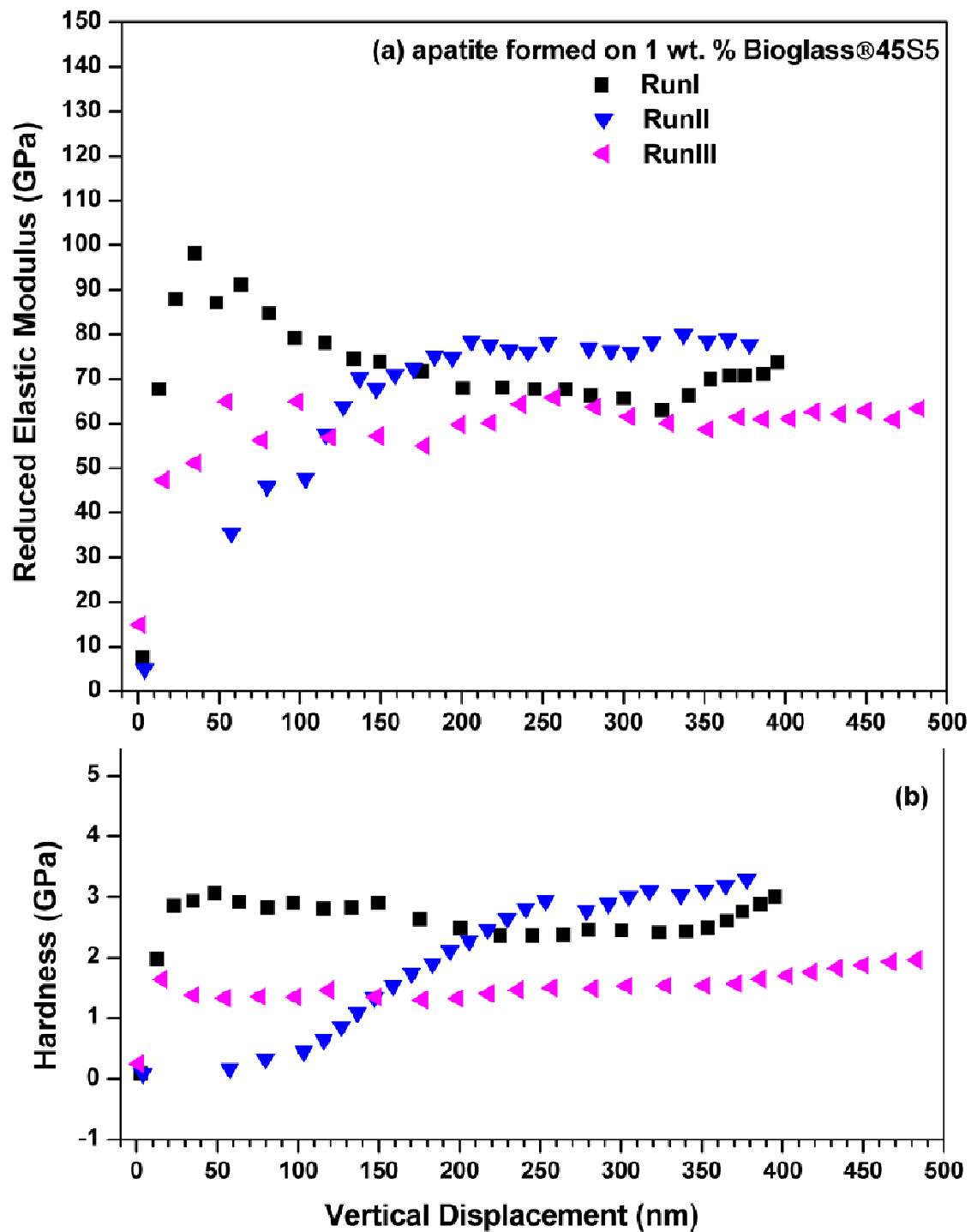
Figure 7.15: (a) Reduced elastic modulus and (b) Nano hardness versus vertical displacement curves attained by cyclic indentation of apatite layers formed on 1 wt. % Bioglass®45S5 added hydroxyapatite bioceramics after immersion in SBF solution for 4 weeks.
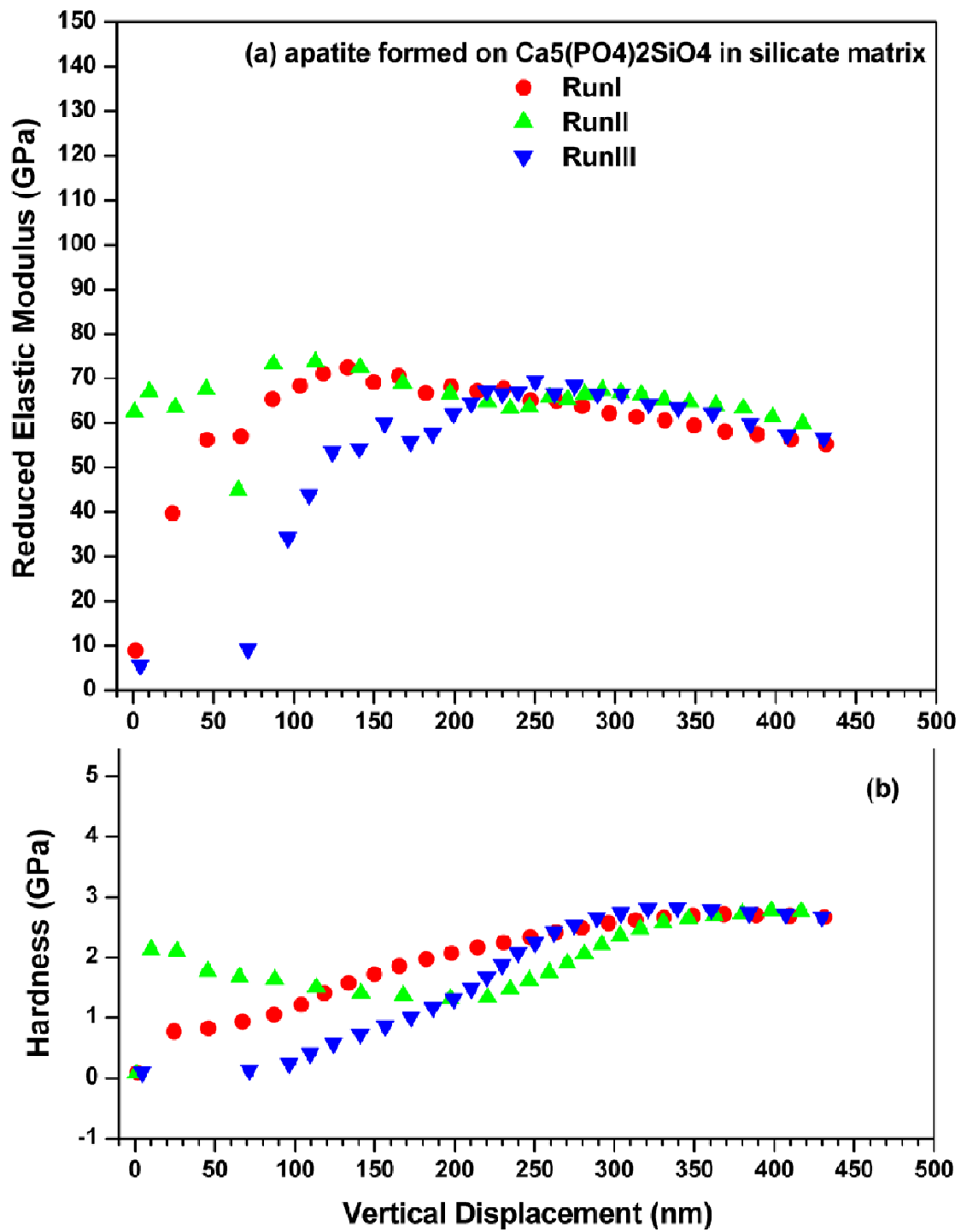
Figure 7.16: (a) Reduced elastic modulus and (b) Nano hardness versus vertical displacement curves attained by cyclic indentation of apatite layers formed on 10 wt. % Bioglass®45S5 added hydroxyapatite bioceramics after immersion in SBF solution for 4 weeks.
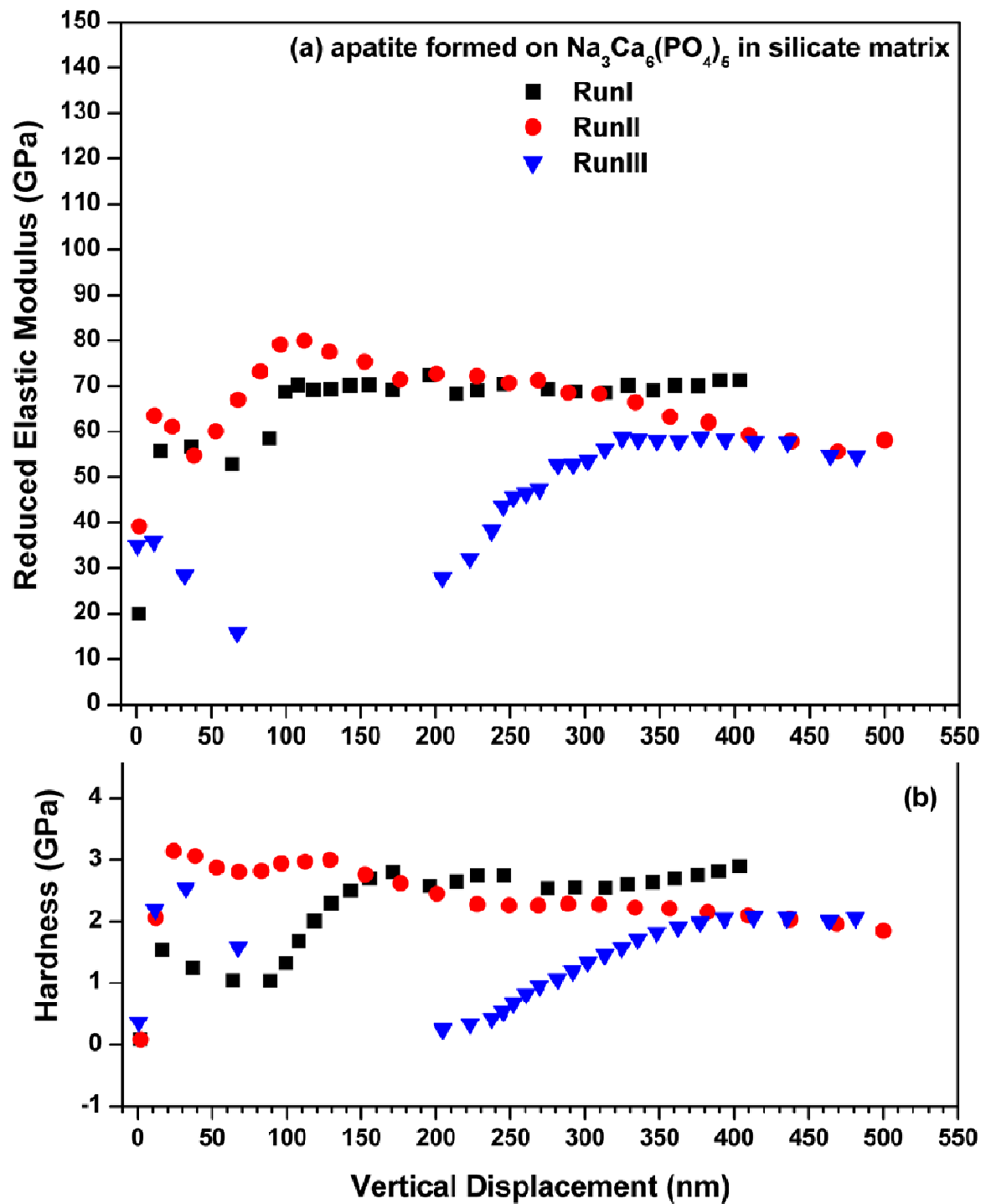
Figure 7.17: (a) Reduced elastic modulus and (b) Nano hardness versus vertical displacement curves attained by cyclic indentation of apatite layers formed on 25 wt. % Bioglass®45S5 added hydroxyapatite bioceramics after immersion in SBF solution for 4 weeks.

<u>7.4 Conclusion</u>

The new compositions formed by adding 10 and 25 wt. % Bioglass®45S5 addition to hydroxyapatite decreases both nano hardness and reduced elastic modulus of the samples. In order to identify the apatite formation on the surface of 1, 10, and 25 wt. % Bioglass®45S5 added bioceramic compositions, they were immersed in SBF solution. The relatively uniform apatite layer formation with minor differences is observed for all bioceramic compositions after 4 week immersion in SBF solution. After 4 weeks immersion in SBF solution 1 wt. % Bioglass®45S5 added hydroxyapatite bioceramic composition form an apatite layer approximately 10µm thick. In contrast, approximately 20µm thick apatite layer is achieved by 10 and 25 wt. % Bioglass®45S5 addition.

The influence of microstructure and phase composition on the nano-mechanical behavior of newly formed bioceramic compositions and identify nano-mechanical properties of apatite layers formed after immersion in SBF solution for 4 weeks single indentation and incremental load cyclic nano indentation tests were performed on 1, 10, and 25 wt. % Bioglass®45S5 added hydroxyapatite bioceramic samples and the apatite layers formed on them, respectively.

For an applied load of 10,000µN, peak depths of about 250, 300, and 470nm were obtained for 1, 25, and 10 wt. % Bioglass®45S5 added hydroxyapatite compositions, respectively. Indicating that, 10 wt. % Bioglass®45S added bioceramic composition (3.4±2 GPa) is being the softest and 1 wt. % Bioglass®45S5 added hydroxyapatite sample (7.4±1 GPa) is the hardest. 25 wt. % Bioglass®45S5 added hydroxyapatite sample (5.1±2 GPa) has a lower hardness compared to 1 wt. % Bioglass®45S5 added bioceramic sample. On the other hand the reduced elastic modulus values are not following the same trend. While 1 wt. % Bioglass®45S5 displays the highest reduced elastic modulus (123.7±1 GPa), 25 wt. % Bioglass®45S5G added hydroxyapatite bioceramic sample shows the lowest value (75±10), but closer to 10 wt. % Bioglass®45S5 added hydroxyapatite bioceramic sample (88.1±13 GPa). The lower nano hardness values achieved for 10 and 25 wt. % Bioglass®45S5 added bioceramic compositions

182

than 1 wt. % Bioglass®45S5 added hydroxyapatite composition can be attributed to bigger grain size attained in those bioceramic compositions.

For an applied load of 10,000µN, peak depths of about 300, 395, and 450nm were obtained for apatite layers formed on 1, 25, and 10 wt. % Bioglass®45S5 added hydroxyapatite compositions, respectively. The apatite layers formed on all bioceramic samples show lower hardness values than the as sintered bioceramic samples indicating that the surface compositions have been subjected to a change which is another indication of a layer with a different composition than as sintered samples are formed. The apatite layers formed on 10 and 25 wt. % Bioglass®45S5G added hydroxyapatite bioceramic compositions show relatively closer calculated hardness values being 2.4±0.1 and 3.1±1 GPa, respectively. On the other hand, the hardness for 1 wt. % Bioglass®45S5 added hydroxyapatite bioceramic composition has a relatively higher hardness value of 4.9±1 GPa. The load versus displacement curves for 1 and 25 wt. % Bioglass®45S5 added hydroxyapatite bioceramic samples have formed steps during loading indicating that there have been many discontinuities probably due to inhomogeneous characteristics of the apatite layer. Also, lower reduced elastic modulus can be attributed to the partially amorphous structure of the apatite formed on 10 wt. % Bioglass®45S5 added hydroxyapatite. Therefore, it can be understood that the amount of apatite forms and the structure of the layer (amorphous or crystalline) exhibit different nano mechanical behaviors; higher nano hardness and reduced elastic modulus and irregularities with thicker apatite layer and more crystallinity.

The nano hardness and reduced elastic modulus values obtained from cyclic indentation has similar trend as the values obtained from single indentation with slightly lower values. The apatite layers formed on 1 and 25 wt. % Bioglass®45S5 added hydroxyapatite bioceramics exhibit similar results to each other and show higher values than the apatite layer formed on 10 wt. % Bioglass®45S5 added hydroxyapatite bioceramic sample which can be related to the partial crystal-partial amorphous nature of the apatite layer. An apparent linear increase in nano

183

hardness of the apatite layer formed on 10 wt. % Bioglass®45S5 added hydroxyapatite bioceramic sample can be seen in Figure 7.13 indicating that the apatite layer is more amorphous closer to the surface. The reduced elastic modulus and hardness values of apatite layers formed on all three samples show that the values are very close to each other indicating that the apatite formed on their surfaces are very similar in structure. On the other hand, the least scattered data has been acquired from 25 wt. % Bioglass®45S5 added hydroxyapatite bioceramic sample shows that the apatite layer formed on this bioceramic sample is more uniform than the other two bioceramic samples. Nevertheless, all bioceramic samples show similar reduced elastic modulus and nano hardness throughout the penetration depth and the values are more or less same as the values achieved from single indentation values.

CHAPTER 8

EFFECT OF SILICATE ON FORMATION AND BIOACTIVITY OF SODIUM CALCIUM
PHOSPHATE BIOCERAMIC COMPOSITION

8.1 Introduction

Bioactive glasses are amorphous silicate based materials which are compatible with the human body and able to form a direct bond with bone. In addition, they can stimulate new bone growth while dissolving over time. It is well accepted that Bioglass® 45S5 is the most bioactive glass composition [20]. This bioglass composition has three key distinguishing properties from traditional glasses. It has less than 60 mol% SiO_2, high Na_2O and CaO content with some P_2O_5 in a Na_2O-SiO_2 matrix. It also has a high CaO/P_2O_5 ratio. These compositional features make the surface of the glass highly reactive when exposed to human body fluids [5] which results in rapid resorption. Hydroxyapatite is a calcium phosphate ceramic that is similar to natural bone mineral which also attains formation of an apatite layer at the interface with bone tissue [7-11]. The interactions occur in those bioactive ceramics that result in a calcium-phosphate rich hydroxyapatite layer on their surface with dissolution, precipitation, and ion exchange process followed by adsorption and incorporation of biological molecules. However, bone integrates with hydroxyapatite at slower rates than bioactive glasses [61]. Therefore, the low resorbability of hydroxyapatite is considered as a limiting factor because the bone conductive effect is restricted [67] and the bone formation produced by Bioglass®45S5 is greater than that produced by synthetic hydroxyapatite. Knowing this fact leads to seeking ways to improve bioactivity of hydroxyapatite. It has been shown by several researchers that bioglass addition to hydroxyapatite increases biological activities of hydroxyapatite [69, 70]. Another study demonstrated that

185

osteoblast like cells divide more rapidly on bioactive glass substrates than they do on synthetic hydroxyapatite [71].

The rate of bone formation correlates with the dissolution of the particles and the provision of soluble silica to the osteoblasts in the growing bone [66]. The rapid surface reactions happen in any silicate containing bioactive glasses allow the subsequent crystallization of apatite which further allows cell adhesion and collagen formation [59]. So, it is believed that silicon is an essential element in skeleton development due to its participation in early stage of bone calcification [60]. In previous chapters, it is confirmed that 25 wt. % Bioglass®45S5 added hydroxyapatite composition has a higher dissolution and apatite formation rate thus improved bone cell formation than the rest of the bioceramic compositions (1 – 10 wt. % Bioglass®45S5 addition). However, it has shown in earlier in this research that high amounts of Bioglass®45S5 addition yield different crystalline and amorphous phases. Therefore, even though it has been shown that even only silicate addition to hydroxyapatite significantly improves bioactivity of hydroxyapatite [61, 180-182], this chapter aimed to demonstrate that not only silicate amount but also the crystalline and amorphous phases formed by addition of different amounts of Bioglass®45S5 to hydroxyapatite and sintering at 1200ºC for 4 hours also play an important role in bioactivity behavior compared to both Bioglass®45S5 and synthetic hydroxyapatite.

8.2. Experimental Procedure

8.2.1 Powder preparation

The bioglass powder consisting of 45 wt. % SiO_2, 6 wt. % P_2O_5, 24.5 wt. % Na_2O, and 24.5 wt. % CaO also known as Bioglass®45S5 was acquired from US Biomaterials, the synthetic hydroxyapatite with a chemical composition of $Ca_{10}(PO_4)_6OH_2$ and CaO powder was acquired from Alfa Aesar, and P_2O_5 and SiO_2 powder was obtained from Sigma-Aldrich. As a Na_2O source baking soda ($NaHCO_3$) was used. Five different ceramic compositions were prepared. The first three are pure synthetic hydroxyapatite, pure Bioglass®45S5, and 25 wt. % Bioglass®45S5 added hydroxyapatite. The last two blends were prepared by blending *(i)* 25 wt. %

186

Bioglass®45S5 precursors with 75 wt. % hydroxyapatite and *(ii)* same amount of Bioglass®45S5 precursors used in *(i)* excluding SiO_2 added hydroxyapatite. These two blends were named as w/SiO_2 and w/oSiO_2 blends, respectively.

In order to demonstrate SiO_2 effect on formation of $Na_3Ca_6(PO_4)_5$ two additional blends were prepared by fixing hydroxyapatite, Na_2O, CaO, and P_2O_5 amount and decreasing SiO_2 amount by half (reduced 50 %) and quarter (reduced 25 %) with respect to 25 wt. % Bioglass®45S5 precursors added hydroxyapatite bioceramic blend and named as reduced SiO_2 glass I and reduced SiO_2 glass II, respectively. Table 8.1 shows the relative amounts of precursors used to prepare 25 wt. % Bioglass®45S5 added hydroxyapatite, reduced SiO_2 glass I, and reduced SiO_2 glass II blends.

Table 8.1: Relative amounts of precursors used to prepare 25 wt. % Bioglass®45S5 added hydroxyapatite, Reduced SiO_2 glass I, and Reduced SiO_2 glass II.

Sample Name	Precursor amount used in 10 g of blends (g)				
	SiO_2	Na_2O	CaO	P_2O_5	Hydroxyapatite $(Ca_{10}(PO_4)_6OH_2)$
25 wt. % Bioglass®45S5 precursors + Hydroxyapatite (w/SiO_2 blend)	1.125	0.6125	0.6125	0.15	7.5
Reduced SiO_2 Glass I	0.5625	0.6125	0.6125	0.15	7.5
Reduced SiO_2 Glass II	0.84375	0.6125	0.6125	0.15	7.5

8.2.2 Sample Preparation

The ceramic powders were mixed in proper amounts in 250 ml polyethylene bottles, and ball milled for 30 hours with acetone. After ball milling, the mixtures were dried in the oven at 80℃ for 24 hours. The dried powder mixtures were s ieved until the particles were separated. The powders were pressed uniaxially in a die with a diameter of 12.7 mm to a pressure 105 MPa. The sintering time and temperatures were chosen depending on the best feasible structure obtained. Pure hydroxyapatite, 25 wt. % Bioglass®45S5 added hydroxyapatite blend, and w/SiO_2 blend, reduced SiO_2 glass I, and reduced SiO_2 glass II are sintered at 1200℃ for 1 hour. Pure

Bioglass®45S5 and w/oSiO$_2$ blend were sintered at 900ºC for 2 and 1 hour, respectively. A heating rate of 4℃/minute and cooling rate of 10℃ /minute was used for all sintering processes.

8.2.3 XRD Analyses

X-ray diffraction studies of all sintered bioceramic samples after sintering and subsequent immersion in simulated body fluid (SBF) solution for 1 hour, 1 day, 1, 2, 3, and 4 weeks were examined using a Siemens Kristalloflex 810 Powder Diffractometer using CuKα radiation. The data were recorded over the 2θ range of 20-60° with a 0.02° step size and a count time of 1 second.

8.2.4 XANES Analyses

In order to compare the solubility of crystalline and amorphous phases formed in bioceramic samples with previous bioceramic compositions (1 – 25 wt. % Bioglass®45S5 added hydroxyapatite blends sintered at 1200ºC for 4 hours) discussed in Chapter 5, the P K-edge spectra were obtained at the Synchrotron Radiation Center in Madison, Wisconsin using the Double Crystal Monochromator Beamline (800 MeV). The spectra for the P K-edge for all bioceramic samples were acquired using two regions: *(1)* 2130-2165.25eV, step size: 0.5eV and *(2)* 2166-2200eV, step size: 2eV with a constant dwell time of 1 second/point. The backgrounds for all spectra were subtracted and plotted using arbitrary units. The peak intensities were measured by calculating the difference between the peak and the background. XANES spectra were recorded in fluorescence yield (FLY) mode.

8.2.5 SEM Analyses

The development of microstructures in the bioceramic samples after sintering and subsequent immersion in simulated body fluid for 1 and 4 weeks were investigated using Zeiss Supra 55VP scanning electron microscope operated in secondary electron mode.

8.2.6 Immersion in SBF Behavior Test

The preparation of SBF was adopted from the protocol developed by Kokubo et al [99] with few modifications. In order to prepare 1000 ml of SBF, first of all 700 ml of ion-exchanged

and distilled water with a stirring bar into 1000 ml glass beaker is set on a hot plate covering with a watch glass maintaining the temperature at 36.5±2°C under stirring. The first 8 order reagents given in Table 8.2 are dissolved in water one by one. The 9th and 10th order reagents are dissolved to adjust pH to 7.4. After the pH adjustment, the solution is cooled down to 20°C and enough ion-exchange and distilled water is added to complete the solution to 1000ml.

After the SBF solution preparation, the sintered bioceramic pellets were immersed in 25mL glass veils of SBF solution, and the glass veils placed on a rotating mixer in an incubator maintaining human body temperature at 37°C and pH 7.4 for various times. Table 8.3 is also given as a reference showing the nominal ion concentrations of SBF solution in comparison with those in human blood plasma. The immersed bioceramic samples were removed from the SBF solution and dried at room temperature after 1 hour, 1 day, 1, 2, 3, and 4 weeks.

Table 8.2: Reagents used to prepare the SBF (pH7.40, 1L) [97]

ORDER NO.	REAGENT	CONTENT
1	NaCl	7,996 g
2	$NaHCO_3$	0,350 g
3	KCl	0,224 g
4	$K_2HPO_4.3H_2O$	0,228 g
5	$MgCl_2.6H_2O$	0,305 g
6	1N-HCl	40 ml
7	$CaCl_2$	0,278 g
8	Na_2SO_4	0,071 g
9	$NH_2C(CH_2OH)_3$	6,057 g
10	1 N-HCl	0-5 ml

Table 8.3: Nominal ion concentrations of SBF in comparison with those in human blood plasma [97].

Ion	Ion concentrations (mM)	
	Blood plasma	SBF
Na^+	142.0	142.0
K^+	5.0	5.0
Mg^{2+}	1.5	1.5
Ca^{2+}	2.5	2.5
Cl^-	103.0	147.8
$HCO3^-$	27.0	4.2
HPO_4^{2-}	1.0	1.0
SO_4^{2-}	0.5	0.5
pH	7.2 – 7.4	7.40

8.3 Results and Discussion

In order to confirm that the bioactivity of hydroxyapatite – Bioglass®45S5 bioceramic compositions depend not only on the silicate amount but also on the newly formed compositions, a set of bioceramic samples were selected based on the previous studies. Figure 8.1 (a-e) shows the X-ray diffraction (XRD) patterns for pure synthetic hydroxyapatite sintered at 1200ºC for 1 hour (a), pure Bioglass®45S5 sintered at 900ºC for 2 hours (b), w/o SiO_2 blend sintered for 900ºC for 1 hour (c), 25 wt. % Bioglass®45S5 added hydroxyapatite sintered at 1200ºC for 1 hour (d), and w/ SiO_2 blend sintered at 1200ºC for 1 hour (e). The XRD pattern of hydroxyapatite after sintering at 1200ºC for 1 hour indicates that hydroxyapatite remains without any decomposition. The bioactivity of Bioglass®45S5 was shown to be insensitive to the level of crystallization with the 100% crystalline material exhibiting the same level of bioactivity as the amorphous material [65]. Sintering Bioglass®45S5 at 900ºC for 2 hours results in the transformation of amorphous Bioglass®45S5 to a crystalline $Na_2CaSi_3O_8$ in a silicate matrix. The XRD pattern for 25 wt. %

190

Bioglass®45S5 added hydroxyapatite bioceramic sample shows that even 1 hour of sintering at 1200ºC results in formation of $Na_3Ca_6(PO_4)_5$ crystalline phase. The same effect can be seen after sintering the blend of Bioglass®45S5 precursors (25 wt.% in total) with hydroxyapatite indicating that regardless of using the branded Bioglass®45S5 or its precursors, after sintering at 1200ºC for 1 hour, a crystalline $Na_3Ca_6(PO_4)_5$ phase is formed. The XRD pattern for bioceramic composition formed by addition of Bioglass®45S5 precursors (25 wt. % in total) to hydroxyapatite (w/SiO_2 blend) also exhibits a small amount of unreacted Na_2O. On the other hand, once the SiO_2 is excluded from the formulation (w/oSiO_2 blend) hydroxyapatite does not decompose. This finding shows that SiO_2 has an important role in formation of $Na_3Ca_6(PO_4)_5$ phase. In addition, in XRD spectrum of Bioglass®45S5 precursors excluding SiO_2 added to hydroxyapatite (w/o SiO_2 blend) shows no crystalline phase composed of Na indicating that it remains in amorphous phase. In order to show the effect of SiO_2 on formation of $Na_3Ca_6(PO_4)_5$ crystalline phase, two different glass – hydroxyapatite blends with reduced SiO_2 was prepared. 6.05 wt. % SiO_2 (reduced SiO_2 glass I) and 8.68 wt. % SiO_2 (reduced SiO_2 glass II) with other Bioglass®45S5 precursors were added to hydroxyapatite and sintered at 1200ºC for 1 hour, and compared to 11.25 wt. % SiO_2 (25 wt. % Bioglass®45S5 precursors added to 57 wt. % hydroxyapatite) composition. The relative amounts of precursors used to prepare 10 g. of these blends are given in Table 8.1. The XRD patterns for all three samples after sintering at 1200ºC for 1 hour are shown in Figure 8.2. The XRD spectra clearly show that even 8.68 wt. % SiO_2 addition (reduced SiO_2 glass II) is not sufficient enough to form $Na_3Ca_6(PO_4)_5$ crystalline phase. The outcome from this sintering study demonstrated that the SiO_2 addition together with the other precursors of Bioglass®45S5 which is indirectly Bioglass®45S5 addition to hydroxyapatite at 25 wt. % is essential to form $Na_3Ca_6(PO_4)_5$ crystalline phase. All the crystalline phases formed in the compositions mentioned above by specific sintering processes are listed in Table 8.4.
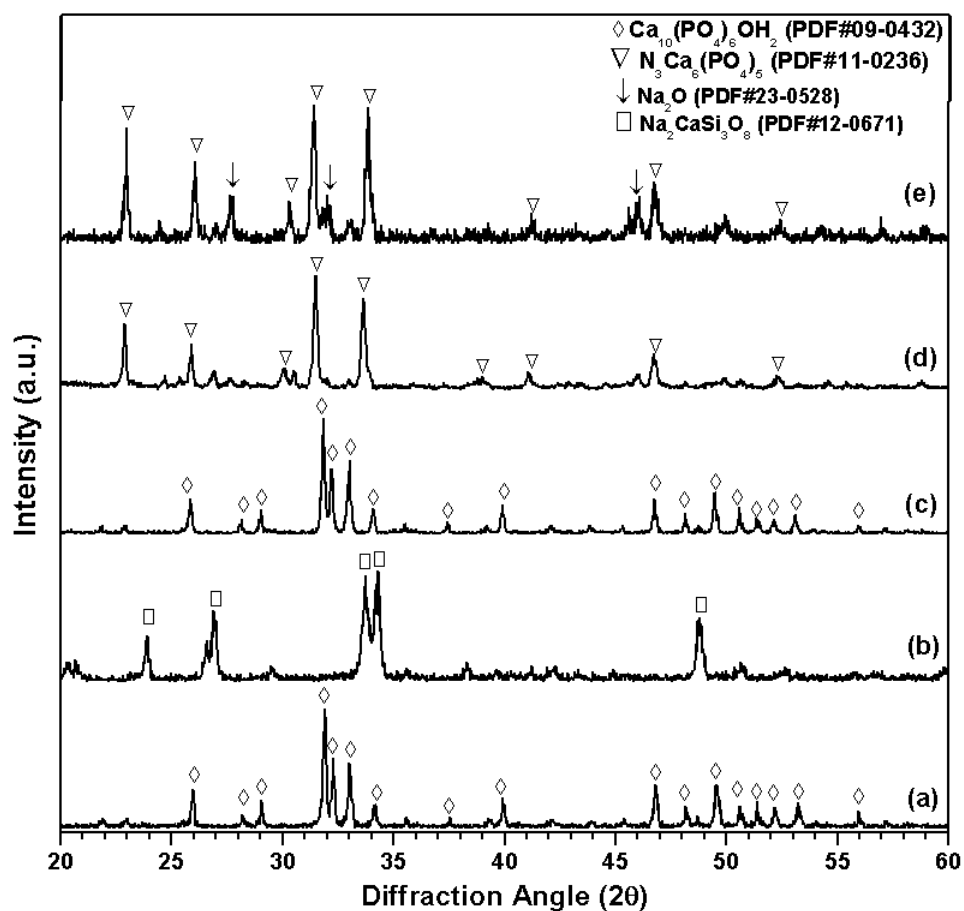
Figure 8.1: XRD patterns for (a) pure synthetic hydroxyapatite sintered at 1200°C for 1 hour, (b) pure Bioglass®45S5 sintered at 900°C for 2 hours, (c) w/oSiO$_2$ blend sintered for 900°C for 1 hour, (d) 25 wt. % Bioglass®45S5 added hydroxyapatite sintered at 1200°C for 1 hour, and (e) w/SiO$_2$ blend sintered at 1200°C for 1 hour.
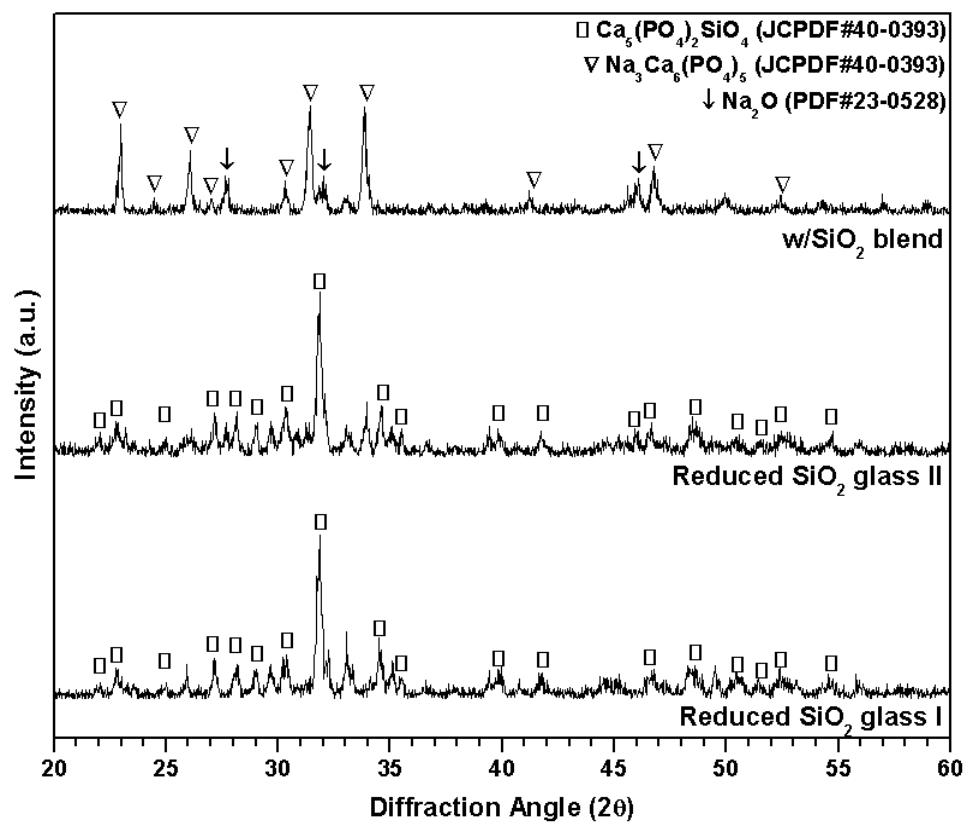
Figure 8.2: XRD pattern for reduced SiO$_2$ glass I (contains 6.05 wt. % SiO$_2$), reduced SiO$_2$ glass II (contains 8.68 wt. % SiO$_2$), and 25 wt. % Bioglass®45S5 precursors in total (contains 11.25 wt. % SiO2) added to hydroxyapatite sintered at 1200ºC for 1 hour.

Table 8.4: The crystalline phases formed in bioceramic samples

Sample	Sintering Process	Crystalline Phases Present
Hydroxyapatite	Sintered at 1200ºC for 1 hour	Synthetic Hydroxyapatite $(Ca_{10}(PO_4)_6OH_2)$
Bioglass®45S5	Sintered at 900ºC for 2hours	Sodium Calcium Silicate $(Na_2CaSi_3O_8)$
(w/oSiO_2 blend) Bioglass®45S5 precursors without SiO_2 + Hydroxyapatite	Sintered at 900ºC for 1 hour	Synthetic Hydroxyapatite $(Ca_{10}(PO_4)_6OH_2)$
Bioglass®45S5 (25 wt. %) + Hydroxyapatite (75 wt. %)	Sintered at 1200ºC for 1 hour	Sodium Calcium Phosphate $(Na_3Ca_6(PO_4)_5)$
(w/SiO_2 blend) Bioglass®45S5 precursors with SiO_2 (11.25 wt. %) + Hydroxyapatite	Sintered at 1200ºC for 1 hour	Sodium Calcium Phosphate $(Na_3Ca_6(PO_4)_5)$ + Sodium Oxide (Na_2O)
(Reduced SiO_2 glass I) Bioglass®45S5 precursors with SiO_2 (6.05 wt. % SiO_2) + Hydroxyapatite	Sintered at 1200ºC for 1 hour	Calcium Phosphate Silicate $(Ca_5(PO_4)_2SiO_4)$
(Reduced SiO_2 glass II) Bioglass®45S5 precursors with SiO_2 (8.68 wt. %) + Hydroxyapatite	Sintered at 1200ºC for 1 hour	Calcium Phosphate Silicate $(Ca_5(PO_4)_2SiO_4)$

In order to have a brief confirmation on solubility of these bioceramic samples, P K-edge XANES spectroscopy was carryout out. The acquired XANES spectra from bioceramic samples (Figure 8.3) are compared to the P K-edge XANES spectra of Bioglass®45S5 added hydroxyapatite bioceramic compositions (Figure 5.9) which are previously compared to model

compounds and discussed in Chapter 5. All bioceramic samples in Figure 8.3 and 5.9 show two post edge peaks at around 2163eV (peak **b**) and 2169eV (peak **c**) in addition to the main P K-edge peak **a** at around 2152eV. In addition to these 3 peaks except Bioglass®45S5 all bioceramic samples have a post-edge shoulder peak at around 2155eV, this shoulder corresponds to a transition of 1s phosphorus to the 3d calcium orbital. Therefore, these four peaks indicating that the P structure environment in all bioceramic samples and compositions are similar to each other and Bioglass®45S5 is not. This may be due to XRD patterns for all bioceramic compositions are identified as a type of calcium phosphate compound, Bioglass®45S5 shows a sodium calcium silicate ($Na_2CaSi_3O_8$) crystalline phase; however, it should still have P_2O_5 in its amorphous phase giving a rise to a P K-edge peak in XANES spectra. On the other hand, the post-edge shoulder peaks get less noticeable in 25 wt. % Bioglass®45S5 added hydroxyapatite and w/SiO_2 compositions indicating that fewer of these transitions are occurring (Figure 8.3). A closer observation of the post-edge shoulder peak at around 2155eV reveals that this shoulder is more defined for calcium phosphate compounds with decreasing solubility and increasing thermodynamic stability [156] as discussed earlier in Chapter 5. This post-edge shoulder peak in Figure 8.3 is more noticeable in hydroxyapatite and w/oSiO_2 bioceramic samples and none of the rest shows a distinctive post-edge peak. This can be explained as the stability of calcium phosphate phase increases, the spectral features such as post-edge shoulder peak may appear more distinctive [157]. However, it may not be suitable to compare the spectra for Bioglass®45S5 since it is not a calcium phosphate compound. Therefore, as the bioceramic samples with crystalline $Na_3Ca_6(PO_4)_5$ phase (25 wt. % Bioglass®45S5 added hydroxyapatite and w/SiO_2 blend) do not show a noticeable peak, these bioceramic samples are more soluble compared to hydroxyapatite and w/oSiO_2 bioceramic samples those have a crystalline hydroxyapatite ($Ca_{10}(PO_4)_6OH_2$) phase.
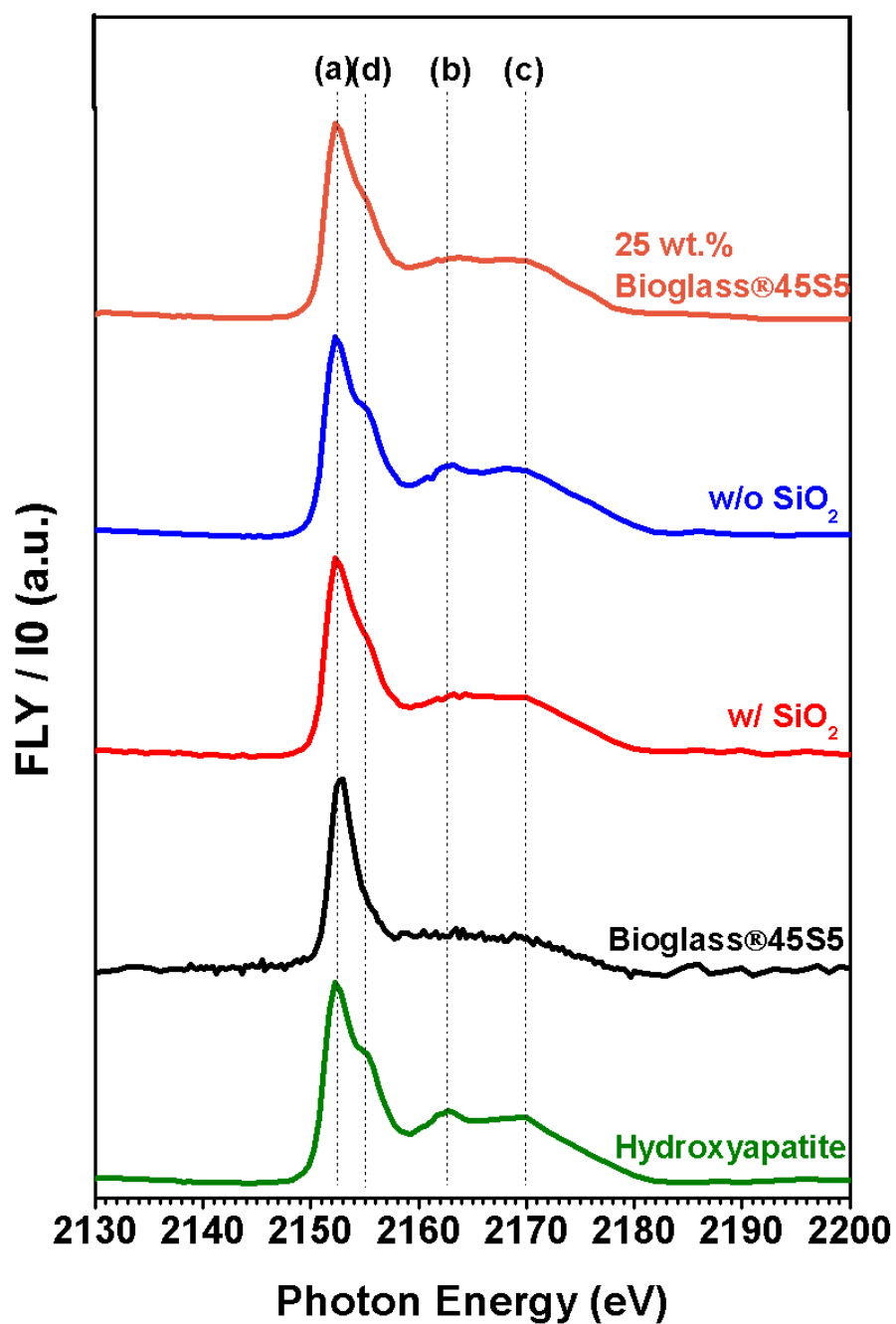
Figure 8.3: From bottom to top P K-edge XANES spectra for hydroxyapatite sintered at 1200ºC for 1 hour, Bioglass®45S5 sintered at 900ºC for 2 hours ($Na_2CaSi_3O_8$ crystalline phase), w/SiO$_2$ blend sintered for 1200ºC for 1 hour, w/oSiO$_2$ blend sintered at 900ºC for 1 hour, and 25 wt. % Bioglass®45S5 added hydroxyapatite sintered at 1200ºC for 1 hour.

The scanning electron microscope (SEM) micrographs for all bioceramic samples showing surface morphologies are given in Figure 8.4 (a-e). Sintered pure hydroxyapatite shows fine distribution of hydroxyapatite grains with a grain size of approximately 2-3 µm with almost no porosity (Figure 8.4(a)). Even though, a feasible sintered body is achieved after sintering Bioglass®45S5 at 900ºC for 2 hours, it can be clearly seen that the particles are not fully reacted and formed strong grain boundaries causing high porosity (Figure 8.4 (b)). The SEM micrograph of w/oSiO$_2$ blend shows that an amorphous layer is formed and covered the hydroxyapatite grains. The surface is very rough and inhomogeneous (Figure 8.4 (c)). Clear grain boundaries with similar grain size (~2 µm) is achieved with the bioceramic composition formed by blending 25 wt. % Bioglass®45S5 precursors with 75 wt. % hydroxyapatite compared (w/SiO$_2$ blend) to 25 wt. % Bioglass®45S5 added hydroxyapatite bioceramic sample (Figure 8.4 (d) and (e), respectively). Although similar crystalline phases are formed in these two bioceramic samples as shown by XRD analyses (Figure 8.1), the w/SiO$_2$ blend shows more distinctive grain boundaries on its surface. This may be due to having an additional Na$_2$O crystalline phase which may cause a decrease in the amount of amorphous glassy matrix which surrounds the grains; therefore a clear definition of grain boundaries occurs. In the case of 25 wt. % Bioglass®45S5 added hydroxyapatite composition due to having relatively larger amount of glassy matrix covers the grain boundaries to some extent. The presence of large SiO$_2$ content in w/SiO$_2$ and 25 wt. % Bioglass®45S5 added hydroxyapatite resulted in an increased porosity as evidences by the large number of micro-porosity (1-2 µm) dispersed throughout the surface compared to hydroxyapatite and w/SiO$_2$ blend.

197
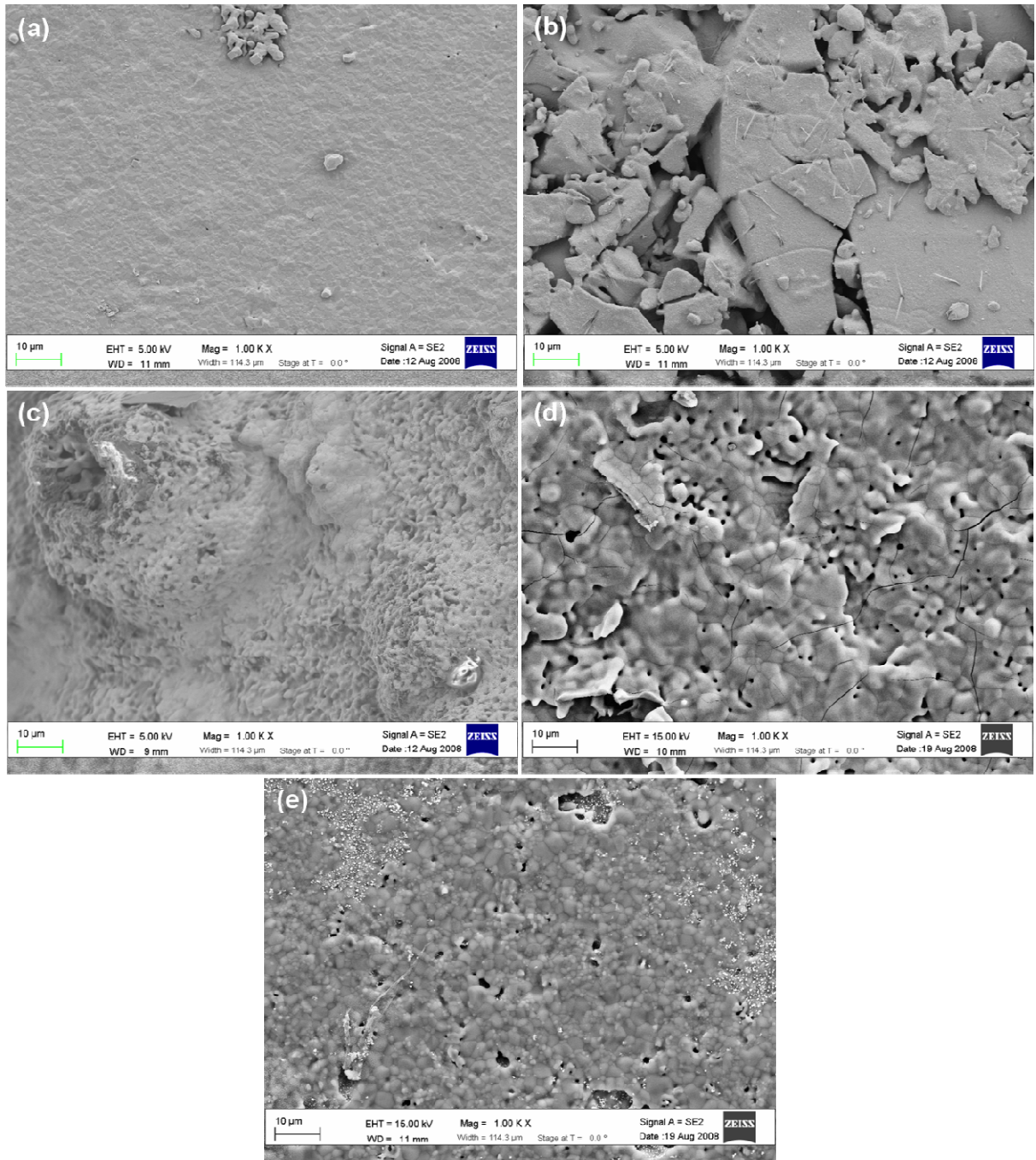
Figure 8.4: SEM micrographs for (a) hydroxyapatite sintered at 1200ºC for 1 hour, (b) Bioglass®45S5 sintered at 900ºC for 2 hours, (c) w/oSiO$_2$ blend sintered for 1200ºC for 1 hour, (d) 25 wt. % Bioglass®45S5 added hydroxyapatite sintered at 1200ºC for 1 hour, and (d) w/SiO$_2$ blend sintered at 900ºC for 1 hour.

X-ray diffraction (XRD) analyses were performed after 1 hour, 1 day, 1, 2, 3, and 4 weeks of immersion periods for all bioceramic samples to illustrate the rate and amount of apatite formation. Figure 8.5 shows the XRD patterns for pure hydroxyapatite sintered at 1200ºC for 1 hour after immersion in SBF from 1 day through 4 weeks. The XRD patterns do not show any noticeable changes through the immersion period may be caused by peak overlapping. Similar immersion behavior for w/oSiO$_2$ blend sintered at 900ºC for 1 hour is shown in Figure 8.6 demonstrates a slight change in the ratio of (211) and (210) peaks. This ratio is decreasing by immersion time indicating that even though an apatite layer with a preferred (210) orientation is forming, it is not sufficient enough to cover whole surface and causes a peak overlapping with hydroxyapatite main peaks. These two bioceramic samples which have a main hydroxyapatite crystalline phase after sintering display the weakest apatite formation ability among all the bioceramic samples. On the other hand, the XRD patterns for same time periods for Bioglass®45S5 sintered at 900ºC for 2 hours which formed a Na$_2$CaSi$_3$O$_8$ crystalline phase show traces of hydroxyapatite formation on its surface with a rise in (210) peak (Figure 8.7); however, the amount of apatite deposited on its surface is not thick enough to eliminate the XRD peaks coming from the substrate. Therefore, the apatite that forms on Bioglass®45S5 also has a preferred orientation of (210). The XRD patterns after immersion in SBF solution for 1 hour through 4 weeks for w/SiO$_2$ blend sintered at 1200ºC for 1 hour (Figure 8.8) shows that until 2 week immersion no significant change is observable; however, 3 weeks of immersion results in formation of a relatively thicker apatite deposition on the substrate as no specific peaks of Na$_3$Ca$_6$(PO$_4$)$_5$ or Na$_2$O are visible. Figure 8.9 shows the XRD patterns for 25 wt. % Bioglass®45S5 added hydroxyapatite after 1 hour, 1 day, 1, 2, 3, and 4 weeks of immersion in SBF solution. There is no doubt this composition shows the best apatite formation behavior among all bioceramic compositions as it is completely covered with a layer of apatite with no Na$_3$Ca$_6$(PO$_4$)$_5$ crystalline phase observable even after 1 week of immersion. Even though 25 wt. % Bioglass®45S5 added hydroxyapatite and w/SiO$_2$ blend samples have same main crystalline

199

phase, they exhibit different apatite formation behavior. The small amount of Na_2O crystalline phase present in the ceramic formed when 25 wt. % Bioglass®45S5 precursors were added to hydroxyapatite bioceramic may have prevented the incorporation of the sodium cations in the amorphous silicate glassy matrix that occurs in the case of 25 wt. % Bioglass®45S5 added hydroxyapatite bioceramic composition. However, further analyses such as XANES spectroscopy should be employed to confirm this assumption. Nevertheless, these results indicate that a faster dissolution in SBF solution of 25 wt. % Bioglass®45S5 added hydroxyapatite bioceramic composition sintered at 1200ºC for 1 hour followed by a rapid precipitation of a bone like apatite layer on its surface occurs even after 1 week immersion. These findings suggest that even though Bioglass®45S5 which has the highest amount of SiO_2, 25 wt. % Bioglass®45S5 added hydroxyapatite bioceramic composition with a crystalline phase of $Na_3Ca_6(PO_4)_5$ in a sodium silicate amorphous glassy matrix exhibits a higher bioactivity which can be attributed to the higher bioactivity of combination of the crystalline $Na_3Ca_6(PO_4)_5$ phase and the amorphous glassy matrix.
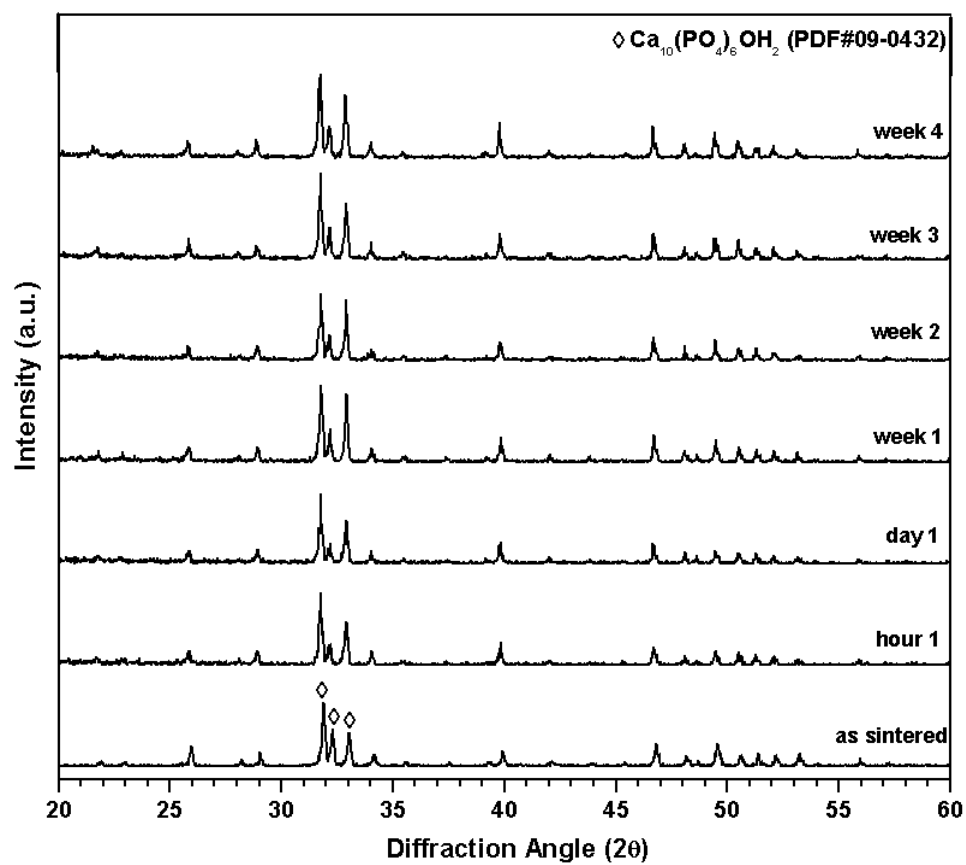
Figure 8.5: XRD patterns of hydroxyapatite sintered at 1200ºC for 1 hour after 1 hour, 1 day, 1, 2, 4, and 4 weeks immersion in SBF solution.
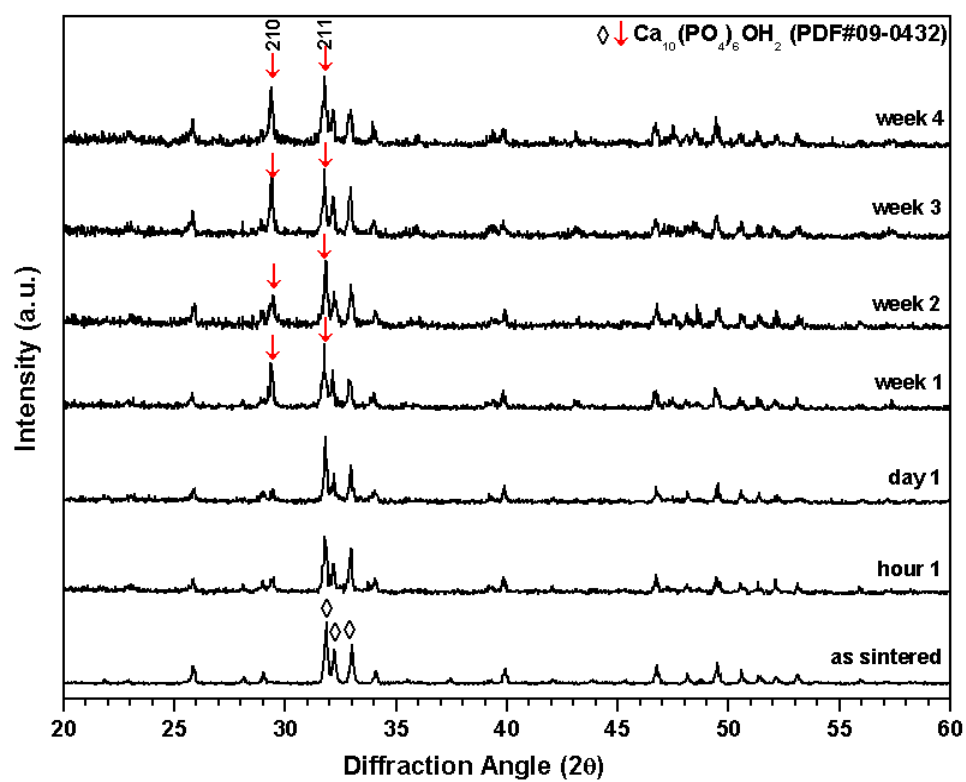
Figure 8.6: XRD patterns of w/oSiO$_2$ blend sintered at 900ºC for 1 hour after 1 hour, 1 day, 1, 2, 4, and 4 weeks immersion in SBF solution.
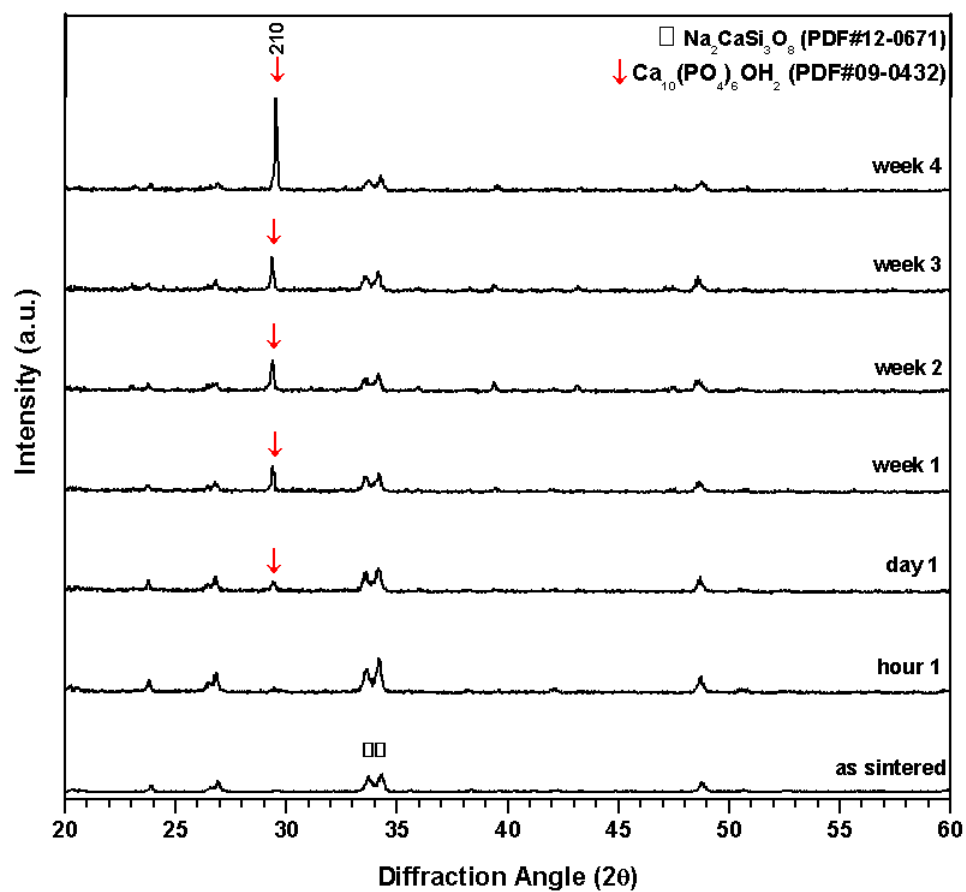
Figure 8.7: XRD patterns of Bioglass®45S5 sintered at 900°C for 2 hours after 1 hour, 1 day, 1, 2, 4, and 4 weeks immersion in SBF solution.
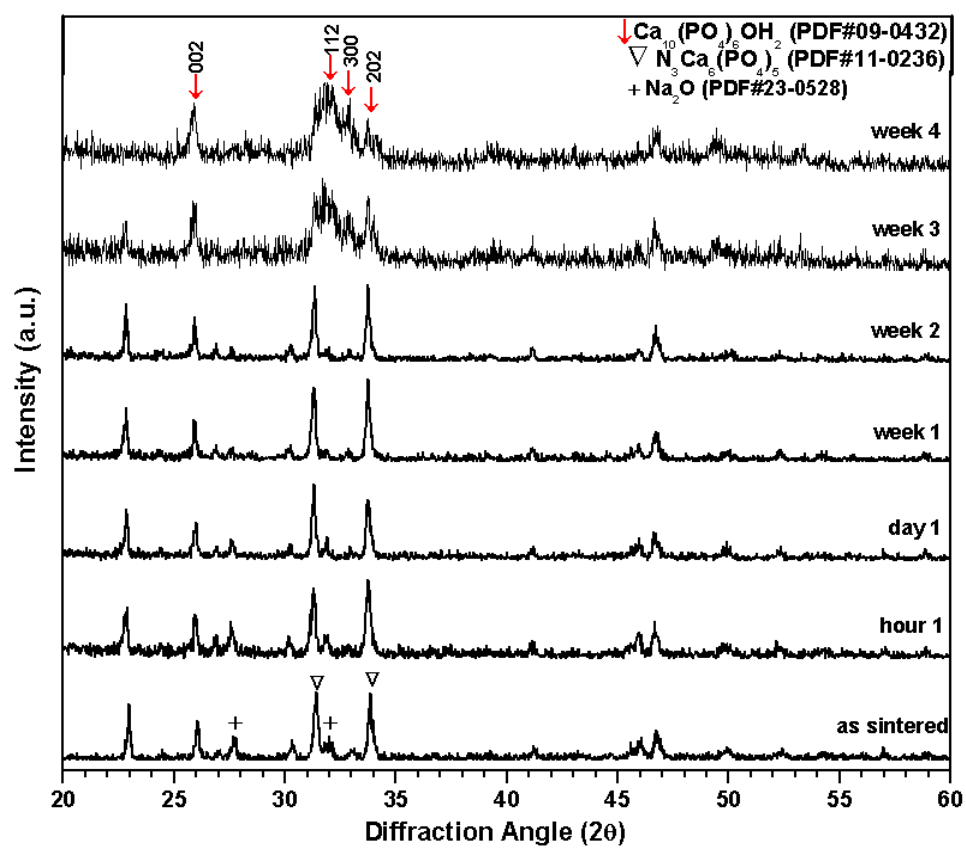
Figure 8.8: XRD patterns of w/SiO$_2$ blend sintered at 1200ºC for 1 hour after 1 hour, 1 day, 1, 2, 4, and 4 weeks immersion in SBF solution.
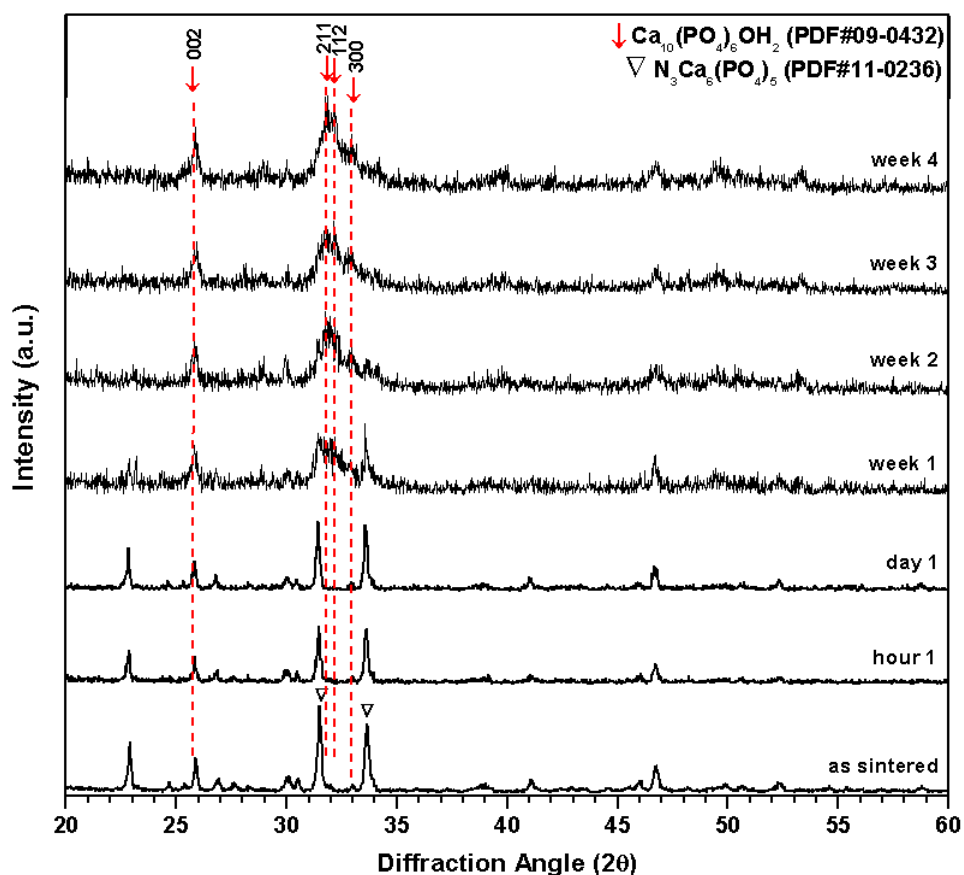
Figure 8.9: XRD patterns of 25 wt. % Bioglass®45S5 added hydroxyapatite sintered at 1200ºC for 1 hour after 1 hour, 1 day, 1, 2, 4, and 4 weeks immersion in SBF solution.

The SEM micrographs showing surface morphology changes of for hydroxyapatite sintered at 1200ºC for 1 hour, w/oSiO$_2$ blend sintered at 900ºC for 1 hour, pure Bioglass®45S5 (with Na$_2$CaSi$_3$O$_8$ crystalline phase) sintered at 900ºC for 2 hours, w/SiO$_2$ sintered for 1200ºC for 1 hour, and 25 wt. % Bioglass®45S5 added hydroxyapatite sintered at 1200ºC for 1 hour after 1 week immersion in SBF solution are shown in Figures 8.10 – 8.14, respectively. Figures 8.15 – 8.19 show surface morphology changes of for hydroxyapatite sintered at 1200ºC for 1 hour, w/oSiO$_2$ blend sintered at 900ºC for 1 hour, pure Bioglass®45S5 (with Na$_2$CaSi$_3$O$_8$ crystalline phase) sintered at 900ºC for 2 hours, w/SiO$_2$ sintered for 1200ºC for 1 hour, and 25 wt. % Bioglass®45S5 added hydroxyapatite sintered at 1200ºC for 1 hour after 4 weeks immersion in SBF solution, respectively. The SEM micrographs of surface morphologies of bioceramic samples

205

after 1 week immersion show that the entire of the surface is covered with apatite only in 25 wt. % Bioglass®45S5 added hydroxyapatite bioceramic composition; however, all other bioceramic compositions show some amount of precipitation even after 1 week immersion. The smallest amount of precipitation (apatite formation) is observed in pure hydroxyapatite sintered at 1200°C for 1hour indicates that it has the lowest dissolution rate hence lowest bioactivity. On the other hand, the XRD patterns shown in Figures 8.5 through 8.9 indicate that apatites formed on all bioceramic samples except 25 wt. % Bioglass®45S5 added hydroxyapatite bioceramic composition are not thick enough to eliminate the diffraction peaks from the substrates. After 4 weeks immersion the whole surface of all bioceramic compositions are covered with a layer of bone like apatite layer yet the thickest layer is achieved in case of 25 wt. % Bioglass®45S5 added hydroxyapatite bioceramic composition as verified with XRD analyses.
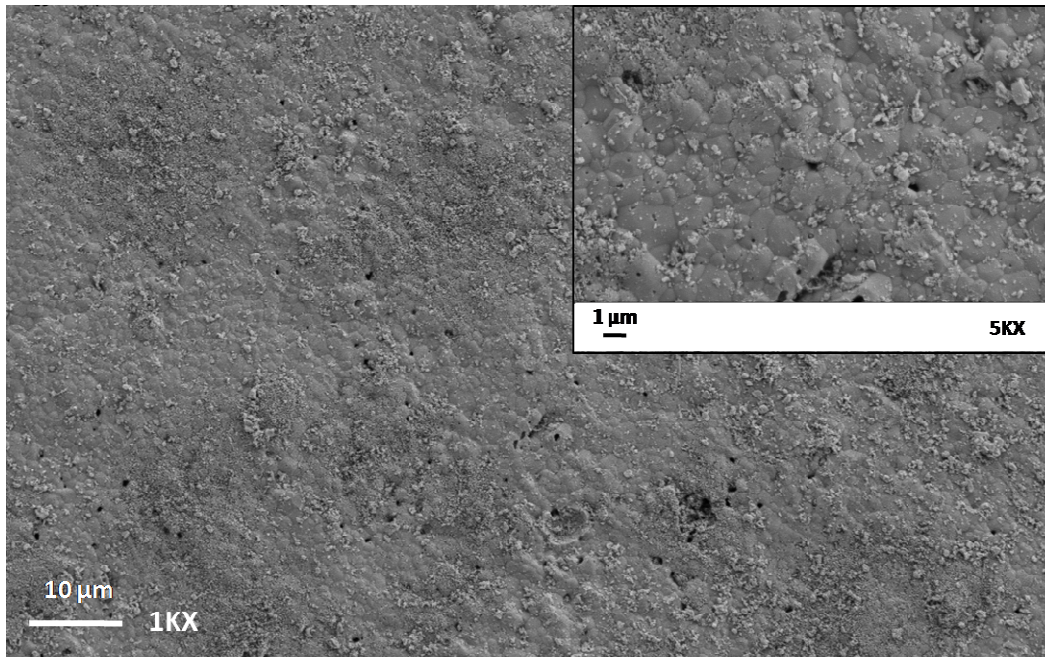
Figure 8.10: The SEM micrographs of hydroxyapatite sintered at 1200°C for 1 hour after 1 week immersion in SBF solution.
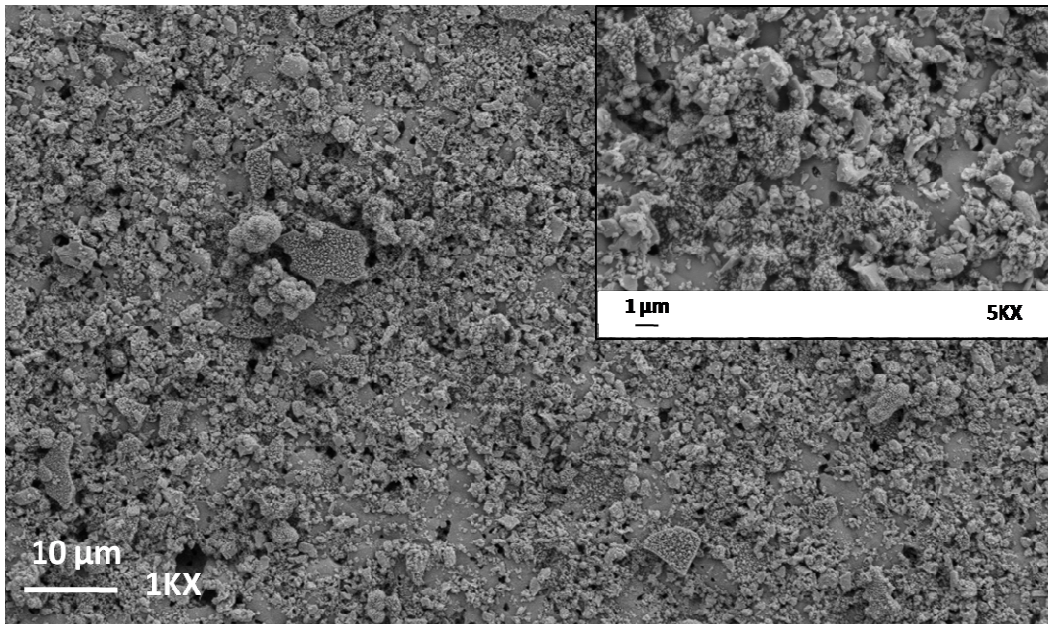
Figure 8.11: The SEM micrographs of w/oSiO$_2$ blend sintered at 900ºC for 1 hour after 1 week immersion in SBF solution.
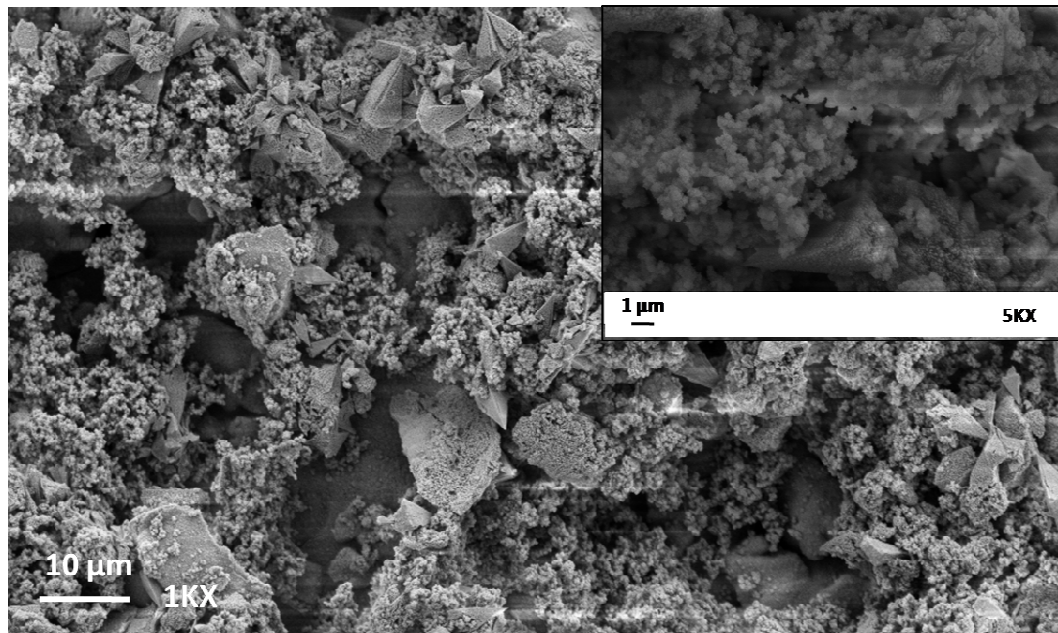
Figure 8.12: The SEM micrographs of Bioglass®45S5 (with Na$_2$CaSi$_3$O$_8$ crystalline phase) sintered at 900ºC for 2 hours after 1 week immersion in SBF solution.
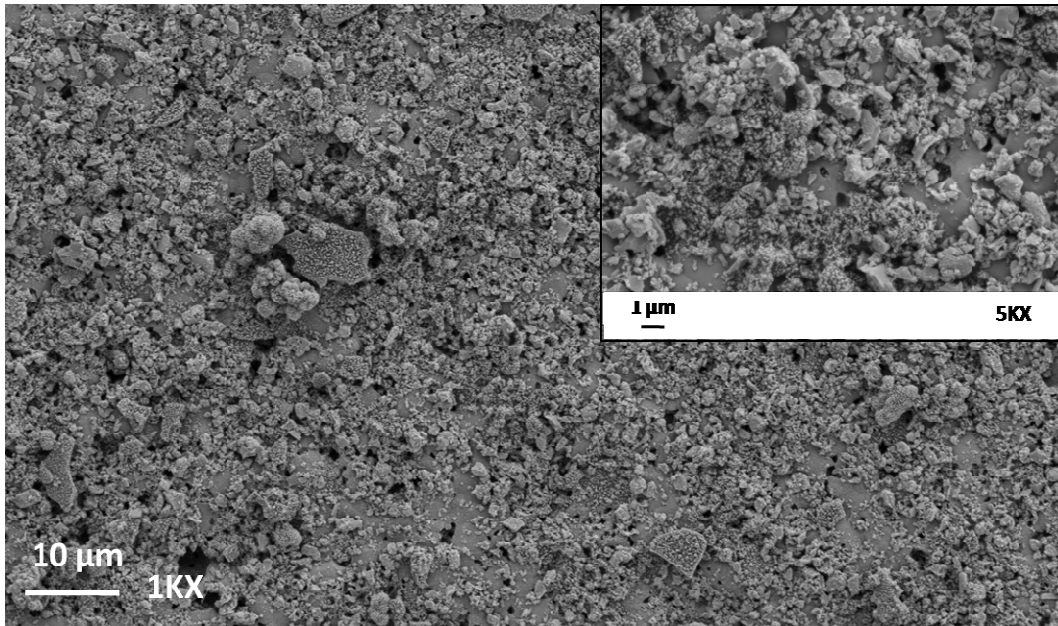
Figure 8.13: The SEM micrographs of w/SiO$_2$ blend sintered for 1200ºC for 1 hour after 1 week immersion in SBF solution.
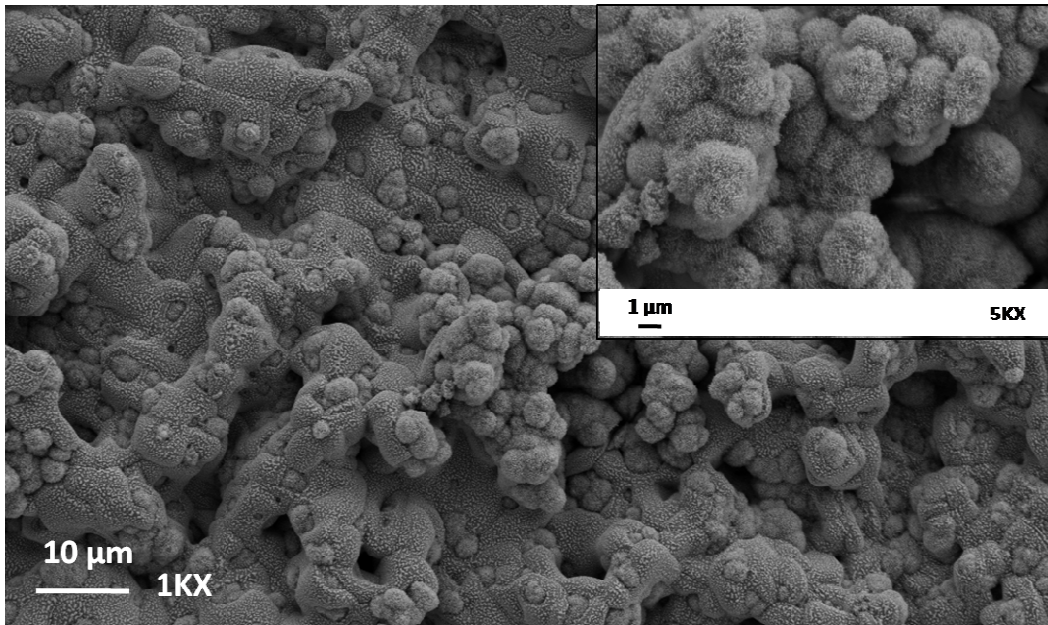
Figure 8.14: The SEM micrographs of 25 wt. % Bioglass®45S5 added hydroxyapatite sintered at 1200ºC for 1 hour after 1 week immersion in SBF solution.
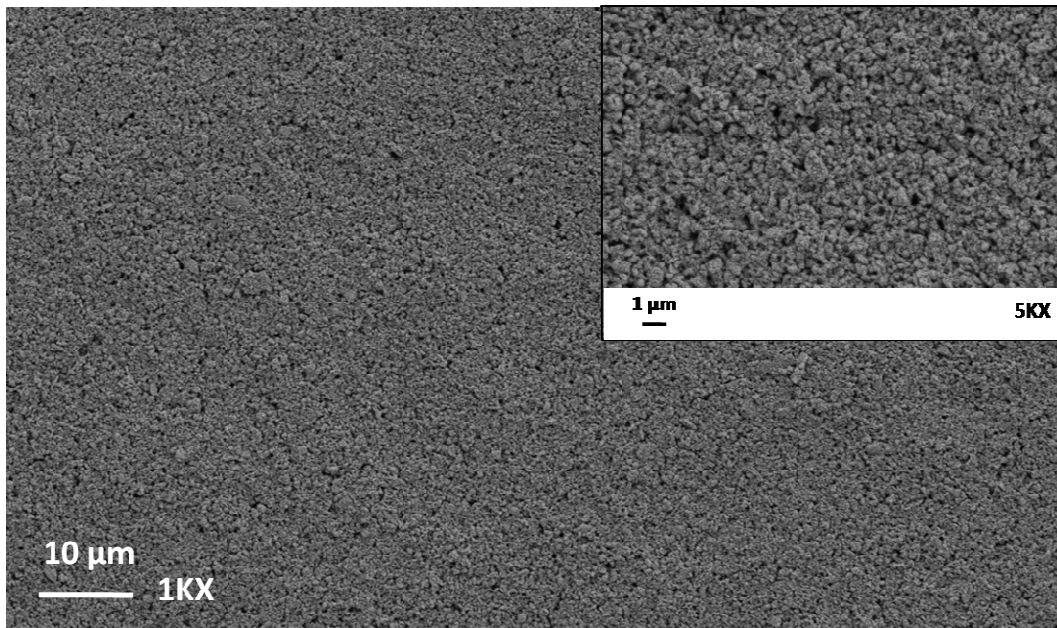
Figure 8.15: The SEM micrographs of hydroxyapatite sintered at 1200ºC for 1 hour after 4 weeks immersion in SBF solution.
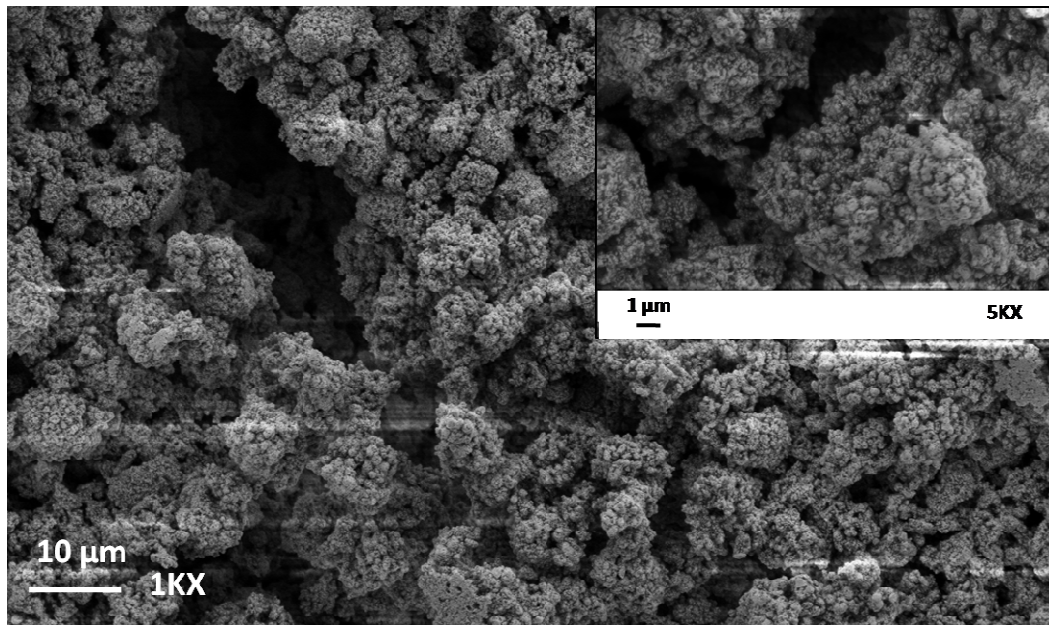
Figure 8.16: The SEM micrographs of w/oSiO$_2$ blend sintered at 900ºC for 1 hour after 4 weeks immersion in SBF solution.
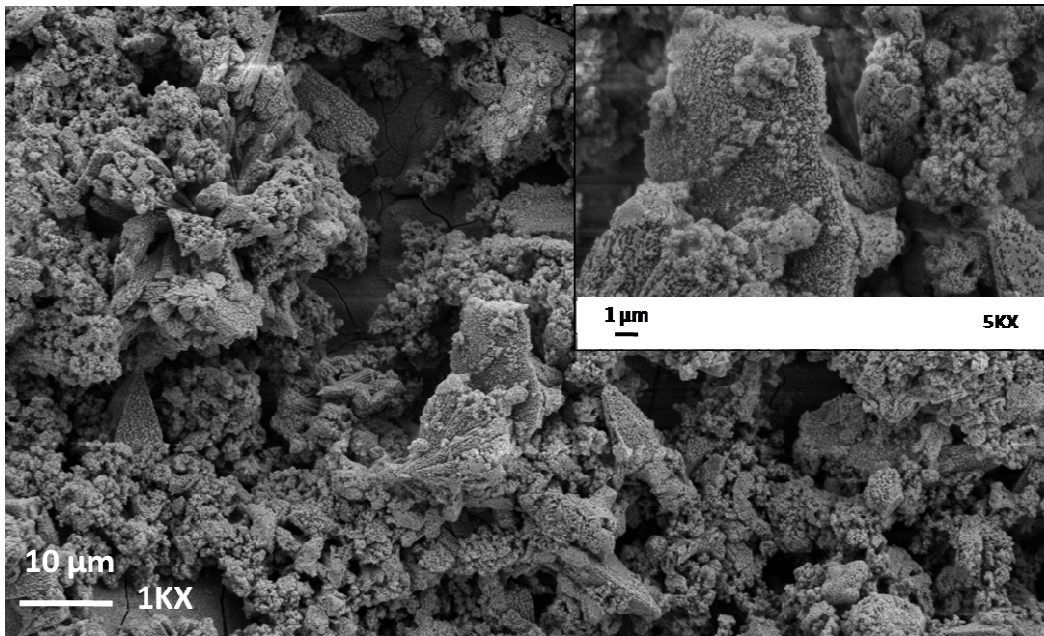
Figure 8.17: The SEM micrographs of Bioglass®45S5 (with $Na_2CaSi_3O_8$ crystalline phase) sintered at 900ºC for 2 hours after 4 weeks immersion in SBF solution.
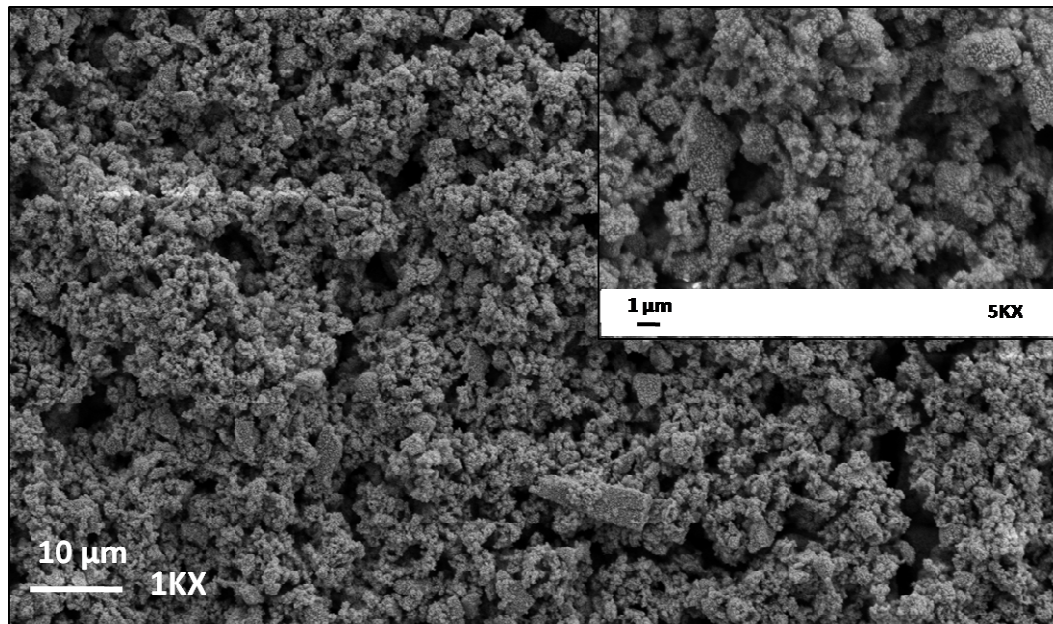
Figure 8.18: The SEM micrographs of w/SiO_2 blend sintered for 1200ºC for 1 hour after 4 weeks immersion in SBF solution.
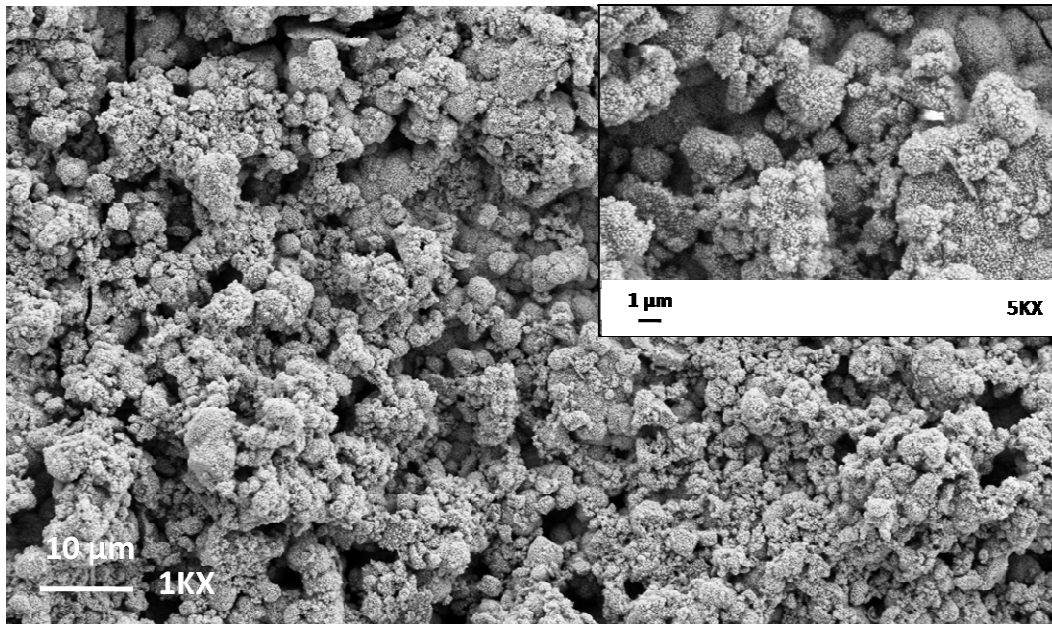
Figure 8.19: The SEM micrographs of 25 wt. % Bioglass®45S5 added hydroxyapatite sintered at 1200ºC for 1 hour after 4 weeks immersion in SBF solution.

8.4 Conclusion

Five different bioceramic compositions were blended and sintered at different temperatures depending on the best feasible structure obtained with the desired chemical compositions. The X-ray diffraction analyses showed that pure hydroxyapatite and Bioglass®45S5 precursors added to hydroxyapatite excluding SiO_2 (w/oSiO$_2$ blend) sintered at 1200 and 900ºC, respectively for 1 hour resulted in main crystalline hydroxyapatite phase. On the other hand, 25 wt. % Bioglass®45S5 added hydroxyapatite and Bioglass®45S5 precursors (25 wt.% in total; w/SiO$_2$ blend) added to hydroxyapatite sintered at 1200ºC for 1 hour resulted in formation of a main $Na_3Ca_6(PO_4)_5$ crystalline phase. Additionally, w/SiO$_2$ blend also showed a secondary Na_2O crystalline phase. Lastly, XRD pattern for Bioglass®45S5 sintered at 900ºC for 2 hours showed that it transformed into main $Na_2CaSi_3O_8$ crystalline phase. In order to find the effect of SiO_2 in formation of $Na_3Ca_6(PO_4)_5$ XRD analyses were performed on three bioceramic blends with different SiO_2 amounts (*(i)* 25 wt. % Bioglass®45S5 added hydroxyapatite (contains 11.25 wt. % SiO$_2$), *(ii)* reduced SiO$_2$ glass I (contains 6.05 wt. % SiO$_2$), and *(iii)* reduced SiO$_2$

glass II (contains 8.68 wt. % SiO_2)). It is found that even reduced SiO2 glass I did not result in formation of $Na_3Ca_6(PO_4)_5$. All these findings imply that the amount of silicate is crucial in formation of $Na_3Ca_6(PO_4)_5$ crystalline phase. The P K-edge XANES spectroscopy was obtained for all bioceramic samples to identify the chemical structure of both the crystalline and amorphous phases compared to the previous bioceramic compositions synthesized in Chapter 5. It is found that 25 wt. % Bioglass®45S5 added hydroxyapatite and w/SiO_2 blend compositions are more soluble compared to hydroxyapatite and w/oSiO_2 blend bioceramic samples. Finally, the *in vitro* apatite formation behavior and the effect of SiO_2 content on bioactivity of these bioceramic samples were evaluated by immersing the samples in SBF solution for 1 hour, 1 day, 1, 2, 3, and 4 weeks. The XRD analyses and scanning electron microscopy illustrate that the highest bioactivity is achieved by 25 wt. % Bioglass®45S5 addition to hydroxyapatite. All these findings entailed that even though the positive affect of SiO_2 on bioactivity of bioceramic materials is irrefutable, it is clearly shown in this study that addition of Bioglass®45S5 precursors to hydroxyapatite yield a novel composition with a crystalline $Na_3Ca_6(PO_4)_5$ in an amorphous sodium silicate glassy matrix which have a significant role in improving the bioactivity respect to pure Bioglass®45S5 and hydroxyapatite.

CHAPTER 9

PHENOMENOLOGICAL APPROACH AND CONCLUSIONS

Any material that is designed to repair or replace a body part in a safe, reliable, and physiologically acceptable manner is called biomaterial [183]. Artificial materials implanted into body generally encapsulated by a fibrous tissue which causes isolation from the surrounding bones. On the contrary, ceramic biomaterials such as hydroxyapatite, bioactive glasses, and glass ceramics bond directly to living bone without a fibrous tissue which is the main draw in using bioceramic materials as biomaterials [167]. All these bioceramic materials have been intensively studied [29] and clinically used as important bone-repairing materials [167] for more than four decades. However, each material has advantages as well as drove backs.

In this research, different amounts of a bioactive glass (Bioglass®45S5) are blended with synthetic hydroxyapatite in order to improve material properties primarily aiming bioactivity. The experiments showed that in compositions with 10 and 25 wt. % Bioglass®45S5 and sintering at 1200ºC for 4 hours yielded novel chemistries. Analytical techniques such as X-ray diffraction, scanning electron microscopy and XANES spectroscopy provided insight into the chemical structure and morphology of these new structures. Cell culture analysis on these substrates provided additional information that indicated these newly formed compositions had improved bioactivity compared to known bioceramic materials. As a conclusion, a phenomenological approach is proposed based on the knowledge acquired from each set of experiments and the observations made in the published literature.

The first set of information obtained from X-ray diffraction analysis illustrated that when up to 5 wt. % Bioglass®45S5 addition to synthetic hydroxyapatite cause decomposition of hydroxyapatite to β-tricalcium phosphate (β-TCP). In addition, it is found that the amount of

213

decomposition to β-TCP increases with increased Bioglass®45S5 amount. On the other hand, compositions with 10 and 25 wt. % Bioglass®45S5 addition resulted in crystalline $Ca_5(PO_4)_2SiO_4$ and $Na_3Ca_6(PO_4)_5$ phases dispersed in silicate glassy matrices, respectively. Further cell culture studies showed that the highest cell proliferation is achieved in 10 wt. % Bioglass®45S5 addition while highest bone cell differentiation is attained in 25 wt. % Bioglass®45S5 addition (Chapter 4). These findings drove this research to clarify the role of these main crystalline phases and to identify the chemical compositions of the amorphous phases as well as their effect on bioactivity. Since up to 5 wt. % Biogass®45S5 addition have not shown any exceptional difference in bioactivity, the bioceramic compositions that demonstrated highest cell proliferation and differentiation were the main focus of this research. High cell proliferation and differentiation observed in these bioceramic compositions can be attributed to the apatite layers formed on their surfaces. Since this apatite layer is a carbonate-containing hydroxyapatite that has a similar composition and structure to the apatite in the bone, bone producing cells also known as osteoblasts can preferentially proliferate and differentiate to produce apatite and collagen on this apatite layer that results in a direct bonding of the implant with the bone without forming a fibrous tissue [167]. The apatite forming ability of these bioceramic compositions were tested by *in vitro* simulated body fluid immersion which demonstrated that the thickest apatite layer has formed in 10 and 25 wt. % Bioglass®45S5 addition and the fastest apatite layer formation was observed in 25 wt. % Bioglass®45S5 addition (Chapter 6). It is well accepted that faster and thicker apatite formations is a sign of high bioactivity [4, 96, 97, 162-164]. Therefore it could be concluded that 25 wt. % Bioglass®45S5 addition in synthetic hydroxyapatite that yields a new composition with $Na_3Ca_6(PO_4)_5$ main crystalline phase in a silicate glassy matrix leads to a highly bioactive bioceramic material compared to both Bioglass®45S5 and synthetic hydroxyapatite.

The second set of information has been used to identify the amorphous phases formed on all bioceramic compositions by X-ray adsorption near edge spectroscopy (XANES). Si K- and $L_{2,3}$-edge XANES results have shown that none of the compositions contains calcium silicates,

and the primary silicates that are present in these compositions are sodium silicates in amorphous phase. Although it is difficult to conclude the exact structure of the phosphate phases from P $L_{2,3}$-edge XANES as they are made up of a mixture of different phosphates, it is clearly shown that there is no evidence of sodium phosphate present in the sintered bioceramic compositions and the primary phosphate present is one of calcium not sodium. One important outcome from P K-edge is the post-edge shoulder peak at around 2155eV discloses this shoulder to be more defined for calcium phosphate compounds with decreasing solubility and increasing thermodynamic stability [157]. This shoulder peak is more noticeable in HA and β-TCP suggesting while the stability of calcium phosphate phase increases, the spectral features such as post-edge shoulder peak may appear more distinctive. The only spectra that does not show a noticeable peak is 25 wt. % Bioglass®45S5 added hydroxyapatite bioceramic composition indicating that it is more soluble compared to the other compositions which is also an indication of high bioactivity.

Now that it has been proven that 25 wt. % Bioglass®45S5 addition to synthetic hydroxyapatite and sintering at 1200ºC for 4 hours yielded a new crystalline phase ($Na_3Ca_6(PO_4)_5$) immersed in silicate glassy matrix exhibits the highest bioactivity with highest bone cell differentiation on its surface, a model will be developed to clarify the role of these crystalline and amorphous phases on bioactivity according to the findings so far.

The schematic cross section views of sintered hydroxyapatite, and 1 – 5 wt. %, 10 wt. %, and 25 wt. % Bioglass®45S5 added hydroxyapatite bioceramics are shown in Figure 9.1 (a-d). Sintering ceramic particles can occur entirely in solid state or from a mixture of solid particles and liquid. It is known that when a glass composition heat up to a temperature that it melts, the network modifiers such as CaO and Na_2O break the Si – O – Si bonds of SiO_2 and decrease the melting temperature. If the amount of liquid phase is small, the liquid phase coats the grain boundaries and forms a dense solid when cooled down. On the contrary, a larger amount of liquid phase can provide a glassy matrix which surrounds the grains [1, 184]. In this study, sintering

215

small amounts (up to 5 wt. %) of Bioglass®45S5 with synthetic hydroxyapatite particles formed a very negligible amount of liquid phase coated the β-TCP that formed by decomposition of hydroxyapatite and retained hydroxyapatite grains forming dense bioceramic compositions. On the other hand, higher amounts of Bioglass®45S5 addition lead to forming larger amount of liquid phase that provided a glassy matrix which the cations and anions from hydroxyapatite and Bioglass®45S5 can dissolve and cause liquid phase reactions and finally results in nucleation of crystalline $Ca_5(PO_4)_2SiO_4$ and $Na_3Ca_6(PO_4)_5$ particles immersed in a glassy matrix consists of a silicate amorphous phase.
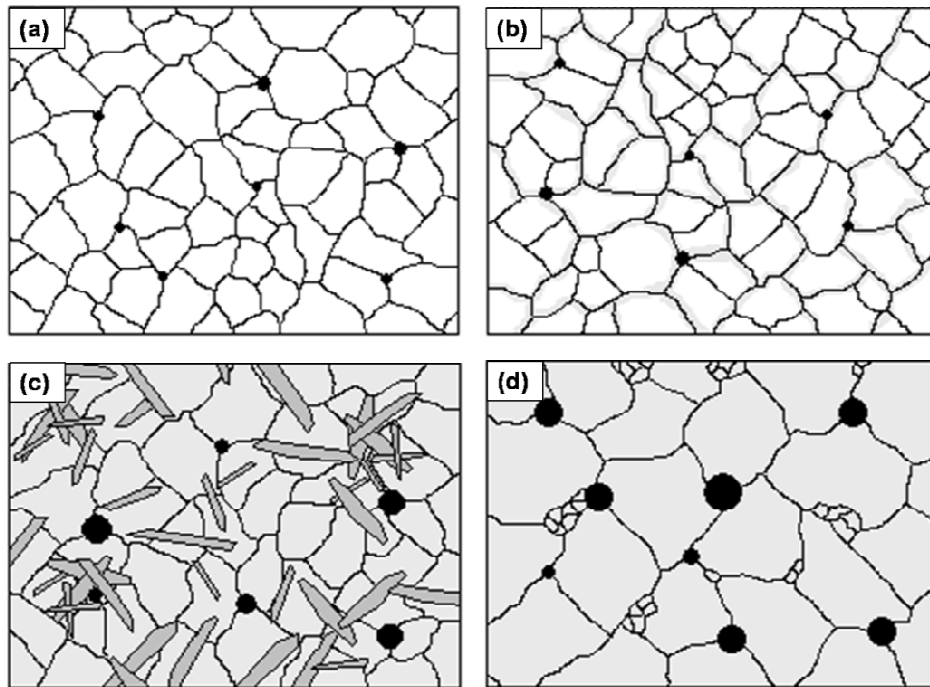
Figure 9.1: Schematic cross section views of (a) sintered hydroxyapatite, (b) sintered 1 – 5 wt. % Bioglass®45S5 added hydroxyapatite, (c) sintered 10 wt. % Bioglass®45S5 added hydroxyapatite, (d) 25 wt. % Bioglass®45S5 added hydroxyapatite bioceramic samples. Dark circles represent porosity, and bright gray color represents glassy matrix.

The surface reactions happen within in the body for any silicate containing bioactive glasses allow the subsequent crystallization of apatite which further allows cell adhesion and collagen formation [59]. So, it is believed that silicon is an essential element in skeleton

216

development due to its participation in early stage of bone calcification [60]. It has been shown in this study that 25 wt. % Bioglass®45S5 added hydroxyapatite has a higher dissolution rate than the rest of bioceramic compositions. In addition it has the highest amount of silicate in its structure (all in amorphous phase). Therefore, when it is immersed in simulated body fluid (SBF), it tends to release Si ions faster than the other compositions which will later form the silica gel layer that is the nucleation sites for CaO-P_2O_5 rich apatite and consequently crystallizes to hydroxyl carbonated apatite. In the case of up to 5 wt. % Bioglass®45S5 addition, there may be two reasons not forming a distinctive apatite layer until longer immersion times. First, hydroxyapatite is more stable than Bioglass®45S5 [17] and up to 5 wt. % Bioglass®45S5 addition to hydroxyapatite is not sufficient enough to accelerate this process. Secondly, β-TCP does not form an apatite layer even though it forms a direct bond with bone [5, 7]. On the other hand, 10 wt. % Bioglass®45S5 addition even though increases the apatite layer formation compared to up to 5 wt. % Bioglass®45S5 addition, the phases formed are more stable than the phases formed in 25 wt. % Bioglass®45S5 addition which results in a slower apatite formation behavior. Another reason behind this may be due to the silicate amount. 10 wt. % Bioglass®45S5 added hydroxyapatite composition contains less silicate amount than 25 wt. % Bioglass added composition; therefore the release of silicate to the solution hence the silica gel layer formation may be less efficient which delays apatite formation to some extent. Therefore, 25 wt. % Bioglass®45S5 addition to synthetic hydroxyapatite yields a novel bioceramic composition that has higher material and biological properties than both pure Bioglass®45S5 and hydroxyapatite which can be used as a bone substitute in orthopedics and tissue culture applications. The schematic mechanism of apatite layer formation in SBF solution on sintered hydroxyapatite which does not contain any SiO_2, 10 wt. %, and 25 wt. % Bioglass®45S5 added hydroxyapatite bioceramics are shown in Figure 9.2 (a-c), respectively.

217
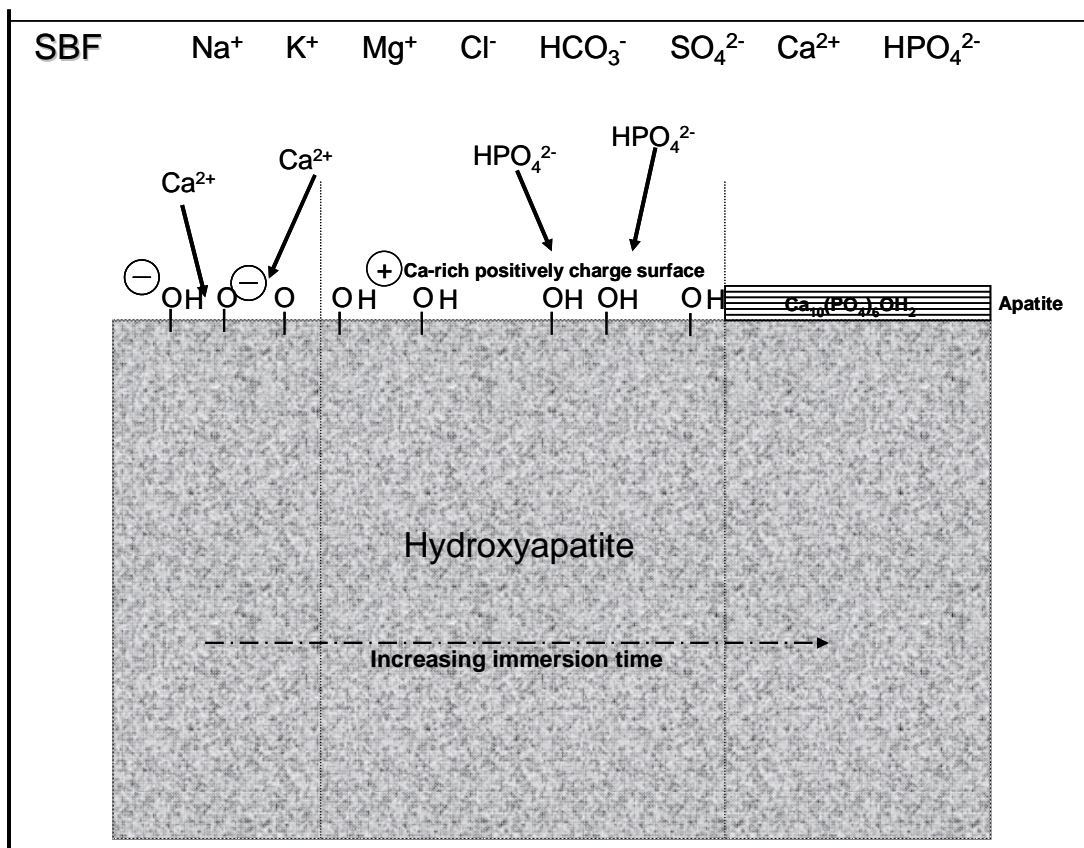
Figure 9.2: Schematic mechanism of apatite formation on sintered hydroxyapatite bioceramic sample.
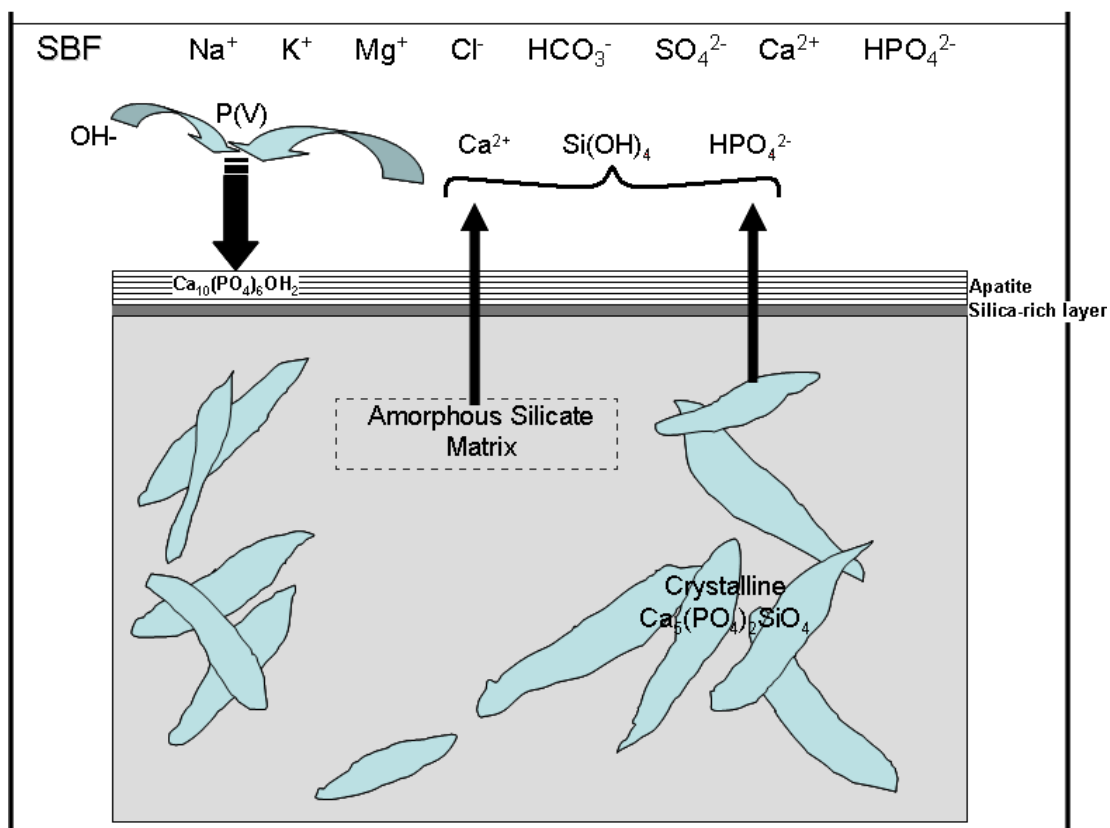
Figure 9.3: Schematic mechanism of apatite formation on sintered 10 wt. % Bioglass®45S5 added hydroxyapatite bioceramic sample.
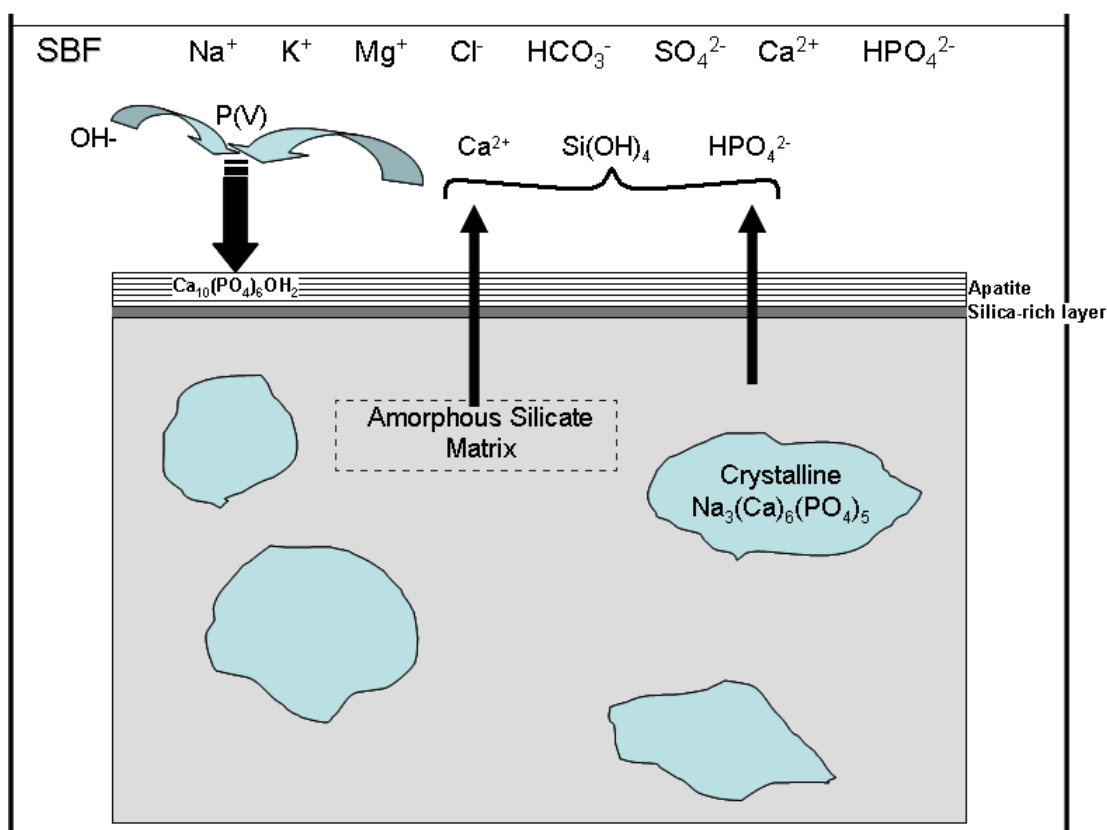
Figure 9.4: Schematic mechanism of apatite formation on sintered 25 wt. % Bioglass®45S5 added hydroxyapatite bioceramic sample.

Finally, in order to evaluate apatite formation ability that is closely related to the bioactivity of materials, apatite formation mechanism, and the structural variations in the apatite layers formed on five different hydroxyapatite – Bioglass®45S5 bioceramic compositions sintered at 1200ºC for 4 hours XANES study is performed. Figures 9.2 – 9.4 show schematically how the apatite layers formed and developed on hydroxyapatite and 1 – 5 wt. %, 10 wt. %, and 25 wt. % Bioglass®45S5 added hydroxyapatite bioceramic compositions after 1, 4, and 10 weeks immersion in SBF solution. Si K-edge XANES spectra for all apatite layers formed except 25 wt. % Bioglass®45S5 showed broader white line peaks than the model compounds indicates that the origin of these peaks may be from Si incorporated to CaO-P$_2$O$_5$- rich (apatite) layers formed even though the TF-XRD patterns show same crystalline phase forming (hydroxyapatite). This finding

is also in good agreement with EDX analysis obtained from apatite layers formed on 1, 10, and 25 wt. % Bioglass®45S5 added hydroxyapatite bioceramic samples after 4 weeks immersion in SBF solution. However, XANES spectroscopy has over a wide range of energies produced much greater than a common X-ray technique ensuring much higher sensitivity of element specific spectroscopic analyses [107]. This may be the reason why as all thin film XRD patterns from all samples after 4 week immersion displays same crystalline phases (apatite), the spectra obtained by XANES gives much detailed information and is able to pick the differences between the apatite layers. It is found that while Si K-edge spectra for apatite layers formed on 1 and 25 wt. % Bioglass®45S5 added hydroxyapatite bioceramics show increasing P to Si ratio, apatite layers formed on 10 wt. % Bioglass®45S5 added hydroxyapatite bioceramic composition remains more or less same following 1, 4, and 10 weeks immersion in SBF solution. This indicates that while the Si incorporated in apatite layers formed on 1 and 25 wt. % added hydroxyapatite bioceramic compositions decreasing in the bulk of apatite layer, it remains same for 10 wt. % Bioglass®45S5 added hydroxyapatite sample. In addition, the Si $L_{2,3}$-edge spectra for 1 and 25 wt. % Bioglass®45S5 added hydroxyapatite bioceramic samples showed that while apatite is depositing on the surface, it incorporates within the silica gel layer which gives a rise in the relative Si to P amount after 10 weeks immersion. On the contrary, the P amount was found larger than the Si amount on the surface of apatite layer formed on 10 wt. % Bioglass®45S5 added hydroxyapatite bioceramic sample. This indicates that while the Si in apatite layers formed on 1 and 25 wt. % Bioglass®45S5 added hydroxyapatite samples mainly found in the surface of apatite layers, apatite layer does not diffuse through the silica gel layer on 10 wt. % Bioglass®45S5 added hydroxyapatite bioceramic composition. The P structure environment in hydroxyapatite – Bioglass®45S5 bioceramic compositions are similar to the apatite layers formed. In contrast, a closer look to P $L_{2,3}$-edge XANES spectra of apatite layers formed after 10 week immersion in SBF solution indicates that the largest changes in the P structure occurs in the case of apatite layers formed on only 1 and 25 wt. % Bioglass®45S5 added bioceramic samples may be due to

221

incorporation of Si into the apatite layer closer to the surface of it after 10 weeks immersion in SBF solution. The Ca K-edge XANES spectra of apatite layers formed after 10 week immersion in SBF solution on bioceramic compositions shows splitting of Ca K-edge white line peaks (specifically in apatitic materials) which can be assigned to the existence of two calcium sites with different coordination spheres [158]. Additionally, as the Bioglass®45S5 content increases these peaks start to combine to be one main peak and the peak intensity relative to peak **a** gradually decreases. Finally when the Bioglass®45S5 amount reaches 25 wt. %, it almost disappears. This finding suggests that the Bioglass®45S5 content in hydroxyapatite closely related to the structural environment of calcium in apatite layers formed. In addition, the Si is incorporating with both P and Ca in $CaO-P_2O_5$-rich layers (apatite layers). However, further analyses including XANES spectroscopy are required to identify these Si incorporated compositions much in detail.

Figure 9.5: Schematic view of (a) sintered hydroxyapatite, (b) sintered 1- 5 wt. % Bioglass®45S5 added hydroxyapatite, (c) 10 wt. % Bioglass®45S5 added hydroxyapatite, and (d) 25 wt. % bioglass®45S5 added hydroxyapatite bioceramic samples after 1, 4, and 10 weeks immersion in SBF solution.

All the results have been reached here provide a framework for further study on the

newly formed bioceramic compositions. For instance, in order to understand the formation

223

mechanism of the crystalline phases and improve the material properties of $Na_3Ca_6(PO_4)_5$, it can be produced as a single phase and one can isolate the biological properties of this crystalline phase in absence of a glassy matrix. In addition, higher mechanical properties may be accomplished by developing a new synthesizing process. Finally, due to high dissolution rate of this novel bioceramic composition $Na_3Ca_6(PO_4)_5$ can also be produced in nano scale and blend with polymers to be examined as a drug delivery system.

REFERENCES

[1] Hench, L.L., and Wilson, J., 1993, "An introduction to bioceramics," World Scientific Publishing Co. Pte. Ltd., Singapore, pp. 406.

[2] Bhat, S.V., 2002, "Biomaterials," Kluwer Academic Publishers, Dordrecht, The Netherlands, pp. 253.

[3] Park, J.B., and Bronzino, J.D., 2003, "Biomaterials: Principles and applications," CRC Press, Boca Raton, Florida.

[4] Heness, G., and Ben-Nissan, B., 2004, "Innovative Bioceramics," Materials Forum, **27**pp. 104-114.

[5] Kokubo, T., 2008, "Bioceramics and their clinical applications," Woodhead Publishing Limited, Cambridge, England, pp. 760.

[6] Dubok, V. A., 2000, "Bioceramics: Yesterday, Today, Tomorrow," Poroshkovaya Metallurgiya, (7-8) pp. 69-87.

[7] Xin, R., Leng, Y., Chen, J., 2005, "A Comparative Study of Calcium Phosphate Formation on Bioceramics in Vitro and in Vivo," Biomaterials, **26**(33) pp. 6477-6486.

[8] Goller, G., Demirkiran, H., Oktar, F. N., 2003, "Processing and Characterization of Bioglass Reinforced Hydroxyapatite Composites," Ceramics International, **29**(6) pp. 721-724.

[9] Wang, Q. L., Ge, S. R., and Zang, D. K., 2004, "Highly Bioactive Nano-hydroxyapatite/partially Stabilized Zirconia Ceramics," Journal of Bionics Engineering, (4) pp. 215-224.

[10] Knowles, J. C., and Bonfield, W., 1993, "Development of a Glass Reinforced Hydroxyapatite with Enhanced Mechanical Properties. The Effect of Glass Composition on Mechanical Properties and its Relationship to Phase Changes," Journal of Biomedical Materials Research, **27**(12) pp. 1581-1598.

[11] Oktar, F. N., and Goller, G., 2002, "Sintering Effects on Mechanical Properties of Glass-Reinforced Hydroxyapatite Composites," Ceramics International, **28**(6) pp. 617-621.

[12] Akao, M., Aoki, H., and Kato, K., 1981, "Mechanical Properties of Sintered Hydroxyapatite for Prosthetic Applications," Journal of Materials Science, **16**(3) pp. 809-812.

[13] Francis, M. D., 1969, "The Inhibition of Calcium Hydroxyapatite Crystal Growth by Polyphosphonates and Polyphosphates," Calcified Tissue Research, **3**pp. 151-151-162.

[14] Santos, J. D., Jha, L. J., and Monteiro, F. J., 1996, "In Vitro Calcium Phosphate Formation on SiO2-Na2O-CaO-P2O5 Glass Reinforced Hydroxyapatite Composite: A Study by XPS Analysis," Journal of Materials Science: Materials in Medicine, **7**(3) pp. 181-185.

[15] Santos, J. D., Jha, L. J., and Monteiro, F. J., 1995, "Surface Modifications of Glass-Reinforced Hydroxyapatite Composites," Biomaterials, **16**(7) pp. 521-526.

[16] Tancred, D. C., Carr, A. J., and McCormack, B. A. O., 2001, "The Sintering and Mechanical Behavior of Hydroxyapatite with Bioglass Additions," Journal of Materials Science: Materials in Medicine, **12**(1) pp. 81-93.

[17] Lee, E., Kim, H., and Kim, H., 2006, "Production of hydroxyapatite/bioactive Glass Biomedical Composites by the Hot-Pressing Technique," Journal of the American Ceramic Society, **89**(11) pp. 3593-3596.

[18] Shimaoka, H., Dohi, Y., Ohgushi, H., 2004, "Recombinant growth/differentiation Factor-5 (GDF-5) Stimulates Osteogenic Differentiation of Marrow Mesenchymal Stem Cells in Porous Hydroxyapatite Ceramic," Journal of Biomedical Materials Research - Part A, **68**(1) pp. 168-176.

[19] Li, X. W., Yasuda, H. Y., and Umakoshi, Y., 2006, "Bioactive Ceramic Composites Sintered from Hydroxyapatite and Silica at 1200°C: Preparation, Microstructures and in Vitro Bone-Like Layer Growth," Journal of Materials Science: Materials in Medicine, **17**(6) pp. 573-581.

[20] Hench, L. L., 2006, "The Story of Bioglass [Registered Trademark]," Journal of Materials Science: Materials in Medicine, **17**(11) pp. 967-978.

[21] Lefebvre, L., Chevalier, J., Gremillard, L., 2007, "Structural Transformations of Bioactive Glass 45S5 with Thermal Treatments," Acta Materialia, **55**(10) pp. 3305-3313.

[22] Prokopiev, O., and Sevostianov, I., 2006, "Dependence of the Mechanical Properties of Sintered Hydroxyapatite on the Sintering Temperature," Materials Science and Engineering A, **431**(1-2) pp. 218-227.

[23] Chatzistavrou, X., Chrissafis, K., Kontorasaki, E., 2006, "Sintered hydroxyapatite/bioactive Glass Composites: Thermal Analysis and Bioactivity," Key Engineering Materials, **309-311**pp. 167-170.

[24] Ding, S. J., Su, Y. M., Ju, C. P., 2001, "Structure and Immersion Behavior of Plasma-Sprayed Apatite-Matrix Coatings," Biomaterials, **22**(8) pp. 833-845.

[25] Iwasaki, T., Tanaka, Y., Nakamura, M., 2008, "Rate of Bonelike Apatite Formation Accelerated on Polarized Porous Hydroxyapatite," Journal of the American Ceramic Society, **91**(12) pp. 3943-3949.

[26] Hsu, Y. H., Turner, I. G., and Miles, A. W., 2007, "Fabrication of Porous Bioceramics with Porosity Gradients Similar to the Bimodal Structure of Cortical and Cancellous Bone," Journal of Materials Science: Materials in Medicine, **18**(12) pp. 2251-2256.

[27] Santos, J. D., Reis, R. L., Monteiro, F. J., 1995, "Liquid Phase Sintering of Hydroxyapatite by Phosphate and Silicate Glass Additions: Structure and Properties of the Composites," Journal of Materials Science: Materials in Medicine, **6**(6) pp. 348-352.

[28] Hench, L. L., 1991, "Bioceramics: From Concept to Clinic," Journal of the American Ceramic Society, **74**(7) pp. 1487-1510.

[29] Best, S. M., Porter, A. E., Thian, E. S., 2008, "Bioceramics: Past, Present and for the Future," Journal of the European Ceramic Society, **28**(7) pp. 1319-1327.

[30] Daoquan, T., and Xiya, Z., 1998, "Research and Development of Bioceramics (II)," Journal of Wuhan University of Technology, **13**(2) pp. 55-61.

[31] Kokubo, T., Kim, H. -., Kawashita, M., 2004, "Bioactive Metals: Preparation and Properties," Journal of Materials Science: Materials in Medicine, **15**(2) pp. 99-107.

[32] ElBatal, H. A., Azooz, M. A., Khalil, E. M. A., 2003, "Characterization of some Bioglass-Ceramics," Materials Chemistry and Physics, **80**(3) pp. 599-609.

[33] Benzaid, R., Chevalier, J., Saadaoui, M., 2008, "Fracture Toughness, Strength and Slow Crack Growth in a Ceria Stabilized Zirconia-Alumina Nanocomposite for Medical Applications," Biomaterials, **29**(27) pp. 3636-3641.

[34] Cao, W., and Hench, L. L., 1996, "Bioactive Materials," Ceramics International, **22**(6) pp. 493-507.

[35] Greenspan, D. C., and Hench, L. L., 1975, "Chemical and Mechanical Behavior of Bioglass-Coated Alumina," Journal of Biomedical Materials Research, **10**(4) pp. 503-509.

[36] Gross, U. M., and Strunz, V., 1980, "Anchoring of Glass Ceramics of Different Solubility in the Femur of the Rat," Journal of Biomedical Materials Research, **14**(5) pp. 607-618.

[37] Andersson, O. H., Liu, G., Karlsson, K. H., 1990, "In Vivo Behaviour of Glasses in the SiO2-Na2O-CaO-P2O5-Al2O3-B2O3 System," Journal of Materials Science: Materials in Medicine, **1**(4) pp. 219-227.

[38] Gross, U., Brandes, J., Strunz, V., 1981, "Ultrastructure of the Interface between a Glass Ceramic and Bone," Journal of Biomedical Materials Research, **15**(3) pp. 291-305.

[39] Nakamura, T., Yamamuro, T., Higashi, S., 1985, "New Glass-Ceramic for Bone Replacement: Evaluation of its Bonding to Bone Tissue," Journal of Biomedical Materials Research, **19**(6) pp. 685-698.

[40] Kokubo, T., Ito, S., Sakka, S., 1986, "Formation of a High-Strength Bioactive Glass-Ceramic in the System MgO-CaO-SiO//2-P//2O//5," Journal of Materials Science, **21**(2) pp. 536-540.

[41] Yoshii, S., Kakutani, Y., Yamamuro, T., 1988, "Strength of Bonding between A-W Glass-Ceramic and the Surface of Bone Cortex," Journal of Biomedical Materials Research, **22**pp. 327-338.

228

[42] Li, S., Izui, H., and Okano, M., 2008, "Densification, Microstructure, and Behavior of Hydroxyapatite Ceramics Sintered by using Spark Plasma Sintering," Journal of Engineering Materials and Technology, Transactions of the ASME, **130**(3) pp. 0310121-0310127.

[43] Lin, K., Pan, J., Chen, Y., 2008, "Adsorption of phenol from aqueous solution by hydroxyapatite nanopowders. Part II: Kinetic, equilibrium and thermodynamic studies," 2nd International Conference on Bioinformatics and Biomedical Engineering, iCBBE 2008, Anonymous Institute of Electrical and Electronics Engineers Computer Society, Piscataway, NJ 08855-1331, United States, pp. 3119-3122.

[44] Hamadouche, M., and Sedel, L., 200, "Ceramics in Orthopedics," The Journal of Boen and Joint Surgery (Br), **82-B**(8) pp. 1095-1099.

[45] Morks, M. F., and Kobayashi, A., 2007, "Mictostructural characterization and mechanical properties of plasma sprayed hydroxyapatite coatings," 2nd International Conference on Characterization and Control of Interfaces for High Quality Advanced Materials, and Joining Technology for New Metallic Glasses and Inorganic Materials, Anonymous American Ceramic Society, Westerville, OH 43082, United States, **198,** pp. 389-394.

[46] Heleno, R. A., Wagner, N. S., and Branco, J. R. T., 2009, "Performance Evaluation of Hydroxyapatite Coatings Thermally Sprayed on Surgical Fixation Pins," Key Engineering Materials, **396-398**pp. 69-75.

[47] Jiang, W., Wang, W. D., Shi, X. H., 2008, "The Effects of Hydroxyapatite Coatings on Stress Distribution Near the Dental Implant-Bone Interface," Applied Surface Science, **255**(2) pp. 273-275.

[48] Pietrasik, J., Szustakiewicz, K., Zaborski, M., 2008, "Hydroxyapatite: An Environmentally Friendly Filler for Elastomers," Molecular Crystals and Liquid Crystals, **483**pp. 172-178.

[49] Roeder, R. K., Converse, G. L., Kane, R. J., 2008, "Hydroxyapatite-Reinforced Polymer Biocomposites for Synthetic Bone Substitutes," JOM, **60**(3) pp. 38-45.

[50] Dupraz, A. M. P., de Wijn, J. R., Meer, S. A. T. v. d., 1996, "Characterization of Silane-Treated Hydroxyapatite Powders for use as Filler in Biodegradable Composites," Journal of Biomedical Materials Research, **30**(2) pp. 231-238.

[51] Morgan, J. P., and Dauskardt, R. H., 2003, "Notch Strength Insensitivity of Self-Setting Hydroxyapatite Bone Cements," Journal of Materials Science: Materials in Medicine, **14**(7) pp. 647-653.

[52] Friedman, C. D., Costantino, P. D., Takagi, S., 1998, "BoneSourceTM Hydroxyapatite Cement: A Novel Biomaterial for Craniofacial Skeletal Tissue Engineering and Reconstruction," Journal of Biomedical Materials Research, **43**(4) pp. 428-432.

[53] Zhang, Y., Xu, H. H. K., Takagi, S., 2006, "In-Situ Hardening Hydroxyapatite-Based Scaffold for Bone Repair," Journal of Materials Science: Materials in Medicine, **17**(5) pp. 437-445.

[54] Renghini, C., Girardin, E., Fomin, A. S., 2008, "Plasma Sprayed Hydroxyapatite Coatings from Nanostructured Granules," Materials Science and Engineering B: Solid-State Materials for Advanced Technology, **152**(1-3) pp. 86-90.

[55] Sandeep, G., Varma, H. K., Kumary, T. V., 2006, "Characterization of Novel Bioactive Glass Coated Hydroxyapatite Granules in Correlation with in Vitro and in Vivo Studies," Trends in Biomaterials and Artificial Organs, **19**(2) pp. 99-107.

[56] Albee, F. H., 1920, "Studies in Bone Growth. Triple Calcium Phosphate as a Stimulus to Osteogenesis," Annals of Surgery, **7**pp. 32-36.

[57] Shackelford, J.F., 1999, "Advanced Ceramics Volume 1 Bioceramics," Gordon and Breach Science Publishers, Amsterdam, .

[58] Suchanek, W., Yashima, M., Kakihana, M., 1997, "Hydroxyapatite Ceramics with Selected Sintering Additives," Biomaterials, **18**(13) pp. 923-933.

[59] Padilla, S., Román, J., Sánchez-Salcedo, S., 2006, "Hydroxyapatite/SiO2–CaO–P2O5 Glass Materials: In Vitro Bioactivity and Biocompatibility," Acta Biomaterialia, **2**(3) pp. 331-342.

[60] Carlisle, E. M., 1970, "Silicon: A Possible Factor in Bone Calcification," Science, **167**(916) pp. 270-280.

[61] Patel, N., Brooks, R. A., Clarke, M. T., 2005, "In Vivo Assessment of Hydroxyapatite and Silicate-Substituted Hydroxyapatite Granules using an Ovine Defect Model," Journal of Materials Science: Materials in Medicine, **16**(5) pp. 429-440.

[62] Kasuga, T., Sawada, M., Nogami, M., 1999, "Bioactive Ceramics Prepared by Sintering and Crystallization of Calcium Phosphate Invert Glasses," Biomaterials, **20**(15) pp. 1415-1420.

[63] Radin, S. R., and Ducheyne, P., 1994, "Effect of Bioactive Ceramic Composition and Structure on in Vitro Behavior. III. Porous Versus Dense Ceramics," Journal of Biomedical Materials Research, **28**(11) pp. 1303-1309.

[64] Wallace, K. E., Hill, R. G., Pembroke, J. T., 1999, "Influence of Sodium Oxide Content on Bioactive Glass Properties," Journal of Materials Science: Materials in Medicine, **10**(12) pp. 697-701.

[65] Filho, O. P., La Torre, G. P., and Hench, L. L., 1996, "Effect of Crystallization on Apatite-Layer Formation of Bioactive Glass 45S5," Journal of Biomedical Materials Research, **30**(4) pp. 509-514.

[66] Oonishi, H., Hench, L. L., Wilson, J., 2000, "Quantitative Comparison of Bone Growth Behavior in Granules of Bioglass, A-W Glass-Ceramic, and Hydroxyapatite," Journal of Biomedical Materials Research, **51**(1) pp. 37-46.

[67] Phan, P. V., Grzanna, M., Chu, J., 2003, "The Effect of Silica-Containing Calcium-Phosphate Particles on Human Osteoblasts in Vitro," Journal of Biomedical Materials Research - Part A, **67**(3) pp. 1001-1008.

[68] Kannan, S., Rocha, J. H. G., Ventura, J. M. G., 2005, "Effect of Ca/P Ratio of Precursors on the Formation of Different Calcium Apatitic Ceramics-an X-Ray Diffraction Study," Scripta Materialia, **53**(11) pp. 1259-1262.

[69] Cai, S., Xu, G. H., Yu, X. Z., 2009, "Fabrication and Biological Characteristics of β-Tricalcium Phosphate Porous Ceramic Scaffolds Reinforced with Calcium Phosphate Glass," Journal of Materials Science: Materials in Medicine, **20**(1) pp. 351-358.

[70] Salih, V., Georgiou, G., Knowles, J. C., 2001, "Glass Reinforced Hydroxyapatite for Hard Tissue surgery—Part II: In Vitro Evaluation of Bone Cell Growth and Function," Biomaterials, **22**(20) pp. 2817-2824.

[71] Vrouwenvelder, W. C. A., Groot, C. G., and de Groot, K., 1993, "Histological and Biochemical Evaluation of Osteoblasts Cultured on Bioactive Glass, Hydroxylapatite, Titanium Alloy, and Stainless Steel," Journal of Biomedical Materials Research, **27**(4) pp. 465-475.

[72] Mickiewicz, R. A., 1998, "Polymer-Calcium Phosphate Composites for use as an Injectable Bone Sustitute," pp. 4-14.

[73] Currey, J. D., 1998, "Mechanical Properties of Vertebrate Hard Tissues," Proceedings of the Institution of Mechanical Engineers, Part H: Journal of Engineering in Medicine, **212**pp. 399-411.

[74] Qin, T., Yang, Z., Mo, X., 2006, "Chemical Composition and Mechanical Properties of Bio-Derived Compact Bone Scaffolds," Key Engineering Materials, **309-311 II**pp. 891-894.

[75] Rho, J., Kuhn-Spearing, L., and Zioupos, P., 1998, "Mechanical Properties and the Hierarchical Structure of Bone," Medical Engineering & Physics, **20**(2) pp. 92-102.

[76] Athanasiou, K. A., Zu, C. F., Lanctot, D. R., 2000, "Fundamentals of Biomechanics in Tissue Engineering of Bone," Tissue Engineering, **6**pp. 361-361-381.

[77] Ravaglioli, A., and Krajewski, A., 1991, "Bioceramics: Materials, properties, applications," Chapman and Hall, London, New York, .

[78] Ong, J. L., and Chan, D. C. N., 2000, "Hydroxyapatite and their use as Coatings in Dental Implants: A Review," Critical Reviews in Biomedical Engineering, **28**(5-6) pp. 667-707.

[79] Krebsbach, P. H., Kuznetsov, S. A., Bianco, P., 1999, "Bone Marrow Stromal Cells: Characterization and Clinical Application," Critical Reviews in Oral Biology & Medicine, **10**(2) pp. 165-181.

[80] Petite, H., and Quarto, R., 2005, "Engineered Bone, Tissue Engineering Intelligence Unit," Eurekah.com / Landes Bioscience, Georgetown, USA, pp. 225.

[81] Weiner, S., Addadi, L., and Wagner, H. D., 2000, "Materials Design in Biology," Materials Science and Engineering C: Biomimetic and Supramolecular Systems, **11**(1) pp. 1-8.

[82] Wilson, J., Clark, A.E., Douek, E., 1994, "Bioceramics,"Butterworth-Heinemann Ltd, Turku, Finland, pp. 415-415-422.

[83] Epple, M., and Baeuerlein, E., 2009, "Handbook of Biomineralization," Wiley-VCH Verlag GmbH & Co. KGaA, Weinheim, pp. 424.

[84] Keeting, P. E., Oursler, M. J., Wiegand, K. E., 1992, "Zeolite A Increase Proliferation, Differentiation, and Transforming Growth Factor Production in Normal Adult Human Osteoblast-Like Cells Invitro," Journal of Bone and Mineral Research, **7**(11) pp. 1281-1281-1289.

[85] Ducheyne, P., Radin, S., and King, L., 1993, "Effect of Calcium Phosphate Ceramic Composition and Structure on in Vitro Behavior. I. Dissolution," Journal of Biomedical Materials Research, **27**(1) pp. 25-34.

[86] Kontonasaki, E., Zorba, T., Papadopoulou, L., 2002, "Hydroxy Carbonate Apatite Formation on Particulate Bioglass in Vitro as a Function of Time," Crystal Research and Technology, **37**(11) pp. 1165-1171.

[87] Jha, L. J., Santos, J. D., and Knowles, J. C., 1996, "Characterization of Apatite Layer Formation on P2O5-CaO, P2O5-CaO-Na2O, and P2O5-CaO-Na2O-Al2O3 Glass Hydroxyapatite Composites," Journal of Biomedical Materials Research, **31**(4) pp. 481-486.

[88] Skipper, L. J., Sowrey, F. E., Pickup, D. M., 2004, "Structural Studies of Bioactivity in Sol-Gel-Derived Glasses by x-Ray Spectroscopy," Journal of Biomedical Materials Research - Part A, **70A**(2) pp. 354-360.

[89] Skipper, L. J., Sowrey, F. E., Pickup, D. M., 2005, "The atomic-scale interaction of bioactive glasses with simulated body fluid," 1st International Meeting on Applied Physics, APHYS-2003,

233

Anonymous Trans Tech Publications Ltd, Stafa-Zuerich, CH-8712, Switzerland, **480-481,** pp. 21-26.

[90] Brundle, C.R., Evans, C.A.J., Wilson, S., 1992, "Encyclopedia of Materials Characterization," Reed Publishing (USA) Inc., Stoneham, USA, pp. 174.

[91] Tarey, R. D., Rastogi, R. S., and Chopra, K. L., 1987, "Characterization of Thin Films by Glancing Incidence x-Ray Diffraction," The Rigaku Journal, **4**(1/2) pp. 11-11-15.

[92] Klopcic, S. B., Kovac, J., and Kosmac, T., 2007, "Apatite-Forming Ability of Alumina and Zirconia Ceramics in a Supersaturated Ca/P Solution," Biomolecular Engineering, **24**(5) pp. 467-471.

[93] Rehman, I., Knowles, J. C., and Bonfield, W., 1998, "Analysis of in Vitro Reaction Layers Formed on BioglassR using Thin-Film X-Ray Diffraction and ATR-FTIR Microspectroscopy," Journal of Biomedical Materials Research, **41**(1) pp. 162-166.

[94] Guo, L., Huang, M., Leng, Y., 2001, "Structure and Composition Comparison of Bone Mineral and Apatite Layers Formed in Vitro," Key Engineering Materials, **192-195**pp. 187-190.

[95] Ratner, B.D.,Ph.D., Hoffman, A.S.,Sc.D., Schoen, F.J.,M.D., 2004, "BIOMATERIALS SCIENCE An Introduction to Materials in Medicine," Elsevier Academic Press, London, UK, pp. 851.

[96] Kokubo, T., 1991, "Bioactive Glass Ceramics: Properties and Applications," Biomaterials, **12**pp. 155-163.

[97] Kokubo, T., and Takadama, H., 2006, "How Useful is SBF in Predicting in Vivo Bone Bioactivity?" Biomaterials, **27**(15) pp. 2907-2915.

[98] Hench, L. L., Splinter, R. J., Allen, W. C., 1972, "Bonding Mechanisms at the Interface of Ceramic Prosthetic Materials," **5**(6) pp. 117-41.

[99] Kokubo, T., Kushitani, H., Sakka, S., 1990, "Solutions Able to Reproduce in Vivo Surface-Structure Changes in Bioactive Glass-Ceramic A-W3," Journal of Biomedical Materials Research, **24**(6) pp. 721-734.

234

[100] Ohgushi, H., and Caplan, A. I., 1999, "Stem Cell Technology and Bioceramics: From Cell to Gene Engineering," Journal of Biomedical Materials Research, **48**(6) pp. 913-927.

[101] Bock, G., and Goode, J., 2003, "Tissue Engineering of Cartilage and Bone," John Wiley and Sons Inc, Chichester, UK, pp. 251.

[102] Koller, M.R., Palsson, B.O., and Masters, J.R.W., 2002, "Human Cell Culture Volume IV: Primary Hematopoietic Cells," Kluwer Academic Publishers, New York, USA, pp. 342.

[103] Silver, I. A., Deas, J., and Erecinska, M., 2001, "Interactions of Bioactive Glasses with Osteoblasts in Vitro: Effects of 45S5 Bioglass, and 58S and 77S Bioactive Glasses on Metabolism, Intracellular Ion Concentrations and Cell Viability," Biomaterials, **22**(2) pp. 175-185.

[104] Ozawa, S., and Kasugai, S., 1996, "Evaluation of Implant Materials (Hydroxyapatite, Glass-Ceramics, Titanium) in Rat Bone Marrow Stromal Cell Culture," Biomaterials, **17**(1) pp. 23-29.

[105] Holtorf, H. L., Jansen, J. A., and Mikos, A. G., 2005, "Ectopic Bone Formation in Rat Marrow Stromal cell/titanium Fiber Mesh Scaffold Constructs: Effect of Initial Cell Phenotype," Biomaterials, **26**(31) pp. 6208-6216.

[106] Mourhatch, R., 2008, "Tribological and Antiwear Mechanisms of Fluorinated Zinc Dialkyl Dithiophosphate in Comparison to Zinc Dialkyl Dithiophosphate in Engine Oils," pp. 161.

[107] Gunter, K. K., Miller, L. M., Aschner, M., 2002, "XANES Spectroscopy: A Promising Tool for Toxicology: A Tutorial," Neuro Toxicology, **23**pp. 127-146.

[108] Ferrari, E. S., Roberts, K. J., and Adams, D., 1999, "A Multi-Edge X-Ray Absorption Spectroscopy Study of the Reactivity of Zinc Di-Alkyl-Di-Thiophosphates (ZDDPS) Anti-Wear Additives: 1. an Examination of Representative Model Compounds," Wear, **236**(1-2) pp. 246-258.

[109] Liou, S., Chen, S., Lee, H., 2004, "Structural Characterization of Nano-Sized Calcium Deficient Apatite Powders," Biomaterials, **25**(2) pp. 189-196.

[110] Naftel, S. J., Sham, T. K., Yiu, Y. M., 2001, "Calcium *L*-Edge XANES Study of some Calcium Compounds," Journal of Synchrotron Radiation, **8**(2) pp. 255-257.

[111] Nakahira, A., Tamai, M., Aritani, H., 2002, "Biocompatibility of Dense Hydroxyapatite Prepared using a SPS Process," Journal of Biomedical Materials Research Part A, **62**(4) pp. 550-557.

[112] Eichert, D., Salome, M., Bleuet, P., 2006, "Contribution of X-ray microscopy to bone mineral studies," 8th International Conference on X-ray Microscopy, S. Aoki, Y. Kagoshima and Y. Suzuki, eds. **IPAP Series 7,** pp. 210-212.

[113] Eiden-Assmann, S., and Viertelhaus, M., 1999, "In-situ XANES spectroscopy at the Ca K edge of calcium phosphate compounds," HASYLAB, Hamburg, Germany.

[114] Li, D., Bancroft, G. M., Kasrai, M., 1994, "High-Resolution Si and P K- and L-Edge XANES Spectra of Crystalline SiP2O7 and Amorphous SiO2-P2O5," American Mineralogist, **79**(7-8) pp. 785-788.

[115] Li, D., Brancroft, G. M., Kasrai, M., 1993, "High-Resolution Si K- and L2,3-Edge XANES of α-Quartz and Stishovite," Solid State Communications, **87**(7) pp. 613-617.

[116] Li, D., Bancroft, G. M., Fleet, M. E., 1995, "Silicon K-Edge XANES Spectra of Silicate Minerals," Physics and Chemistry of Minerals, **22**pp. 115-122.

[117] Garvie, L. A. J., Rez, P., Alvarez, J. R., 2000, "Bonding in Alpha-Quartz (SiO_2): A View of the Unoccupied States," American Mineralogist, **85**pp. 732-738.

[118] Li, D., Bancroft, G. M., and Fleet, M. E., 1996, "Coordination of Si in Na_2O-SiO_2-P_2O_5 Glasses using K- and L-Edge XANES," American Mineralogist, **81**pp. 111-111-118.

[119] Bare, S.R., 2005, "XANES Measurements and Interpretation," UOP LLC, EXAFS Data Collection and Analysis Course, APS, July 26-29,2005, Des Plaines, IL.

[120] Henderson, G. S., 1995, "A Si K-Edge EXAFS/XANES Study of Sodium Silicate Glasses," Journal of Non-Crystalline Solids, **183**(1-2) pp. 43.

[121] Varlot, K., Kasrai, M., Bancroft, G. M., 2001, "X-Ray Absorption Study of Antiwear Films Generated from ZDDP and Borate Micelles," Wear, **249**(12) pp. 1029-1035.

[122] Oliver, W. C., and Pharr, G. M., 1992, "An Improved Technique for Determining Hardness and Elastic Modulus using Load and Displacement Sensing Indentation Experiments," Journal of Materials Research, **7**(6) pp. 1564-1580.

[123] Roop Kumar, R., and Wang, M., 2002, "Modulus and Hardness Evaluations of Sintered Bioceramic Powders and Functionally Graded Bioactive Composites by Nano-Indentation Technique," Materials Science and Engineering A, **338**(1-2) pp. 230-236.

[124] Rho, J. -., Tsui, T. Y., and Pharr, G. M., 1997, "Elastic Properties of Human Cortical and Trabecular Lamellar Bone Measured by Nanoindentation," Biomaterials, **18**(20) pp. 1325-1330.

[125] Zysset, P. K., Edward Guo, X., Edward Hoffler, C., 1999, "Elastic Modulus and Hardness of Cortical and Trabecular Bone Lamellae Measured by Nanoindentation in the Human Femur," Journal of Biomechanics, **32**(10) pp. 1005-1012.

[126] Roop Kumar, R., and Wang, M., 2001, "Growth of Brushite Crystals in Sodium Silicate Gel and their Characterization," Key Engineering Materials, **192-195**pp. 19-22.

[127] Dey, A., Mukhopadhyay, A. K., Gangadharan, S., "Nanoindentation Study of Microplasma Sprayed Hydroxyapatite Coating," Ceramics International, **In Press, Accepted Manuscript**.

[128] Cheng, G. J., Pirzada, D., Cai, M., 2005, "Bioceramic Coating of Hydroxyapatite on Titanium Substrate with Nd-YAG Laser," Materials Science and Engineering: C, **25**(4) pp. 541-547.

[129] Wang, M., Ye, X. J., and Khor, K. A., 2004, "Assessing interfacial properties of plasma sprayed bioceramic coating on metal substrate using indentation techniques," Transactions - 7th World Biomaterials Congress, Anonymous Biomaterials 2004 Congress Managers, Sydney, NSW 2001, Australia, pp. 1789.

[130] Chowdhury, S., Thomas, V., Dean, D., 2005, "Nanoindentation on Porous Bioceramic Scaffolds for Bone Tissue Engineering," Journal of Nanoscience and Nanotechnology, **5**(11) pp. 1816-1820.

237

[131] Tang, C. Y., Uskokovic, P. S., Tsui, C. P., "Influence of Microstructure and Phase Composition on the Nanoindentation Characterization of Bioceramic Materials Based on Hydroxyapatite," Ceramics International, **In Press, Accepted Manuscript**.

[132] Khor, K. A., Li, H., and Cheang, P., 2003, "Characterization of the Bone-Like Apatite Precipitated on High Velocity Oxy-Fuel (HVOF) Sprayed Calcium Phosphate Deposits," Biomaterials, **24**(5) pp. 769-775.

[133] Shibata, Y., He, L. H., Toda, Y., 2008, "Micromechanical Evaluation of Mineralized Multilayers," Journal of Biomechanics, **41**(16) pp. 3414-3418.

[134] Tang, B., Ngan, A. H. W., and Lu, W. W., 2007, "An Improved Method for the Measurement of Mechanical Properties of Bone by Nanoindentation," Journal of Materials Science: Materials in Medicine, **18**(9) pp. 1875-1881.

[135] Nagase, M., Abe, Y., Chigira, M., 1992, "Toxicity of Silica-Containing Calcium Phosphate Glasses Demonstrated in Mice," Biomaterials, **13**(3) pp. 172.

[136] Ye, F., Lu, X., Lu, B., 2007, "A Long-Term Evaluation of Osteoinductive HA/β-TCP Ceramics in Vivo: 4.5 Years Study in Pigs," Journal of Materials Science: Materials in Medicine, **18**(11) pp. 2173-2178.

[137] Matsushita, N., Terai, H., Okada, T., 2004, "A New Bone-Inducing Biodegradable Porous β-Tricalcium Phosphate," Journal of Biomedical Materials Research - Part A, **70**(3) pp. 450-458.

[138] Moore, D. C., Chapman, M. W., and Manske, D., 1987, "Evaluation of Biphasic Calcium Phosphate Ceramic for use in Grafting Long-Bone Diaphyseal Defects," Journal of Orthopaedic Research, **5**(3) pp. 356-365.

[139] Oktar, F. N., Genç, Y., Göller, G., 2004, "Sintering of synthetic hydroxyapatite compacts," Proceedings of the 8th Conference and Exhibition of the European Ceramic Society, June 29,2003 - July 03, Anonymous Trans Tech Publications Ltd, Istanbul, Turkey, **264-268,** pp. 2087-2090.

[140] Erkmen, Z. E., Genç, Y., and Oktar, F. N., 2007, "Microstructural and Mechanical Properties of Hydroxyapatite-Zirconia Composites," Journal of the American Ceramic Society, **90**(9) pp. 2885-2892.

[141] Oktar, F. N., 2007, "Microstructure and Mechanical Properties of Sintered Enamel Hydroxyapatite," Ceramics International, **33**(7) pp. 1309-1314.

[142] Cihlar, J., Buchal, A., and Trunec, M., 1999, "Kinetics of Thermal Decomposition of Hydroxyapatite Bioceramics," Journal of Materials Science, **34**(24) pp. 6121-6131.

[143] Tamai, M., Isshiki, T., Nishio, K., 2006, "Transmission Electron Microscopic Observation of a Metastable Phase on the Thermal Decomposition Process of Ca-Deficient Hydroxyapatite," Journal of Materials Science, **41**(2) pp. 525-530.

[144] Liao, C., Lin, F., Chen, K., 1999, "Thermal Decomposition and Reconstitution of Hydroxyapatite in Air Atmosphere," Biomaterials, **20**(19) pp. 1807-1813.

[145] Barralet, J., Knowles, J. C., Best, S., 2002, "Thermal Decomposition of Synthesised Carbonate Hydroxyapatite," Journal of Materials Science: Materials in Medicine, **13**(6) pp. 529-533.

[146] Sayer, M., Stratilatov, A. D., Reid, J., 2003, "Structure and Composition of Silicon-Stabilized Tricalcium Phosphate," Biomaterials, **24**(3) pp. 369-382.

[147] Langstaff, S., Sayer, M., Smith, T. J. N., 2001, "Resorbable Bioceramics Based on Stabilized Calcium Phosphates. Part II: Evaluation of Biological Response," Biomaterials, **22**(2) pp. 135-150.

[148] Leonor, I. B., Ito, A., Onuma, K., 2002, "In Situ Study of Partially Crystallized Bioglass [Registered Trademark] and Hydroxylapatite in Vitro Bioactivity using Atomic Force Microscopy," Journal of Biomedical Materials Research, **62**(1) pp. 82-88.

[149] Zhang, X., Jiang, F., Groth, T., 2008, "Preparation, Characterization and Mechanical Performance of Dense β-TCP Ceramics with/without Magnesium Substitution," Journal of Materials Science: Materials in Medicine, **19**(9) pp. 3063-3070.

239

[150] Ruan, J. M., Zou, J. P., Zhou, J. N., 2006, "Porous Hydroxyapatite-Tricalcium Phosphate Bioceramics," Powder Metallurgy, **49**(1) pp. 66-69.

[151] Tu, J., Wang, Y. J., Chen, X. F., 2007, "Bio-Mineralization Properties of Bioglass Anf Effect of Ionic Products from Bioglass Dissolution on Osteoblast Functions," Journal of Inorganic Materials, **22**pp. 123-127.

[152] Li, D., Bancroft, G. M., Kasrai, M., 1994, "X-Ray Absorption Spectroscopy of Silicon Dioxide (SiO2) Polymorphs: The Structural Characterization of Opal," American Mineralogist, **79**(7-8) pp. 622-632.

[153] Terekhov, V. A., Kashkarov, V. M., Turishchev, S. Y., 2008, "Structure and Optical Properties of Silicon Nanopowders," Materials Science and Engineering: B, **147**(2-3) pp. 222-225.

[154] Henderson, G. S., and St-Amour, J. C., 2004, "A Si K-Edge XANES Study of Ti Containing alkali/alkaline-Earth Silicate Glasses," Chemical Geology, **213**pp. 31-40.

[155] Yin, Z., Kasrai, M., Bancroft, G. M., 1995, "X-Ray-Absorption Spectroscopic Studies of Sodium Polyphosphate Glasses," Physical Review B: Condensed Matter, **51**(23) pp. 742.

[156] Sato, S., Solomon, D., Hyland, C., 2005, "Phosphorus Speciation in Manure and Manure-Amended Soils using XANES Spectroscopy," Environmental Science and Technology, **39**(19) pp. 7485-7491.

[157] Gungor, K., Jurensen, A., and Karthikeyan, K. G., 2007, "Determination of Phosphorus Specification in Dairy Manure using XRD and XANES Spectroscopy," Journal of Environmental Quality, **36**pp. 1856-1863.

[158] Eichert, D., Salome, M., Banu, M., 2005, "Preliminary Characterization of Calcium Chemical Environment in Apatitic and Non-Apatitic Calcium Phosphates of Biological Interest by X-Ray Absorption Spectroscopy," Spectrochimica Acta - Part B Atomic Spectroscopy, **60**(6) pp. 850-858.

[159] Sowrey, F. E., Skipper, L. J., Pickup, D. M., 2004, "Systematic Empirical Analysis of Calcium-Oxygen Coordination Environment by Calcium K-Edge XANES," Physical Chemistry Chemical Physics, **6**(1) pp. 188-192.

[160] Blood, D.C., Studdert, V.P., and Gay, C.C., 2007, "Saunders Comprehensive Veterinary Dictinary," Elsevier, Inc., St. Louis, Missouri, USA, pp. 2172.

[161] Thompson, I. D., and Hench, L. L., 1998, "Mechanical Properties of Bioactive Glasses, Glass-Ceramics and Composites," Proceedings of the Institution of Mechanical Engineers, Part H: Journal of Engineering in Medicine, **212**(2) pp. [d]127-136.

[162] Wang, X., Lu, X., Jiang, F., 2008, "The Formation of Bone-Like Apatite on the Surfaces of the Bioceramics and Biocomposites," Gongneng Cailiao/Journal of Functional Materials, **39**(4) pp. 647-650.

[163] Weng, J., Liu, Q., Wolke, J. G. C., 1997, "Formation and Characteristics of the Apatite Layer on Plasma-Sprayed Hydroxyapatite Coatings in Simulated Body Fluid," Biomaterials, **18**(15) pp. 1027-1035.

[164] Xiao, B., Yang, W., Zhou, D., 2007, "Apatite Forming on the Surface of Apatite-wollastonite/β-Tricalcium Phosphate Bioactive Ceramic," Key Engineering Materials, **336-338 II**pp. 1692-1695.

[165] Fan, Y., and Lu, X., 2008, "A Study of Apatite Formation on Natural Nano-hydroxyapatite/chitosan Composite in Simulated Body Fluid," Frontiers of Materials Science in China, **2**(1) pp. 91-94.

[166] Yoon, S. I., Lee, Y. -., Kim, K. N., 2006, "A Comparison of the Bone-Like Apatite Formation Potency between Hydroxyapatite and β-Tricalcium Phosphate in Glass Ionomer Dental Luting Cement," Key Engineering Materials, **309-311 II**pp. 885-888.

[167] Kokubo, T., 1998, "Apatite Formation on Surfaces of Ceramics, Metals and Polymers in Body Environment," Acta Materialia, **46**(7) pp. 2519-2527.

[168] Kokubo, T., Kim, H., and Kawashita, M., 2003, "Novel Bioactive Materials with Different Mechanical Properties," Biomaterials, **24**(13) pp. 2161-2175.

[169] Murugan, R., Ramakrishna, S., and Panduranga Rao, K., 2006, "Nanoporous Hydroxy-Carbonate Apatite Scaffold made of Natural Bone," Materials Letters, **60**(23) pp. 2844-2847.

[170] Hamagami, J., Yamaguchi, G., Kanamura, K., 2002, "In situ AFM observation of apatite formation on Bioglass," 14th International Symposium on Ceramics in Medicine-Annual Meeting of the International Society for Ceramics in Medicine BIOCERAMICS'01 (ISCM), November 14,2001 - November 17, Anonymous Trans Tech Publications Ltd, Palm Springs, CA, United states, **218-220,** pp. 279-282.

[171] Martin, R. A., Twyman, H., Qiu, D., 2009, "A Study of the Formation of Amorphous Calcium Phosphate and Hydroxyapatite on Melt Quenched Bioglass&reg using Surface Sensitive Shallow Angle X-Ray Diffraction," Journal of Materials Science: Materials in Medicine, **20**(4) pp. 883-888.

[172] Kim, H., Himeno, T., Kokubo, T., 2005, "Process and Kinetics of Bonelike Apatite Formation on Sintered Hydroxyapatite in a Simulated Body Fluid," Biomaterials, **26**(21) pp. 4366-4373.

[173] Peitl, O., Dutra Zanotto, E., and Hench, L. L., 2001, "Highly Bioactive P2O5-Na2O-CaO-SiO2 Glass-Ceramics," Journal of Non-Crystalline Solids, **292**(1-3) pp. 115-126.

[174] Ryu, H., Lee, J., Seo, J., 2004, "Novel Bioactive and Biodegradable Glass Ceramics with High Mechanical Strength in the CaO-SiO2-B2O3 System," Journal of Biomedical Materials Research - Part A, **68**(1) pp. 79-89.

[175] Fathi, M. H., Hanifi, A., and Mortazavi, V., 2008, "Preparation and Bioactivity Evaluation of Bone-Like Hydroxyapatite Nanopowder," Journal of Materials Processing Technology, **202**(1-3) pp. 536-542.

[176] So, K., Fujibayashi, S., Neo, M., 2005, "Improvement of Bioactivity of Hydroxyapatite Ceramics by Adding Glass," Key Engineering Materials, **284-286**pp. 381-384.

[177] Ragel, C. V., Vallet-Regí, M., and Rodríguez-Lorenzo, L. M., 2002, "Preparation and in Vitro Bioactivity of hydroxyapatite/solgel Glass Biphasic Material," Biomaterials, **23**(8) pp. 1865-1872.

[178] Wang, C. X., Zhou, X., and Wang, M., 2004, "Influence of Sintering Temperatures on Hardness and Young's Modulus of Tricalcium Phosphate Bioceramic by Nanoindentation Technique," Materials Characterization, **52**(4-5) pp. 301-307.

[179] Zhang, C., Leng, Y., and Chen, J., 2001, "Elastic and Plastic Behavior of Plasma-Sprayed Hydroxyapatite Coatings on a Ti-6Al-4V Substrate," Biomaterials, **22**(11) pp. 1357-1363.

[180] Patel, N., Best, S. M., and Bonfield, W., 2005, "Characterisation of Hydroxyapatite and Substituted-Hydroxyapatites for Bone Grafting," Journal of the Australasian Ceramic Society, **41**(2) pp. 1-22.

[181] Balas, F., Pérez-Pariente, J., and Vallet-Regí, M., 2003, "In Vitro Bioactivity of Silicon-Substituted Hydroxyapatites," Journal of Biomedical Materials Research - Part A, **66**(2) pp. 364-375.

[182] Gibson, I. R., Hing, K. A., Revell, P. A., 2002, "Enhanced in vivo response to silicate-substituted hydroxyapatite," 14th International Symposium on Ceramics in Medicine-Annual Meeting of the International Society for Ceramics in Medicine BIOCERAMICS'01 (ISCM), November 14,2001 - November 17, Anonymous Trans Tech Publications Ltd, Palm Springs, CA, United states, **218-220,** pp. 203-206.

[183] Park, J., and Lakes, R.S., 2007, "Biomaterials An Introduction," Springer, New York, NY, USA, pp. 561.

[184] Doremus, R. H., 1992, "Bioceramics," Journal of Materials Science, **27**(2) pp. 285-297.

BIOGRAPHICAL INFORMATION

Hande Demirkıran received her B.Sc. in Metallurgical and Materials Science Engineering from Yıldız Technical University in Istanbul in Turkey in 2001. Following that she started her graduate study in Metallurgical and Materials Science Engineering in Istanbul Technical University in Turkey, and she received her M.S. in 2003. She then began working as a full time graduate student towards her Ph.D. degree in 2004 in University of Texas at Arlington under the supervision of Dr. Pranesh B. Aswath. Her research focuses on processing and evaluation of bioceramic materials for orthopedics and tissue culture applications. And lastly she received her doctorate in Material Science and Engineering at the University of Texas at Arlington in 2009.